DISSERTATION

THE DYNAMICS OF HADLEY CIRCULATION VARIABILITY AND CHANGE

Submitted by

Nicholas Alexander Davis

Department of Atmospheric Science

In partial fulfillment of the requirements

For the Degree of Doctor of Philosophy

Colorado State University

Fort Collins, Colorado

Summer 2017

Doctoral Committee:

Advisor: Thomas Birner

David A. Randall
Elizabeth A. Barnes
Subhas K. Venayagamoorthy
William J. Randel

ABSTRACT

THE DYNAMICS OF HADLEY CIRCULATION VARIABILITY AND CHANGE

The Hadley circulation exerts a dominant control on the surface climate of earth's tropical belt. Its converging surface winds fuel the tropical rains, while subsidence in the subtropics dries and stabilizes the atmosphere, creating deserts on land and stratocumulus decks over the oceans. Because of the strong meridional gradients in temperature and precipitation in the subtropics, any shift in the Hadley circulation edge could project as major changes in surface climate. While climate model simulations predict an expansion of the Hadley cells in response to greenhouse gas forcings, the mechanisms remain elusive.

An analysis of the climatology, variability, and response of the Hadley circulation to radiative forcings in climate models and reanalyses illuminates the broader landscape in which Hadley cell expansion is realized. The expansion is a fundamental response of the atmosphere to increasing greenhouse gas concentrations as it scales with other key climate system changes, including polar amplification, increasing static stability, stratospheric cooling, and increasing global-mean surface temperatures. Multiple measures of the Hadley circulation edge latitudes co-vary with the latitudes of the eddy-driven jets on all timescales, and both exhibit a robust poleward shift in response to forcings. Further, across models there is a robust coupling between the eddy-driving on the Hadley cells and their width.

On the other hand, the subtropical jet and tropopause break latitudes, two common observational proxies for the tropical belt edges, lack a strong statistical relationship with

the Hadley cell edges and have no coherent response to forcings. This undermines theories for the Hadley cell width predicated on angular momentum conservation and calls for a new framework for understanding Hadley cell expansion.

A numerical framework is developed within an idealized general circulation model to isolate the mean flow and eddy responses of the global atmosphere to radiative forcings. It is found that it is primarily the eddy response to greenhouse-gas-like forcings that causes Hadley cell expansion. However, the mean flow changes in the Hadley circulation itself crucially mediate this eddy response such that the full response comes about due to eddy-mean flow interactions. A theoretical scaling for the Hadley cell width based on moist static energy is developed to provide an improved framework to understand climate change responses of the general circulation.The scalingpredicts that expansion is driven by increases in the surface latent heat flux and the width of the rising branch of the circulation and opposed by increases in tropospheric radiative cooling. A reduction in subtropical moist static energy flux divergence by the eddies is key, as it tilts the energetic balance in favor of expansion.

ACKNOWLEDGEMENTS

I thank my committee for their invaluable comments and guidance on this dissertation, and my family and friends for their support and understanding. Thomas, you have helped me hone a skeptical eye toward my own research, taught me patience, and instilled in me the willingness to take the hard path.

You can never get lost on an adventure.

TABLE OF CONTENTS

1 The Hadley Circulation

It was inevitable that the Hadley circulation would become a major focus of early atmospheric science. Three hundred years ago, the idea of unraveling the physics governing passing weather disturbances in the midlatitudes and the afternoon thunderstorms in the tropics must have seemed impossible. By contrast the steady surface easterlies and westerlies, each occupying distinct zones on the earth, must have seemed like a good place to start. It's tempting to argue that our understanding of the Hadley circulation has progressed substantially beyond the ideas of its namesake, George Hadley, in 1735. But perhaps it's worth examining Hadley's own words to decide how much they've been rewritten rather than merely refined.

In 1686, Edmund Halley crafted a model of the general circulation from hand-drawn maps of surface winds over the oceans. Previous scholars had thought that the rotation of the earth on its axis produced the tropical easterlies, or " trade winds", as the "loose air" let the rotating surface of the earth rotate past. Halley challenged this notion and instead argued that the sun drove the winds. He imagined that as the sun passed over the earth, it heated the air directly below, and as the sun moved from east to west, the cooler air far to the east would rush in toward the west and toward the equator to try to fill in the less-dense air heated by the sun. Through mass continuity, Halley thought air must be constantly rising on the equator and flowing poleward. While his proposed mechanism for the trade winds was wrong, it had at least introduced the sun as a thermodynamic driver of the circulation.

It was George Hadley, a lawyer and amateur meteorologist, who captured the essence of the circulation that now bears his name. Hadley's model was a pioneering combination of ideas that are still as worth pondering today as they were in 1735 (Hadley, 1735):

> Thus I think the N.E. Winds on this Side of the Equator, and the S.E. on the other Side, are fully accounted for. The same Principle as necessarily extends to the Production of the West Trade-Winds without the Tropicks; the Air rarefied by the Heat of the Sun about the Equatorial Parts, being removed to make room for the Air from the cooler Parts, must rise upwards from the Earth, and as it is a Fluid, will then spread itself abroad over the other Air, and so its Motion in the upper Regions must be to the N. and S. from the Equator. Being got up at a Distance from the Surface of the Earth, it will soon lose great Part of its Heat, and thereby acquire Density and Gravity sufficient to make it approach its Surface again, which may be supposed to be by that Time 'tis arrived at those Parts beyond the Tropicks where the Westerly Winds are found. Being suppos'd at first to have the Velocity of the Surface of the Earth at the Equator, it will have a greater Velocity than the Parts it now arrives at; and thereby become a westerly Wind, with Strength proportionable to the Difference of Velocity, which in several Revolutions will be reduced to a certain Degree, as is laid before, of the Easterly Winds, at the Equator. And thus the Air will continue to circulate, and gain and lose velocity by Turns from the Surface of the Earth or Sea, as it approaches to, or recedes from the Equator.

Hadley identified the salient dynamics for any thermally-direct circulation on a rotating body: temperature gradients, rotation, and friction. Density differences due to differential solar heating drive the circulation, as Hadley argued, but Hadley also gave the circulation a dynamic character that Halley did not - air transported to higher latitudes within the Hadley circulation cools, becomes more dense, and sinks, bringing heat to the extratropics. Direct circulations act to transport heat from warm to cold regions - whether it is the Hadley circulation, a thunderstorm, or convection in a pot of boiling water.

It is true that Hadley was not exactly right. Angular momentum conservation, and not linear momentum conservation, is the momentum conservation law in a rotating atmosphere (Ferrel, 1856). But it would be hard to argue that the basics of Hadley's

physical arguments for the circulation weren't on the right track. As air moves poleward from the equator and becomes closer to the axis of rotation, it gains westerly momentum relative to the surface of the earth, producing westerlies in the upper troposphere. Hadley argued that the air that sank in the midlatitudes would eventually lose some momentum (presumably through friction) before flowing equatorward, creating the tropical easterlies.

In reality, another process works with the general circulation to complete the angular momentum cycle and drive the midlatitude surface westerlies: waves. In the midlatitudes, large-scale waves in earth's atmosphere dominate the poleward energy (Trenberth and Solomon, 1994) and angular momentum transport (Schneider, 2006), with the angular momentum transport peaking at the edge of the Hadley circulation (Lorenz, 1967). Rossby waves generated in the midlatitude eddy-driven jet propagate equatorward, drawn to the strong meridional planetary vorticity gradient in the tropics and the strong meridional relative vorticity gradient in the subtropical jet (Charney and Drazin, 1961). By virtue of their easterly phase speeds, the waves remove easterly momentum (i.e., leave westerly momentum) in the midlatitudes, accelerating the surface winds. As the waves propagate equatorward into the subtropical jet at the edge of the Hadley circulation, they eventually encounter zonal-mean zonal winds that are greater than their critical velocity. At this point the waves decay and break, depositing their easterly momentum (i.e., removing westerly momentum) from the subtropical upper troposphere. This initially decreases the local zonal-mean zonal wind, the consequence of which is a reduction in the equatorward Coriolis torque by the zonal-mean zonal wind. This reduction in the Coriolis torque drives an acceleration of the poleward meridional wind in the Hadley circulation, which produces an eastward Coriolis torque that eventually balances the westward deceleration by the

breaking Rossby waves. Rossby waves also flux heat poleward early in their life cycle, cooling the subtropics and warming the midlatitudes and the poles. This subtropical cooling is balanced by a convergence of thermal energy by the Hadley circulation. At the surface, moisture is transported to the equator by the trade winds, where it rises into the Intertropical Convergence Zone. Condensation converts this latent energy into thermal and potential energy, which is then transported poleward by the Hadley circulation and converged in the subtropics, balancing the eddy cooling. Together, the Hadley circulation - a massive moist-to-dry energy heat engine - and the eddies - organized turbulent motions that mix cool air equatorward and warm air poleward - create a seamless poleward transport of energy (Trenberth and Stepaniak, 2003).

Modern theoretical perspectives of the circulation generally fall into two categories: those focused on energy transport and those focused on eddy dynamics. Hadley's conception of the circulation as a giant heat transport mechanism with its own internal thermodynamics is at times completely removed from the model of the circulation as a response to eddy forcings. In these latter models of the circulation, the Hadley cells, or at least the parts of the cells away from the equator, are considered a Coriolis torque response to the momentum forcings on the zonal flow by Rossby waves. Which of these two models of the circulation dominate, or are both equally important but alone inadequate to explain the width of the circulation and its response to forcings?

Crucially, a Hadley-cell-like circulation[1] can exist in an atmosphere without eddies. Any theory of the Hadley circulation must be able to link back to basic thermodynamics

[1]Here, Hadley "circulation" refers to the sum of the characteristics of the circulation - the zonal-mean meridional flow, the zonal flow in the Walker cells, and their combined impacts on radiative, momentum, heat, and moisture budgets, while Hadley "cell" refers strictly to the zonal-mean meridional cells

because they are the lowest-order driver of such a circulation. This is not an impossible task. The eddy- and thermodynamically-driven flow in the Hadley cells are coupled (Kim and Lee, 2001). And the eddies, though they are often viewed through the lens of momentum, are ultimately driven by thermodynamic gradients. The challenge posed in this dissertation is to bring these two perspectives together and construct a more unified perspective of Hadley cell expansion - one that does not live in the limits of either axisymmetric, thermally-direct circulations or purely eddy-driven, quasigeostrophic dynamics, but instead at their intersection.

1.1 The Hadley Cells and the Tropical Belt

Earth's tropical belt can be defined by the band of rainy equatorial regions bordered by the arid subtropics to the north and the south. The Hadley circulation significantly influences the surface climate of the tropical belt. Converging easterly near-surface trade winds transport moisture into the Intertropical Convergence Zone, a meandering front of convection that brings rain to the equatorial latitudes and heats tropical air through the condensation of water vapor. This heated air rises through the troposphere and diverges poleward into the upper troposphere of both hemispheres, eventually subsiding in the subtropics where it dries and stabilizes the atmosphere against convection. Because of the strong meridional gradients in temperature and precipitation at the edges of the tropical belt, any shift in its edges could drive major changes in surface climate (Birner et al., 2014).

There is mounting evidence that such changes are already taking place. Soil moisture (Dorigo et al., 2012), precipitation (New et al., 2001; Zhang et al., 2007), and sea surface

salinity (Helm et al., 2010) trends over the past several decades consistently indicate an intensification and poleward shift of the hydrological cycle. The intensification is widely considered to be driven primarily by increasing water vapor concentrations in a warming atmosphere (Held and Soden, 2006). A concurrent weakening of the Hadley circulation is predicted in models, reflecting the reduction in upward mass flux in a warmer climate (Mitas and Clement, 2006; Vecchi and Soden, 2007). The circulation changes that drive poleward shifts in the hydrological cycle are not as well understood. Further subtropical drying and a poleward expansion of arid lands is projected to continue (Lu et al., 2007; Scheff and Frierson, 2012; Feng and Fu, 2013).

It is difficult if not impossible to directly measure the Hadley circulation (Waliser et al., 1999). Accordingly, numerous metrics have been created to assess the Hadley cell edge latitudes, some motivated by physics and some motivated by the availability of particular observational datasets. The subtropical tropopause break, tropopause height statistics, the subtropical jets, the structure of outgoing longwave radiation, the structure of precipitation minus evaporation, sea-level pressure, and the zonal wind at the surface have all been used to infer the Hadley cell edge latitudes.

In the tropics, the tropopause generally occurs at an altitude of 16 km, while in the midlatitudes it occurs at altitudes ranging from 8 to 12 km. Bisecting these regimes is the subtropical jet core, which straddles the upper troposphere and lower stratosphere in the subtropics. A result of the strong meridional temperature gradient in the subtropics, the subtropical jet is sustained against the deceleration due to Rossby wave breaking by the poleward flux of zonal momentum in the Hadley circulation. Through quasigeostrophic scaling, the surface zonal-mean zonal wind occurs at the latitude where there is no net

convergence or divergence of zonal momentum by the eddies - essentially, the division between the Hadley and Ferrel cells. This reversal in the sign of the wind from easterlies to westerlies necessarily occurs where the gradient in sea-level pressure reverses sign in the subtropical ridge. Finally, subsidence in the Hadley circulation at its poleward edges dries the atmosphere and opposes the formation of free-tropospheric clouds. Marine stratocumulus form at the top of the boundary layer on the eastern side of ocean basins where the combined Hadley-Walker circulation has its strongest subsidence. However, they have an emission temperature close to that of the surface. Thus, wherever there is large-scale subsidence in the Hadley circulation, radiation easily escapes to space. Not surprisingly, outgoing longwave radiation maximizes in the subtropics. That these metrics are interrelated and proxies for one another is a hypothesis, and it is unclear how they relate on interannual timescales and in their response to forcings (Seidel et al., 2008; Davis and Rosenlof, 2012).

Evidence of tropical expansion has been reported based on satellite observations of outgoing longwave radiation (Hu and Fu, 2007; Johanson and Fu, 2009; Hu et al., 2011; Fu and Lin, 2011) and total column ozone (Hudson et al., 2003; Hudson, 2012). Observational estimates of the tropical belt width based on dynamical fields, such as the subtropical ridges in sea level pressure, also indicate tropical expansion, though the trends are weaker than those based on outgoing longwave radiation and precipitation (Hu et al., 2011).

Other metrics for the tropical belt edge latitudes, such as the latitudes of the jet streams (Archer and Caldeira, 2008; Fu and Lin, 2011; Davis and Birner, 2013) and the latitudes of the subtropical tropopause breaks (Seidel and Randel, 2007; Birner, 2010; Davis and Rosenlof, 2012; Lucas et al., 2012; Davis and Birner, 2013; Ao and Hajj, 2013;

Lucas and Nguyen, 2015) indicate historical tropical expansion, as well. An expansion of the Hadley cells has been detected in reanalyses (Hu and Fu, 2007; Johanson and Fu, 2009; Stachnik and Schumacher, 2011; Davis and Rosenlof, 2012; Davis and Birner, 2013; Nguyen et al., 2013; Chen et al., 2014). Tropical expansion estimates based on reanalyses, however, may suffer from spurious trends and discontinuities in basic meteorological fields (Trenberth et al., 2001; Bengtsson et al., 2004). The rate of Hadley cell expansion and even the mean strength of the Hadley cells varies among the reanalyses (Stachnik and Schumacher, 2011), which could indicate that the meridional winds are not well constrained. There is also significant uncertainty in the observed rate of tropical expansion because it is highly variable for different metrics and data products (Birner, 2010; Davis and Rosenlof, 2012; Davis and Birner, 2013; Lucas et al., 2014).

Attributing surface impacts to tropical expansion and attributing tropical expansion itself to particular climate forcings is difficult given the number of external forcings changing over the historical period, as well as the impact of natural climate variability on the trends. Factors such as the Pacific Decadal Oscillation, the El Niño-Southern Oscillation (Lu et al., 2008), and the Southern Annular Mode influence the tropical belt width and may explain non-negligible fractions of its historical trend (Grassi et al., 2012; Allen et al., 2014; Lucas and Nguyen, 2015; Garfinkel et al., 2015).

1.2 Modeling

Climate model simulations offer an avenue for assessing the response of the Hadley cells and tropical belt to different climate forcings and forcing evolutions, and long integrations

minimize the impact of interannual variability (Hawkins and Sutton, 2009). Both Lu et al. (2009) and Hu et al. (2013) found that significant tropical expansion occurs only when greenhouse gas concentrations increase in historical climate simulations. Increasing greenhouse gas concentrations in future climate simulations similarly cause the tropical belt to expand relative to its preindustrial control width (Gastineau et al., 2008), with the amount of expansion scaling with the concentration of greenhouse gases (Lu et al., 2007; Tao et al., 2015). However, Adam et al. (2014) have shown that the Hadley cell width is generally sensitive to changes in both mean sea surface temperatures and meridional temperature gradients. Any climate forcing that modifies mean temperatures or their gradients could thus drive variations in the tropical belt width. Stratospheric ozone depletion and its resulting polar stratospheric cooling has been argued to be a potentially dominant driver of Southern Hemisphere tropical expansion (Polvani et al., 2011b; Min and Son, 2013), and ozone recovery over the coming decades may oppose any future greenhouse-gas-driven expansion (Son et al., 2009; Polvani et al., 2011a). Black carbon, tropospheric ozone (Allen et al., 2012), and aerosols (Allen and Sherwood, 2011; Allen et al., 2014) may have also played a role in historical tropical expansion, especially in the Northern Hemisphere. While examining the response of climate models to realistic sets of past and future forcings is appealing, it is not ideal for identifying how the tropical belt responds to particular forcings. Many climate forcing agents are simultaneously changing in these simulations, and separating their effects is often intractable.

Idealized modeling, which involves changing a single climate forcing or model parameter, complements those more realistic simulations. The models are often simplified versions of fully-coupled climate models that may solve only the equations of motion and

thermodynamics without explicitly resolving radiation and convection. They are thus attractive for studying mechanisms of change and variability in the climate system, as there are fewer resolved processes and feedbacks. Polvani and Kushner (2002) and Kushner and Polvani (2004) found that stratospheric cooling in such an idealized model produced a poleward shift of the midlatitude jet. It also produced a poleward shift in the pattern of surface easterlies and westerlies which indicates an expansion of the tropical belt. While Lorenz and DeWeaver (2007) found that cooling the stratosphere and raising the height of the tropopause was sufficient to produce a poleward shift of the tropospheric jets, Tandon et al. (2011) found that stratospheric cooling without perturbing the tropopause height was sufficient to drive an expansion of the Hadley cells. Similar to Tandon et al. (2011), Maycock et al. (2013) found that idealized increases in stratospheric water vapor drove enhanced stratospheric cooling and a poleward shift of the tropospheric jets. Warming in the troposphere alone can also drive an expansion of the Hadley cells (Frierson et al., 2007b; Tandon et al., 2013). Thus, stratospheric cooling and tropospheric warming can both drive poleward shifts in the circulation.

However, idealized models do not explicitly model clouds or cloud-related feedbacks. Convection is a fundamental aspect of the Hadley circulation (Frierson, 2007) and cloud radiative effects can impact modeled circulation changes (Ceppi et al., 2012, 2014; Voigt and Shaw, 2015). Some studies have begun to bridge this gap by examining the response of comprehensive models to idealized and more realistic greenhouse gas forcings. While Grise and Polvani (2014) found evidence that Southern Hemisphere Hadley cell expansion scales with climate sensitivity, Vallis et al. (2015) found little relationship between the transient climate response and Hadley cell expansion. Studies have also found evidence of a

seasonality (Polvani et al., 2011b) and a lack of seasonality (McLandress et al., 2011) in Southern Hemisphere expansion. The scaling and seasonality seem to emerge if there is a steady greenhouse gas forcing (e.g., as in Polvani et al. (2011b) and Grise and Polvani (2014)). Work is still needed to understand this response and how it may scale with other changes in the climate system.

1.3 Potential mechanisms for change

The mechanisms for Hadley circulation expansion remain elusive, despite the abundance of idealized and comprehensive model studies. The Held (2000) scaling theory has become the dominant framework for understanding the Hadley circulation response to greenhouse gas forcings. It is simple and successful at explaining variations in the width of the Hadley circulation seasonally (Kang and Lu, 2012) and over a wide range of earth-like climates (Frierson et al., 2007b). Based on the two-layer Phillips' model of baroclinic instability, the scaling argues that the edge of the Hadley cell is the latitude at which the angular-momentum-conserving poleward flow in the upper layer of the circulation becomes baroclinically unstable.

Central to the scaling theory are two free parameters set by external forcings, such as the sun, and intrinsic features of the earth system, such as the concentration of greenhouse gases: the tropopause height and the dry bulk static stability of the troposphere, or the difference in temperature between the tropopause and the surface. Over reasonable variations of these two parameters, the static stability term dominates (Frierson et al., 2007b). Static stability increases in the lower and middle troposphere in response to

increases in greenhouse gas concentrations, primarily through moist adiabatic adjustment (Romps, 2011). In the Held (2000) framework, increased static stability acts to further stabilize the poleward flow in the Hadley circulation, delaying the onset of baroclinic instability to higher latitudes and thus causing the Hadley cells to expand.

However, the evidence that static stability drives Hadley circulation expansion has been drawn from equilibrium changes in general circulation model experiments. There are other major climate system changes, such as stratospheric cooling, Arctic amplification, weakening of meridional temperature gradients, and increases in specific humidity and the strength of the hydrologic cycle, that could all contribute to expansion. As a result, the evidence that static stability increases in particular drive Hadley circulation expansion is unsatisfying; there is only evidence that static stability increases and Hadley cell expansion scale at equilibrium. There are more critical issues with the scaling theory itself, including the applicability of the two-layer instability criterion to continuous atmospheres (discussed thoroughly in Korty and Schneider (2008)). Further, while the theory can be mistaken for including the effects of eddies, by assuming angular momentum conservation it is essentially an axisymmetric formulation.

Korty and Schneider (2008) provide a unique perspective on the eddy-mean flow processes governing the width of the Hadley circulation. The tropics are characterized by easterly surface winds maintained against friction by net eddy momentum flux divergence, while the midlatitudes are characterized by westerly surface winds maintained against friction by net eddy momentum flux convergence. The latitudes with zonal-mean easterlies and westerlies are equivalently latitudes with net meridional convergence and divergence of the wave activity flux (Edmon et al., 1980), or the sink and source latitudes of Rossby

waves. In general, wave activity propagates upward from the surface in baroclinic zones before turning equatorward toward the subtropical jet where the absolute vorticity gradient is large. Thus, the edge of the Hadley circulation should occur near the latitude where the vertical wave activity flux reaches the upper-troposphere, i.e., the latitude where meridional eddy fluxes of potential temperature are deep enough to reach the upper-troposphere and where the wave activity transitions from upward to meridional propagation. Korty and Schneider (2008) show that a scaling based on the supercriticality, a nondimensional ratio that measures the slope of isentropic surfaces, predicts the Hadley circulation edge latitude across a wide range of simulated climates.

This theory, while grounded in a substantially more realistic treatment of eddy dynamics, is diagnostic and neglects two potentially important processes. First, the Hadley circulation, through meridional fluxes of heat and radiative cooling, can itself modify subtropical static stability and meridional temperature gradients. Second, the Hadley circulation can act as a gatekeeper for waves propagating into the tropics and subtropics by modifying the upper-tropospheric zonal winds through heat and momentum fluxes (Schneider and Bordoni, 2008). If there is a thermally-direct, axisymmetric response to greenhouse gas forcings, it will likely modify the upper-tropospheric momentum budget and hence modify the distribution of wave-breaking and its resulting eddy fluxes. From an energetic perspective, an axisymmetric response necessarily modifies the potential temperature structure of the atmosphere, impacting not only the supercriticality but also the background thermodynamic gradients that give rise to the eddies in the first place. In other words, it is physically possible (and arguably probable) that Hadley circulation expansion depends upon the superposition and interaction of the eddy and mean-flow

responses. In a post-hoc analysis it would be difficult if not impossible to untangle this relationship.

In summary, there are multiple avenues through which tropical processes and the Hadley circulation itself can mediate its interaction with extratropical eddies. Whether these pathways are important for the response to forcings has not been sufficiently explored. This is not condemnation of scaling theories or previous modeling studies, but merely an argument that previously presented evidence is not yet sufficient to support the role of particular dynamical processes in driving Hadley cell expansion. A more careful, clean approach to separating the mean-flow and eddy responses to greenhouse gas forcings is necessary to provide further insight.

This dissertation is organized as follows. In Chapter 2, the basic equilibrium response of the Hadley circulation and climate system to greenhouse gas and solar forcings is explored to illuminate the broader landscape in which circulation change occurs. Chapter 3 examines the variability and response of multiple subtropical and extratropical circulation phenomena, including an unusual relationship between eddy fluxes, the Hadley circulation, and a common climate model parameter, to parse out the most robust eddy-mean flow relationships. Synthesizing these previous results, Chapter 4 uses an idealized general circulation model to study the mean flow and eddy-mediated response of the Hadley circulation to greenhouse-gas-like forcings and uses these results to build a new conceptual theory for the Hadley circulation width in Chapter 5. The model and its modifications are described in the appendix following the concluding discussion.

2 The Hadley Circulation Response to Greenhouse Gas Forcings

Before delving into the particular dynamics of Hadley cell expansion, it is worth assessing the myriad changes that occur in the climate system in response to greenhouse gas forcings. We will first examine the equilibrium response of the Hadley circulation to highly idealized forcings in the Geoengineering Model Intercomparison Project (GeoMIP) (Kravitz et al., 2011). GeoMIP, a companion project to the Coupled Model Intercomparison Project Phase 5 (CMIP5) (Taylor et al., 2012), is designed to improve the understanding of the response of the earth system to idealizations of different proposed climate geoengineering activities. Geoengineering impacts aside, the GeoMIP experiments offer a unique opportunity to study the response of fully-coupled climate models to very simple climate forcings, which may provide insight into the processes responsible for observed past and possible future tropical width changes.

While numerous climate forcings can impact the width of the tropical belt, we focus on variations in carbon dioxide and insolation simulated in GeoMIP. Our analysis is based on monthly-mean output from nine climate models (Table 2.1) that performed three sets of experiments: the GeoMIP Geoengineering 1 (G1) experiment (Kravitz et al., 2011), the preindustrial control (piControl), and the abrupt quadrupled carbon dioxide ($4\times CO_2$) experiments in CMIP5 (Taylor et al., 2012). The piControl experiment fixes all climate forcings at preindustrial levels to provide an estimate of the unperturbed climate system and will be the control experiment in this study. The $4\times CO_2$ experiment applies an instantaneous quadrupling of piControl carbon dioxide concentrations, while the G1

Table 2.1: The model name, modeling group or agency, the $4\times CO_2$ experiment top-of-atmosphere radiative forcing relative to piControl, and the G1 experiment residual top-of-atmosphere radiative forcing relative to the piControl experiment for each of the nine models examined. All radiative forcings are from Huneeus et al. (2014) and are in W/m^2. Information on the radiative forcings in the CSIRO-Mk3L-1-2 model is unavailable.

Model	$4\times CO_2$ radiative forcing (Wm^{-2})	G1 radiative forcing (Wm^{-2})
CanESM2	8.0	0.0
CCSM4	6.2	-0.5
CSIRO-Mk3L-1-2	N/A	N/A
GISS-E2-R	7.8	1.4
HadGEM2-ES	6.4	0.4
IPSL-CM5A-MR	6.2	0.2
MIROC-ESM	8.7	0.0
MPI-ESM-LR	8.6	0.2
NorESM1-M	6.8	0.4

experiment balances this abrupt quadrupling with a decrease in the solar constant such that the global-mean top-of-atmosphere radiative forcing is zero (Kravitz et al., 2011). This crudely models the effect of a global climate intervention scheme based on albedo modification (National Research Council, 2015), but more generally tests the impact of a decrease in insolation on the climate system, with some relevance for paleoclimate research. We only use the G1 experiment from GeoMIP because of its simple forcing scheme that is applied uniformly in all models.

For the G1 experiment, not all models achieved a perfect cancellation of the top-of-atmosphere radiative forcings. Table 2.1 lists the top-of-atmosphere radiative forcing in the $4\times CO_2$ experiment and the residual top-of-atmosphere radiative forcing in the G1 experiment after the solar constant reduction for each model (e.g., Huneeus et al. (2014)).

Because the $4\times CO_2$ and G1 experiments involve an abrupt forcing at the start of the simulation, we discard the first 5 years of each experiment, a conservative choice as the circulation metrics adjust to the abrupt forcing within two years. The piControl

simulations from each model range from 500 to 3000 model years, the $4\times CO_2$ simulations range from 140 to 150 model years, and the G1 simulations range from 50 to 100 model years. For each experiment, we use the same number of model years from each model simulation based on the shortest simulation, e.g., for the piControl experiment we use the first 500 years from all of the model simulations.

All calculations and analyses use monthly-mean model output. For testing the significance of changes in the tropical belt edge latitudes and width we use two-sided Student's t-tests for the difference of means with unequal variances and sample sizes. The tests thus take into account the different lengths and internal variability of each experiment. We use the effective degrees of freedom, which are calculated using the lag-1 autocorrelation of the monthly-mean anomalies (Bretherton et al., 1999). This yields approximately 400 degrees of freedom for the G1 simulations and 4000 degrees of freedom for the piControl simulations, with some inter-model variability. Differences are deemed statistically significant for $p \leq 0.05$ (the 95% confidence level).

We define the tropical belt edge latitudes as the latitudes where the vertically-averaged mean meridional streamfunction is zero, poleward of its tropical maximum (minimum) in the Northern (Southern) Hemisphere (Davis and Birner, 2013). The tropical belt width is defined as the difference, in degrees latitude, between the Northern and Southern Hemisphere edge latitudes. The mean meridional streamfunction is the vertical integral of the zonal-mean meridional mass flux between a given level and the top of the atmosphere, and is the primary field used to study variations in the Hadley cells' width and intensity. It

is expressed mathematically as

$$\Psi(p,\phi) = \frac{2\pi a \cos(\phi)}{g} \int_p^0 [v] dp \tag{1}$$

where Ψ is the mean meridional streamfunction at the pressure p and latitude ϕ, $[v]$ is the zonal-mean meridional wind, $a = 6.371 \times 10^6$ m is the mean radius of the earth, and $g = 9.81$ ms^{-2} is the acceleration due to gravity. While the Hadley cell edge latitudes are often calculated as the latitudes where the 500 hPa streamfunction is zero, the choice of a single, arbitrary pressure level subjects the metric to spurious trends due to mean-state changes, such as a deepening of the troposphere, and to inter-model differences in the circulation (Birner, 2010; Davis and Rosenlof, 2012; Davis and Birner, 2013). Instead we vertically-average the streamfunction in pressure before calculating the edge latitudes. The interpretation of this vertical average of the streamfunction is simple: it measures the average meridional overturning circulation strength at a given latitude, and the latitude where it is zero indicates the separation of the Hadley and Ferrel cells.

We note that this metric and our analyses focus on the zonal mean. However, historical tropical expansion exhibits significant zonal asymmetries (Chen et al., 2014; Lucas and Nguyen, 2015), and some zonally asymmetric dynamics contribute to the longitudinal structure of the meridional overturning circulation (Karnauskas and Ummenhofer, 2014).

2.1 Climatology

Before analyzing the 4×CO_2 and G1 experiments, we will first examine the climatology of the tropical belt edge latitudes in the piControl experiment (Fig. 2.1). The median

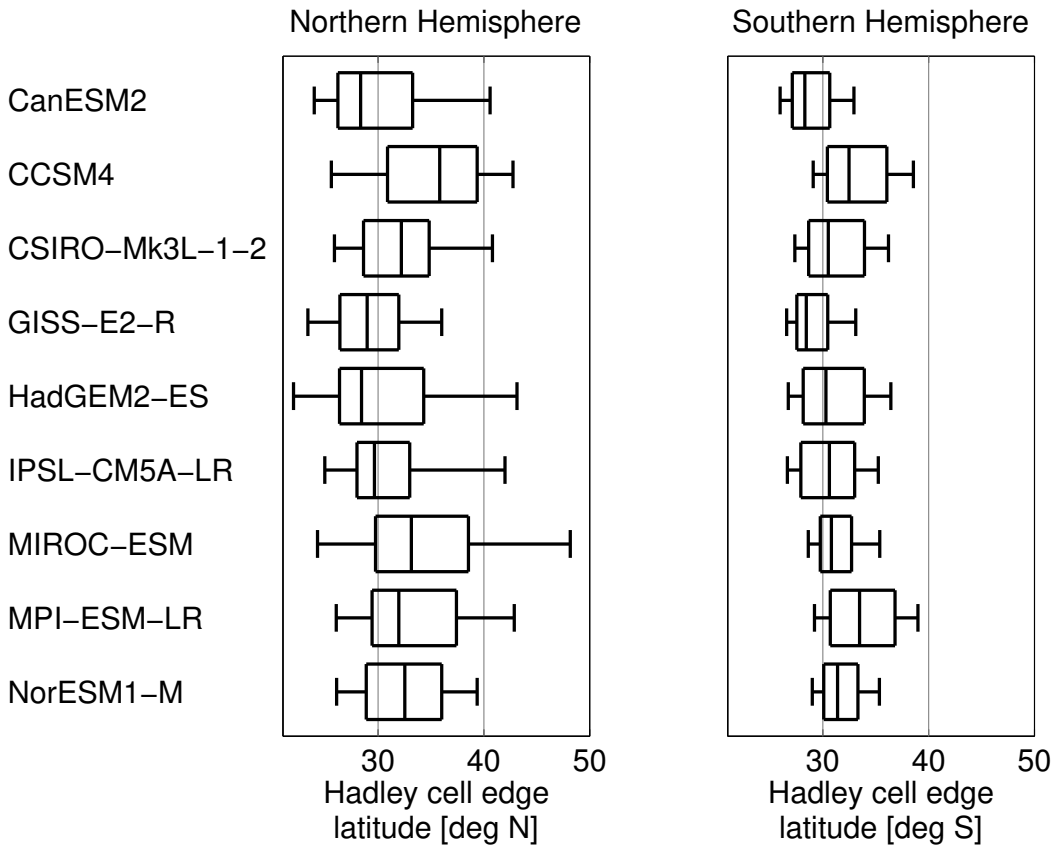

Figure 2.1: The piControl experiment climatology of the tropical belt edge latitudes for each of the nine models. The middle bar of each box represents the median and the left and right bars of each box represent the lower and upper quartiles, respectively, of the tropical belt edge latitudes. Whiskers indicate the maximum and minimum tropical belt edge latitude for the piControl experiment.

.

tropical belt edge latitudes in each hemisphere are comparable among the models. In general, models with more equatorward edge latitudes in one hemisphere have more equatorward edge latitudes in the other hemisphere ($R^2 = 0.7$). There is greater interannual variability in the Northern Hemisphere edge latitude, which is borne out in reanalyses and observations (Davis and Birner, 2013). Some models, including the IPSL-CM5A-LR and GISS-E2-R models, have little interannual variability in their Northern Hemisphere edge latitudes.

2.2 Temperature response

We will first characterize the temperature changes in each model between the $4\times CO_2$ and piControl and between the G1 and piControl experiments. The motivation to examine the basic zonal-mean temperature response in all nine models is threefold: (1) temperature changes are associated with changes in the tropical belt width (e.g., Adam et al. (2014)), (2) the zonal-mean temperature response may provide information about a model's sensitivity to different forcings, and (3) examining only the multi-model-mean may obscure important information about the robustness of the response and its inter-model variations.

Quadrupled carbon dioxide concentrations drive the expected surface and tropospheric warming and stratospheric cooling (Manabe and Wetherald, 1967) (Fig. 2.2). The tropical upper-tropospheric warming is due to moist adiabatic adjustment communicating the surface warming to upper levels (Held et al., 1993; Romps, 2011). Enhanced Arctic warming, or "Arctic amplification", is partly due to decreases in surface albedo brought on by reductions in snow cover and sea ice (Pithan and Mauritsen, 2014) and enhanced downwelling longwave radiation through the so-called "ice-insulation" feedback (Burt et al., 2016). The stratospheric cooling is partly driven by enhanced infrared cooling to space due to increased carbon dioxide concentrations. Other processes such as changes in the strength of the Brewer-Dobson circulation may contribute to the latitudinal structure of the cooling. While all models capture this canonical greenhouse gas response in zonal-mean temperature, the temperature changes vary by nearly a factor of three. The IPSL-CM5A-LR has the strongest response with 13 K upper-tropospheric and Arctic warming, while the CCSM4 model has the weakest response with 5 K upper-tropospheric

and 8 K Arctic warming. The IPSL-CM5A-LR model also has the strongest surface temperature increase in the abrupt 4xCO$_2$ experiment at 6.1 K, while the CCSM4 model has the second weakest response at 3.5 K.

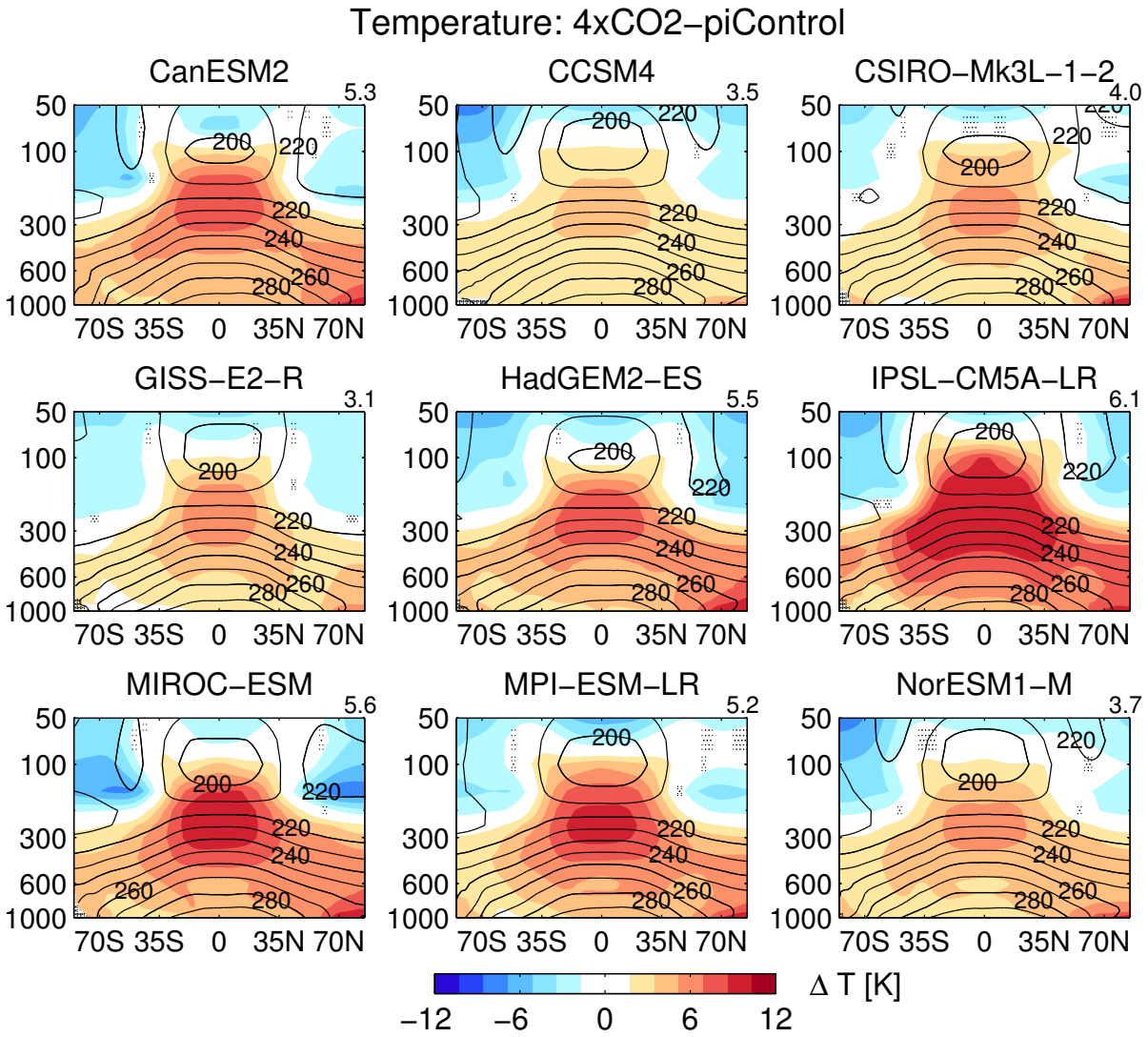

Figure 2.2: The difference in the zonal-mean temperature between the 4×CO$_2$ and piControl experiments for each of the nine models. The 4×CO$_2$ experiment temperature minus the piControl experiment temperature is shown in shading (Kelvin), while the piControl experiment temperature is shown by the black contours (Kelvin). Stippling indicates differences not significant at the 95% confidence level. The change in global-mean surface temperature (Kelvin) between the 4xCO$_2$ and piControl experiments is shown in the upper right of each panel.

The G1 experiment's solar constant reduction generally balances most of the warming from quadrupled carbon dioxide (Fig. 2.3). Because Fig. 2.3 shows the difference in temperature between the G1 and piControl experiments, it can be interpreted as the temperature response to $4\times CO_2$ that is *not* counteracted by the solar constant reduction in the G1 experiment. In the G1 experiment, the stratosphere is cooler than it is in the piControl experiment in all models. This is likely because of the reduction in absorbed solar radiation by ozone and infrared radiation emission by the (still enhanced) carbon dioxide concentrations. However, the troposphere is marginally cooler in some models (CCSM4, GISS-E2-R, and MIROC-ESM) and marginally warmer in others (CanESM2, HadGEM2-ES, and MPI-ESM-LR). Unlike the robust temperature response in the $4\times CO_2$ experiment, there is no robust residual warming or cooling in the troposphere in G1 compared to piControl. Contrary to expectations, the model with the strongest residual radiative forcing in the G1 experiment, GISS-E2-R, does not have a warmer troposphere, while one of the models with a radiative forcing of zero, CanESM2, has a significantly warmer troposphere.

2.3 Tropical belt width response

Quadrupled carbon dioxide drives a statistically significant expansion of the tropical belt as measured by the Hadley cell edge latitudes in both the Southern and Northern Hemisphere (Fig. 2.4). There is a large spread in the magnitude of tropical expansion, though, with values ranging from 1 degree of total (width) expansion in the CSIRO-Mk3L-1-2 model to nearly 7 degrees of total expansion in the IPSL-CM5A-LR

model (the model with the strongest temperature response to quadrupled carbon dioxide). The nearly factor of seven difference in the circulation response is far larger than the factor of two to three difference in the temperature response.

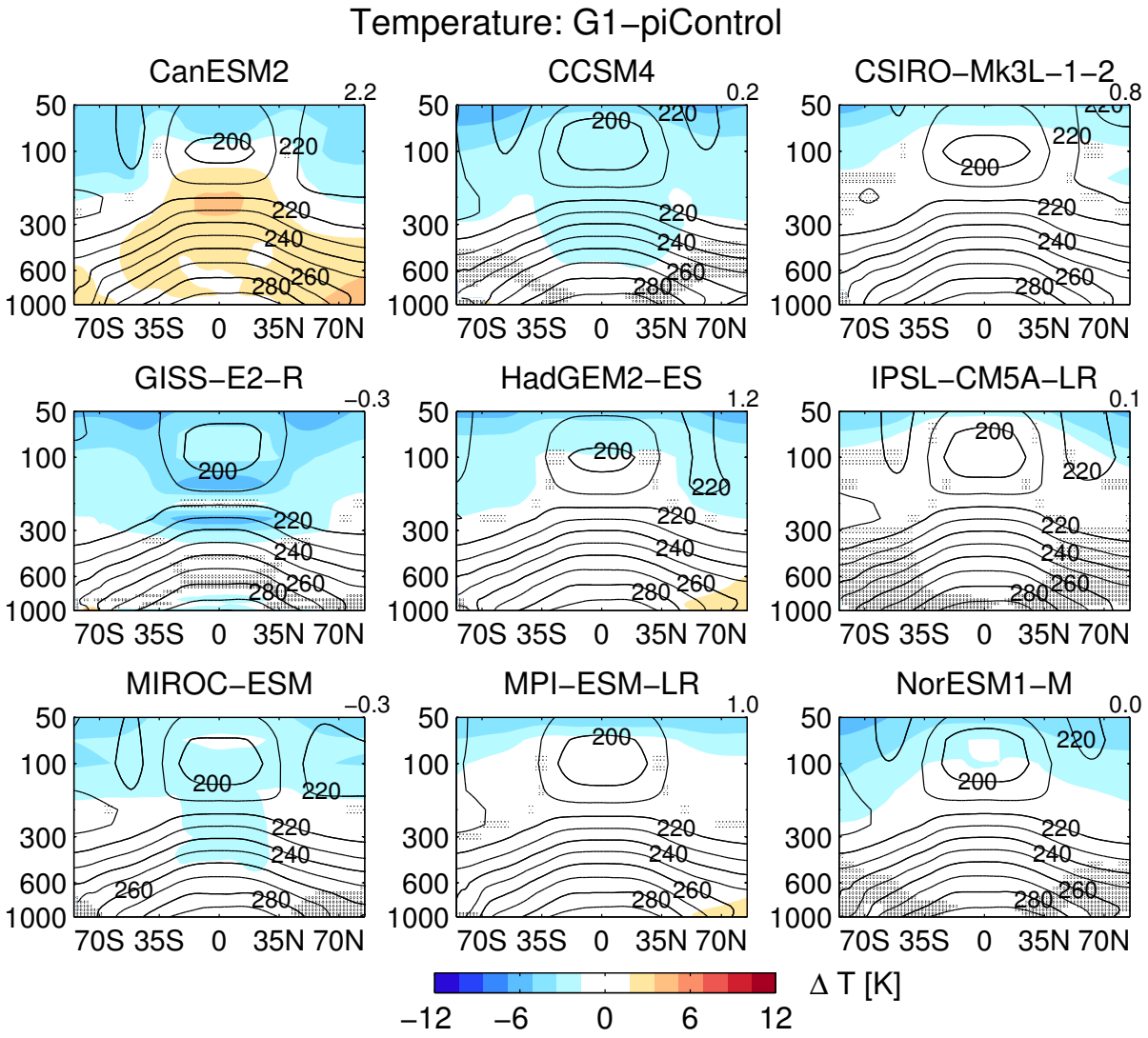

Figure 2.3: The difference in the zonal-mean temperature between the G1 and piControl experiments for each of the nine models. The G1 experiment temperature minus the piControl experiment temperature is shown in shading (Kelvin), while the piControl experiment temperature is shown by the black contours (Kelvin). Stippling indicates differences not significant at the 95% confidence level. The change in global-mean surface temperature (Kelvin) between the G1 and piControl experiments is shown in the upper right of each panel.

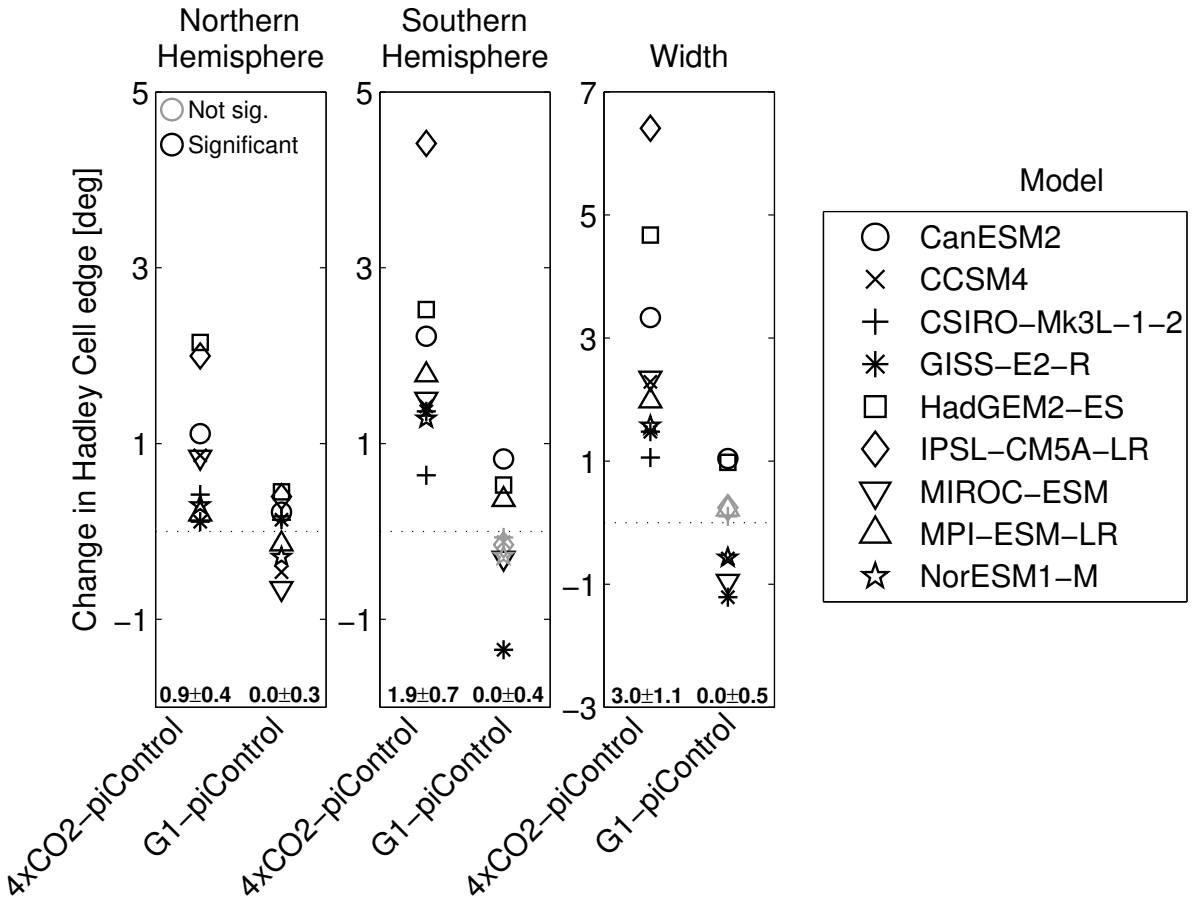

Figure 2.4: The change in the Hadley cell edge latitudes and width between the $4\times CO_2$ and piControl experiments and between the G1 and piControl experiments, for the Northern Hemisphere and Southern Hemisphere edge latitudes and for the total change in Hadley cell width (Width). Positive values indicate poleward expansion or an increase in width. Models with edge latitude or width changes significant at the 95% confidence level are shown in black. The mean change in the tropical belt width or edge latitude and its 95% confidence interval in degrees latitude is shown at the bottom of each plot.

More surprising is that the Southern Hemisphere expansion is on average twice the Northern Hemisphere expansion (Fig. 2.4). Southern Hemisphere stratospheric ozone depletion has been argued to be a dominant driver of the more rapid observed expansion of the Southern Hemisphere Hadley cell (Polvani et al., 2011b; Min and Son, 2013; Waugh et al., 2015). However, the results here indicate that even with a hemispherically-symmetric climate forcing which does not include ozone changes, the tropical belt responds

asymmetrically with greater expansion in the Southern Hemisphere. Furthermore, the expansion is strongest in the Southern Hemisphere in austral summer and autumn (Fig. 2.5), consistent with Grise and Polvani (2016). These are the seasons when the stratospheric cooling due to ozone depletion is expected to have its greatest impact on Southern Hemisphere expansion trends as ozone is depleted throughout austral spring.

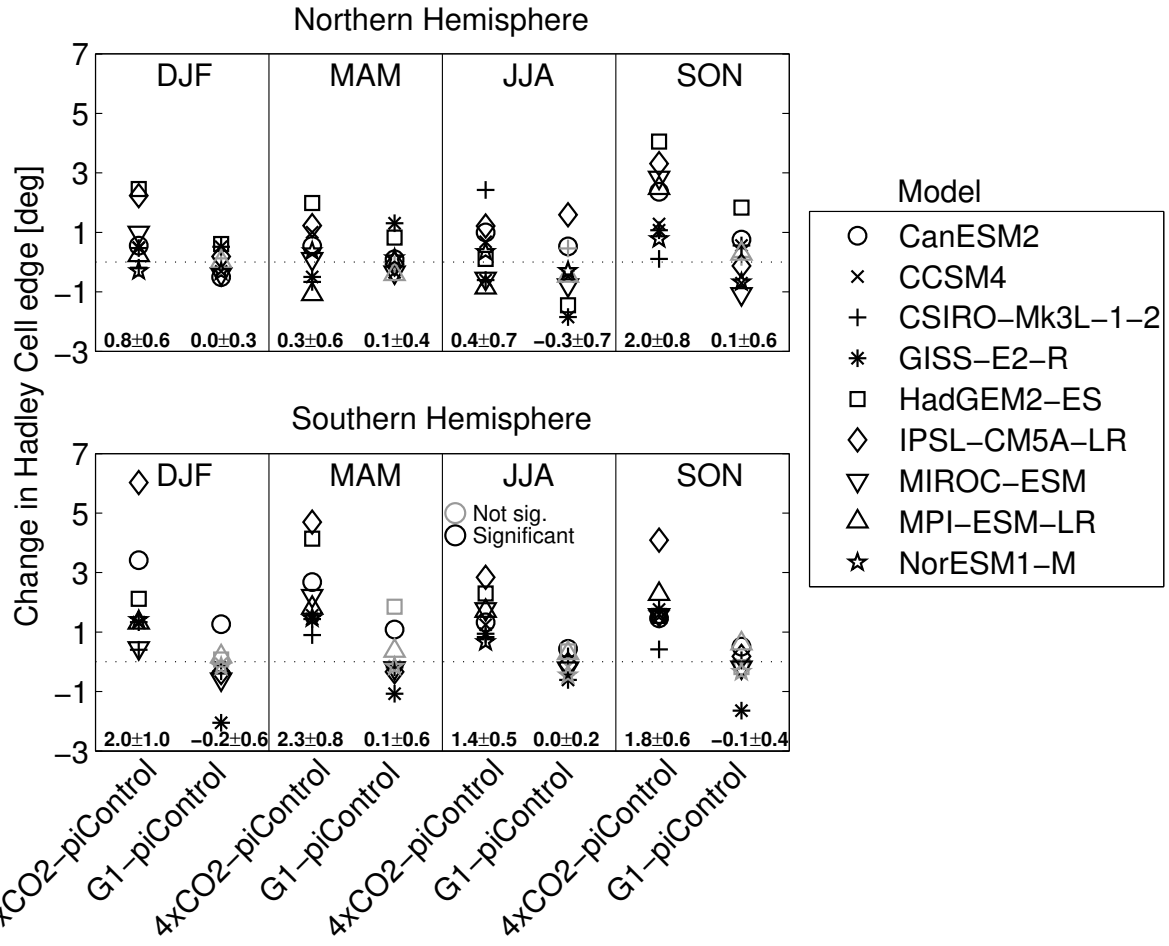

Figure 2.5: The seasonal change in the Hadley cell edge latitudes and width between the $4\times CO_2$ and piControl experiments and between the G1 and piControl experiments, for the Northern Hemisphere and Southern Hemisphere edge latitudes. Positive values indicate poleward expansion. Models with edge latitude changes significant at the 95% confidence level are shown in black. Values are shown for December through February (DJF), March through May (MAM), June through August (JJA), and September through November (SON). The mean change in the tropical belt width or edge latitude and its 95% confidence interval in degrees latitude is shown at the bottom of each plot.

The solar constant reduction in the G1 experiment counteracts most of the CO_2-driven expansion in the $4\times CO_2$ experiment, despite the residual stratospheric cooling. This suggests that stratospheric cooling on the order of 1-6 K with the maximum cooling over the poles (Fig. 2.3) is not sufficient to appreciably widen the tropical belt. However, the altitude of the cooling may be an important factor in determining whether the tropical belt responds or not. For example, in idealized dry simulations Tandon et al. (2011) found that extratropical stratospheric cooling must extend down to the tropopause to drive a strong circulation response. In the G1 experiment, the cooling is well above the typical height of the extratropical tropopause (Fig. 2.3), which is generally located at approximately 250-300 hPa. This may be why there is no robust tropical expansion in the G1 experiment. Processes in fully-coupled models that are not represented in idealized dry simulations, including cloud and radiation feedbacks, could act to further damp the response of the tropical belt to stratospheric cooling.

For most models the differences between their G1 and piControl experiment edge latitudes and width are small, often less than ± 0.5 degrees latitude (with an average difference of zero). Just as there is no robust tropospheric temperature difference between the G1 and piControl experiments, there is no robust residual tropical expansion or contraction. Changes in the tropical belt width are not statistically significantly correlated with the residual radiative forcings in the G1 experiment.

In the Northern Hemisphere (Fig. 2.5), tropical expansion in response to increased carbon dioxide concentrations is approximately constant from December-January-February (DJF) through June-July-August (JJA). It is twice as large in September-October-November (SON). The enhanced expansion in boreal autumn is

consistent with realistic (Hu et al., 2013; Kang and Lu, 2012) and more idealized (Kang and Lu, 2012) CMIP5 forcing simulations and with historical reanalyses (Hu and Fu, 2007). While Allen et al. (2012) proposed that the observed tropical expansion in Northern Hemisphere summer and autumn was driven by the combined effects of black carbon and tropospheric ozone, it appears that increased carbon dioxide concentrations alone could also drive some of this enhanced expansion. As a caveat, however, the seasonality of Northern Hemisphere tropical expansion is not particularly robust as the tropical belt contracts in some models and seasons in response to quadrupled carbon dioxide concentrations. This may arise from the opposing effects of the direct radiative forcing and changes in sea surface temperatures on land-sea temperature contrasts (Shaw and Voigt, 2015). The resulting circulation response appears to be senstitive to which of the two dominate.

To explore whether the large range in the responses and the asymmetric response in the two hemispheres are associated with any particular zonal-mean temperature structures, we composite the difference in temperature between the $4\times CO_2$ and piControl experiments in the four models with the greatest and in the four models with the least total tropical expansion (Fig. 2.6). Both groups show the same general pattern of tropospheric warming and stratospheric cooling. In fact, the difference in the temperature response to quadrupled carbon dioxide between the models with the greatest and the least tropical expansion itself resembles the temperature response to quadrupled carbon dioxide. An exception can be found in the upper stratosphere, where the cooling is similar between the two subsets of models. There is not a substantial difference between the separate composites on Northern and Southern Hemisphere expansion, but both show a slightly weaker stratospheric cooling signal (not shown). Overall there are no unique relationships in the strength of the tropical

upper-tropospheric amplification, the Arctic amplification, the surface warming, or the stratospheric cooling. Rather, these temperature responses all consistently scale among the models with greater tropical expansion.

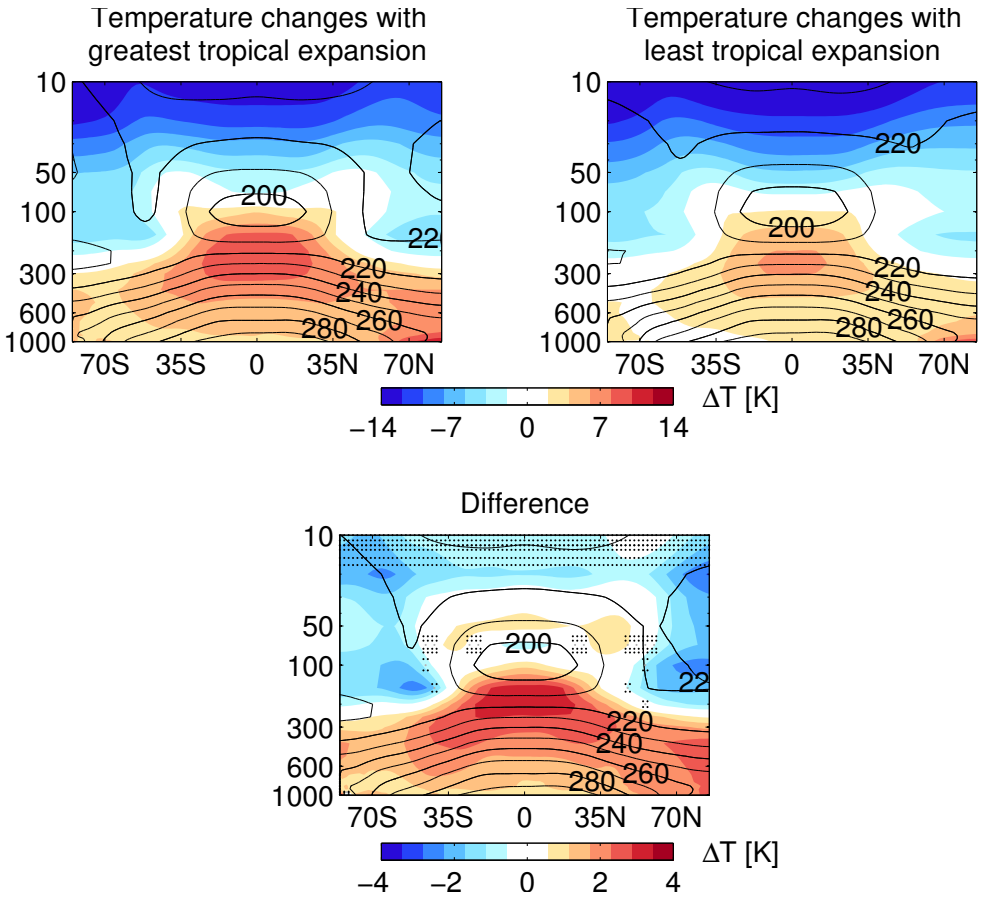

Figure 2.6: The difference in zonal-mean temperature between the $4\times CO_2$ and piControl experiments in the four models with the greatest tropical expansion (upper left) and in the four models with the least tropical expansion (upper right). The $4\times CO_2$ experiment minus the piControl experiment temperatures are shown in shading (Kelvin), while the piControl experiment temperatures are shown by the black contours (Kelvin). The difference in the $4\times CO_2$ experiment minus the piControl experiment temperatures between the models with the greatest and least tropical expansion is shown on the bottom, with shading indicating the difference (Kelvin) and black contours indicating the mean piControl experiment temperature (Kelvin) for all models. Stippling indicates changes not significant at the 95% confidence level.

2.4 Inter-model differences in the tropical width response and associated thermodynamic changes

Subtropical static stability increases due to tropical upper-tropospheric amplification may be important for driving tropical expansion (Fig. 2.6). Held (2000) derived a scaling theory for the Hadley cell width based on the critical shear for baroclinic instability in the Phillips two-layer model (Phillips, 1951). If one assumes that the poleward flow in the Hadley cells conserves angular momentum, and that the flow terminates at the latitude of the onset of baroclinic instability, then the edge latitude of the Hadley cell is only a function of the tropopause height and the gross static stability (the difference between the potential temperature of the tropopause and the surface). Increases in static stability or tropopause height would both act to further stabilize the flow against baroclinic instability and allow the Hadley cell to expand poleward. Lu et al. (2008) found changes in static stability to be strongly correlated with changes in the Hadley cell edge latitude, and a cursory scale analysis shows that the scaling theory is dominated by the static stability term for typical variations in static stability and tropopause height (Frierson et al., 2007b). For these reasons we will focus exclusively on changes in subtropical static stability.

The Held (2000) scaling theory has been used to study tropical expansion in models ranging from dry dynamical cores to fully-coupled climate models (Frierson et al., 2007b; Lu et al., 2007, 2008), although modified scaling theories that relax the angular momentum conservation constraint (Kang and Lu, 2012), as well as theories based on other criteria (Lu et al., 2008; Korty and Schneider, 2008; Tandon et al., 2013; Levine and Schneider, 2015) may be more realistic. Similar to Levine and Schneider (2015), we evaluate the gross

static stability, hereafter "subtropical static stability", at the tropical belt edge latitude. We define the subtropical static stability as the difference in potential temperature between 100 hPa (approximately the tropical tropopause) and 1000 hPa (approximately the surface) averaged over 5 degrees of latitude equatorward of the tropical belt edge latitude for each month in each hemisphere.

In both hemispheres, tropical expansion between the $4\times CO_2$ and piControl experiments is associated with an increase in subtropical static stability, with the increase in stability explaining 29-55% of the inter-model variation in tropical expansion (Fig. 2.7). This relationship also holds for the tropical expansion and contraction between the G1 and piControl experiments, where changes in static stability explain 42-46% of the total inter-model variation in the tropical belt edge latitudes. These results are noteworthy for two reasons. First, the relationships remain linear for small and large changes in subtropical static stability and the Hadley cell edge latitude. Second, despite differences in the models' mean edge latitudes and their parameterizations of convection and other processes, and despite a dearth of physical inter-model relationships (Davis and Birner, 2016), this particular relationship is robust across models and scenarios.

Tropical upper-tropospheric temperatures tend to warm more than surface temperatures due to moist adiabatic adjustment (Held et al., 1993; Romps, 2011). Because the moist adiabatic lapse rate scales with surface temperature, any change in static stability in the tropics and subtropics reflects changes in surface temperature. Accordingly, tropical expansion in both hemispheres also scales with increases in global-mean surface temperature (Fig. 2.8), explaining 47-49% of the inter-model variation in tropical expansion between the $4\times CO_2$ and piControl experiments. Despite being the residual rather than the

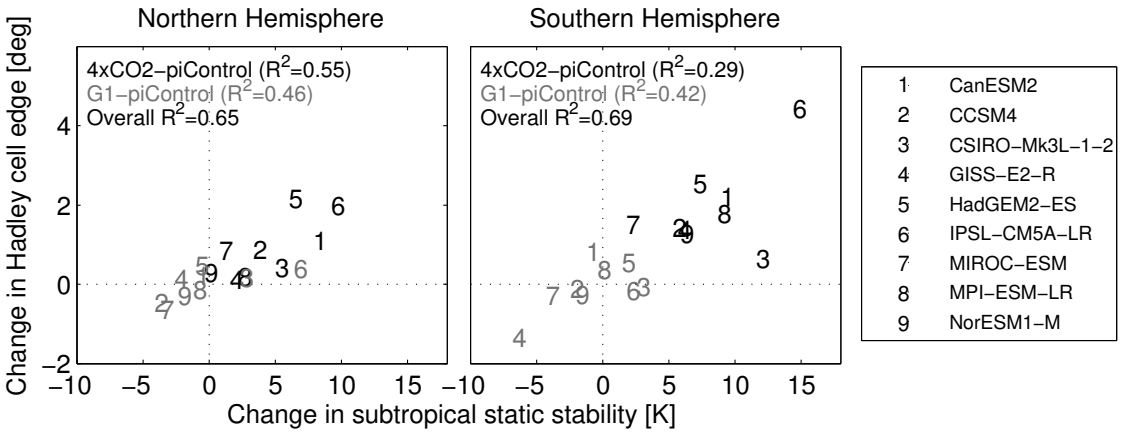

Figure 2.7: The change in the Hadley cell edge latitude versus the change in subtropical static stability in the Northern Hemisphere and in the Southern Hemisphere. For both hemispheres, positive changes in the Hadley cell edge latitude indicate poleward expansion. Shown are values for the $4\times CO_2$ experiment minus the piControl experiment (black) and for the G1 experiment minus the piControl experiment (gray). The percent of the inter-model variation in the change in the Hadley cell edge latitude explained by the change in subtropical static stability between each experiment is indicated in each plot.

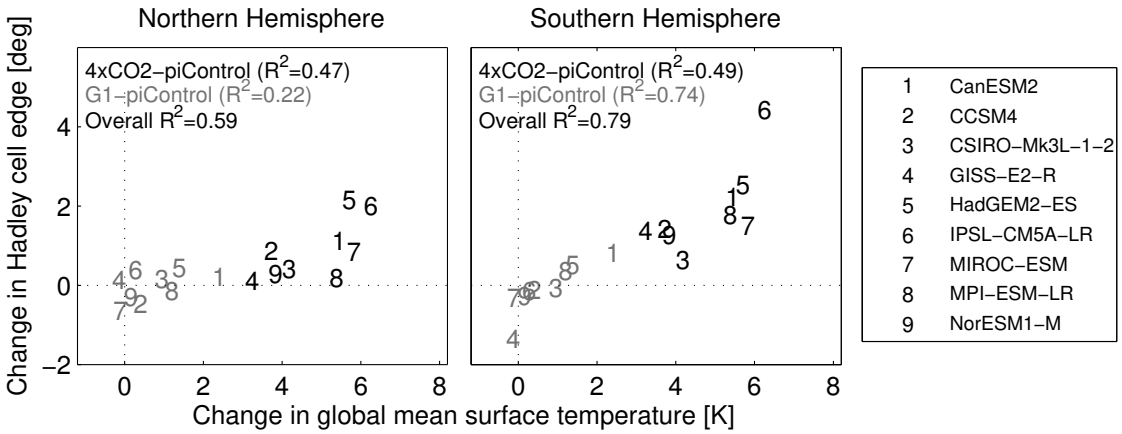

Figure 2.8: As in Fig. 3.7, but for the change in the Hadley cell edge latitude versus the change in global-mean surface temperature in the Northern Hemisphere and in the Southern Hemisphere.

forced response, increases in global-mean surface temperature also explain 74% of the inter-model variation in tropical expansion in the Southern Hemisphere in the G1 experiment, though less so in the Northern Hemisphere. Compared to the Southern Hemisphere, Northern Hemisphere tropical expansion seems to scale nonlinearly for large increases in global-mean surface temperature.

The seasonality of these correlations (not shown) generally reflects the seasonality of the response (Fig. 2.5). For example, tropical expansion in the Northern and Southern Hemispheres is most highly correlated with the change in global-mean surface temperature in SON ($R^2 = 0.31$) and MAM ($R^2 = 0.43$), respectively. In the other seasons, no significant correlation is found between the change in global-mean surface temperature and tropical expansion in the Northern Hemisphere.

Tropical expansion as measured by the total change in tropical belt width disproportionately increases as the global-mean surface temperature increases (Fig. 2.9). This reflects the nonlinearity seen in the expansion of the Northern Hemisphere tropical belt edge latitudes. The change in the tropical belt width is better correlated with the change in global-mean surface temperature than with the change in subtropical static stability, explaining 54-79% of the total inter-model variation in the change in the tropical belt width.

We also examined Arctic warming and tropical upper-tropospheric warming separately, as the two may have different impacts on tropical expansion and/or may explain some additional inter-model variation in the tropical belt response. However, both of these indices are correlated with the total change in global-mean surface temperature (Fig. 2.10), even seasonally (not shown). Tropical upper-tropospheric temperature changes are

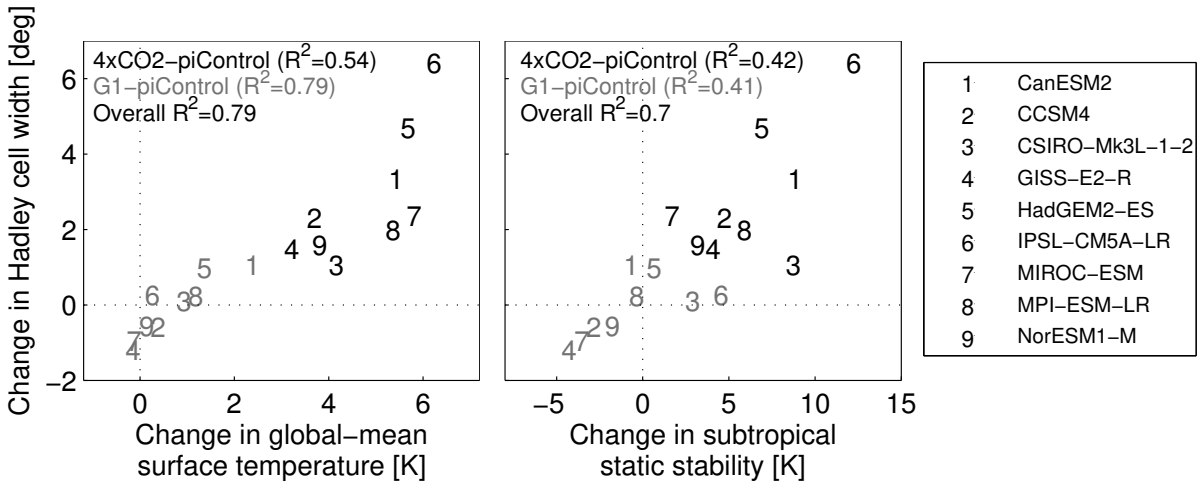

Figure 2.9: The change in the total Hadley cell width versus the change in global-mean surface temperature and the change in subtropical static stability. Positive changes in the Hadley cell width indicate tropical expansion. Shown are values for the $4\times CO_2$ experiment minus the piControl experiment (black) and for the G1 experiment minus the piControl experiment (gray). The percent of the inter-model variation in the change in the Hadley cell edge latitude explained by the change in global-mean surface temperature and the change in subtropical static stability between each experiment is indicated in each plot.

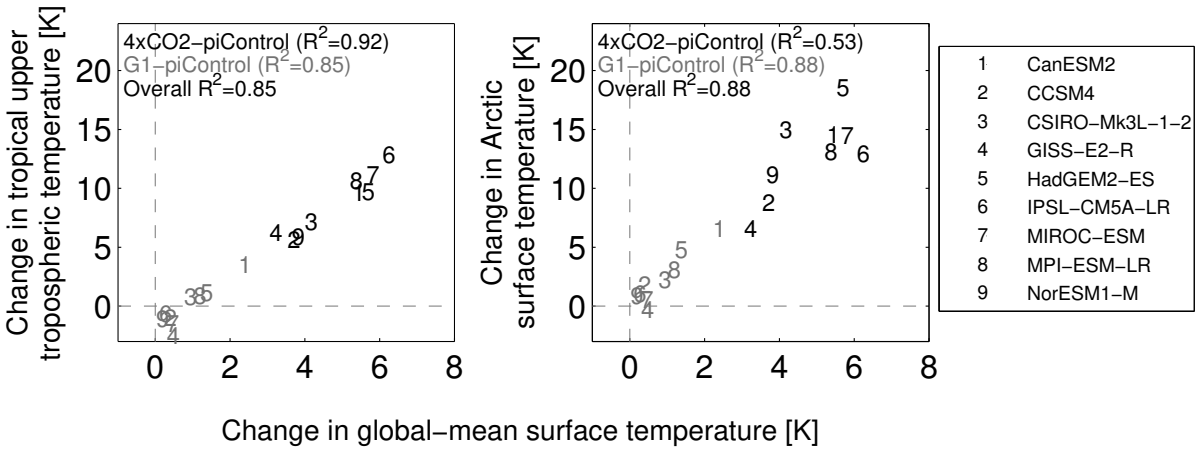

Figure 2.10: The change in tropical upper-tropospheric temperature versus the change in global-mean surface temperature (left), and the change in Arctic surface temperature versus the change in global-mean surface temperature (right), between the $4\times CO_2$ and piControl experiments (black) and between the G1 and piControl experiments (gray). Tropical upper-tropospheric temperature is defined as the mean temperature between 200 and 300 hPa and between 10S and 10N. Arctic temperature is defined as the mean surface temperature between 75N and 90N.

well-correlated with the change in global-mean surface temperature across the models for both the difference between the $4\times CO_2$ and piControl experiments and the difference between the G1 and piControl experiments. For the Arctic warming, the correlations do not depend upon whether one defines Arctic amplification as the total temperature change at the surface in the Arctic (as is done here) or as the difference between the total temperature change at the surface in the Arctic minus the change in global-mean surface temperature; if one is correlated with global-mean surface temperature, the other will be as well.

2.5 Summary

This chapter examined the equilibrium response of the tropical belt to simple radiative forcings in the GeoMIP experiments. Quadrupled concentrations of carbon dioxide in the $4\times CO_2$ experiment produce the canonical temperature response and drive significant tropical expansion in all models. The insolation reduction in the G1 experiment generally counteracts the carbon-dioxide-induced tropospheric warming, but leaves the stratosphere colder than it was in the piControl experiment. The lack of any significant change in the tropical belt width between the G1 and piControl experiments indicates that broad stratospheric cooling alone may not drive tropical expansion, at least when the cooling does not extend down to the tropopause.

The expansion in response to quadrupled carbon dioxide concentrations is greater in the Southern Hemisphere and peaks in austral summer and autumn, consistent with recent findings by Grise and Polvani (2016) who also analyzed the 4xCO_2 experiment. Both responses have previously been identified as signatures of Antarctic ozone depletion on observed Southern Hemisphere tropical expansion. They also appear to reflect the basic response of the circulation to simple hemispherically-symmetric, non-ozone climate forcings. This does not imply that ozone depletion and other climate forcings have not contributed to observed tropical expansion. Rather, it may be that ozone depletion and increased greenhouse gas concentrations have together enhanced the expansion in the Southern Hemisphere and in summer and autumn. The Southern Hemisphere Hadley cell may exist in a different dynamical regime than the Northern Hemisphere cell (Davis and Birner, 2013) due to the Southern Hemisphere cell's strong coupling to the eddy-driven jet (Kang and Polvani, 2011; Ceppi and Hartmann, 2013; Staten and Reichler, 2014). This jet has a more robust poleward shift in response to greenhouse gas increases than its Northern Hemisphere counterparts (Barnes and Polvani, 2013) which may enhance Southern Hemisphere tropical expansion. Further, the Hadley cells are more susceptible to the influence of extratropical Rossby waves in summer (Schneider and Bordoni, 2008), which may contribute to the seasonality of the expansion in both hemispheres.

Models with a stronger temperature response to increased carbon dioxide (which includes stronger surface, upper-tropospheric, and Arctic warming and stronger stratospheric cooling) have greater tropical expansion. While tropical expansion scales with increases in both subtropical static stability and global-mean surface temperature, these indices effectively measure the same thermodynamic response because of moist adiabatic

adjustment. Increases in global-mean surface temperature can explain up to 79% of the total inter-model variation in tropical expansion, noteworthy because it occurs within the inter-model space of fully-coupled climate models. Different mean states (Kidston and Gerber, 2010), the representation of parameterized processes (Frierson, 2007), the strength of cloud feedbacks (Feldl and Bordoni, 2016), and model design choices such as horizontal resolution (Landu et al., 2014; Lorant and Royer, 2001; Davis and Birner, 2016) can all influence the circulation and its response. Tropical belt width changes are thus part and parcel of global climate change. They are strongly correlated with changes in other key climate features and are not a separate phenomenon. Tropical expansion could be considered as robust a response of the climate system to increasing greenhouse gas concentrations as an acceleration of the hydrological cycle.

How the temperature or static stability changes could actually drive tropical expansion is an open question. While the dynamical response is relatively fast, ocurring within the first several years of the abrupt $4xCO_2$ experiment, the increase in global-mean surface temperature takes much longer. Rather than being indicative of a mechanism for expansion, it is more accurate to conclude that dynamical sensitivity as measured by the Hadley cells scales with climate sensitivity, at least in response to changes in carbon dioxide concentrations and insolation.

While it is consistent with the modeled tropical expansion, the scaling theory used here includes some unrealistic assumptions. Angular momentum is not perfectly conserved in the poleward flow of the Hadley cell due to eddy momentum fluxes (Schneider, 2006), and the boundary between the Hadley and Ferrel cells is shaped by these eddy fluxes (Schneider, 2006; Lu et al., 2008; Ceppi and Hartmann, 2013; Choi et al., 2014). While the

scaling theory can be adjusted to take into account the degree to which eddy fluxes draw the circulation away from angular momentum conservation (Kang and Lu, 2012), some bootstrap or input of the properties of the eddies is still needed to form a complete theoretical scaling for the Hadley cell width (Held, 2000). Further, localized (Tandon et al., 2011) and even non-localized cooling in the subtropical lower stratosphere (Butler et al., 2010) can drive variations in the Hadley cell width, potentially independent of changes to tropospheric static stability. This must be accounted for by any theory for the width of the Hadley cells and their response to radiative forcings.

Additionally, baroclinic instability is generally a feature of the eddy-driven jets, which can be well-separated from the subtropical jets at the edges of the Hadley cells. Despite the inter-model correlation between tropical expansion and increases in static stability, increases in static stability may not be the only process associated with tropical expansion. Instead, changes to the eddy phase speeds that lead to poleward shifts in the latitudes of wave breaking (Chen and Held, 2007) are associated with poleward shifts of the Hadley cell edges (Ceppi and Hartmann, 2013). Both occur simultaneously with increasing greenhouse gas concentrations and global-mean surface temperatures. It is therefore impossible to exclude other factors and conclude that the static stability increases alone drive tropical expansion.

Both Arctic warming and tropical upper-tropospheric warming scale with increases in global-mean surface temperature. Separating these influences on the tropical belt and any other feature of the climate system is not feasible in the experiments examined here and may not be possible in projections of future climate. Despite the significant variation in the magnitude of the model response to simple forcings, there is a robust physical scaling

throughout the climate system, between the tropics and the poles and between the thermodynamics and the circulation.

3 The Hadley Circulation in Realistic Forcing Scenarios

While the response of the Hadley circulation and climate system to greenhouse gas forcings appears to be robustly coupled, their response to the comprehensive suite of anthropogenic and natural forcings over the past and coming century could be more complicated. An unresolved question is whether the Hadley circulation has expanded over the recent historical record, a question compounded by the fact that the Hadley circulation cannot be resolved by observations (Waliser et al., 1999). Various approaches have been taken including analyzing atmospheric reanalyses and constructing proxies for the Hadley circulation edge latitudes.

Historical tropical expansion in reanalyses and models has been characterized using the edge latitudes of the Hadley cells (Hu and Fu, 2007; Frierson et al., 2007b; Lu et al., 2008; Johanson and Fu, 2009; Stachnik and Schumacher, 2011; Davis and Rosenlof, 2012; Allen et al., 2012; Nguyen et al., 2013; Chen et al., 2014; Nguyen et al., 2015), with estimates of expansion in reanalyses ranging from 0.3 deg/decade (Stachnik and Schumacher, 2011) to 1.5 deg/dec (Davis and Rosenlof, 2012). However, there may be spurious trends in the tropical belt width in reanalyses (Lucas et al., 2012; Quan et al., 2014) due to inhomogeneities in the observing system (Bengtsson et al., 2004).

The Hadley cell is only one aspect of the tropical belt, and other characteristics can be used to estimate tropical expansion. The structure of the tropopause, which has an abrupt drop in altitude in the subtropics, can be used to characterize the edges of the tropical belt (Seidel and Randel, 2007; Lu et al., 2009; Birner, 2010; Wilcox et al., 2011; Davis and

Rosenlof, 2012; Lucas et al., 2012; Davis and Birner, 2013; Ao and Hajj, 2013). Tropopause metrics are advantageous because they can be estimated from radiosonde observations or from any remotely-sensed temperature observations with sufficient vertical resolution, such as Global Navigation Satellite System radio occultation profiles. Estimates of historical tropical expansion using tropopause metrics range from -0.5 deg/dec (Davis and Birner, 2013) to 3.1 deg/dec (Seidel and Randel, 2007).

Another aspect used to characterize the edges of the tropical belt is the subtropical jet stream (Archer and Caldeira, 2008; Davis and Rosenlof, 2012; Allen et al., 2012). This can be inferred with some difficulty from observational data (Fu and Lin, 2011; Davis and Birner, 2013). Trends in the tropical belt width based on the subtropical jets have a smaller range than other metrics, at 0.1 deg/dec (Davis and Rosenlof, 2012) to 0.6 deg/dec (Davis and Birner, 2013).

The wide range of trends among metrics within the same dataset and between datasets poses a problem (Seidel et al., 2008; Staten et al., 2016; Davis et al., 2016). While they are in proximity to each other in the subtropics, it isn't clear if or how the latitude of the subtropical jet, the tropopause break, the Hadley cell edge, and various surface metrics relate to one another climatologically, interannually, or in response to climate forcings. Given that the seasonality of the metrics and their response to the El Niño-Southern Oscillation differ (Davis and Birner, 2013), their temporal variability and basic response to radiative forcings may differ as well.

Another unresolved issue is that tropical expansion tends to be an order of magnitude weaker in climate models than in reanalyses over the historical period (Johanson and Fu, 2009; Quan et al., 2014). Even trends assessed from climate model simulations with the

most extreme greenhouse gas forcings are weaker than those assessed from reanalyses (Johanson and Fu, 2009; Hu et al., 2013). This could be related to the relative insensitivity of the models' Hadley cells to changes in global-mean surface temperature (Adam et al., 2014; Nguyen et al., 2015). Additionally, modes of natural variability such as the Pacific Decadal Oscillation (Grassi et al., 2012; Allen et al., 2014), the Southern Annular Mode, and the El Niño-Southern Oscillation (Lucas and Nguyen, 2015) may have enhanced historical tropical expansion. Model simulations simply may not be able to reproduce the high rates of estimated historical expansion unless they are forced with the observed history of sea surface temperatures (Allen et al., 2014; Garfinkel et al., 2015).

When asking whether tropical expansion is different between reanalyses and models, it is important to define a null hypothesis that takes into account their fundamental differences. Reanalyses more or less reproduce observed natural variability by assimilating observations. Climate model historical experiments instead simulate an ensemble of possible histories of natural variability given the forcings on the system, such as insolation and greenhouse gas concentrations. If natural variability impacts tropical expansion trends then the models will produce a range of possible trends in the tropical belt width. If there are no relevant model biases that lead to biases in the trends then the real world evolution of the tropical belt width should fall somewhere within this distribution (Quan et al., 2014; Garfinkel et al., 2015).

The question that assumes the least about model and reanalysis deficiencies is whether trends based on reanalyses fall within the distribution of model trends. If the reanalyses' trends fall outside of the range of climate model trends, then we may have a basis to claim that the reanalyses' and models' trends disagree. If they do not, then the level of evidence

necessary to declare such a discrepancy will not have been met. This study will assess tropical expansion in a large sample of climate models and in only the most modern reanalyses. While we do not directly quantify internal variability as in Quan et al. (2014) or Garfinkel et al. (2015), we instead take a holistic view and ask whether the statistics alone demonstrate a discrepancy between models and reanalyses. Formally stated, our null hypothesis is that the reanalyses' trends are not significantly different from all model trends using a given tropical belt width metric.

This intercomparison focuses on a representative subset of metrics. In addition to exploring the trends, it will also examine the inter-model and temporal relationships among the metrics in climate models and reanalyses. These results will be used to interpret any differences in tropical expansion between the different metrics. We will investigate the connection between these different tropical belt metrics and surface climate indices to determine which, if any, are most useful for climate impact studies.

3.1 Data

We use 25 models from the CMIP5 Historical and Representative Concentration Pathway 8.5 (RCP8.5) experiments: ACCESS1-0, ACCESS1-3, CanESM2, CMCC-CESM, CMCC-CMS, CNRM-CM5, CSIRO-Mk3-6-0, FGOALS-g2, FIO-ESM, GFDL-CM3, GFDL-ESM2M, GISS-E2-H, GISS-E2-R, HadGEM2-ES, IPSL-CM5A-LR, IPSL-CM5A-MR, IPSL-CM5B-LR, INM-CM4, MIROC-ESM, MIROC-ESM-CHEM, MIROC5, MPI-ESM-LR, MPI-ESM-MR, MRI-CGCM3, and NorESM1-M. The CMIP5 Historical experiment simulates earth's past climate from 1850-2005 by imposing observed

forcings on the climate system (Taylor et al., 2012). The RCP8.5 experiment runs from 2006-2100 and gradually increases the top-of-atmosphere radiative forcing to 8.5 W/m^2 by 2100, the highest radiative forcing RCP simulation in CMIP5.

We also briefly use 17 models from the Chemistry Climate Model Validation Activity for SPARC-2 (CCMVal-2) Reference B1 (REF-B1) experiment: CAM3.5, CCSRNIES, CMAM, CNRM-ACM, E39CA, EMAC, EMAC-FUB, GEOSCCM, MRI, Niwa-SOCOL, SOCOL, ULAQ, UMETRAC, UMSLIMCAT, UMUKCA-METO, UMUKCA-UCAM, and WACCM. The CCMVal-2 REF-B1 experiment is analogous to the CMIP5 Historical experiment as it simulates earth's past climate using observed forcings (Eyring et al., 2008). CMAM is the only CCMVal-2 model with a coupled ocean while the other models have prescribed sea surface temperatures. All CCMVal-2 models include interactive chemistry.

Monthly-mean output from four modern reanalyses are used in this study: the European Centre for Medium-Range Weather Forecasts' Reanalysis, Interim (ERA-Interim) (Dee et al., 2011), the National Aeronautics and Space Administration's Modern Era Retrospective Reanalysis 2 (MERRA2) (Bosilovich et al., 2015), the Japanese Meteorological Agency's Japanese Reanalysis, 55-year (JRA-55) (Kobayashi et al., 2015), and the National Centers for Environmental Prediction's Climate Forecast System Reanalysis (CFSR) (Saha et al., 2010).

Our analysis of the historical time period using the reanalyses, CMIP5 Historical experiment, and CCMVal-2 REF-B1 experiment spans 1979-2005, while our analysis of the future climate projections in the CMIP5 RCP8.5 experiment spans 2006-2100.

3.2 Tropical belt metrics

We use five objective metrics that measure different aspects of the subtropical circulation and climate to characterize the edge latitudes of the tropical belt. These metrics are in many cases inspired by other metrics in the existing literature. However, none of the metrics examined here are evaluated with subjectively-chosen numerical thresholds or on arbitrary vertical levels. Such objective metrics are especially critical when examining trends (Birner, 2010; Davis and Rosenlof, 2012). For example, changes in the mean structure of the atmosphere, such as an increase in the depth of the troposphere, could alias into expansion trends if metrics are evaluated on specific vertical levels or with numerical thresholds. The metrics examined here define the tropical belt edges based on the latitudes of the subtropical tropopause breaks ("$\Delta\theta$"), the latitudes of the subtropical jets ("$U_{\max}$"), the latitudes of the edges of the Hadley cells ("$\int \Psi dp$"), the latitudes of maximum subsidence in the Hadley cells ("$\partial_y \int \Psi dp$"), and the latitudes of zero zonal-mean surface zonal wind ("U_{sfc}"). We also employ the commonly-used Hadley cell metric based on the 500 hPa mean meridional streamfunction ("Ψ_{500}") to compare some results with previous work.

3.2.1 Hadley cell edge latitudes, $\int \Psi dp$

The Hadley cells are defined by the mean meridional streamfunction, which measures the overturning circulation in the zonal mean (Fig. 3.1, shading in top panel). The Hadley cell edge latitudes are often measured by the latitudes of the zero contour of the 500 hPa mean meridional streamfunction (Frierson et al., 2007b; Lu et al., 2008; Davis and Rosenlof,

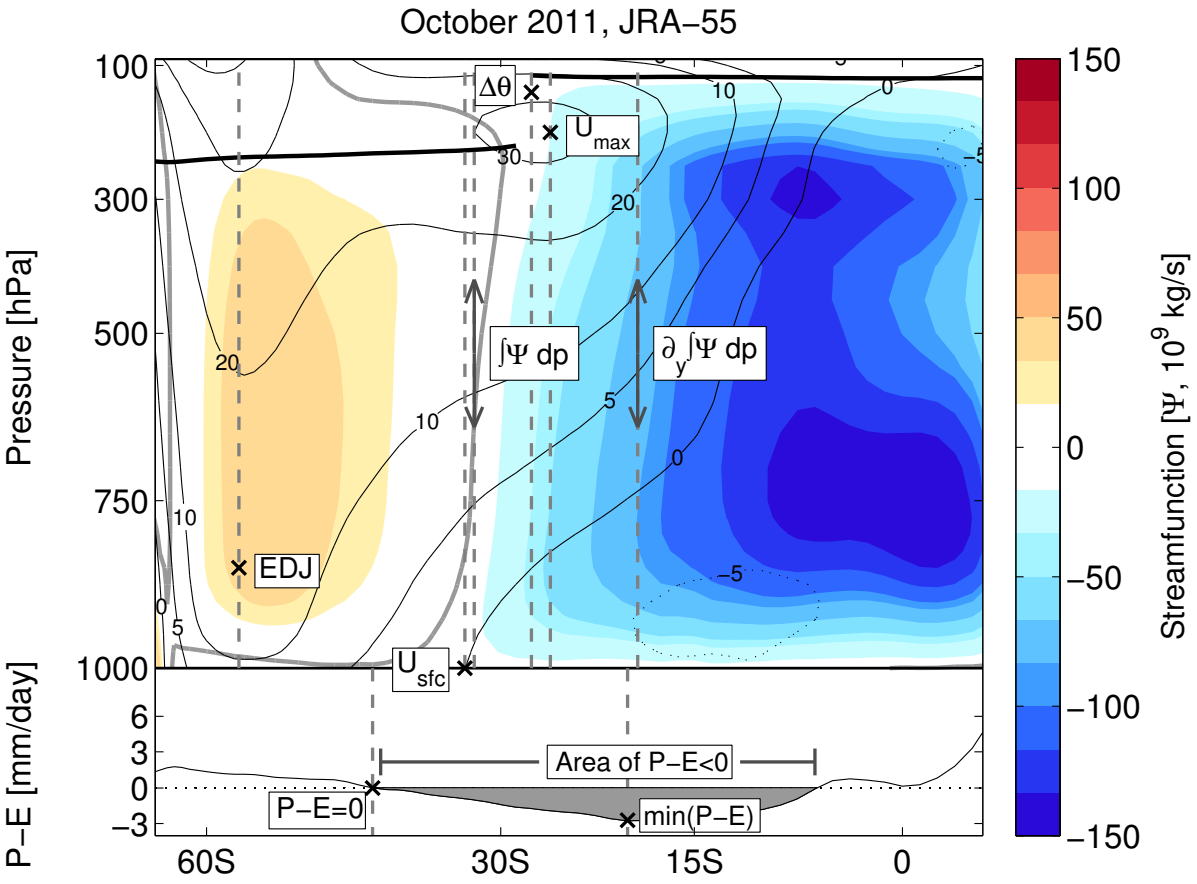

Figure 3.1: The mean meridional streamfunction (top panel, shading, 10^9 kg/s, zero contour indicated by thick gray line), zonal-mean zonal wind (top panel, contours, m/s), tropopause pressure (top panel, thick black line), and precipitation minus evaporation (bottom panel, mm/day) for October 2011 from JRA-55. The latitudes of the tropical belt edges based on the five objective metrics – $\Delta\theta$ (the latitude of the tropopause breaks), $U_{\max}$ (the latitude of the subtropical jet), $\int \Psi dp$ (the latitude of the edge of the Hadley cell), $\partial_y \int \Psi dp$ (the latitude of maximum downwelling in the Hadley cell), and $U_{\rm sfc}$ (the latitude of zero zonal-mean surface wind) – are indicated by the gray vertical lines. Metrics based on integrals are indicated by vertical gray arrows, while other metrics are indicated by black "x" marks. The latitudes of the eddy-driven jet, EDJ, the latitudes of the minimum of precipitation minus evaporation, min(P-E), and the latitudes where precipitation minus evaporation is zero, P-E=0, are similarly indicated by gray vertical lines and black "x" marks. The area where P-E<0 is indicated by the shading in the bottom panel.

2012; Allen et al., 2012; Hu et al., 2013; Tao et al., 2015). However, evaluating the streamfunction on arbitrary vertical levels could alias vertical shifts of the circulation into poleward shifts, as the zero-contour varies in latitude throughout the troposphere (Fig. 3.1). Such metrics also implicitly assume that Hadley cell expansion is homogeneous in the vertical, whereas model simulations indicate it is not (see Fig. 3.2 of Tao et al. (2015)). While the Hadley cell edge can similarly be estimated using the latitude of the zero contour of a mid-tropospheric layer-average of the mean meridional streamfunction (Hu and Fu, 2007; Johanson and Fu, 2009; Stachnik and Schumacher, 2011; Nguyen et al., 2013, 2015), it could still be subject to the same problems.

To avoid these issues, as in the previous chapter the $\int \Psi dp$ metric estimates the Hadley cell edge latitudes as the latitudes where the vertically-averaged mean meridional streamfunction is zero in each hemisphere (Fig. 3.1), poleward of its tropical extrema (Davis and Birner, 2013). This quantity measures the average meridional overturning circulation strength at a given latitude, and the latitude at which it is zero indicates the average latitude of the poleward edge of the Hadley cell. As the stratosphere represents approximately 10% of the mass of the tropical atmosphere and the streamfunction values in the stratosphere are orders of magnitude smaller than those in the troposphere, the contribution by the stratospheric circulation is negligible. Linear interpolation is used to estimate the edge latitude between grid points.

3.2.2 Subtropical jet latitudes, $U_{\max}$

The subtropical jets are located in the subtropical troposphere where the vertically-integrated meridional temperature gradient, or thermal wind shear, is largest.

The $U_{\max}$ metric estimates the subtropical jet latitudes as the latitudes of maximum upper-tropospheric/lower-stratospheric zonal-mean zonal wind in the subtropics between 1000 hPa and 50 hPa above the tropopause in each hemisphere (Fig. 3.1) (Davis and Birner, 2013). Limiting the search to 50 hPa above the tropopause prevents an erroneous identification of the stratospheric jets. The 1000 hPa wind speed is subtracted from each column so that the zonal wind at a given level represents the vertically-integrated thermal wind shear (Davis and Birner, 2016). This makes the subtropical jet distinct in all seasons from the eddy-driven jet, which is characterized by strong surface westerly winds. Linear interpolation of the meridional gradient of the zonal-mean zonal wind is used to identify the jet latitude between grid points.

3.2.3 Tropopause break latitudes, $\Delta\theta$

The tropopause abruptly drops from its tropical to extratropical altitude in the region of maximum baroclinicity near the subtropical jet. Here, the $\Delta\theta$ metric estimates the latitudes of the tropopause breaks as the latitudes of maximum zonal-mean tropospheric dry bulk stability in each hemisphere (Fig. 3.1) (Davis and Birner, 2013). The tropospheric dry bulk stability is defined as the difference in potential temperature between the tropopause and the surface, which exhibits an unambiguous maximum value in the subtropics at the tropopause break. Because this field is discontinuous at the tropopause break, no interpolation method can be used to estimate the tropical belt edge latitude between grid points. This metric itself enters into scaling theories for the width of the Hadley cell (e.g., Held (2000)) and is most similar to tropopause metrics based on the meridional gradient of tropopause height (Davis and Rosenlof, 2012).

3.2.4 Latitudes of maximum downwelling, $\partial_y \int \Psi dp$

The Hadley cell edge is typically measured as the latitude where the meridional overturning circulation transitions from the Hadley cell to the Ferrel cell. However, the location of maximum subsidence within the Hadley cell may be more relevant for surface climate as it suppresses convection and dries the atmosphere, contributing to the formation of deserts. As shown in Fig. 3.1, the minimum of precipitation minus evaporation does not occur at the edge of but within the subsidence of the Hadley cells, where the meridional gradient of the streamfunction (the vertical velocity) is the largest. The $\partial_y \int \Psi dp$ metric estimates the latitudes of maximum vertically-averaged subsidence in the Hadley cells in each hemisphere (Fig. 3.1). Linear interpolation of the second meridional gradient of the vertically-averaged mean meridional streamfunction is used to estimate the edge latitude between grid points.

3.2.5 Latitudes of zero surface zonal wind, U_{sfc}

In the time- and zonal-mean and assuming linear surface drag, the vertically-averaged zonal-mean quasigeostrophic zonal momentum equation reduces to a balance between the vertically-averaged eddy momentum flux convergence and surface drag on the zonal-mean surface zonal wind,

$$\frac{[u_s]}{\tau} = -\left\langle \frac{\partial}{\partial y}[u^* v^*] \right\rangle \tag{1}$$

where u and v are the zonal and meridional winds, u_s is the surface zonal wind, τ is a time scale for drag, $[u^* v^*]$ is the eddy momentum flux where stars indicate deviations from the zonal mean, and angled brackets indicate the vertical average. Any latitude with non-zero

zonal-mean zonal wind at the surface has a net convergence or divergence of momentum in the column by the eddies. Net eddy momentum flux divergence out of the tropics balances the drag on the surface easterlies while net eddy momentum flux convergence into the midlatitudes balances the drag on the surface westerlies. The latitude with zero zonal-mean surface zonal wind divides these two regimes. The U_{sfc} metric estimates the latitudes of zero zonal-mean surface zonal wind as the first latitudes where the zonal-mean zonal wind is zero at 1000 hPa, poleward of the tropical easterlies in each hemisphere (Fig. 3.1). Linear interpolation is used to estimate the edge latitude between grid points. Modeling groups may extrapolate winds to 1000 hPa differently, but we do not have the information necessary to quantify or correct any errors this may introduce. The results are insensitive to using the 10 meter wind field, at least in reanalyses.

This method is similar to the mean sea-level pressure metric used by Choi et al. (2014), which measures the edge of the tropical belt as the location where the meridional derivative of sea-level pressure within the subtropical ridge is zero. In the zonal-mean this corresponds to the latitude where the zonal-mean sea-level zonal wind changes sign from westerlies to easterlies.

3.2.6 Latitudes of the 500 hPa Hadley cell edge, Ψ_{500}

We also employ the commonly-used Ψ_{500} metric for continuity with past literature. The Ψ_{500} metric estimates the tropical belt edge latitudes as the latitudes where the 500 hPa mean meridional streamfunction is zero, poleward of its tropical extrema in each hemisphere.

3.2.7 Eddy-driven jet metric

Eddy fluxes associated with Rossby waves connect the eddy-driven jets to the Hadley cells and significantly impact the mean meridional circulation (Kim and Lee, 2001; Schneider, 2006). Additionally, the direct balance condition between the eddy momentum flux convergence and the mean meridional wind in the zonal-mean quasigeostrophic zonal momentum equation implies that the Hadley cell edge could be sensitive to shifts in the eddy-driven jet and its associated eddy momentum fluxes.

The eddy-driven jet latitude, or EDJ, is defined as the latitude of maximum wind at 850 hPa in each hemisphere (Fig. 3.1) (Kang and Polvani, 2011). Using the 1000 hPa wind speed or a lower-tropospheric average produces indistinguishable results. A more objective metric might define the jet as the location of maximum vertically-averaged eddy momentum flux convergence. However, this is difficult to obtain with the available data for the model simulations examined here. Linear interpolation of the gradient of the 850 hPa zonal-mean zonal wind is used to estimate the EDJ latitude between grid points.

3.2.8 Surface climate indices: min(P-E), P-E=0, and area of P-E<0

Three indices are used to understand the impact of variations in the tropical belt edge latitudes on surface climate: the latitudes of the minimum in precipitation minus evaporation (min(P-E)) (Zhou et al., 2011; Hu et al., 2011; Allen et al., 2012), the latitudes where precipitation minus evaporation is zero (P-E=0) (Davis and Rosenlof, 2012; Allen et al., 2012), and the surface area of negative precipitation minus evaporation in the subtropics (area of P-E<0). The min(P-E) latitudes are defined as the latitudes of the

minimum of precipitation minus evaporation (P-E) in each hemisphere (Fig. 3.1). These latitudes reflect the location of the maximum in subtropical aridity and could be associated with the latitudes of maximum subsidence in the Hadley cells, $\partial_y \int \Psi dp$. The P-E=0 latitudes are defined as the latitudes where P-E is zero poleward of the min(P-E) latitudes (Fig. 3.1). As the transition between the arid subtropics and the rainy midlatitudes, this metric could be most correlated with the $\int \Psi dp$ metric edge latitudes, which divide the Hadley and Ferrel cells. A new metric, the area of P-E<0 in the subtropics, is calculated as the area of negative P-E in the subtropics in each hemisphere weighted by the cosine of latitude (Fig. 3.1), and can be interpreted as the surface area prone to arid or desert climates.

3.3 Calculation details

The tropical belt width is defined as the difference in degrees latitude between the tropical belt edge latitudes. All correlations and linear least-squares regressions are performed on monthly-mean deseasonalized tropical belt edge latitudes and widths. We deseasonalize by removing the climatological-mean monthly value from each monthly mean (e.g., the mean of all January's is subtracted from each January), where the climatological-mean is taken over the historical (1979-2005) or future projection (2006-2100) time periods as appropriate.

Trends are calculated based on linear least-squares regressions. The significance of trends is assessed using each time series' effective degrees of freedom based on each time series' lag-1 autocorrelation (Santer et al., 2008), on average yielding one degree of freedom

per two to three months. Trends are considered significantly different from zero if their 95% confidence intervals do not include zero. Using annual-mean data does not impact the trend values, but it is disadvantageous in that it reduces the number of degrees of freedom.

3.3.1 Reanalysis-mean time series

Reanalyses are atmospheric forecast models coupled to data assimilation systems that ingest satellite and in-situ observations to produce a dynamically-consistent estimate of the historical evolution of the atmosphere. Because they are *in principle* simulating the same evolution of earth's atmosphere, averaging their time series provides a potentially more robust estimate of the historical tropical belt width and edge latitudes. Because of the non-linearity of linear least-squares regression, the trends based on the reanalysis-mean time series are not guaranteed to be equal to the mean of the reanalyses' trends. We will always examine the individual reanalyses' results in conjunction with the reanalysis mean.

3.4 Temporal and inter-model co-variability

We begin with a basic examination of the time series of tropical belt widths based on the five objective metrics (Fig. 3.2). The $\Delta\theta$, the $U_{\max}$, and especially the U_{sfc} metric widths are well-constrained in reanalyses (Fig. 3.2a, 2c, and 2i). On the other hand, the streamfunction-based metric widths disagree and are less constrained (Fig. 3.2e and 2g). The intensity of the overturning similarly varies across reanalyses (Stachnik and Schumacher, 2011). While the $U_{\max}$ and $\partial_y \int \Psi dp$ metric widths contract in response to the 1997/1998 El Niño in the reanalyses, the $\Delta\theta$ metric widths contract in response to the Mount Pinatubo eruption in both models and reanalyses. The inconsistency in the

responses of the tropical belt width to these particular events are an indication that different metrics do not necessarily measure the "same" tropical belt.

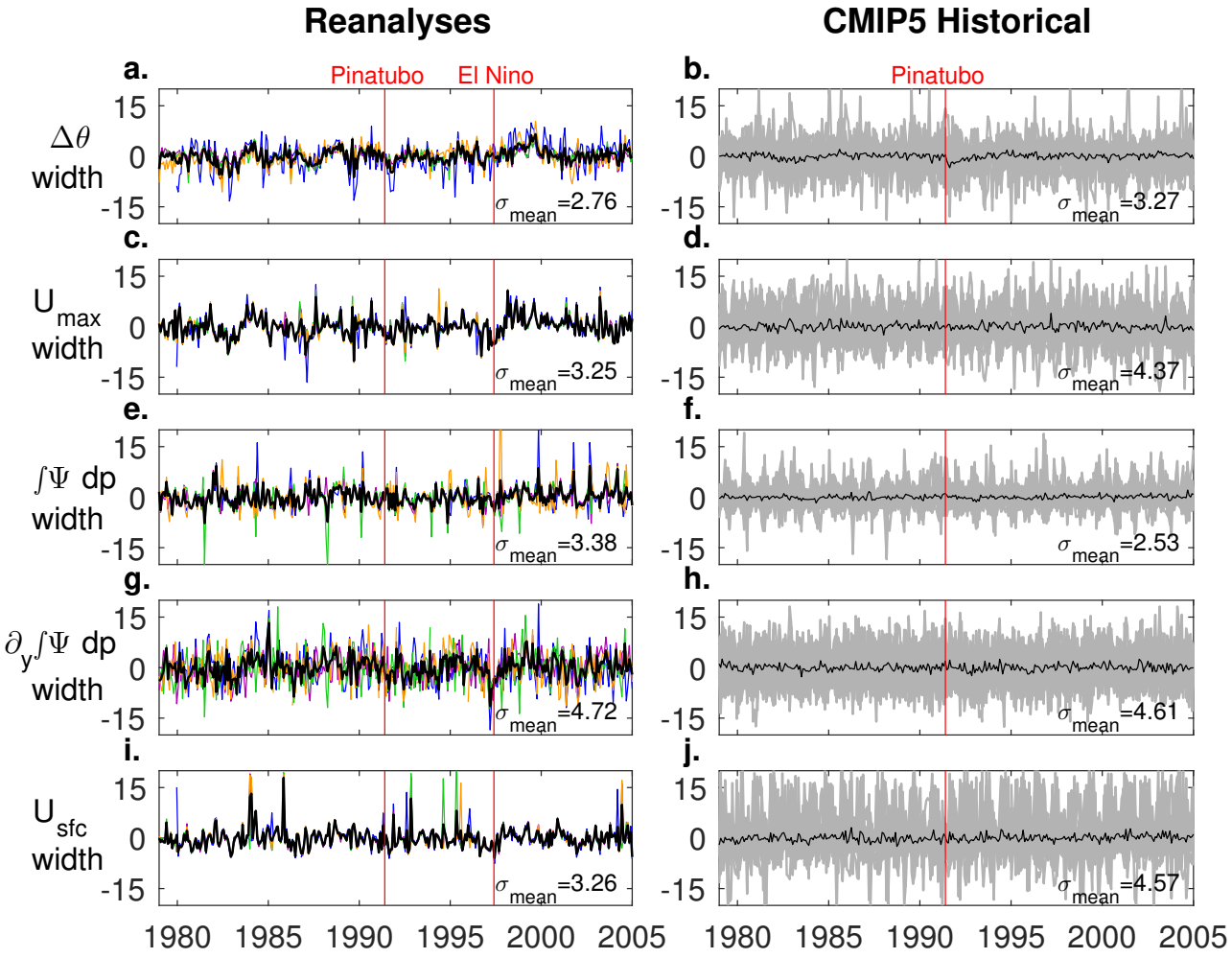

Figure 3.2: Deseasonalized tropical belt width time series from January 1979 to December 2005 for the (left column) reanalyses and (right column) CMIP5 Historical experiment, for the (a., b.) $\Delta\theta$, (c., d.) $U_{\max}$, (e., f.) $\int \Psi dp$, (g., h.) $\partial_y \int \Psi dp$, and (i., j.) U_{sfc} metric widths. (a., c., e., g., i.) Reanalysis time series are shown for ERA-i (purple), MERRA2 (blue), CFSR (yellow), JRA-55 (green), and the reanalysis-mean (black), while (b., d., f., h., j.) CMIP5 Historical time series are shown for individual models (gray) and the multi-model-mean (black). The vertical red lines correspond to the dates of the Mount Pinatubo eruption and the peak of the 1997/1998 El Niño. The mean standard deviation of the monthly anomalies is shown in the bottom right of each panel.

A majority of the metrics have greater natural variability in the CMIP5 Historical simulations than in the reanalyses. This could be caused by a model deficiency in the

representation of the seasonal cycle of the tropical belt edge latitudes. CMIP5 models do not produce a consistent seasonal cycle, especially in the Northern Hemisphere where the tropical belt edge latitudes shift poleward by 10 to 15 degrees latitude over one month in the early summer (Davis and Birner, 2016). Minor year-to-year differences in the phasing of the seasonal cycle may act as a source of some of this enhanced variability. This could be why, for example, the $\int \Psi dp$ metric width (Fig. 3.2f) has near-annual periodicity in its tropical belt edge latitude anomalies.

A direct assessment of the coupling between metrics is the temporal correlation, or co-variability, between their tropical belt edge latitudes within individual model simulations and reanalyses. The latitudes of the Hadley cell edge ($\int \Psi dp$), the latitudes of maximum downwelling ($\partial_y \int \Psi dp$), and the latitudes of zero zonal-mean surface zonal wind (U_{sfc}) are all correlated with each other in both hemispheres in the reanalyses (Fig. 3.3 and Fig. 3.4), with mean correlation coefficients ranging from 0.8 to 0.9. On the other hand, the subtropical jet (U_{max}) and tropopause break ($\Delta\theta$) latitudes are weakly correlated with only each other with correlation coefficients of 0.3. As a further point of distinction between the two sets of metrics, the latitude of the eddy-driven jet is correlated with the streamfunction and surface wind metric edge latitudes and uncorrelated with the subtropical jet and tropopause break metric edge latitudes in both hemispheres (Fig. 3.3 and Fig. 3.4).

The CMIP5 Historical simulations have weaker correlations among the metrics than the reanalyses, but most of the same relationships emerge in the Southern Hemisphere. There are some models with correlations between the $\int \Psi dp$, $\partial_y \int \Psi dp$, and U_{sfc} metric edge latitudes nearly as high as in the reanalyses. At the same time, some model correlations between these metric edge latitudes are nearly zero. There is even a spurious

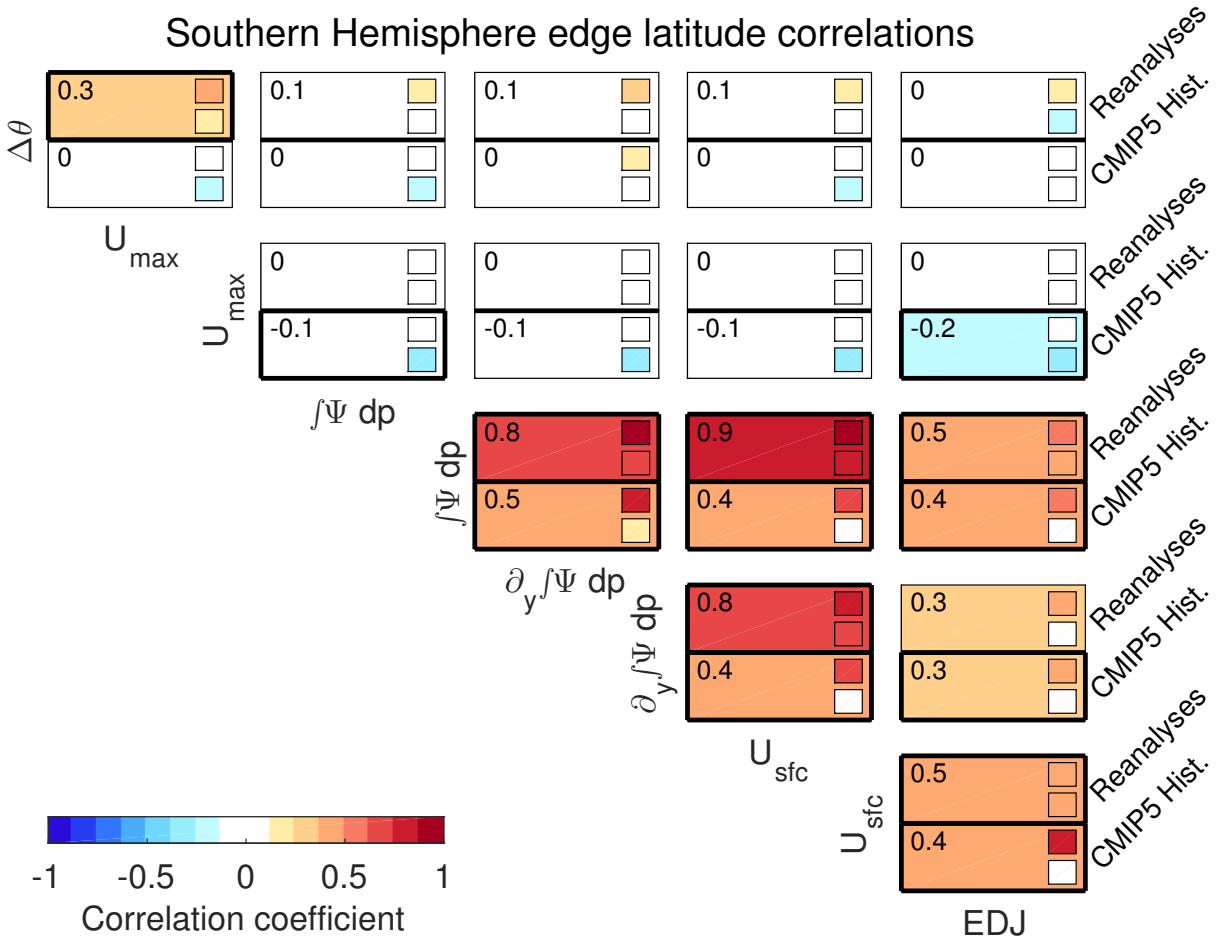

Figure 3.3: Correlation coefficients among the monthly deseasonalized tropical belt edge latitudes and eddy-driven jet latitude in the Southern Hemisphere over the historical period. Bold outlines indicate at least 75% of the models (19) or reanalyses (3) have correlations significant at the 95% confidence level. The top and bottom patch of each panel displays the ensemble-mean correlation coefficients between each set of indices for the reanalyses and CMIP5 Historical simulations, respectively. The small patches indicate the lowest and highest correlation coefficient in each ensemble, while the numerical value of the mean correlation coefficient in each ensemble is printed in the upper left of each patch.

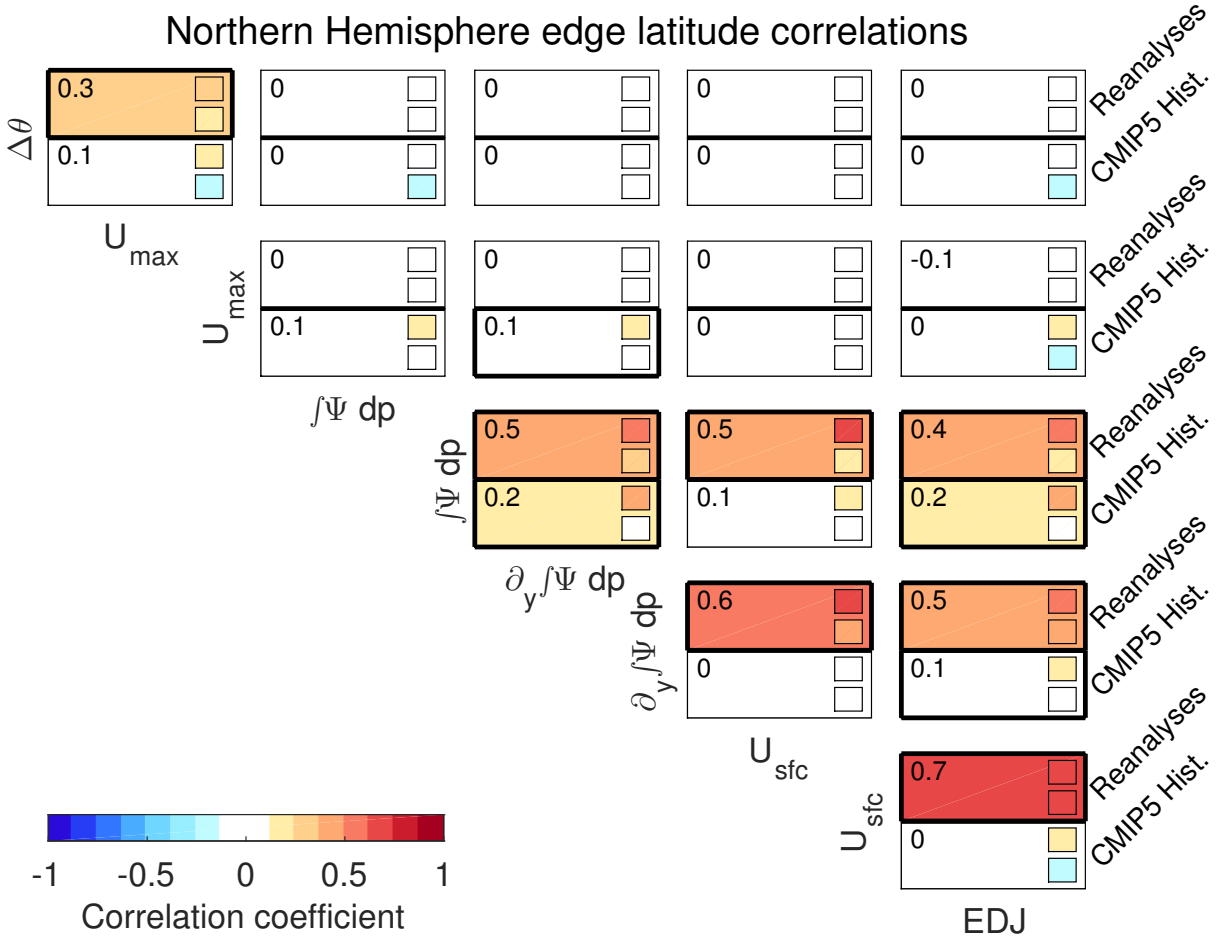

Figure 3.4: As in Fig. 3.3 but for the Northern Hemisphere.

anti-correlation between the $U_{\max}$ metric edge latitudes and the $\int \Psi dp$ and EDJ metric latitudes (Fig. 3.3). Correlations among all the metrics are poor in the Northern Hemisphere in the models, consistent with results from the CCMVal-2 REF-B1 simulations (not shown). Especially concerning is the lack of correlation between the Hadley cell edge and surface wind metrics, and between the subtropical jet and tropopause break metrics. The cause of these deficiencies in simulated circulation variability over the Northern Hemisphere is unclear.

To provide a different perspective, we also examine the inter-model (or across model) correlations between the mean tropical belt edge latitudes measured by the different metrics (Fig. 3.5). If two metrics' edge latitudes scale across models, they may be impacted by similar physical processes that not only set their mean edge latitudes but also contribute to any tropical expansion trends. We show the mean edge latitudes, rather than the correlation coefficients alone, to emphasize their large range among the models. The only correlation that is significant in both hemispheres is between the mean latitude of the Hadley cell edge ($\int \Psi dp$) and the mean latitude of maximum downwelling ($\partial_y \int \Psi dp$) (Fig. 3.5h). Dynamical fields such as the distribution of eddy momentum fluxes consistently scale with these measures of the tropical belt width, as well (Davis and Birner, 2016). The U_{sfc} metric edge latitudes also scale with the $\int \Psi dp$ and $\partial_y \int \Psi dp$ metric edge latitudes but only in the Southern Hemisphere (Fig. 3.5i, 5j), perhaps reflecting the models' poor correlations among metrics in the Northern Hemisphere (Fig. 3.4).

There is no relationship between the climatological $\Delta\theta$ and $U_{\max}$ metric edge latitudes in either hemisphere, suggesting a lack of co-variability between these two edge latitude metrics in both hemispheres in the models. Surprisingly, in the Northern Hemisphere the

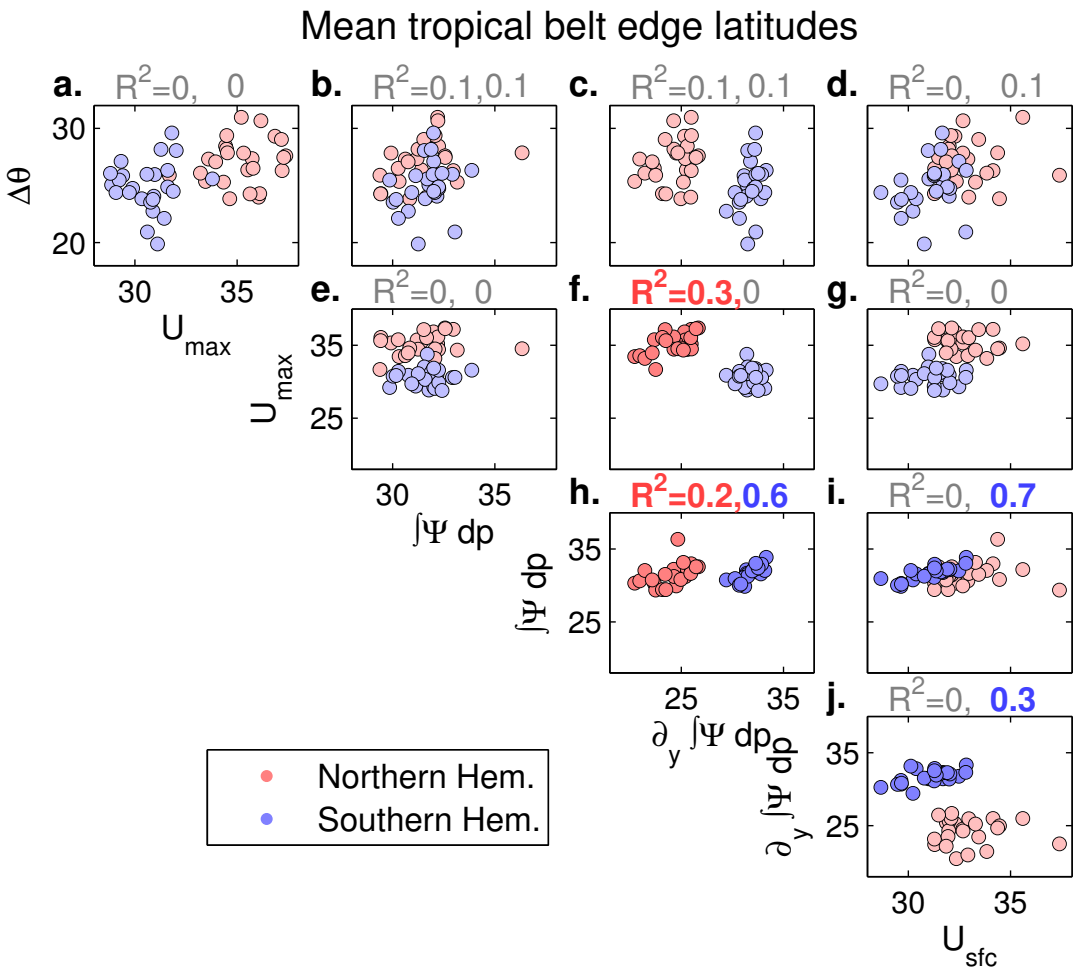

Figure 3.5: The inter-model correlation between the mean tropical belt edge latitudes as measured by each metric in the CMIP5 Historical simulations, for the Northern (red) and Southern (blue) Hemispheres. The percentage of variance explained (R^2) in each hemisphere is shown above each plot in red and blue, respectively, for correlations significant at the 95% confidence level. Correlations that are not significant are shown in gray, with the corresponding edge latitude colors lightly faded. Note the change in axes for the $\Delta\theta$ and $\partial_y \int \Psi dp$ panels.

$U_{\max}$ metric edge latitudes scale with the $\partial_y \int \Psi dp$ metric edge latitudes. While they may be situated in the subtropics and their mean latitudes may scale relative to each other across models, their month-to-month variability is uncorrelated (Fig. 3.4).

The results so far illustrate distinct properties of two sets of tropical belt metrics. Metrics based on the streamfunction ($\int \Psi dp$ and $\partial_y \int \Psi dp$) and the latitudes of zero zonal-mean surface zonal wind (U_{sfc}) are temporally coupled with each other and the latitudes of the eddy-driven jet. On the other hand, metrics based on the subtropical jet ($U_{\max}$) and tropopause break ($\Delta\theta$) latitudes are weakly correlated with each other, and not at all with the eddy-driven jet. There are no correlations across these classes of metrics within a given realization of earth's atmosphere, and only the mean tropical belt edge latitudes based on the Hadley cell itself scale robustly across models in both hemispheres.

3.4.1 Historical trends in the tropical belt width

Having assessed the co-variability and inter-model scaling among the metrics, in this section we seek to answer (1), whether the metrics respond differently to observed and projected forcings on the climate system and (2), whether reanalysis trends in the width of the tropical belt disagree with model trends. There is a well-documented seasonality to tropical expansion in both hemispheres, with expansion generally enhanced in each hemisphere's respective summer and autumn seasons (Hu and Fu, 2007; Hu et al., 2013; Allen et al., 2012; Tao et al., 2015). Here we focus primarily on the total change in the tropical belt width and do not examine its seasonality. The trends are more robust and the results that follow are similar when individual seasons and hemispheres are examined.

Trends in the tropical belt width in reanalyses assessed from the streamfunction and surface wind metrics are generally between 0.0 deg/dec and 0.6 deg/dec (Fig. 3.6), similar to those found by Stachnik and Schumacher (2011), Allen et al. (2012), Nguyen et al. (2013), and Davis and Birner (2013), though there are some outliers. Only ERA-Interim's $\partial_y \int \Psi dp$ metric expansion trend is as large as those found in Hu and Fu (2007) and Johanson and Fu (2009). The small range of reanalysis $U_{\max}$ metric width trends, from -0.1 deg/dec to 0.7 deg/dec, agree well with the jet-based tropical belt width trends found by Archer and Caldeira (2008), Davis and Rosenlof (2012), Allen et al. (2012), and Davis and Birner (2013). For the $\Delta\theta$ metric width the trends range from -0.4 deg/dec to 1.2 deg/dec with a reanalysis-mean trend of 0.6 deg/dec, generally lower than tropopause-based metrics that use numerical thresholds (Seidel and Randel, 2007; Davis and Rosenlof, 2012; Lucas et al., 2014) and more similar to objective tropopause-based metrics (Birner, 2010; Davis and Rosenlof, 2012). These objective metrics measure different aspects of the structure of the tropopause but arrive at similar historical trends.

The large spread in tropical expansion for the $\Delta\theta$ and $\partial_y \int \Psi dp$ metrics among the reanalyses could be interpreted as a consequence of assimilation system changes, though it may also include some genuine uncertainty regarding the historical changes in the tropical belt width. At least in the case of the $\partial_y \int \Psi dp$ metric, a substantial fraction of the disagreement among the reanalyses may come from the inability to constrain the mean meridional streamfunction (Fig. 3.2g). In spite of this, the $\int \Psi dp$ metric expansion trends have the smallest range of any metric in the reanalyses. None of the reanalysis trends for each of the $U_{\max}$, Ψ_{500}, $\int \Psi dp$, and U_{sfc} metric tropical belt widths are significantly different from each other at the 95% confidence level.

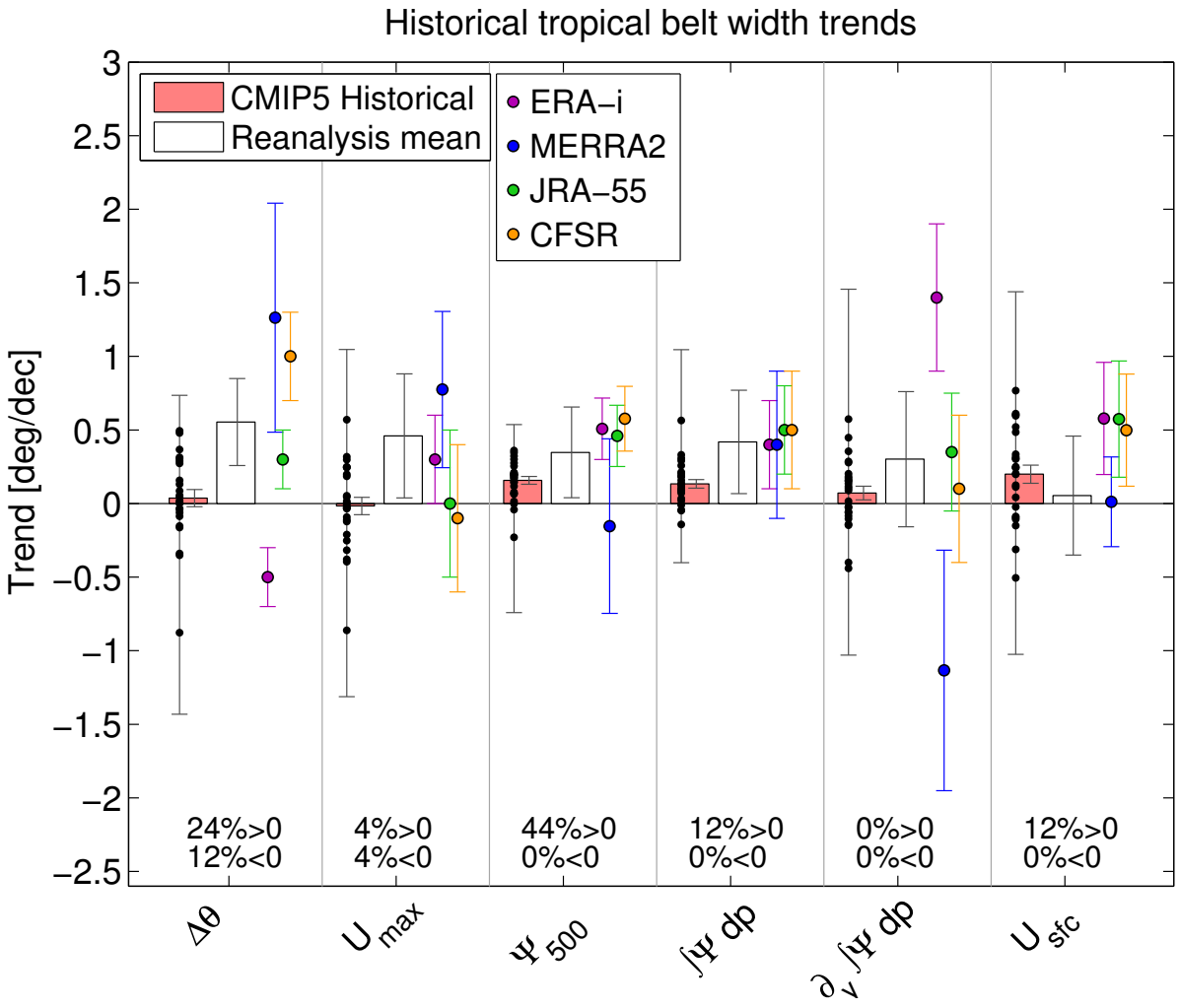

Figure 3.6: Trends in the tropical belt width for the 1979-2005 time period. Bars indicate the mean trend from the CMIP5 Historical simulation (light red) and the reanalysis-mean time series (white). For the CMIP5 Historical simulation, whiskers indicate the maximum and minimum 95% confidence interval bounds among CMIP5 models and the 95% confidence intervals for the multi-model-mean trend. Individual model estimates are indicated by black dots. Individual reanalysis estimates are shown for ERA-i (purple), MERRA2 (blue), JRA-55 (green), and CFSR (yellow). For the reanalysis-mean time series and individual reanalyses, whiskers indicate 95% confidence intervals. The percentage of CMIP5 model trends that are significantly positive (top) and negative (bottom) is shown at the bottom of each panel.

Further, none of the reanalysis-mean tropical belt width trends are significantly different from each other at the 95% confidence level. However, the reanalysis-mean trends should not be interpreted as representative of the observed trends. With only four reanalyses, it is unlikely that all individual reanalysis biases have been averaged out. The reanalysis-mean may instead be more appropriate for determining which individual reanalysis trends are significant outliers. For example, MERRA2's and ERA-Interim's $\partial_y \int \Psi dp$ trends could be considered outliers because they are significantly different than the reanalysis-mean trend. Conversely, it may be possible to say that the reanalyses' $\int \Psi dp$ metric tropical expansion trends could be assigned some additional confidence because none are significantly different from the reanalysis-mean $\int \Psi dp$ metric expansion trend. However, without an estimate of historical tropical expansion derived from observations, it may not be possible to further conclude whether the reanalysis trends actually reflect the observed trends.

The multi-model-mean trends in the tropical belt width average out much of the natural variability in the trends, which manifests differently in different model simulations. The actual historical evolution of the tropical belt width contains natural variability and is therefore hard to discern from the multi-model-mean. The multi-model-mean trends are small, ranging between 0.0 deg/dec for the $U_{\max}$ metric width and 0.2 deg/dec for the U_{sfc} metric width. For the subtropical jet and tropopause break metrics, the multi-model-mean trends are not statistically significant, while for the streamfunction and surface wind metrics, the multi-model-mean trends are significant and range from 0.1 to 0.2 deg/dec. This is similar to the 0.1 to 0.3 deg/dec Hadley-cell-based tropical widening trends found by Hu et al. (2013) for the same data and time period.

It is worth considering the range of model trends as well, as multi-model-mean trends describe only the forced response. There is a 1.0-1.5 deg/dec spread in the individual model trends for any given metric, and for each metric there are CMIP5 simulations with positive and negative trends. However, all of the significant trends based on the streamfunction and surface wind metrics indicate expansion, while there are both significant expansion and contraction trends based on the subtropical jet and tropopause break metrics. 44% of the Ψ_{500} metric expansion trends are significant. This drops to 12% for the objective version of this metric ($\int \Psi dp$), and no trends based on the latitudes of maximum downwelling ($\partial_y \int \Psi dp$) indicate tropical expansion. The multi-model-mean trends and the ranges of trends for the streamfunction and surface wind metrics are similar to those that Johanson and Fu (2009) found using the Ψ_{500} metric in CMIP3 historical simulations, despite modeling advances between CMIP3 and CMIP5.

We now examine whether the reanalyses' trends in the tropical belt width fall outside the range of model trends. A reanalysis trend could be said to fall outside of the range of model trends if it is significantly different from every model trend for a given metric. An alternative and perhaps simpler formulation may be to ask whether the reanalysis trends were drawn from a distribution with the mean given by the multi-model-mean and the standard deviation given by the standard deviation of model trend estimates. However, since the distribution of trends from which the models draw is unknown, we take into account the uncertainties in the individual model trend estimates.

We assess the significance of the differences by performing two-sided Student's t-tests for the difference of means for each reanalysis and model trend combination for a given tropical belt width metric. Note that one cannot typically visually compare 95% confidence

intervals to determine whether two trends are statistically significantly different. For two trend estimates, their difference is not statistically significant at the 95% confidence level if either of the trend estimates themselves fall within the other's 95% confidence intervals (cf. Eq. 2 of Lanzante (2005)). However, in any other case, the difference may or may not be statistically significantly different.

In some cases it appears that the reanalysis trends are larger than the model trends. However, for every reanalysis trend using a given metric, at least one model trend exists that is not statistically significantly different from the reanalysis trend. That is, for any given metric none of the reanalysis trends are statistically significantly different from every CMIP5 Historical simulation's trend.

As an illustrative example, consider CFSR's Ψ_{500} trend, the highest reanalysis trend estimate using the Ψ_{500} metric. Two climate model trend estimates fall within its 95% confidence interval, and nearly half of the model trend estimates are not significantly different from its trend estimate at the 95% confidence level. In this specific case, we conclude that CFSR's trend does not fall outside of the range of model trends because it is not statistically significantly different from every model trend.

We find that none of the reanalysis trends fall outside the range of model trends, and thus cannot reject our null hypothesis. As a result, we do not find sufficient evidence to claim there is a discrepancy in tropical expansion estimated in climate models and reanalyses over the historical period. One could argue that there is still a distinction between tropical expansion in the reanalyses and the models: few models have multiple significant trends estimated by different metrics (only five models have significant trends in at least two metrics), while the majority of trends within the reanalyses are significant.

However, this could be due to the enhanced variability in the models' tropical belt widths (Fig. 3.2), which increases the significance thresholds for a majority of the metrics.

3.4.2 Projected trends in the tropical belt width

The multi-model-mean trends in the CMIP5 RCP8.5 experiment (Fig. 3.7) are virtually the same as they are in the Historical experiment. As in the Historical experiment, all of the streamfunction and surface wind metric trends that are significant indicate tropical expansion. For the Ψ_{500} and $\int \Psi dp$ metric widths, *all* models predict statistically significant tropical expansion, ranging between 0.1 and 0.5 deg/dec. The $\partial_y \int \Psi dp$ metric indicates significant expansion for only 68% of the models, with rates of expansion ranging between -0.1 and 0.4 deg/dec. 76% of the models have significant tropical expansion based on the U_{sfc} metric, with rates of expansion ranging between 0.0 and 0.3 deg/dec.

The subtropical jet and tropopause metrics have no robust forced response, with approximately equal numbers of models exhibiting tropical belt expansion and contraction. The trends in the tropical belt width range between between -0.7 and 1.0 deg/dec for the $\Delta\theta$ metric and between -0.2 and 0.2 deg/dec for the U_{max} metric, with no significant multi-model-mean trends.

While the range of CMIP5 model trends for each metric generally overlap, this does not mean that models with stronger expansion in one metric necessarily have stronger expansion in another metric. There is a robust scaling in tropical expansion trends among the streamfunction and surface wind metrics in the RCP8.5 simulations (Fig. 3.8h-j) that is stronger in the Southern Hemisphere than in the Northern Hemisphere. In the Northern Hemisphere the U_{sfc} metric edge latitude trends unexpectedly scale with all other tropical

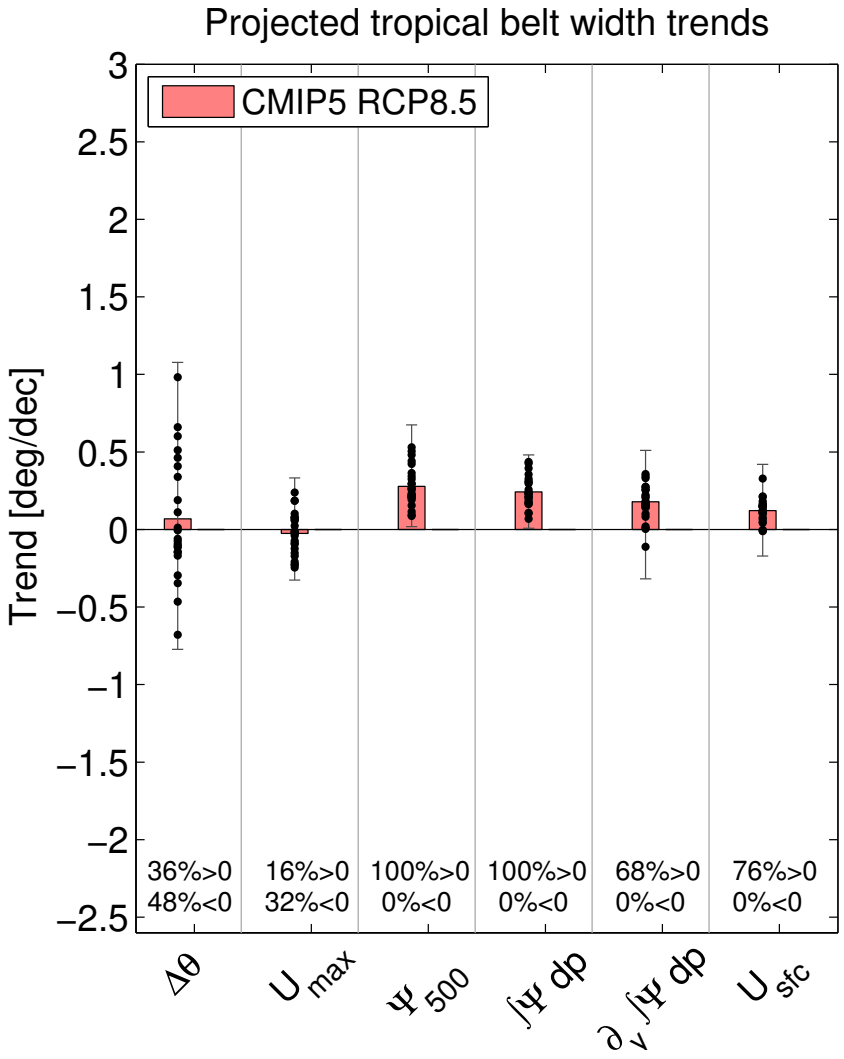

Figure 3.7: Trends in the tropical belt width for the 2006-2100 time period. Bars indicate the mean trend from the CMIP5 RCP8.5 simulation. Whiskers indicate the maximum and minimum 95% confidence interval bounds. Individual model estimates are indicated by black dots. The percentage of CMIP5 model trends that are significantly positive (top) and negative (bottom) is shown at the bottom of each panel.

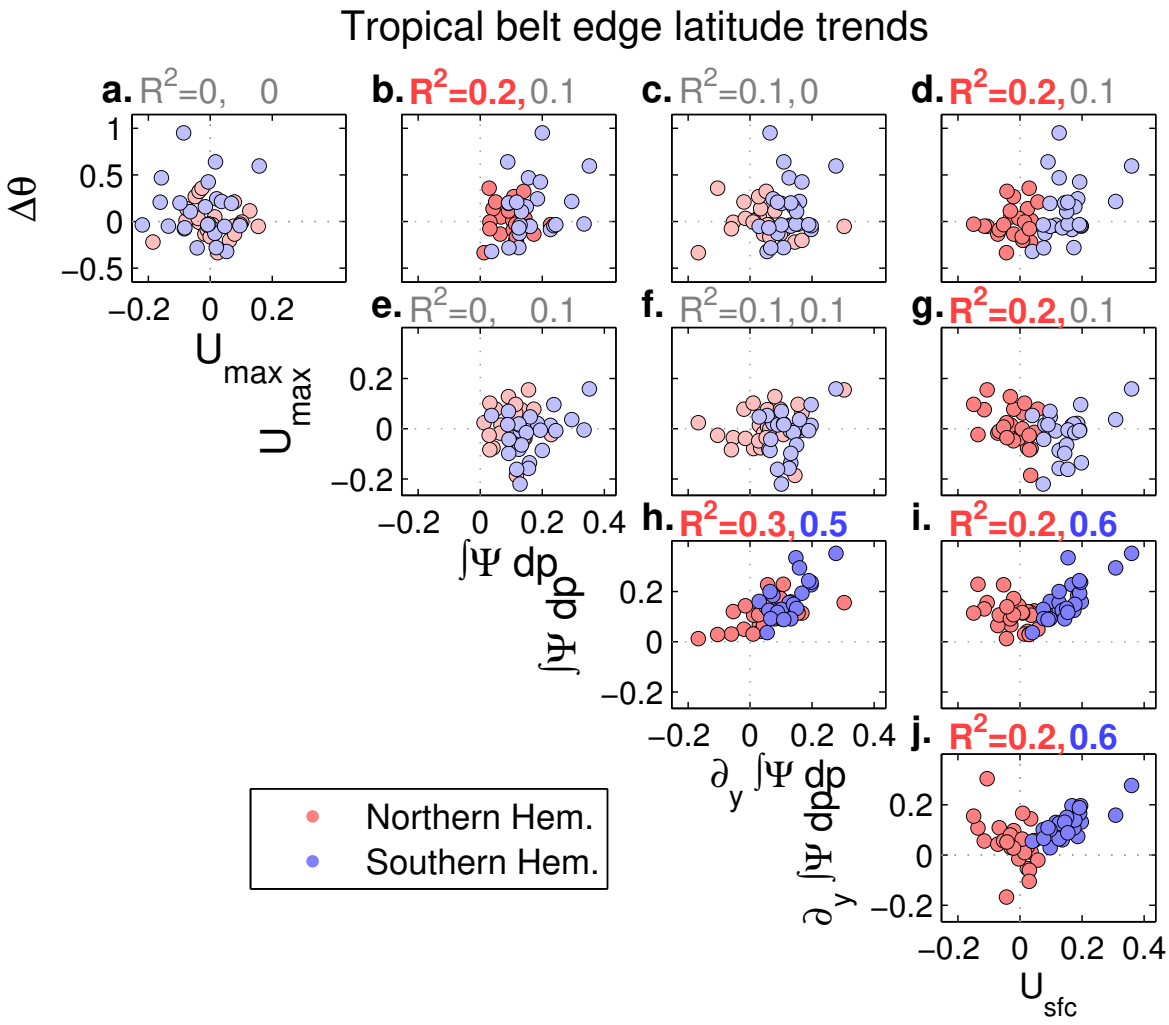

Figure 3.8: As in Fig. 3.5, but for the trends in the tropical belt edge latitudes.

belt edge latitude metric trends. There is also an unexpected correlation between $\Delta\theta$ and $\int \Psi dp$ metric expansion in the Northern Hemisphere only. These metrics have no co-variability (Fig. 3.3, 4) and do not scale in the mean (Fig. 3.5). In the models there are spurious correlations between some metrics and a lack of correlation between metrics that are correlated in the reanalyses (Fig. 3.3, 4). Whether this potential misrepresentation of the Northern Hemisphere zonal-mean circulation results in these unexpected scalings is unclear, and we hesitate to comment further without a deeper analysis.

3.4.3 Relation to the eddy-driven jet

Why do the streamfunction and surface wind metrics exhibit robust tropical expansion in response to radiative forcings while the tropopause and subtropical jet metrics do not? There is a well-documented relationship between interannual variations in the eddy-driven jet latitude and the edge latitude of the Hadley cell in the Southern Hemisphere (Kang and Polvani, 2011; Staten and Reichler, 2014). While several mechanisms could govern a poleward shift of the eddy-driven jet in response to radiative forcings (Chen and Held, 2007; Kidston et al., 2011), they all result in a poleward shift of the region of wave breaking and eddy momentum flux divergence in the subtropics, which would tend to drag the Hadley cell edge poleward (neglecting any changes to its internal dynamics).

Accordingly, there is a statistically significant correlation between tropical expansion measured by the latitudes of the Hadley cell edge ($\int \Psi dp$), the maximum downwelling ($\partial_y \int \Psi dp$), and zero zonal-mean surface zonal wind (U_{sfc}) and the shift in the latitude of the eddy-driven jet in the Southern Hemisphere in the RCP 8.5 experiment (Fig. 3.9c-f). Note that these correlations and regressions use only models with statistically significant trends in both the eddy-driven jet latitude and tropical belt edge latitude, though using all trends does not substantially change these relationships. There is no significant correlation between either the subtropical jet or tropopause break edge latitude trends and the trend in the latitude of the eddy-driven jet. The trends in the eddy-driven jet latitude are also not significantly correlated with any of the meridional circulation metric trends in the Northern Hemisphere (not shown), due to both the low number of significant trends and the poor temporal coupling between the two in the Northern Hemisphere in the models

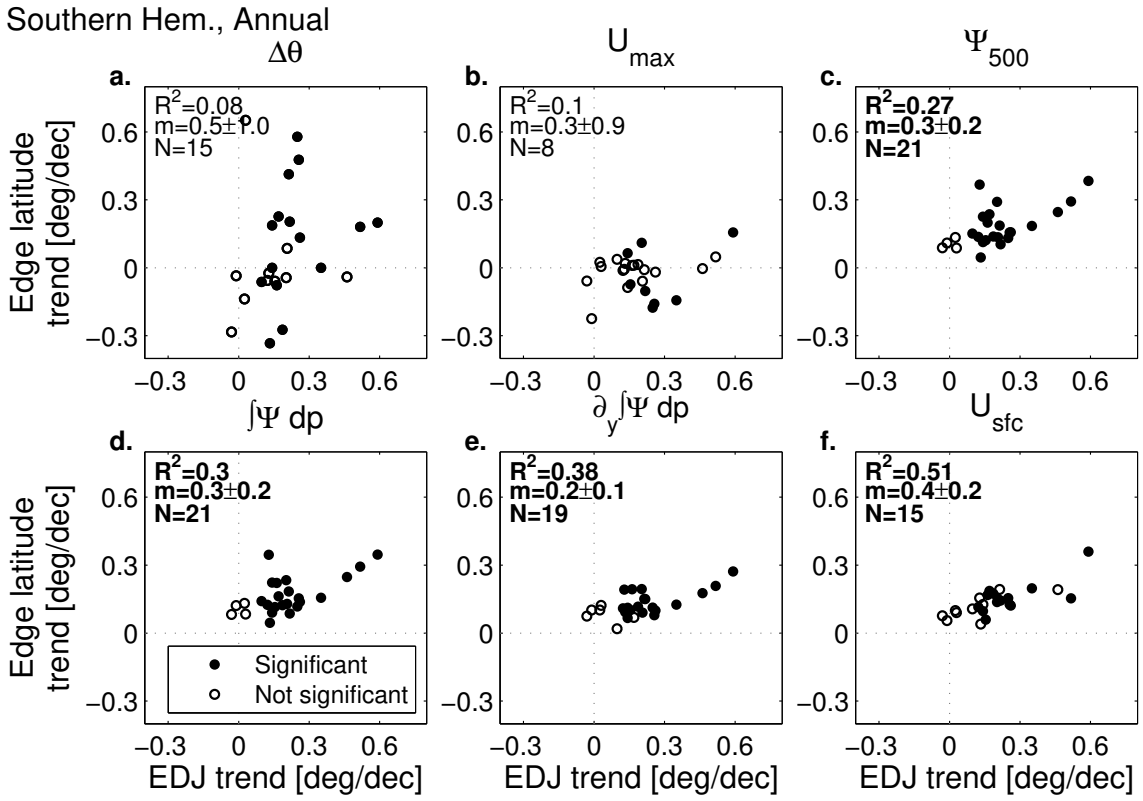

Figure 3.9: Trends in the tropical belt edge latitude versus trends in the latitude of the eddy-driven jet in the Southern Hemisphere in the CMIP5 RCP8.5 experiment, where filled symbols indicate both a significant trend in the eddy-driven jet latitude and tropical belt edge latitude. The percentage of variance explained (R^2), linear least-squares regression slope (m, deg/dec), and number of models with significant trends in both the eddy-driven jet latitude and the tropical belt edge latitude (N) is shown in each plot, where bold text indicates a correlation significant at the 95% confidence level.

(Fig. 3.4). Additionally, the eddy-driven jets in the Northern Hemisphere tend to have basin-specific variability and change (Barnes and Polvani, 2013). The resulting impacts on the zonal-mean eddy momentum flux divergence may not be as linear as they are in the Southern Hemisphere.

The scaling between the trend in the latitude of the eddy-driven jet and tropical expansion in the Southern Hemisphere is strongest in December-January-February (Fig. 3.10). Between 50 and 87% of the total inter-model variation in tropical expansion in the streamfunction and surface wind metrics can be explained by the poleward shift of the latitude of the eddy-driven jet. There remain no significant correlations between the shift in the latitude of the eddy-driven jet and tropical expansion as measured by the subtropical jet or tropopause metrics (Fig. 3.10a-b).

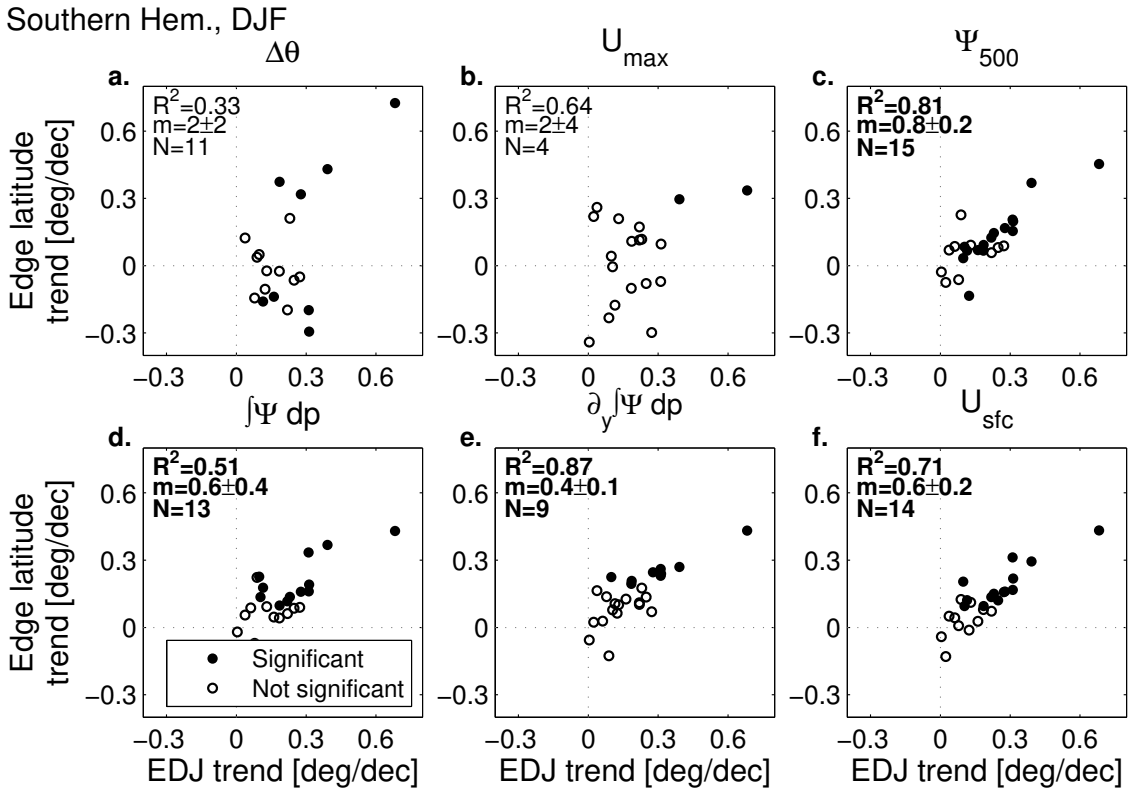

Figure 3.10: As in Fig. 3.9 but for December-January-February trend values.

The regression coefficients based on trends calculated for the full time series indicate a ratio of a 0.2 to 0.4 deg/dec trend in the Hadley cell edge for every 1.0 deg/dec trend in the eddy-driven jet latitude, slightly less than the interannual ratios reported in Kang and Polvani (2011) and Staten and Reichler (2014) and similar to the trend ratios in the Southern Hemisphere in austral winter reported by Staten and Reichler (2014). In austral summer, the regression coefficients double, confirming that the Hadley cell is more strongly connected to shifts in the latitude of the eddy-driven jet when the baroclinicity is low (Staten and Reichler, 2014).

3.4.4 Connection to surface climate

To conclude our exploration of the different metrics we perform a simple analysis of how they relate to three zonal-mean indices of surface climate in the reanalyses: the latitudes of the minimum of precipitation minus evaporation (min(P-E)), the latitudes where precipitation minus evaporation is zero (P-E=0), and the total surface area of the arid subtropics (area of P-E<0).

On monthly timescales, there is no substantial correlation between any of the surface climate indices and the tropical belt edge latitudes in either hemisphere. Soil moisture, vegetation, and other factors that communicate circulation and precipitation variability to evaporation rates may operate on seasonal to annual timescales, so we extend these correlations to non-deseasonalized, annual-mean data (Fig. 3.11).

Each surface climate metric is correlated with slightly different sets of tropical belt edge latitude metrics. In the Southern Hemisphere, the latitude where P-E=0 is not significantly correlated with any metric edge latitudes, while in the Northern Hemisphere it

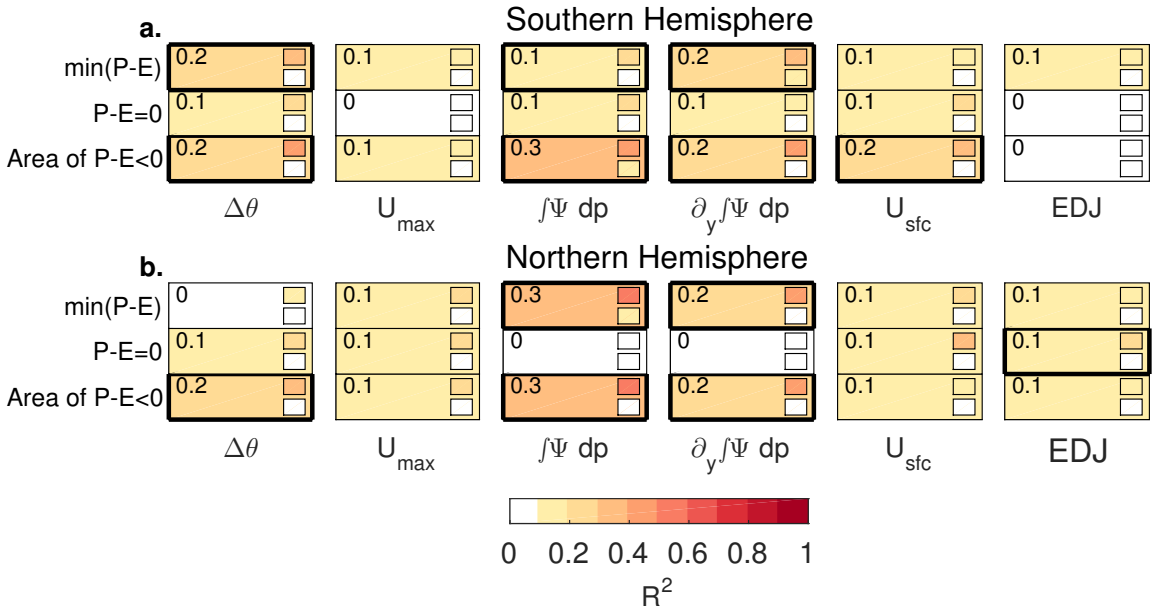

Figure 3.11: Correlation coefficients between the annual-mean tropical belt edge latitudes and eddy-driven jet latitudes and the surface climate indices in the (a.) Southern and (b.) Northern Hemispheres in reanalyses. The top, middle, and bottom patch of each panel displays the ensemble-mean correlation coefficients between the three surface climate indices and the latitudes of the tropical belt edge or eddy-driven jet. The small patches indicate the lowest and highest correlation coefficient among the reanalyses, while the numerical value of the mean correlation coefficient is printed in the upper left of each patch. Bold outlines indicate at least 3 of the 4 reanalyses have correlations significant at the 95% confidence level.

is correlated with only the EDJ latitude. In both hemispheres, the streamfunction metrics are significantly correlated with the area of P-E<0 and the min(P-E) latitudes. The strongest correlations are in the Northern Hemisphere, where the $\int \Psi dp$ metric edge latitudes and the min(P-E) latitudes and area of P-E< 0 are correlated with mean R^2 values of 0.3 and peak values of 0.5. This highlights the potential impact of variations in the Hadley cell width on surface climate on timescales as short as a year. The $\Delta\theta$ metric latitudes are correlated with the area of P-E<0 in both hemispheres and the min(P-E) latitudes in the Southern Hemisphere only, and the $U_{\max}$ metric has no significant correlation with any surface climate metric.

While there are some broad differences in the surface climate connections between the two sets of metrics, there is a substantial range in the values of the correlation coefficients among reanalyses. No particular reanalysis stands out with consistently weaker or larger correlation coefficients.

3.5 Summary of trend, variability results

Numerous metrics have been used to study tropical expansion. Two open questions are: (1) "Why do different metrics measure different rates of historical and future tropical expansion?"; and (2) "Why do rates of tropical expansion in reanalyses appear to be greater than those measured in climate models?" (Seidel et al., 2008; Staten et al., 2016; Davis et al., 2016).

We explored these questions with five objective tropical belt width metrics. Metrics that measure the latitudes of the Hadley cell edges, the latitudes of maximum downwelling in the Hadley cells, and the latitudes of zero zonal-mean surface zonal wind are temporally correlated within simulations, scale across simulations in the mean and in their rates of tropical expansion, and exhibit robust historical and future tropical expansion. On the other hand, metrics that measure the latitudes of the tropopause breaks and subtropical jets are weakly coupled and have no detectable forced response to radiative forcings, even in the most extreme radiative forcing scenario in CMIP5. There are few correlations in any sense across these two sets of metrics.

To understand these differences, consider the zonal-mean thermal wind equation,

$$\frac{\partial [u]}{\partial p} = \frac{1}{f}\frac{\partial}{\partial y}\left(-\frac{R[T]}{p}\right) \tag{2}$$

which holds approximately – away from the surface and the equator – and follows from geostrophic balance in the zonal-mean meridional momentum equation. T is the temperature and R is the gas constant for dry air. The subtropical jet metric quantifies an aspect of the zonal-mean zonal circulation, which is related to zonal-mean temperature. The tropopause metric also quantifies an aspect of zonal-mean temperature, which by Eq. 3 is related to the zonal circulation as well. In this sense both metrics are "zonal circulation" metrics as their connection occurs through momentum balance.

On the other hand, the zonal-mean meridional circulation is by definition ageostrophic and is connected to the eddy momentum fluxes and the zonal-mean zonal wind at the surface through the zonal-mean zonal momentum equation,

$$-f[v] = -\partial_y[u^* v^*] - \begin{cases} 0 & \text{if } p < p_s \\ \frac{[U_{\text{sfc}}]}{\tau} & \text{if } p = p_s \end{cases} \tag{3}$$

where p_s is the surface pressure. This equation provides a relation between the streamfunction metrics, which are based on [v], and the zonal-mean surface zonal wind metric. Both are constrained by the eddy momentum fluxes. Taking the vertical integral as in Eq. 2 shows that the drag on the zonal-mean surface zonal wind balances the vertically-integrated eddy momentum flux convergence. In the free atmosphere the eddy

momentum flux convergence is balanced by the Coriolis torque exerted by the mean meridional wind. The zonal-mean surface zonal wind at the surface is unlike the zonal-mean zonal wind everywhere else in the atmosphere because it is not proportional to the meridional gradient of temperature.

It follows that metrics that measure the tropical belt edge latitudes based on the mean meridional streamfunction or the zonal-mean surface zonal wind are physically linked to the distribution of eddy momentum fluxes. The latitude of zero zonal-mean surface zonal wind shares characteristics of and is conceptually linked to the meridional circulation and the Hadley cell edges. Zonal circulation metrics based on the tropopause and subtropical jet are instead physically linked to the distribution of temperature. While it is true that eddy momentum fluxes also modify the zonal circulation and could physically couple the zonal and meridional circulation metrics, this coupling does not emerge in our analysis.

One could alternatively segregate the metrics in terms of their height in the atmosphere (Solomon et al., 2016). The subtropical jet and tropopause break are both located at the top of the troposphere. On the other hand, the zonal-mean surface zonal wind could be cast as a "surface" metric. The streamfunction is by definition a vertically-integrated measure, so it isn't easily classified by a single level in the atmosphere, though the maximum occurs near 500 hPa and could be classified as "mid-tropospheric". However, the subtropical jet is a product of the vertically-integrated meridional temperature gradient. Similarly, the zonal-mean surface zonal wind, while technically located at the surface, is related to the vertical integral of the eddy momentum flux convergence. The tropopause height is linked to surface temperature, average tropospheric lapse rates, and the stratospheric circulation (Thuburn and Craig, 1997; Juckes, 2000), even on regional scales

(Wu and Shaw, 2016). Segregating metrics by their height may neglect the physical processes important for their co-variability and response to forcings.

The poleward shift of the Southern Hemisphere eddy-driven jet is a consistent model response to historical climate forcings (Chen and Held, 2007), idealized greenhouse gas forcings (Kushner et al., 2001), and to the suite of forcings in simulations of future climate (Yin (2005); Miller et al. (2006); Kidston and Gerber (2010); Swart and Fyfe (2012); Barnes and Polvani (2013), and confirmed here in Fig.'s 9 and 10). We hypothesize that its coupling on all timescales with the meridional circulation metric edge latitudes through subtropical eddy momentum flux divergence may result in their robust tropical expansion in historical and future climate simulations.

Conversely, we hypothesize that the zonal circulation metrics may not have robust tropical expansion because they do not have such direct theoretical and statistical relationships with the eddy momentum flux divergence or the eddy-driven jet. The subtropical jets shift upward through a thermal wind response to lower-stratospheric cooling and upper-tropospheric warming produced by increasing greenhouse gas concentrations (Shepherd and McLandress, 2010). Whether they shift poleward or equatorward may be sensitive to the structure of those temperature anomalies, and not a change in eddy-driven jet dynamics.

The CMIP5 Historical experiments simulate an envelope of possible tropical expansion trends given the external constraints on the climate system. We find there is insufficient evidence to conclude that there is a discrepancy between tropical expansion trends in reanalyses and models, as all of the reanalysis trends fall within the range of model trends for any given tropical belt width metric.

The model spread is not only due to natural variability, but also differences in parameterizations. Reanalyses' trends are impacted by data assimilation methods. Our analysis did not take such effects into account and only demonstrates that the level of evidence necessary to declare a discrepancy has not yet been met. Differences in model and reanalysis configurations and natural variability need to be disentangled to reach a more conclusive result.

While Johanson and Fu (2009) concluded that there was a discrepancy between the tropical expansion trends in models and in reanalyses and observations, they did not consider the uncertainties in the trend estimates. In the case of model trend distributions, the trend estimates do not form a "known" distribution but instead have their own uncertainties that should be considered. Johanson and Fu (2009) also used an older set of reanalyses, which may further contribute to the apparent contradiction between their results and ours.

While there is a large range of tropical expansion rates in the reanalyses, for a majority of tropical belt width metrics they are not statistically significantly different. In other words, there is scant evidence to demonstrate a discrepancy among the reanalyses.

The multi-model-mean trends, while small, illustrate the forced component of tropical expansion, while the reanalysis trends indicate one particular realization impacted by natural variability. Given that the reanalysis trends tend toward being greater than the multi-model-mean, the observed widening of the tropical belt over the past 30 years may be the result of a forced signal amplified by natural variability. However, simulations which are forced with observed sea surface temperatures do not have constrained tropical belt width climatologies (eg., Fig. 5 of Davis and Birner (2016)). Further, the range of tropical belt

width trends in the CCMVal-2 REF-B1 experiment, which is forced by observed sea surface temperatures, is as large as the range of tropical belt width trends in the CMIP5 Historical experiment (Fig. 3.12). A naive expectation may be that forcing models with observed sea surface temperatures would lead to a convergence in their tropical expansion trends. Differences in climate feedbacks among models (Feldl and Bordoni, 2016) and both internal atmospheric (Garfinkel et al., 2015) and coupled ocean-atmosphere variability (Kang et al., 2013) can produce significant inter-model variations in tropical expansion. The physical processes driving such internal variability in the tropical belt width are unclear.

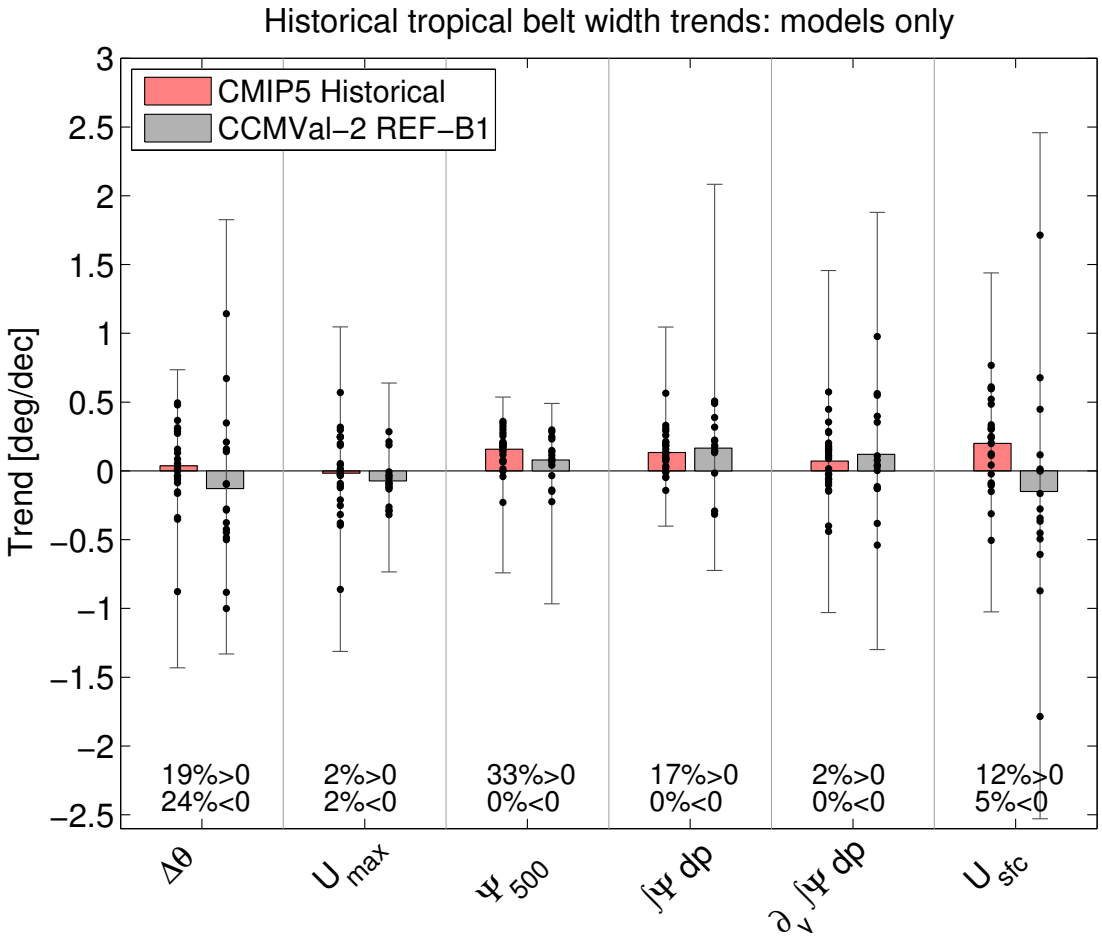

Figure 3.12: As in Fig. 3.6, but for the CMIP5 Historical and CCMVal-2 REF-B1 experiment tropical belt width trends.

Regarding surface climate, the Hadley cells' strongest impact appears to be on the most arid regions where P-E is at a minimum and on the areal extent of the arid regions themselves, with little impact on regions situated near or within the Ferrel cell where P-E=0. Precipitation declines at the poleward flanks of the subtropics, where precipitation minus evaporation is nearly zero, may be associated with the poleward shift of the midlatitude storm tracks (Scheff and Frierson, 2012). There is a weak association between the eddy-driven jet latitudes and the latitudes of P-E=0 on annual timescales in the Northern Hemisphere (Fig. 3.11b), but not in the Southern Hemisphere (Fig. 3.11a). However, the ratio of precipitation to potential evapotranspiration has recently been used to study global changes in arid climates (Scheff and Frierson, 2012; Feng and Fu, 2013). This quantity may be better for assessing the connections between circulation variability and surface climate as it measures the precipitation deficit against the evaporative demand of the atmosphere (Feng and Fu, 2013).

The future of earth's subtropical circulations are unclear, even if the forced signal is known. The lack of inter-model scaling in tropical expansion between the meridional and zonal circulation metrics suggests that in any given individual realization of earth's future climate the Hadley cells, subtropical jets, and surface circulations may shift in latitude at different rates and potentially in different directions. Distinct realizations may even exhibit different structural changes to the circulation. This presents a challenge for assessing historical tropical expansion from observations. While the metrics based on the Hadley cells are consistent with each other, in-situ radiosonde measurements have insufficient sampling to accurately construct an estimate of the zonal-mean meridional winds comprising the Hadley cells (Waliser et al., 1999). Observations can be used to asses

tropical expansion based on the tropopause and the subtropical jets, but these metrics have little connection in any sense to metrics based on the Hadley cells. However, the metric based on the zonal-mean surface zonal wind is well-constrained in reanalyses, is generally representative of the Hadley cell edge latitude, and can be obtained from observations, similar to the sea-level pressure metric used by Choi et al. (2014).

At the most basic level, tropical expansion can only be understood by examining more than just the mean meridional streamfunction. Each metric holds unique information about variability and change in the subtropical circulation, and assessing their relationships can yield a more complete story about the circulation response to radiative forcings.

3.6 Relationship to Rossby wave fluxes

With the variability and response to forcings characterized and explored, this section examines the remaining moment of the Hadley circulation - the mean state - in comprehensive models. Understanding variations in the mean circulation can uncover robust relationships that can inform a hypothesis of the mechanisms governing variability and change in the circulation. A subset of three tropical belt width metrics from the previous sections are used here, each appearing to capture a different aspect of the tropical belt: the $\int \Psi dp$, U_{max}, and $\Delta\theta$ metrics.

In addition to ERA-i, two older reanalyses are used in this section: the Modern-Era Retrospective Analysis (Rienecker et al., 2011), referred to here as MERRA, and the National Centers for Environmental Prediction/National Center for Atmospheric Research (NCEP/NCAR) Reanalysis (Kalnay et al., 1996), referred to here as NCEP. We use each

reanalysis' monthly-mean, pressure-gridded product. MERRA, ERA-i, and NCEP are supplied on a $1/2^\circ \times 2/3^\circ$, $3/4^\circ \times 3/4^\circ$, and $2.5^\circ \times 2.5^\circ$ degrees latitude $\times$ degrees longitude resolution grid, respectively. The three reanalyses' pressure-gridded outputs have the same vertical resolution about the tropical tropopause. MERRA and NCEP institute a 3D-Var assimilation scheme (Rienecker et al., 2011; Kalnay et al., 1996) whereas ERA-i uses a 4D-Var assimilation scheme (Dee et al., 2011). Only the 1979-2013 period is used in this analysis.

Finally, we employ Global Positioning System radio occultation (GPS-RO) retrievals from the Constellation Observing System for Meteorology, Ionosphere, and Climate (COSMIC) supplied by the University Corporation for Atmospheric Research (UCAR). The bending angle of GPS radio waves measured by the COSMIC satellite constellation is proportional to the vertical gradient of the refractive index, which below the ionosphere is itself a function of the air pressure, the air temperature, and the water vapor partial pressure (Anthes et al., 2008). At temperatures below about 250 K the contribution from water vapor is negligible. That is, in the upper troposphere and stratosphere temperature profiles can be constructed as a function of pressure, neglecting the water vapor contribution – these are referred to as dry profiles. The COSMIC data supplied by UCAR also provide so-called wet profiles, which are constructed by running a 1D-VAR data assimilation scheme with ECMWF operational weather analyses to separate the water vapor and temperature contributions to the refractive index (see Anthes et al. (2008) for further details). Here, we only make use of the dry profiles and limit our analysis to the region above 400 hPa.

We average daily profiles of COSMIC temperature and pressure into 181 equally-spaced latitude bins between 90 °S and 90 °N and 200 equally-spaced altitude bins between 0 km and 40 km to produce monthly zonal means. These zonal means on altitude are then interpolated onto a pressure grid to create a zonal mean of temperature and geopotential height on pressure. COSMIC retrievals typically do not penetrate to the surface, so we use the ERA-i climatology for zonal-mean surface potential temperature as the surface field for COSMIC for the tropopause metric described later. We use retrievals from 2007-2013, excluding 2006 due to the low number of profiles during this spin-up period. In our analysis of tropical belt widths, COSMIC is down-sampled to the ERA-i pressure grid to ensure any differences are not due to the vastly different vertical resolutions.

3.6.1 Tropical belt grid size effect

To conclude this exploration of the Hadley circulation and tropical belt in models, we performed an exhaustive analysis of plausible model biases and scalings in the tropical belt width. For example, increases in tropical surface air temperature are associated with Hadley cell expansion (Adam et al., 2014; Frierson et al., 2007b), potentially through the modification of tropical static stability via moist adiabatic adjustment. It is reasonable to hypothesize, then, that tropical surface air temperature may predict intermodel variations in the mean tropical belt width. However, we find no significant correlations between the tropical surface air temperature and the mean tropical belt width, with insignificant correlation coefficients ranging from -0.01 to 0.17 (Fig. 3.13). Here, tropical surface air temperature is defined as the mean 2 meter air temperature between 20°S and 20°N (Adam et al., 2014) weighted by the cosine of latitude, and the mean tropical belt width is the

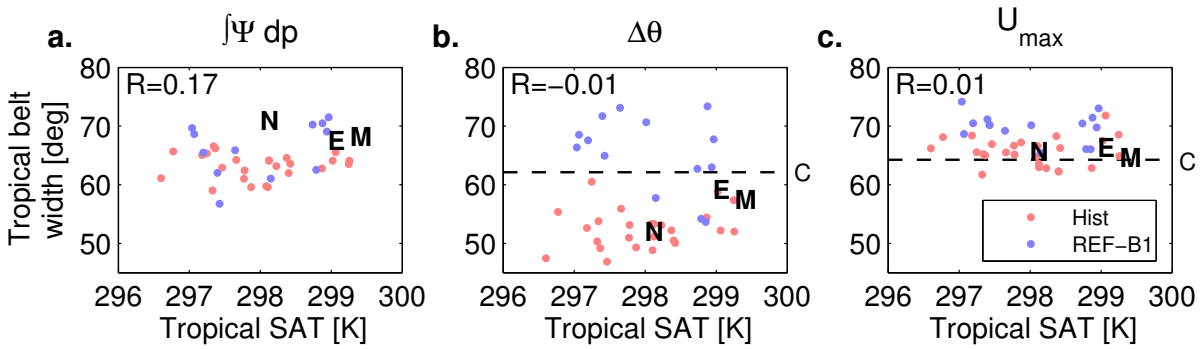

Figure 3.13: Mean tropical surface air temperature (SAT) versus each model's (a.) $\int \Psi dp$, (b.) $\Delta\theta$, and (c.) U_{max} metric mean tropical belt width for the CMIP5 Historical (red) and CCMVal-2 REF-B1 (blue) model ensembles. E, M, and N correspond to ERA-i, MERRA, and NCEP, respectively. The mean $\Delta\theta$ and U_{max} metric widths from COSMIC are indicated by dashed lines. Tropical surface air temperature is defined as the cosine-weighted average of 2 meter air temperature over 20S to 20N. No correlations are significant at the 95% confidence level.

mean of every monthly-mean tropical belt width over the entire historical run. Changes in the gradient in surface air temperature might also be associated with changes in the Hadley cell width (Adam et al., 2014; Frierson et al., 2007b), though we also find no such intermodel relationship with the mean tropical belt width. This indicates the quantities associated with changes in the tropical belt width within models are not necessarily the same quantities defining the intermodel variation in the mean tropical belt width.

The sole quantity dictating any significant intermodel variation in the mean tropical belt width that we were able to identify was horizontal grid size, with finer horizontal grid size leading to a narrower tropical belt with correlation coefficients ranging between 0.4 and 0.62 (Fig. 3.14). These correlations extend to the tropical belt edge latitudes as well, with similar values (not shown). The highest correlation for the CMIP5 Historical and CCMVal-2 REF-B1 models separately is for CCMVal-2 REF-B1's $\int \Psi dp$ metric width (R=0.71), indicating that 50% of the total intermodel variation in the $\int \Psi dp$ metric width

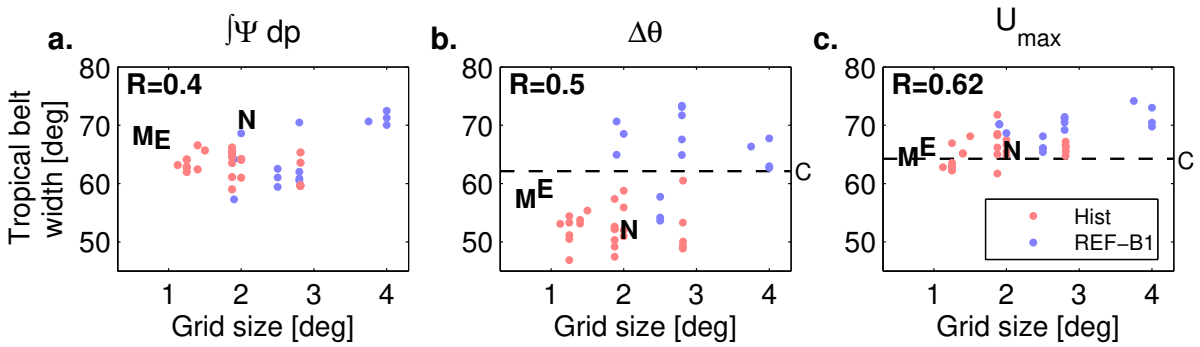

Figure 3.14: Model grid size in degrees latitude versus each model's (a.) $\int \Psi dp$, (b.) $\Delta\theta$, and (c.) U_{max} metric mean tropical belt width for the CMIP5 Historical (red) and CCMVal-2 REF-B1 (blue) model ensembles. E, M, and N correspond to ERA-i, MERRA, and NCEP, respectively. The mean $\Delta\theta$ and U_{max} metric widths from COSMIC are indicated by dashed lines. All correlation coefficients are statistically significant at the 99% confidence level.

in the CCMVal-2 REF-B1 scenario is attributable to grid size. We have excluded the ULAQ model from this analysis as the correlations are sensitive to its large grid size of 11.5 deg, however it obeys the relationship between grid size and tropical belt width (e.g., for the $\Delta\theta$ metric, its width is 79.2 deg, the widest tropical belt width for this metric).

The IPSL-CM5A model from CMIP5 is run at both low horizontal resolution (IPSL-CM5A-LR) and moderate horizontal resolution (IPSL-CM5A-MR). This grid size effect manifests within this model, as the low resolution $\int \Psi dp$ metric width of 62.9 deg and U_{max} metric width of 66.9 deg are larger than the moderate resolution $\int \Psi dp$ metric width of 61.1 deg and U_{max} metric width of 66.2 deg. However, the model's $\Delta\theta$ metric width is marginally larger in the low resolution run (46.9 deg versus 47.4 deg). This is evidence that the grid size effect in the tropical belt width, at least in the circulation-based metrics, is consistent at the level of an individual model.

Most models have a U_{max} metric tropical belt width that is wider than observed in COSMIC (Fig. 3.14c), but with finer resolution the modeled width approaches the

observed value. However, increasing model resolution does not lead to a more accurate tropical belt width for the $\Delta\theta$ metric width, where all models (including reanalyses) with a resolution finer than 2 degrees latitude exhibit a narrower tropical belt than COSMIC (Fig. 3.14b). Most of the models have a narrower $\int \Psi dp$ width than the reanalyses, the opposite of which is true for the U_{max} width.

Model performance in simulating the mean tropical belt width does depend upon the particular metric, but there is a significant, positive correlation between model grid size and mean tropical belt width regardless of the metric used. The source of this model bias is investigated next, as it may help to resolve the model differences in the mean tropical belt width and illuminate the processes governing the width of the tropical belt.

3.6.2 Eddy-grid size effect

Hadley cell scaling theories that assume angular momentum conservation (Held, 2000) effectively assume an absolute vorticity of zero within the Hadley cell (the meridional derivative of zonal-mean angular momentum is the zonal-mean absolute vorticity). In these theories the zonal-mean zonal momentum balance is between the meridional advection of zonal momentum, $-[v][\zeta]$, and the Coriolis torque, $-f[v]$, so that the sum $\overline{\zeta} + f$, or the absolute vorticity, remains zero within the poleward flow of the upper branch of the cell. However, in reality the magnitude of f substantially increases in the subtropics and the relative vorticity contribution becomes small. A more accurate balance outside the tropics is between the Coriolis torque and the eddy momentum flux convergence,

$$-f[v] \approx -\frac{\partial[u'v']}{\partial y} \tag{4}$$

where $[u'v']$ is the horizontal eddy momentum flux, where primes denote departures from the zonal mean and we have assumed a steady-state away from the surface and that $|\overline{\zeta}| << f$. Under the quasi-geostrophic scaling typically employed to study dynamics away from the equator, $-[v][\zeta]$ vanishes from the momentum equation - advection in the quasi-geostrophic framework is done by the geostrophic wind, and the zonal-mean of the geostrophic meridional wind is zero.

The horizontal resolution of a model has been shown to influence the eddy momentum fluxes (Boville, 1991; Held and Phillipps, 1993) as well as Rossby wave breaking frequency (Béguin et al., 2013). Given that $[v]$ vanishes where the eddy momentum flux convergence is zero, the edges of the Hadley cells, where $[v] = 0$, will be located near the latitude of the maximum eddy momentum flux and thus be subject to model differences in its strength and structure. The zonal wind and tropopause structure have no simple balance condition with the eddy fluxes, so we now focus exclusively on the Hadley cells and the $\int \Psi dp$ metric.

We wish to answer: how much of the grid size effect in Hadley cell width, as measured by the $\int \Psi dp$ metric, can be explained by a grid size effect in the eddy momentum flux convergence which projects onto changes in the meridional wind via the Coriolis torque? Perhaps more generally, how much of the total intermodel variation in Hadley cell width can be explained not only by a grid size effect, but by a grid size effect in this eddy forcing?

CMIP5 Historical output at daily time resolution that is necessary to directly calculate eddy fluxes is limited to a subset of vertical levels and models, insufficient to study the vertical structure of any eddy grid size effect across a large enough sample space of model grid sizes. However, the CCMVal-2 REF-B1 models span a large sample of grid sizes and allow the estimation of eddy fluxes because a subset of 9 CCMVal-2 models provide eddy fluxes as monthly-mean model output.

3.6.3 Estimating eddy fluxes from time-mean fields

The zonal-mean zonal momentum equation in Cartesian coordinates is given by

$$\frac{\partial[u]}{\partial t} + [\omega]\frac{\partial[u]}{\partial p} - [v]([\zeta] + f) = -\frac{\partial[u'v']}{\partial y} - \frac{\partial[u'\omega']}{\partial p} + [F_x] \tag{5}$$

where $[u]$, $[v]$, and $[\omega]$ are the zonal-mean zonal, meridional, and vertical components of the wind, $[\zeta] = -\partial_y[u]$ is the zonal-mean relative vorticity, $[u'v']$ and $[u'\omega']$ are the meridional and vertical eddy momentum fluxes, and $[F_x]$ is the zonal-mean of non-conservative forces such as friction. Brackets indicate zonal means and primed quantities denote departures from the zonal mean.

In the time mean and away from the surface, the horizontal eddy momentum flux convergence is proportional to the Coriolis torque and the advection of zonal momentum,

$$-\frac{\partial[u'v']}{\partial y} \approx -[v](f + [\zeta]) + [\omega]\frac{\partial[u]}{\partial p} \tag{6}$$

where we have retained the vertical advection of zonal momentum to ensure an accurate

calculation. It should be noted that we cannot calculate the vertical eddy momentum flux (the second-to-last term in Eq. 5) from CCMVal-2 model output, and it may be non-negligible in the subtropical mid-troposphere where there are strongly-sloped isentropes and strong, zonally-asymmetric subsidence. The eddy momentum flux convergence can be estimated by calculating the terms on the right-hand side of Eq. 6 from the model-mean, time-mean fields from the CCMVal-2 models.

Similarly, in the time-mean and away from the surface, the Eliassen-Palm flux divergence is proportional to the Coriolis torque of the transformed Eulerian-mean meridional wind and the advection of zonal momentum by the transformed Eulerian-mean wind,

$$\nabla \cdot F \approx -[v^*](f + [\zeta]) + [\omega^*]\frac{\partial [u]}{\partial p} \tag{7}$$

where $[v^*]$ and $[\omega^*]$ are the transformed Eulerian-mean meridional and vertical winds (Andrews and McIntyre, 1976). All 15 CCMVal-2 REF-B1 models examined here output the transformed Eulerian-mean winds. Thus, the Eliassen-Palm flux divergence can be estimated by calculating the terms on the right-hand side of Eq. 7 from the model-mean, time-mean fields from the CCMVal-2 models.

Under quasi-geostrophic scaling, the Eliassen-Palm flux divergence is given by

$$\nabla \cdot F = \frac{\partial F_y}{\partial y} + \frac{\partial F_p}{\partial p} = -\frac{\partial [u'v']}{\partial y} + \frac{\partial (f[v'\theta']/[\overline{\theta_p}])}{\partial p} \tag{8}$$

where F_y and F_p are the meridional and vertical components of the Eliassen-Palm flux, θ the potential temperature, and $[\overline{\theta_p}]$ is the static stability. The eddy heat flux convergence,

or the vertical component of the Eliassen-Palm flux divergence, can simply be estimated as the difference between the Eliassen-Palm flux divergence and the eddy momentum flux convergence.

The meridional component of the Eliassen-Palm flux is calculated by integrating the eddy momentum flux convergence meridionally with the "boundary" condition that the estimated horizontal component equals the multi-model-mean horizontal component at the equator from the subset of 9 models. Similarly, the vertical component of the Eliassen-Palm flux is calculated by integrating the eddy heat flux convergence with the "boundary" condition that the estimated vertical component equals the multi-model-mean vertical component at 500 hPa. The components of the Eliassen-Palm flux are used only for illustrative purposes in Fig. 3.16 and do not factor into our calculations of the impact of the eddy grid size effect on the Hadley cell width.

A comparison between the estimated and actual Eliassen-Palm flux and its divergence and the eddy momentum flux convergence for the 9 CCMVal-2 models is shown in Fig. 3.15. The Eliassen-Palm flux vectors are scaled as in Edmon et al. (1980), where the meridional and vertical components of the Eliassen-Palm flux are multiplied by the distance in each plot occupied by 1 radian of latitude and 1 pascal of pressure, respectively. The vector magnitudes are equivalent in all panels Fig. 3.15 but as in Edmon et al. (1980) are scaled to an arbitrary maximum magnitude. The approximations produce reasonable results compared with the modeled values, although the magnitude of the Eliassen-Palm flux divergence in midlatitudes is underestimated. Midlatitude wave generation at the surface is poorly captured by the estimation method.

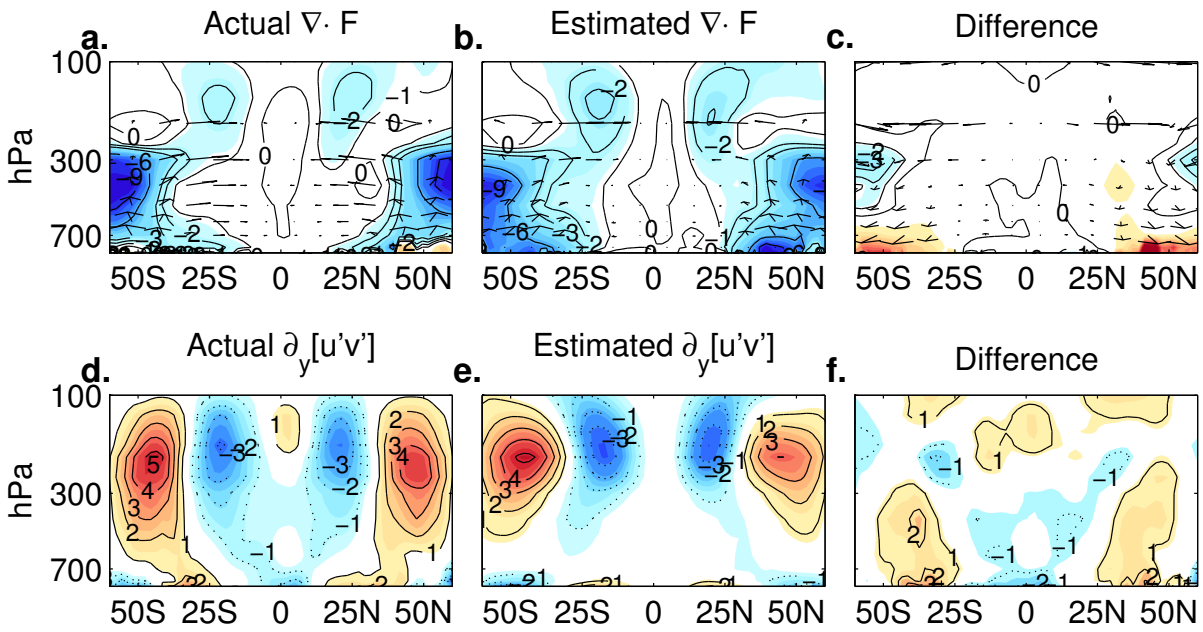

Figure 3.15: CCMVal-2 model mean (a.) Eliassen-Palm flux (arrows) and its divergence (shading) and (d.) eddy momentum flux convergence from the subset of 9 models supplying these fields as model output, the estimated (b.) Eliassen-Palm flux and its divergence and (e.) the estimated eddy momentum flux convergence from the same subset of models, and (c., f.) their difference. The Eliassen-Palm flux divergence and eddy momentum flux convergence are both in units of m s^{-1} day^{-1}. Eliassen-Palm flux vectors scaled as in Edmon et al. (1980).

The estimated and actual eddy momentum flux convergence do differ lower in the troposphere, which likely reflects the need to account for other terms in the zonal momentum equation that we were not able to estimate from CCMVal-2 output, such as the vertical eddy momentum flux convergence. Nevertheless, the method is reliable over much of the troposphere, with a pattern correlation of 0.86 ($R^2 = .74$) between the actual and estimated eddy momentum flux convergences.

These approximations are extended to all REF-B1 models to calculate their model-mean eddy fluxes and Eliassen-Palm flux divergences, which are used henceforth.

3.6.4 Eddy momentum flux-grid size effect

We first regress the CCMVal-2 model-mean estimated Eliassen-Palm flux and its divergence and eddy momentum flux convergence on CCMVal-2 model grid size and model mean $\int \Psi dp$ edge latitudes, shown in Fig. 3.16. The Eliassen-Palm flux is parallel to the group velocity of linear Rossby waves, while its divergence measures the wave forcing on the mean flow (Edmon et al., 1980). Vectors of the Eliassen-Palm flux thus indicate Rossby wave propagation in the latitude-pressure plane.

An important point to remember for this and later regressions on grid size is that the patterns are not necessarily capturing a mode of physical variability, because the independent variable is not a physical index within the atmosphere of each model. For the edge latitude regressions, regressions are taken on each respective hemisphere's $\int \Psi dp$ edge latitude, e.g., the Northern Hemisphere regression coefficients correspond to the regression on the Northern Hemisphere edge latitude. The regression coefficients are all multiplied by either a one standard deviation reduction in model grid size or a one standard deviation equatorward shift in $\int \Psi dp$ edge latitude. The regression (shading) can thus be interpreted as the representative changes to the eddy momentum flux convergence associated with finer model resolution and a narrower Hadley cell.

There are strikingly similar changes to the patterns of wave breaking and propagation between the regression on grid size and $\int \Psi dp$ edge latitudes. With finer resolution and an equatorward-shifted $\int \Psi dp$ edge latitude, there is enhanced wave breaking ($\nabla \cdot F < 0$) and enhanced equatorward wave propagation (arrows) in the subtropical lower and upper troposphere around 700 hPa and 150 hPa (Figures 7a and 7b), with a reduction in wave

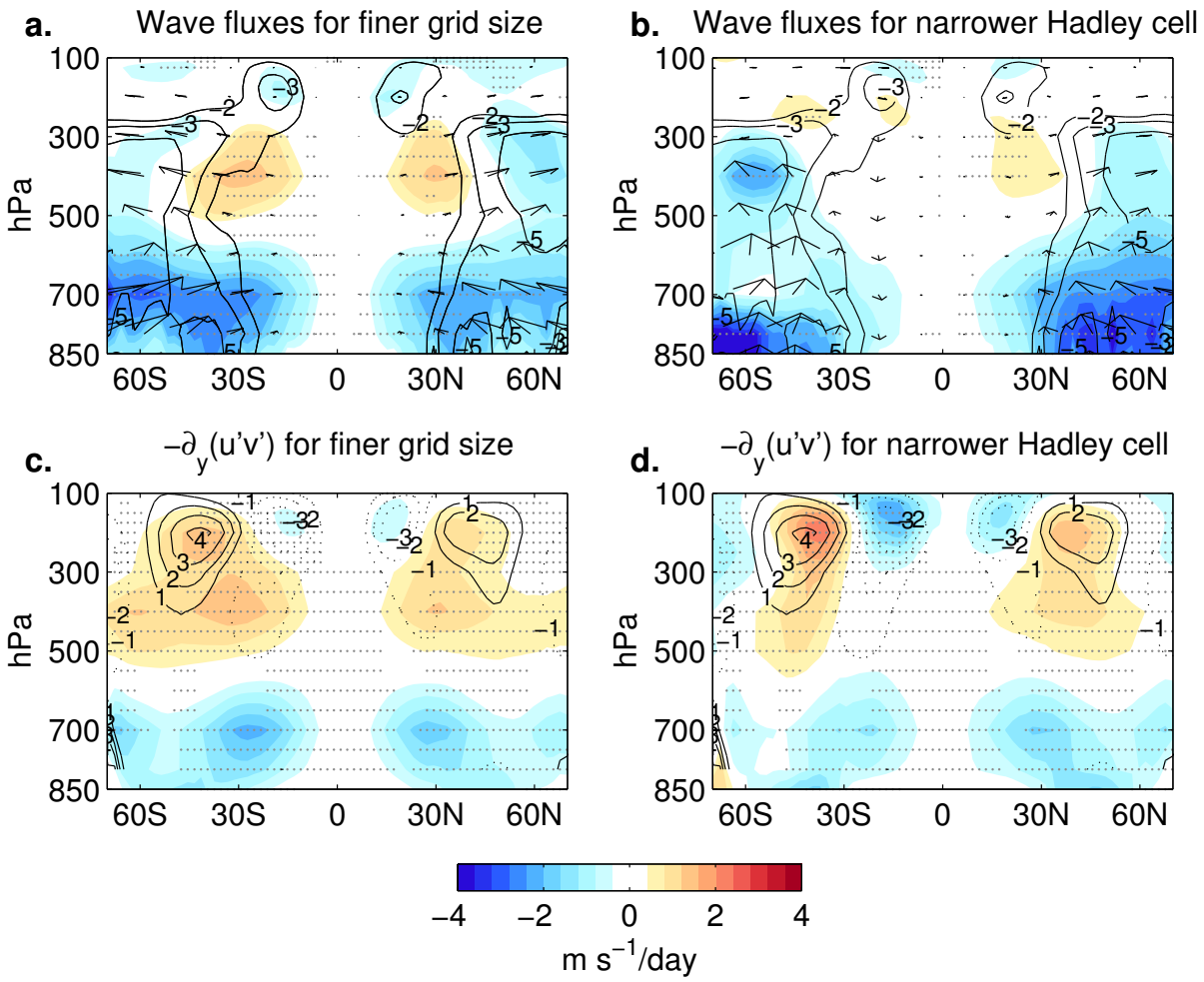

Figure 3.16: Regression of CCMVal-2 model-mean Eliassen-Palm flux and divergence on (a.) CCMVal-2 model grid size and (b.) model-mean $\int \Psi dp$ edge latitudes in each hemisphere, and regression of CCMVal-2 eddy momentum flux convergence on (c.) CCMVal-2 model grid size and (d.) model-mean $\int \Psi dp$ edge latitudes in each hemisphere. For the edge latitude regressions in (b.) and (d.), the regressions are on each respective hemisphere's edge latitude, e.g., the Northern Hemisphere regression coefficients correspond to the regression on the Northern Hemisphere edge latitude. Shading indicates the regression coefficients for the EP flux divergence (top row) and eddy momentum flux convergence (bottom). Vectors in (a.) and (b.) indicate the regression coefficients for the vertical and horizontal components of the Eliassen-Palm flux. Regression coefficients have been multiplied by a one standard deviation reduction in grid size (left column) or equatorward shift of model-mean $\int \Psi dp$ edge latitude (right column). Solid contours indicate the CCMVal-2 mean EP flux divergence (top row) and eddy momentum flux convergence (bottom row). Eliassen-Palm flux vectors scaled as in Edmon et al. (1980). Stippling indicates regression coefficients significant at the 95% confidence level.

breaking ($\nabla \cdot F > 0$) and anomalous poleward wave propagation in the subtropical middle troposphere. Both finer resolution (Fig. 3.16c) and equatorward-shifted $\int \Psi dp$ edge latitudes (Fig. 3.16d) are associated with enhanced, equatorward-shifted eddy momentum flux divergence in the tropical upper troposphere and enhanced, equatorward-shifted eddy momentum flux convergence in the subtropical upper troposphere. Taken together, both indicate an equatorward shift of wave activity and enhanced wave breaking into the poleward flank of the Hadley cell with finer resolution and a narrower Hadley cell.

3.6.5 Impact of the effect on the Hadley cell width

To directly relate the impact of the grid-size-biased horizontal eddy momentum flux convergence on the Hadley cells, we diagnose the MMS in balance with the anomalous eddy momentum flux convergence by substituting Eq. 4 into the definition of the MMS to obtain the balanced MMS associated with the anomalous horizontal eddy momentum flux convergence,

$$\Psi_{eddy}(p,\phi) = \frac{2\pi a \cos(\phi)}{g} \int_0^p \frac{1}{f} \frac{\partial}{\partial y}([u'v'])dp \tag{9}$$

where Ψ_{eddy} is the MMS in balance with the anomalous eddy momentum flux convergence. The grid used in these calculations avoids the equator so that there is no singularity in the balanced MMS.

The MMS in balance with the eddy momentum flux convergence associated with finer resolution exhibits thermally-indirect middle tropospheric cells that maximize along the edge of the Hadley cells in the subtropics (Fig. 3.17a), indicating a contraction of the Hadley cells. The MMS in balance with the eddy momentum flux convergence associated

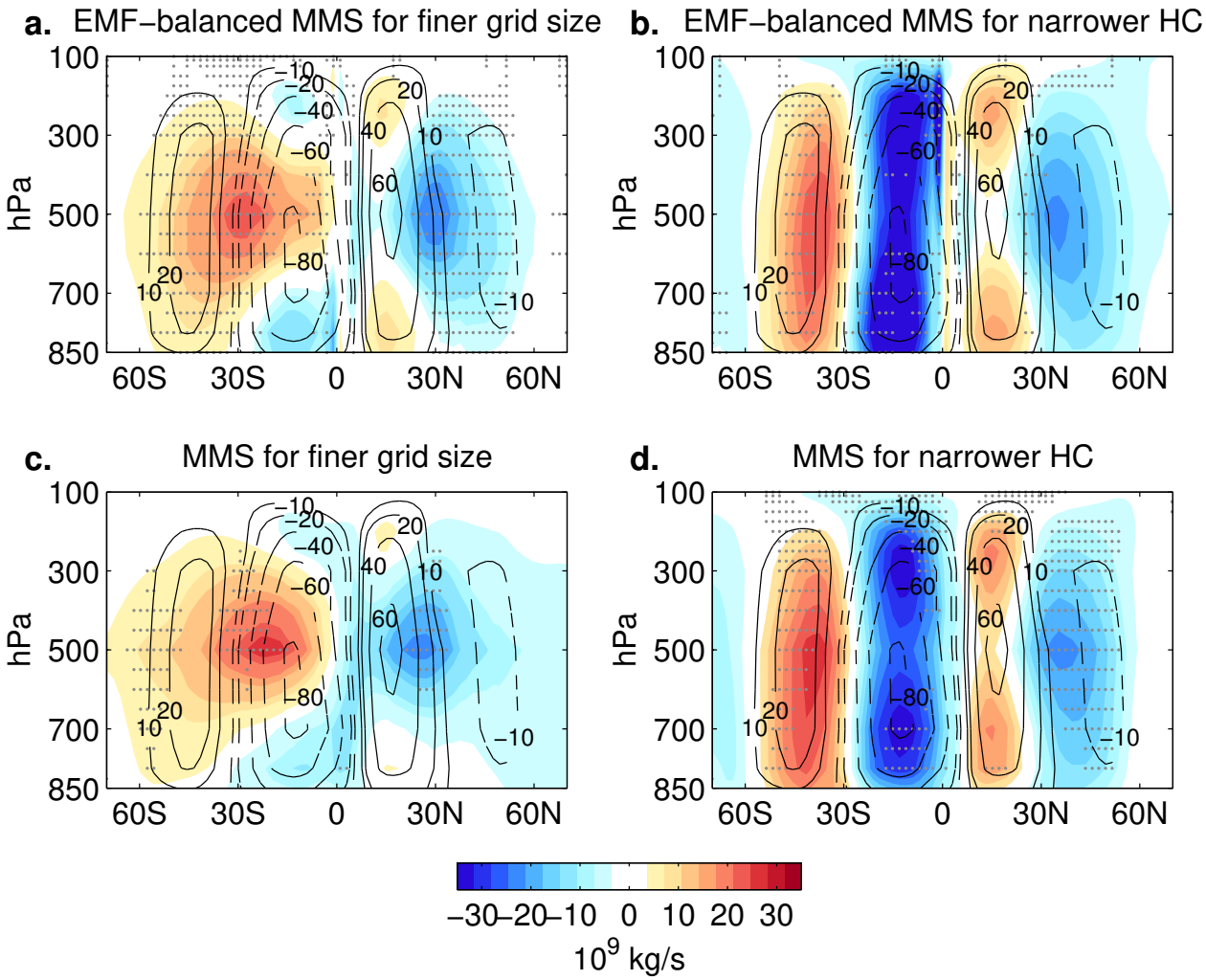

Figure 3.17: CCMVal-2 balanced MMS response to (a.) the anomalous eddy momentum flux convergence associated with a one standard deviation reduction in model grid size, (b.) the anomalous eddy momentum flux convergence associated with a one standard deviation equatorward shift in model-mean $\int \Psi dp$ edge latitude in each hemisphere, and MMS regression on (c.) a one standard deviation reduction in model grid size and (d.) a one standard deviation equatorward shift in model-mean $\int \Psi dp$ edge latitude in each hemisphere. Shading indicates the MMS regression coefficients multiplied by a one standard deviation (c.) reduction in grid size and (d.) equatorward shift in $\int \Psi dp$ edge latitude, while shading in (a.) and (b.) indicates the MMS in balance with the respective eddy momentum flux convergence fields from Fig. 3.16. Contours indicate the CCMVal-2 mean MMS in 10^9 kg/s. Stippling indicates (c., d.) regression coefficients significant at the 95% confidence level or (a., b.) with an eddy-momentum-flux-convergence-weighted (Fig. 3.16c. and 7d.) $p \leq 0.05$ (95% confidence) vertically-averaged from each level to the top of the atmosphere (i.e., similar to the calculation for the MMS itself).

with equatorward-shifted $\int \Psi dp$ edge latitudes exhibits a more complex structure (Fig. 3.17b). It does include a similar subtropical middle-tropospheric Hadley cell contraction, but it also indicates a strengthening of the Hadley cells as they narrow. This suggests that part of the intermodel variation in $\int \Psi dp$ width is characterized by changes in the tropical eddy momentum flux convergence that are not associated grid size.

To begin answering how much of the grid size effect in the $\int \Psi dp$ metric width is connected to the grid-size-biased eddy momentum flux convergence, we regress the CCMVal-2 model-mean MMS's on grid size (Fig. 3.17c). The grid size effect in the MMS looks almost identical to the MMS in balance with the grid-size-biased eddy momentum flux convergence, suggesting that the structural changes to the MMS with finer resolution are associated almost exclusively with changes to the eddy momentum flux convergence. Given the lack of any significant equatorial structures in the regression, we conclude that the bias is not primarily associated with a grid size effect in the convection scheme, though intensity changes are not necessarily the only effect convective scheme differences could have.

Finally, we regress the CCMVal-2 model-mean MMS's on the model-mean $\int \Psi dp$ edge latitudes to see the structure of the total intermodel variation in the MMS (Fig. 3.17d). This also appears similar to the MMS in balance with the eddy momentum flux convergence associated with a narrower Hadley cell (Fig. 3.17b), suggesting that the bulk of the intermodel variation in the MMS between models can be tied to the MMS in balance with the differences in the eddy momentum flux convergence, or at least wherever Eq. 3 is the dominant balance.

For the regressions in Fig. 3.17 we add the anomalous MMS to the CCMVal-2 multi-model-mean MMS and vertically average it (Fig. 3.18) so that we can apply the $\int \Psi dp$ metric and quantify the total effect of the eddy momentum flux grid size effect on the $\int \Psi dp$ edge latitudes. The percentage of the total intermodel variation explained by the grid size effect and the grid-size biased eddies is found by taking the difference between their $\int \Psi dp$ edge latitudes (dashed and dotted curves) and the multi-model-mean edge latitudes (red curve), and dividing this by the difference between the total intermodel variation in the $\int \Psi dp$ edge latitudes (solid curve) and the multi-model-mean edge latitudes (red curve). Grid size alone explains 46% of the intermodel variation in $\int \Psi dp$ edge latitudes in the Northern and 59% in the Southern Hemispheres. The MMS in balance with the grid-size-biased eddy momentum flux convergence explains 51% of the intermodel variation in $\int \Psi dp$ edge latitudes in the Northern and 58% in the Southern Hemispheres. The grid-size-biased eddy momentum flux convergences thus explain essentially all of the grid size effect in the Hadley cell width.

The total intermodel variation indicates that narrower Hadley cells tend to have stronger overturning, whereas the regression on grid-size-biased eddy momentum fluxes indicates little change to the intensity of the circulation with decreasing width. However, there is a change in the intensity of the circulation with finer grid size alone that is not associated with the grid-size-biased eddy fluxes, which could be due to a grid size effect in the convection schemes in the deep tropics (Lorant and Royer, 2001; Frierson, 2007; Rauscher et al., 2012). As for the intensity changes not associated with grid size, differences in convection schemes, such as the abruptness of the convection trigger (Frierson, 2007) and surface evaporation (Numaguti, 1993) can impact the strength of the Hadley cells. At

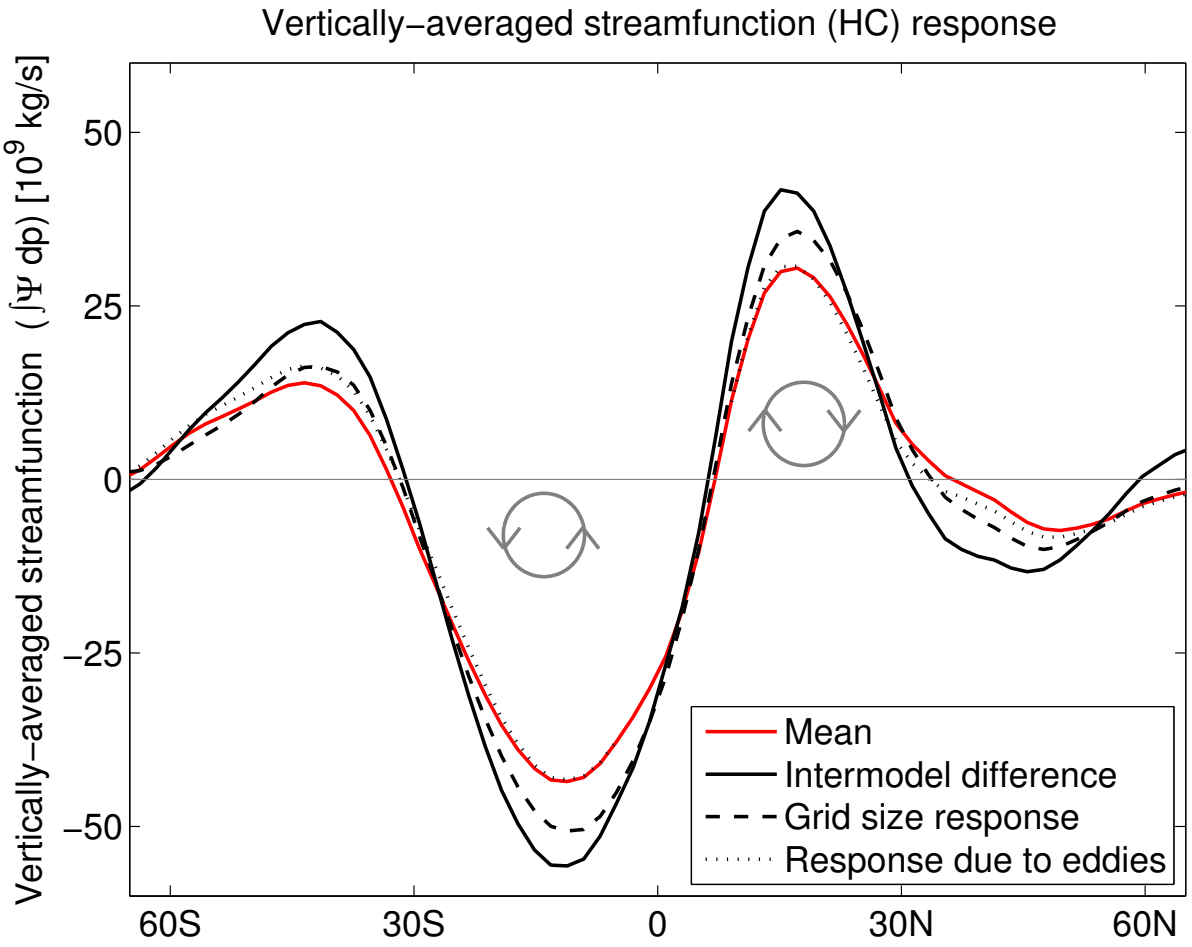

Figure 3.18: The CCMVal-2 mean vertically-averaged MMS (red), the vertically-averaged MMS associated with a one standard deviation equatorward shift in model-mean $\int \Psi dp$ edge latitude (black), the vertically-averaged MMS associated with a one standard deviation reduction in model grid size (dashed black), and the vertically-averaged MMS containing a balanced MMS response to the eddy momentum flux convergence associated with a one standard deviation reduction in model grid size (dotted black). The gray circular arrows indicate the orientation of the meridional overturning circulation if the vertical axis was a vertical coordinate.

least in boreal winter, intermodel variability in the strength of Northern hemisphere stationary eddy momentum flux divergence can also impact the strength of the overturning (Caballero, 2008). Grid size and its effect on the eddy momentum flux convergence only explain a portion of the structural differences in the Hadley cells between models, though they certainly explain a substantial fraction of the variation in the Hadley cells' width.

3.6.6 Summary of the grid size effect

Tropical surface air temperature was found to have little correlation with the modeled Hadley cell width, despite the fact that changes in tropical surface air temperature are expected to be associated with changes in the Hadley cell width (Frierson et al. (2007b), Adam et al. (2014)). Instead, we found that climate model grid size statistically explains 15-50% of the total intermodel variation in the mean tropical belt width, with finer horizontal resolution leading to a narrower tropical belt. Using an approximation that was found to accurately estimate the modeled eddy fluxes, we examined how the eddy momentum and Eliassen-Palm fluxes change with CCMVal-2 model grid size and model-mean Hadley cell width. Both finer resolution and narrower model-mean Hadley cells were associated with enhanced equatorward wave propagation in the lower and upper troposphere and enhanced, equatorward-shifted eddy momentum flux convergence and divergence in the subtropical and tropical upper troposphere, respectively. By considering the balance between the Coriolis torque and the eddy momentum flux convergence, we have shown that these grid-size-biased eddy momentum fluxes are associated with an equatorward contraction of the MMS in the subtropics. The resulting effect on the Hadley cell edge latitudes was found to explain about half of the total intermodel variation in the

edge latitudes of the Northern and Southern Hemisphere Hadley cells, and explained essentially all of the grid size effect in the Hadley cell width.

The ultimate source of the grid size effect in the eddies is not fully clear. It seems plausible that grid size may impact the ability of a model to resolve the small-scale structures associated with wave generation and breaking. However, no causality was examined here, as a balance condition was invoked to study the interaction between the eddies and the Hadley cells. While a grid size effect in the eddies is a plausible mechanism for producing the grid size effect in the tropical belt width, this does not preclude a mechanism by which the eddies are responding to a grid size effect in, for example, the zonal wind.

The impact of grid size on the zonal momentum itself is more complicated than its impact on the eddies or the meridional circulation (Fig. 3.19a). With finer horizontal resolution, the zonal winds become more easterly in the deep tropics and more westerly in the midlatitudes, with a robust easterly response in the tropical surface zonal wind. This is the signature of an enhanced transfer of momentum out of the tropics and into the midlatitudes by eddies, consistent with our analysis of the eddy momentum flux convergence (Fig. 3.16c). In contrast, the changes to the zonal wind seen with narrower Hadley cells (Fig. 3.19b) indicate a stengthening of westerly zonal winds in the subtropics and a weakening of westerly zonal winds in the midlatitudes. The strengthening of winds is likely due to enhanced advection of momentum by the mean meridional wind, which intensifies as the Hadley cell narrows (Fig. 3.17d). The surface wind response is similar to the grid size response with tropical easterlies and midlatitude westerlies, though the pattern is shifted equatorward and is less robust. Despite the fact that the zonal wind

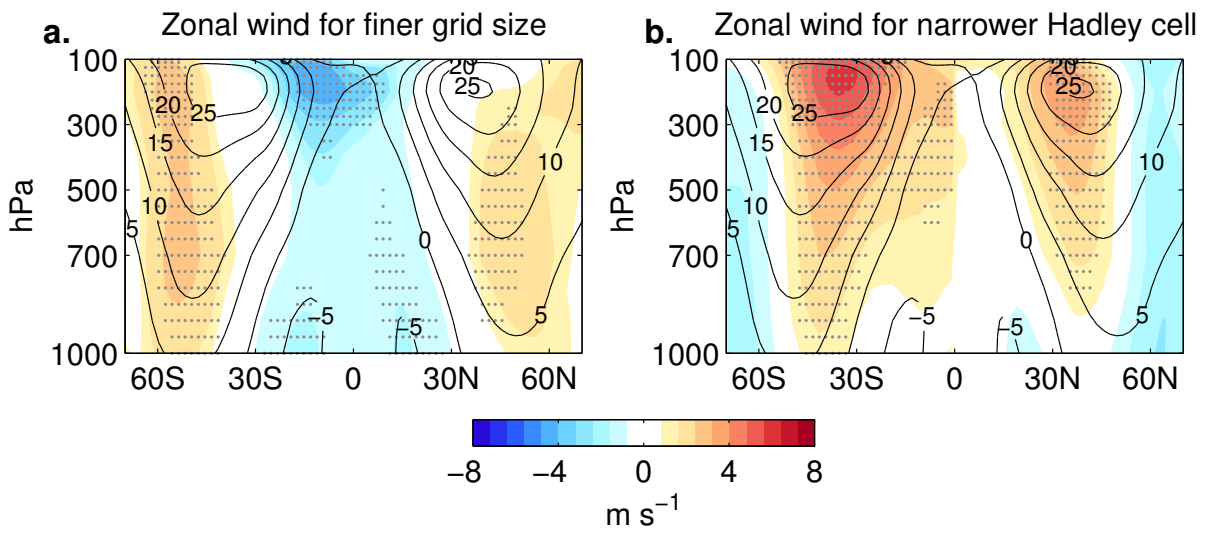

Figure 3.19: Regression of CCMVal-2 model-mean zonal-mean zonal wind on (a.) CCMVal-2 model grid size and (b.) CCMVal-2 model-mean $\int \Psi dp$ edge latitude. For the edge latitude regression in (b.), the regressions are on each respective hemisphere's edge latitude, e.g., the Northern Hemisphere regression coefficients correspond to the regression on the Northern Hemisphere edge latitude. Shading indicates the regression coefficients, while black contours indicate the CCMVal-2 mean zonal-mean zonal wind. Regression coefficients have been multiplied by a one standard deviation (a.) reduction in grid size and (b.) equatorward shift of model-mean $\int \Psi dp$ edge latitude. Stippling indicates regression coefficients significant at the 95% confidence level.

response in the troposphere is of opposite sign, both finer resolution and narrower Hadley cells are associated with enhanced vertical shear and subtropical relative vorticity throughout the subtropical troposphere. These are consistent with a narrower Hadley cell based on the Hadley cell scaling theory for a variable Rossby number (Kang and Lu, 2012).

The large intermodel variation in the tropical belt width has important implications for intermodel comparisons. Multi-model means of these fields will not be representative of the actual models' circulation structures as the subtropical jet core and Hadley cell edge vary by more than five degrees latitude in each hemisphere across the models examined here. Further, given the impacts of the Hadley cells on precipitation and surface aridity, it is clear that attempts to quantify future climate impacts on a regional scale may be obscured

by the intermodel variation in the tropical belt edge latitudes. Multi-model analyses that make use of relative coordinates (Scheff and Frierson, 2012) will avoid such statistical problems.

While we explored intermodel variations in the mean state of the tropical belt width, we did not ignore the question of how a model's mean state may impact its tropical widening trend (Fig. 3.20). None of the correlation coefficients between the trend and the mean tropical belt width are significant, for neither the CMIP5 and CCMVal-2 models together nor for the two model ensembles separately. In simulations of climate change the midlatitude jets tend to shift more poleward the more equatorward they are in the 20th century climatology (Kidston and Gerber, 2010), but it appears that the eddy-mean flow processes biasing the poleward shifts of the midlatitude circulation do not similarly bias the trends in the tropical belt width, despite their interannual coupling (Kang and Polvani, 2011).

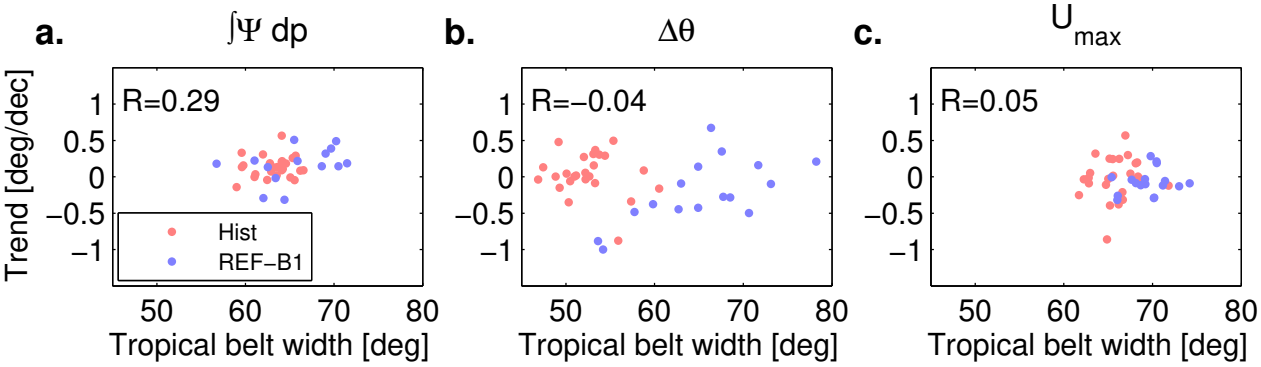

Figure 3.20: Linear least-squares trend versus tropical belt width for (a.) the $\Delta\theta$, (b.) the U_{max}, and (c.) the $\int \Psi dp$ metrics. No correlation coefficients are significant at the 95% confidence level.

We found that stronger eddy momentum flux divergence, or the eddy-driving on the circulation, is associated with a climatologically narrower Hadley circulation. While in

general the presence of eddies may widen the Hadley cells in comparison to axisymmetric circulations (Kim and Lee, 2001), this does not necessarily dictate whether stronger or weaker eddy momentum flux divergence out of the cells will widen or narrow them. Hadley cell scaling theories based on a variable Rossby number would suggest that stronger eddy momentum flux divergence should permit wider Hadley cells by shifting poleward the latitude of the onset of baroclinic instability (Kang and Lu, 2012). However, theories for the width of the Hadley cells based on angular-momentum-conservation-thinking are by nature unable to account for the role of eddies in setting the width of the Hadley cells.

4 Physical Processes Governing the Expansion of the Hadley Circulation

The results of the previous chapters point to a robust coupling among thermodynamic and eddy-mean flow variability and change. At equilibrium, Hadley cell expansion scales directly with global-mean surface temperature, subtropical static stability, tropical upper-tropospheric warming, Arctic amplification, and stratospheric cooling in response to greenhouse gas and solar forcings. On month-to-month timescales, the eddy-driven jet and Hadley circulation edge latitudes co-vary together and with other features of the meridional circulation in the subtropics, including the pattern of surface zonal winds. Additionally, poleward shifts of the eddy-driven jet are correlated with Hadley circulation expansion. On the other hand, subtropical jet latitude variability and change is uncorrelated with Hadley circulation width variability and change, suggesting that "angular-momentum-thinking" may not be sufficient to capture the first order dynamics of the circulation. In a mean sense, narrower Hadley circulations are more intense, with stronger overturning and stronger surface winds. This increased intensity is associated with increased eddy-driving on the circulation. If angular-momentum-thinking were valid, the opposite should be the case.

In other words, there is an inextricable scaling among global thermodynamics, eddies, and the mean circulation, but it does not appear that the crux of this coupling can be uncovered with an angular momentum perspective. Progress in understanding the processes that drive expansion necessitates more than post-hoc analysis as was performed here. It even requires more than simple forcing experiments, whether those forcings are

local or global, precisely because of this scaling. Instead, it requires a novel approach to separate the direct thermodynamic from the eddy-driven response of the mean circulation.

In Chapter 2, the unique capabilities of idealized modeling were briefly noted. To whit: idealized models are computationally cheap to run, relatively easy to understand in a mechanistic sense, and straightforward to modify. At the same time, models that are too idealized have limited applicability to earth's atmosphere. Cloud radiative processes are an important contributor to variability and change in earth's atmosphere, but they are unrepresented in idealized models. Models such as dry dynamical cores are exceptionally simple, but they often parameterize zeroth-order climate processes like radiative transfer with a relaxation to some assumed temperature profile.

The Geophysical Fluid Dynamics Laboratory Gray Radiation Aquaplanet Model (GRAM) is a climate model of intermediate complexity that is well-suited to the task at hand (Frierson et al., 2006). It carries all of the advantages of a simpler model, such as a dry core, with fewer disadvantages, including an idealized but interactive radiation scheme, surface and boundary layer turbulence, and moisture. A thorough description can be found in the appendix, but the relevant details are described here. GRAM makes the two-stream approximation for radiation, with upward and downward fluxes of bulk longwave and shortwave radiation and a prescribed time-invariant insolation at the top of the atmosphere. Surface fluxes of heat, moisture, and momentum are modeled with an idealized Monin-Obukhov closure scheme, while the ocean surface is treated as a slab ocean with a fixed heat capacity. Convection is modeled in two ways: large-scale condensation and an idealized Betts-Miller scheme that adjusts temperature profiles toward psuedoadiabats, both of which necessitate the representation of water vapor as an active tracer. The model

is modified with an idealized ozone distribution to improve the representation of the stratosphere (described in the appendix), as well as a scheme for assessing the axisymmetric response of the circulation to forcings, described in the next section.

Fig. 4.1 and Fig. 4.2 compare the climate of GRAM to the mean equinox climate of ERA-Interim from both a tropospheric and stratospheric perspective. The circulation in ERA-Interim's climate extends approximately 50-100 hPa higher than that in GRAM. However, the equator-to-pole temperature contrast, the circulation strength as measured by the zonal winds and the mean meridional circulation, and the structure of the circulation are comparable, especially to the Southern Hemisphere. GRAM is not comparable to the zonal-mean climate of the Northern Hemisphere because the Northern Hemisphere includes a substantial land fraction and massive mountain ranges, both of which create a more zonally-asymmetric climate with more stationary waves.

4.1 Response to Greenhouse Gas-like Forcings

At issue is how much of Hadley circulation expansion is driven by the eddy-driven jet shift and its associated changes to Rossby waves versus the thermodynamic response of the circulation. Understanding the specific contributions of these processes to expansion is important. In past studies, expansion has been attributed to: direct radiative forcings (Lu et al., 2009), including ozone loss (Polvani et al., 2011b; Min and Son, 2013) and greenhouse gases (Gastineau et al., 2008; Hu et al., 2013; Tao et al., 2015), aerosols (Allen and Sherwood, 2011; Allen et al., 2014), black carbon and tropospheric ozone (Allen et al., 2012), and sea-surface temperature variability and change, including variability associated

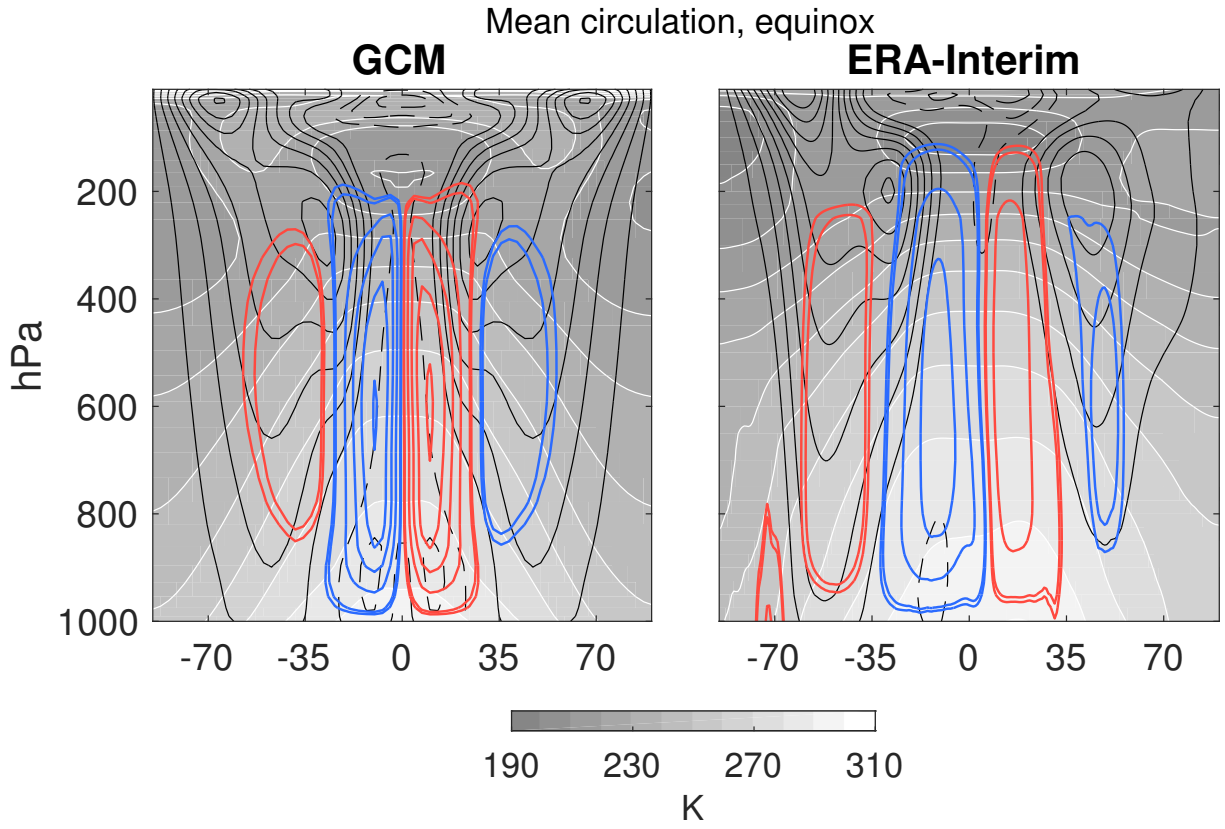

Figure 4.1: The zonal mean climate of (left) GRAM and (right) equinox seasons in ERA-Interim. Temperature in shading every 10 K, zonal-mean zonal wind in contours every 5 m/s with negative values dashed, and the mean meridional streamfunction in blue/red contours, with positive values indicated in red, every 40×10^9 kg/s starting at 20 $\times10^9$ kg/s.

with the PDO (Grassi et al., 2012; Allen and Kovilakam, 2017). It is not clear which, if any, are most important, especially over the historical period, and it is difficult to make inroads with regression analysis and comprehensive model experiments, alone. A theoretical framework through which Hadley circulation expansion can be understood in basic physical terms can help sort through this zoo of forcings and physical causes of expansion. Greenhouse gas forcing experiments are an ideal starting place - they are highly relevant for future climate change with a relatively simple, global impact.

Separating the eddy-driven and thermodynamically-direct response of the circulation would be most easily accomplished with the use of a typical (hereafter "wave-permitting"

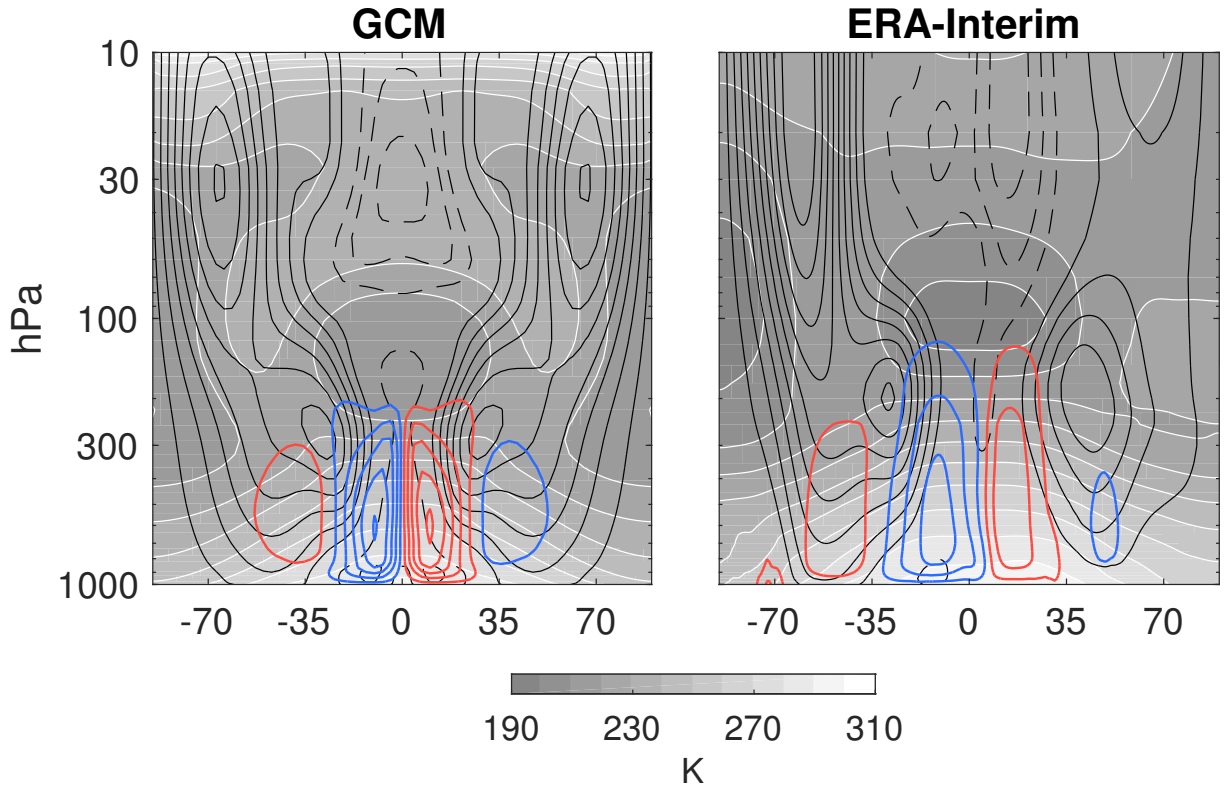

Figure 4.2: As in Fig. 4.1 but from a stratospheric perspective.

or WP) model configuration and an axisymmetric (herefter "AXI") model configuration, both with an equivalent or nearly-equivalent control climate. If the same forcing is applied to both model configurations, the former will model the direct radiative and wave-mean flow response, while the latter will only model the direct radiative and thermally-direct, axisymmetric response of the circulation. Axisymmetric models of the circulation have been used to understand the basic dynamics governing the Hadley circulation (Held and Hou, 1980; Lindzen and Hou, 1988; Sobel and Schneider, 2009), including the impact of eddies on its mean width and strength (Becker et al., 1997; Kim and Lee, 2001). However, it is difficult to separate the role of eddies in driving an expansion of the circulation in response to forcings using a diagnostic analysis of these different model configurations. This is in part due to the nonlinearity of the interaction between eddy momentum forcings

and the mean flow (Sobel and Schneider, 2009). Additionally, the mean circulation and eddies co-evolve rapidly in response to forcings (Grise and Polvani, 2017), an additional barrier that makes a diagnostic analysis of abrupt forcings difficult if not impossible.

While spectral models like GRAM can be run with a limited number of zonal wavenumbers to separate synoptic and planetary wave responses (Domeison et al., 2013), it is not possible to resolve only the zonal-mean flow by specifying "zero" zonal wavenumbers. Because the spectral representation of any field includes the summation over all zonal wavenumbers, all fields in such a model would be identically zero (see Eq. 85 in the appendix). Instead, the axisymmetric model is created by is initiating GRAM from a state of rest with no zonal perturbations. The model will preserve an axisymmetric climate indefinitely, provided the time-step is fast enough to prevent the unchecked growth of symmetric instabilities[2]. However, a further complication is that an axisymmetric general circulation in a moist model such as GRAM bears no resemblance to a wave-permitting general circulation (Fig. 4.3).

In the WP model, there are surface easterlies and westerlies, indicative of a momentum exchange with the liquid earth. This necessitates an eddy-driven jet in midlatitudes and a Hadley circulation in the tropics that extends throughout the troposphere. In contrast, the AXI model has no surface winds and a Hadley circulation confined to the upper-troposphere with a slight poleward tilt with height, reflecting the $\nu = 0.25$ simulation in (Held and Hou, 1980). When the vertical diffusion of momentum and heat is almost vanishingly small or zero, as it is in GRAM, an axisymmetric Hadley cell cannot

[2]When "WP model" and "AXI model" are used, they refer to this difference in the initialization; the model configurations and code and otherwise identical.

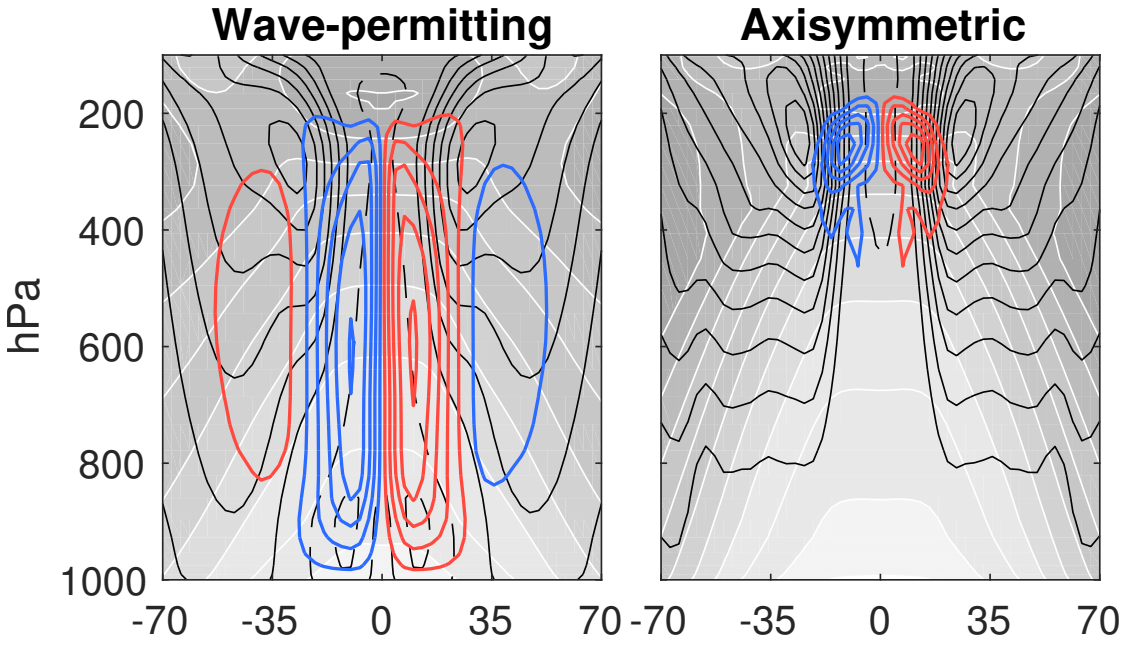

Figure 4.3: The zonal mean climate of the WP (left) and AXI (right) model. Temperature in shading every 10 K, zonal-mean zonal wind in contours every 5 m/s with negative values dashed, and the mean meridional streamfunction in blue/red contours, with positive values indicated in red, every 40×10^9 kg/s starting at 20 $\times10^9$ kg/s.

exist except within the narrow confines of the upper troposphere. In this wave-free world, convection dominates the tropics and stabilizes the atmosphere, damping the circulation and preventing it from reaching the surface.

The key difference between the AXI and WP mean climates is the lack of eddies in the AXI model. Of course, this is by construction, but such a model configuration demands that all energy fluxes and their resulting impacts on momentum and moisture be carried out by the mean flow. If the impact of the eddies on the mean state could be applied as a steady forcing to the WP model, in principle the WP model should reproduce the WP mean climate while still only explicitly modeling the mean flow and its response to forcings.

4.2 Axisymmetric vs. wave-permitting model

Consider the zonal-mean prognostic equations for momentum, heat, and moisture in the WP model in spherical coordinates,

$$\frac{D[u]}{Dt} - 2\Omega \sin(\phi)[v] = -\frac{1}{a\cos(\phi)^2}\frac{\partial}{\partial\phi}\left([u'v']\cos(\phi)^2\right) - \frac{\partial[\omega'u']}{\partial p} + [F_\lambda] \tag{1}$$

$$\frac{D[v]}{Dt} + 2\Omega \sin(\phi)[u] + \frac{[u]^2\tan(\phi)}{a} + \frac{1}{a}\frac{\partial[\Phi]}{\partial\phi} = - \frac{1}{a\cos(\phi)}\frac{\partial}{\partial\phi}\left([v'v']\cos(\phi)\right) - \frac{\partial[\omega'v']}{\partial p} + [F_\phi] - \frac{[u'^2]\tan(\phi)}{a} \tag{2}$$

$$\frac{D[T]}{Dt} - \frac{R_d[T][\omega]}{c_p p} = \frac{R_d[T'\omega']}{c_p p} - \frac{1}{a\cos(\phi)}\frac{\partial}{\partial\phi}\left([v'T']\cos(\phi)\right) - \frac{\partial[\omega'T']}{\partial p} + \frac{[Q]}{c_p} + \frac{\partial[T]}{\partial t}_{lscale} + \frac{\partial[T]}{\partial t}_{conv} \tag{3}$$

$$\frac{D[q]}{Dt} = -\frac{1}{a\cos(\phi)}\frac{\partial}{\partial\phi}\left([v'q']\cos(\phi)\right) - \frac{\partial[\omega'q']}{\partial p} + \frac{\partial[q]}{\partial t}_{lscale} + \frac{\partial[q]}{\partial t}_{conv} \tag{4}$$

where *lscale* and *conv* refer to large-scale and convective condensation, respectively.

Because the AXI model has no zonal asymmetries, the eddy terms in Eq.'s 1 - 4 vanish and the resulting governing equations are implicitly given by

$$\frac{D[u]}{Dt} - 2\Omega \sin(\phi)[v] = [F_\lambda] \tag{5}$$

$$\frac{D[v]}{Dt} + 2\Omega \sin(\phi)[u] + \frac{[u]^2\tan(\phi)}{a} + \frac{1}{a}\frac{\partial[\Phi]}{\partial\phi} = [F_\phi] \tag{6}$$

$$\frac{D[T]}{Dt} - \frac{R_d[T][\omega]}{c_p p} = \frac{[Q]}{c_p} + \frac{\partial[T]}{\partial t}_{lscale} + \frac{\partial[T]}{\partial t}_{conv} \tag{7}$$

$$\frac{D[q]}{Dt} = \frac{\partial[q]}{\partial t}_{lscale} + \frac{\partial[q]}{\partial t}_{conv} \tag{8}$$

To produce a mean climate in the AXI model that is similar to the mean climate in the WP model, a time-invariant forcing is applied to the the right hand sides of Eq.'s 5-8 in the AXI model that is equal to the sum of the eddy terms on the right hand sides of Eq.'s 1 - 3 from the unperturbed WP simulations.

These eddy forcing terms are averaged over the final 1,000 days of a 4,000 day control run in the WP model and are shown in Fig. 4.4. The eddy fluxes (not the convergences) are calculated on-line in the model so that they capture the true structure and magnitude of the fluxes. We note that calculating the eddy fluxes offline from instantaneous model output does not produce a climate similar to the WP model. The eddy forcing terms are applied to the heat and momentum equations in the physical domain of the AXI model before the first transform to spectral space (e.g., step 1 in the model's workflow described in the appendix), while the moisture tendency is applied with other physical tendencies just before the advection scheme (step 14 in the model's workflow). The humidity tendency is only applied if it will not produce negative humidity in the grid box. The inclusion of all eddy terms is critical to reproducing the mean state - vertical eddy fluxes and non-quasigeostrophic horizontal eddy terms contribute substantially to the structure and strength of the mean climate.

Eddies also contribute to surface fluxes of moisture, momentum, and heat. Their contribution can be approximated by noting that the zonal-mean surface fluxes are partly a

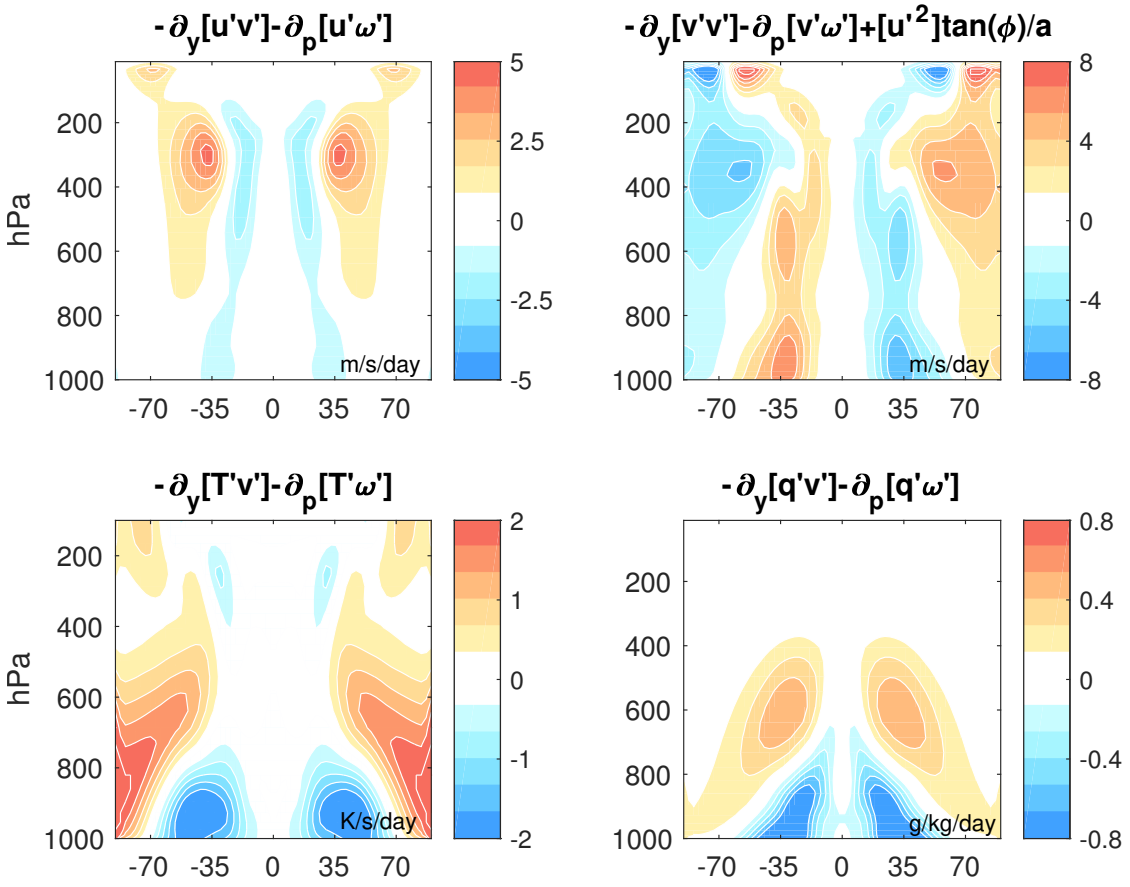

Figure 4.4: The zonal-mean tendencies of zonal and meridional momentum, temperature, and moisture due to eddies applied to the AXI model, derived from the WP model.

function of the surface wind speed, e.g., $E, S, (\tau_\lambda, \tau_\phi) \sim |\vec{v_h}|$, where E and S are the surface latent and sensible heat fluxes, $(\tau_\lambda, \tau_\phi)$ is the wind stress vector, and $|\vec{v_h}|$ is the wind speed. There is a dependence on the vertical gradients, but for simplicity they are ignored. The contribution of the eddies to $|\vec{v_h}|$ can be estimated by taking the zonal mean of the eddy wind speed, $[\sqrt{u'^2 + v'^2}]$, and dividing it by the zonal-mean wind speed, $\sqrt{[u]^2 + [v]^2}$. The fluxes are then estimated as

$$F_{eddy;E,S,\tau_\lambda,\tau_\phi} \approx \frac{[\sqrt{u'^2 + v'^2}]}{\sqrt{[u]^2 + [v]^2}} F_{E,S,\tau_\lambda,\tau_\phi} \tag{9}$$

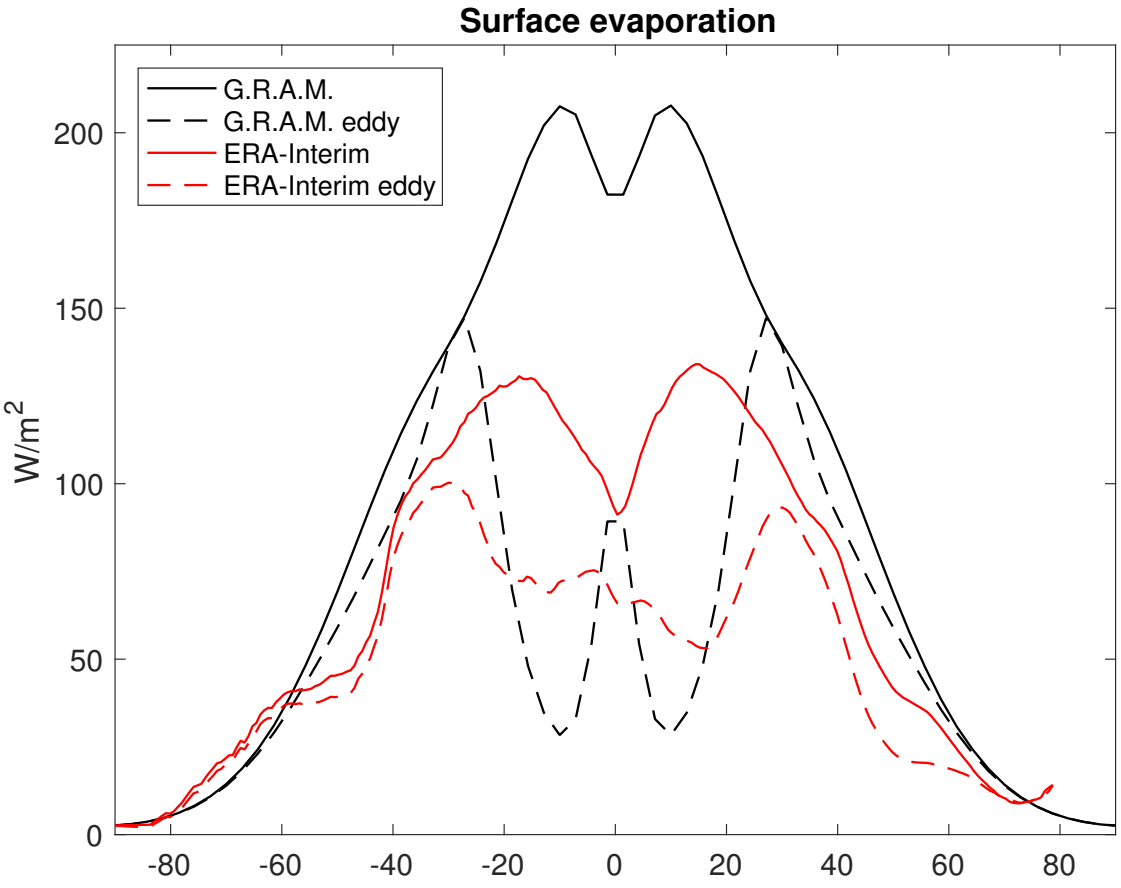

Figure 4.5: The zonal-mean latent heat flux (solid) and the zonal-mean latent heat flux due to eddies (dashed) from GRAM (black) and ERA-Interim (dashed).

where $F_{E,S,\tau_\lambda,\tau_\phi}$ is the zonal-mean surface flux. The contribution by the eddies dominates in the extratropics but is less than 30% of the zonal-mean flux in the tropics. An example for the latent heat flux is shown in Fig. 4.5 with ERA-Interim for comparison. GRAM's latent heat flux is larger in the tropics in part because it does not have any ocean heat transport nor cloud radiative effects in the tropics. As a result, the surface temperature is higher and more peaked than it is in ERA-Interim, which leads to a stronger surface evaporation.

An additional step is necessary to produce an accurate representation of the Ferrel cells and the subtropical jet in the axisymmetric simulation: the addition of large-scale condensational associated with the eddies. On its own, the axisymmetric simulation will

produce sharp, shallow regions of intense large-scale condensational heating and cooling in the midlatitudes, with overall less extratropical latent heating. The resulting Ferrel cell has a jagged appearance on its poleward flank. Through the thermal-wind relation, the net reduction in extratropical latent heating relative to the WP model creates too strong of a subtropical jet. Typically, midlatitude large-scale condensation and convection occurs within baroclinic waves, but without the waves in the AXI model some fraction of the heating does not occur. In other words, the processes contributing to the $\partial_t[T]_{lscale}$ and $\partial_t[T]_{conv}$ terms in the WP model include contributions from the eddies independent of their heat, moisture, and momentum fluxes, even though Reynolds' averaging would suggest otherwise.

Determining the direct contribution of eddies to extratropical latent heating versus the indirect contributions that follow from eddy fluxes of heat, momentum, and moisture is not straightforward. A simple method used here is to simply correlate daily WP moisture and temperature tendencies from cloud processes on eddy flux fields. A combination of trial-and-error and physical motivation suggests that the correlation of the tendencies of humidity and temperature due to large-scale condensation with $[v'v']$ and $[\omega'\omega']$ (i.e., the variances) can provide a reasonable estimate of the impact of the eddies on large-scale condensation and create a better representation of the WP climate. The variance explained (r^2) by the variances is multiplied by the zonal-mean tendency to produce an estimate of the tendency due to the direct effect of the eddies, e.g.,

$$\frac{\partial[T,q]}{\partial t}_{eddy}(p,\phi) = r^2 \frac{\partial[T,q]}{\partial t}(p,\phi) \tag{10}$$

The resulting temperature and humidity tendencies from large-scale condensation is shown in Fig. 4.6. $[v'v']$ can be thought of as indicative of the meridional waviness of the flow at a particular latitude, most characteristic of midlatitude waves where meridional flow perturbations can be large. The waviness brings warm, moisture-laden air poleward where it rapidly cools and becomes saturated, producing enhanced large-scale heating at the top of and cooling at the bottom of the boundary layer (approximately 850 hPa and 1000 hPa, respectively). In other words, $[v'v']$ is associated with stratiform convection. $[\omega'\omega']$ is essentially the asymmetry of rising and sinking air at a particular latitude. Subtropical and midlatitude deep convection is not zonal, but instead occurs in highly-localized regions of warm moist air typically surrounded by regions of cooler, dryer air. Presumably, the strong correlation of $[\omega'\omega']$ with resolved convective heating from 800 to 400hPa suggests that the model sets up quasi-meso-to-synoptic-scale circulations at these latitudes, with rising motion in the convective regions that is broad enough to saturate grid boxes and subsidence everywhere else. Vertical motion variance guarantees net column latent heating, and likely more than zonally-symmetric vertical motion could produce.

A final note is that we smooth the cloud tendencies due to eddies with a very light [1 6 1] weighting in both sigma and latitude. In the tropics and near the surface, there are sharp gradients in the fraction of large-scale condensation associated with the mean flow and with eddies. Prescribing a heating/moisture tendency field with such sharp features creates some instabilities in the mean flow.

Control experiments are allowed to spin up for 3,000 days, with the proceeding 1,000 days used for analysis. Perturbation experiments are allowed a further spin-up of 600 days from the control climate before analysis of the proceeding 1,000 days. The AXI model is

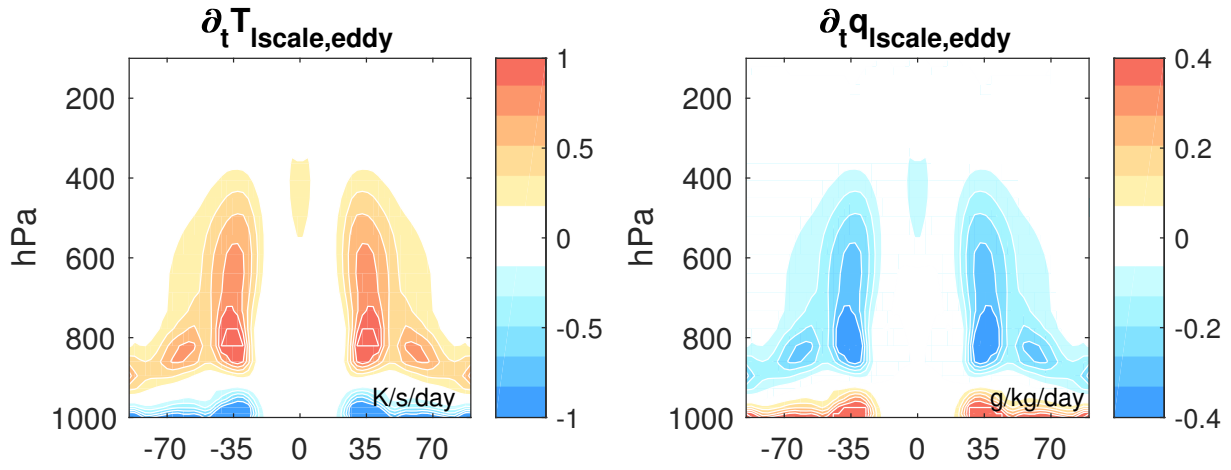

Figure 4.6: The zonal-mean tendencies of temperature (top) and humidity (bottom) due to resolved convection (left) and parameterized convection (right) associated with eddy wind variance.

initialized with the zonal-mean sea-surface temperatures from the WP model, but the sea-surface temperatures are allowed to freely evolve thereafter. The control WP and AXI climates are shown in Fig. 4.7. In general, the AXI polar temperatures are cooler than the WP polar temperatures. The resulting climate has slightly stronger westerly winds in the midlatitudes and subtropics and a slightly stronger meridional overturning circulation, but it is otherwise representative of the control WP climate. A comparison of the control climates to ERA-Interim is shown in the appendix. Hereafter, AXI refers to the axisymmetric model with time-mean eddy effects applied as a steady-state forcing.

Fig. 4.8 displays the full vertically-integrated heat budget for the WP and AXI models. There are some notable differences between the climates of the two models. In the AXI model, convection and upward motion at the equator are lower than the WP run, while they are comparable at almost all higher latitudes. At the poles, the AXI model balances longwave cooling with a greater proportion of horizontal advection at the expense of adiabatic warming. A substantial fraction of this behavior originates from the

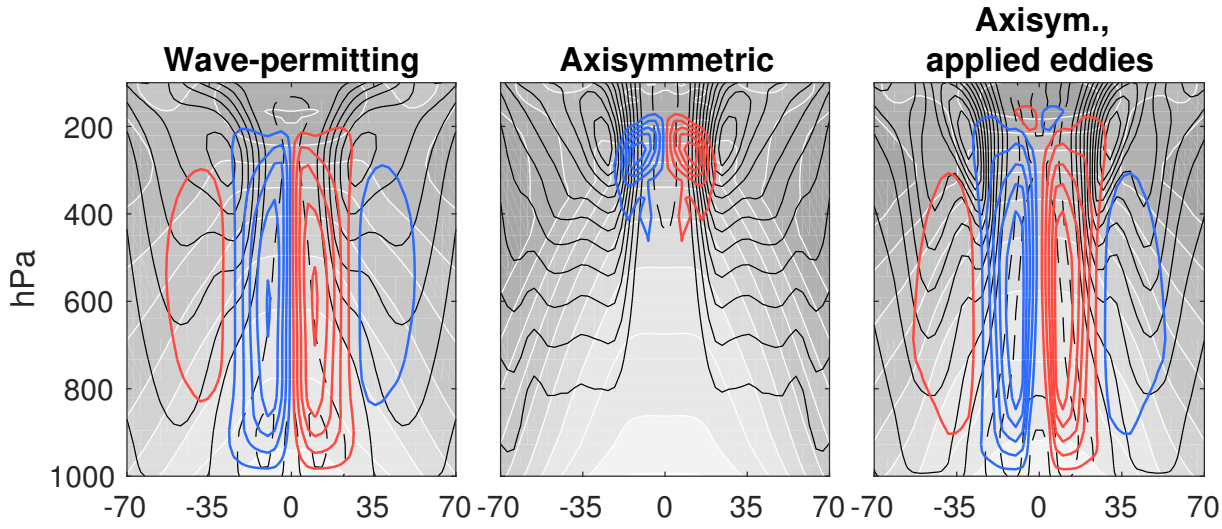

Figure 4.7: The zonal mean climate of the WP (left), the axisymmetric model without time-mean eddy effects (middle), and the AXI (right) model. Temperature in shading every 10 K, zonal-mean zonal wind in contours every 5 m/s with negative values dashed, and the mean meridional streamfunction in blue/red contours, with positive values indicated in red, every 40×10^9 kg/s starting at 20 $\times10^9$ kg/s.

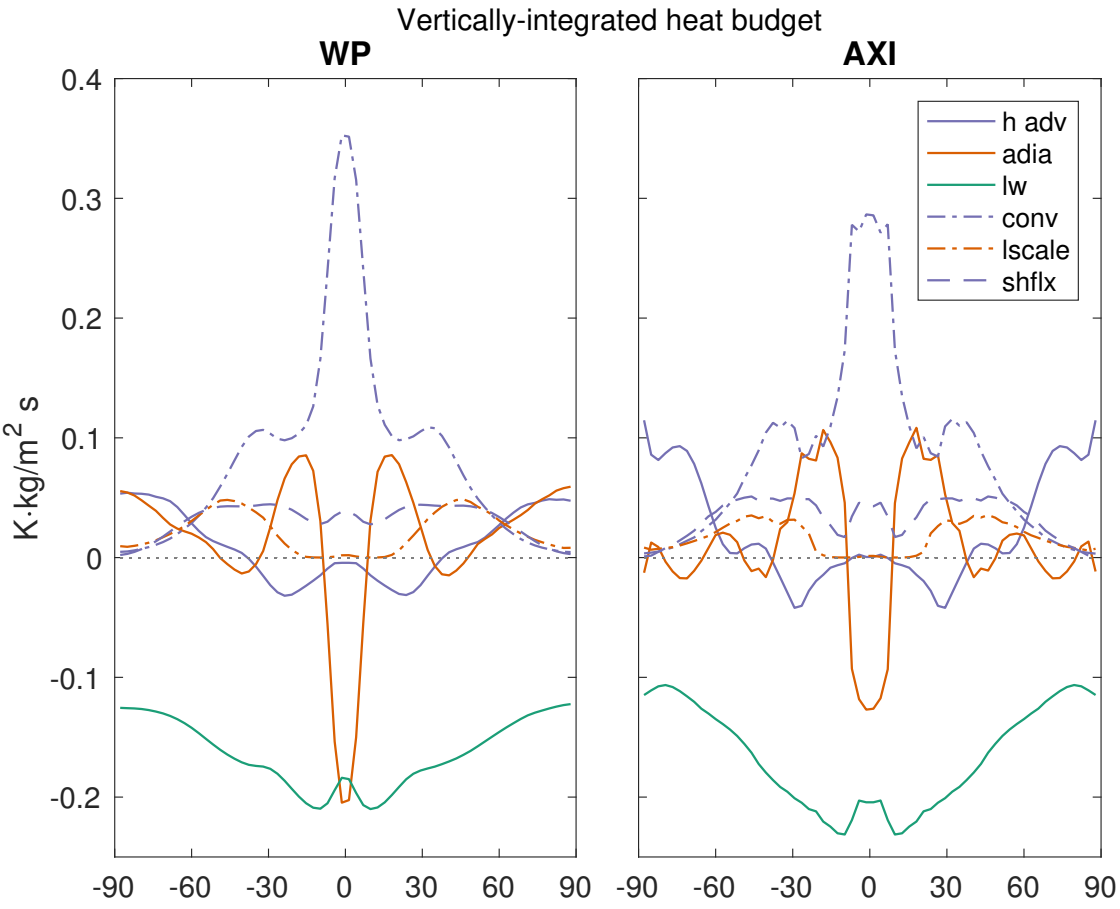

Figure 4.8: Vertically-integrated heat budget for the (left) WP and (right) AXI models. Shown are the contributions from horizontal advection (h adv), adiabatic warming and cooling (adia), longwave cooling (lw), convective heating (conv), large-scale condensational heating (lscale), and the surface heat flux (shflx).

upper-troposphere and lower stratosphere. On the other hand, the large-scale and surface flux terms are comparable between the models. Thus, the AXI model tends to balance heating with more horizontal advection rather than vertical overturning.

The heat budget of the "true" axisymmetric simulation without applied eddy tendencies is shown in Fig. 4.9. Convection and surface fluxes dominate the energy budget, with the contribution from the overturning circulation being negligible. The atmosphere of this simulation is effectively in radiative-convective equilibrium. Heat transport by the Hadley cells is accomplished primarily through adiabatic cooling and warming, with little

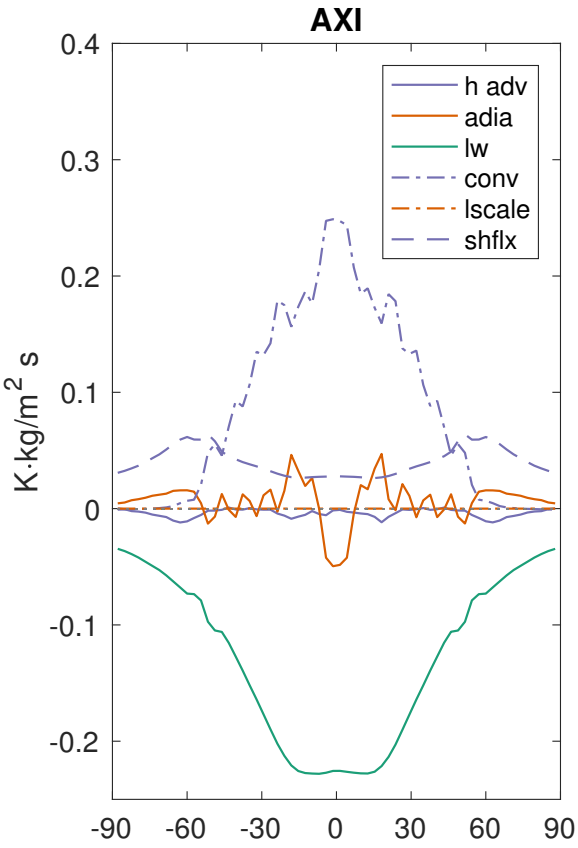

Figure 4.9: As in Fig. 4.8 but for the axisymmetric simulation without applied eddy tendencies.

contribution from horizontal advection. The noise in the midlatitudes appears to be contributions from the boundary layer and model lid (not shown).

4.3 General characteristics of expansion

In the gray radiation approximation, optical depth changes are analogous to changes in greenhouse gas concentrations. A useful starting point is a doubling of the optical depth, which in the mean varies by latitude in the model to reflect the equal-to-pole gradient of water vapor (see the appendix). For comparison, doubling the optical depth from the control climate optical depth elicits a slightly larger equilibrium warming response in GRAM than does the quadrupled carbon dioxide scenario in the CMIP5 simulations.

To begin, four experiments are performed. "WP 2xτ" is a doubling of the optical depth in the WP model, while "AXI 2xτ" is a doubling of the optical depth in the AXI model. In the third experiment, "AXI 2xτ eddies", the WP 2xτ eddy fluxes are applied to the AXI model without applying a doubling of the optical depth to test the response of the climate system to the perturbed eddy fluxes alone. The fourth experiment, "AXI 2xτ tropical eddies", prescribes the WP 2xτ eddy fluxes from the AXI 2xτ experiment to the AXI model, but only inside of the control AXI Hadley cells. To limit the prescribed tendencies to these latitudes, the fields are tapered with a 50th-order exponential with a half-width of 26.5 degrees, e.g., tapering by $\exp\left(-(\phi/26.5)^{50}\right)$ - a near step-function at the edge of the circulation. The latter two experiments separate the direct radiative and axisymmetric responses from the total eddy and tropical eddy responses.

GRAM reproduces the canonical greenhouse gas response (Fig. 4.10, upper left), similar in pattern to the coupled simulations examined in Chapter 2. The free-tropospheric response is characterized by tropical upper-tropospheric amplification and increased stability in the tropics and subtropics, as well as stratospheric cooling in the midlatitudes and subtropics. Warming is greatly enhanced at the poles with a maximum at the surface. It should be noted that this model has a slab ocean with no representation of sea ice, a constant albedo everywhere, and no interaction between water vapor concentrations and the radiation scheme. Of the possible drivers within this idealized climate, it seems likely that both increases in downwelling longwave radiation (Pithan and Mauritsen, 2014; Burt et al., 2016), i.e. a Stefan-Boltzmann feedback asymmetry between the tropics and poles, and an increased poleward eddy energy flux into the tropics contribute to the amplification. Because temperatures at the poles are substantially cooler than temperature

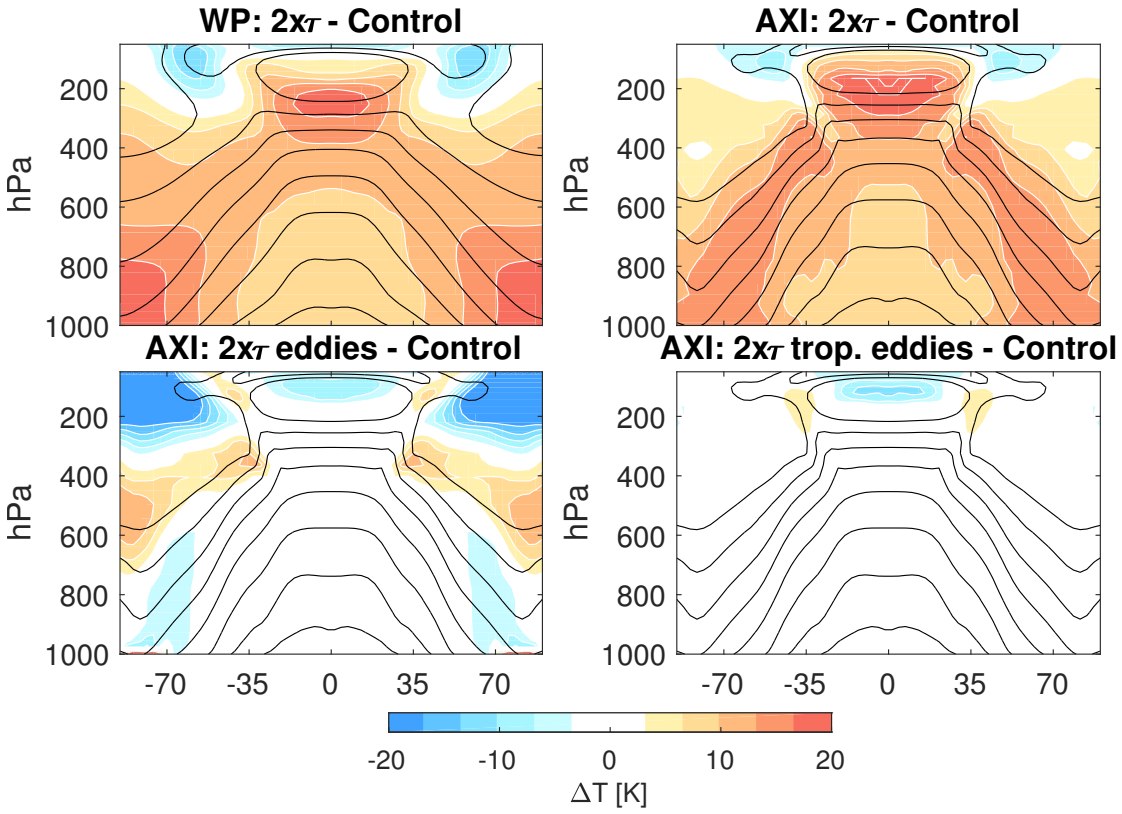

Figure 4.10: The zonal-mean temperature response to (upper left) a doubled optical depth in the WP model, (upper right) a doubled optical depth in the AXI model, (bottom left) the doubled-optical-depth eddy fluxes, and (bottom right) the doubled-optical-depth eddy fluxes within the tropics. The control climate temperatures are shown in contours every 10 K.

in the tropics, for a given perturbation to the surface radiative budget the polar surface temperature must increase more than the tropical surface temperature. The AXI model produces polar amplification while keeping the eddies fixed to their unperturbed climate, lending support to the Stefan-Boltzmann feedback mechanism. Further enhanced polar warming in the WP model suggests that changes to the eddy fluxes further increase the polar temperature response.

Curiously, the direct effect of the eddies on the response to a doubling of the optical depth is to produce minor cooling in the polar lower troposphere, warming in the polar and midlatitude upper troposphere, and strong, broad cooling in the lower stratosphere. Thus,

the direct effect of the eddies is not to warm the poles, as hypothesized above. Additionally, there is reason to suspect an acceleration of the Brewer-Dobson circulation in the WP 2xτ experiment. An expected impact of an acceleration would generally be warming of the polar stratosphere due to increased adiabatic warming, but it appears that this tendency may be opposed by an equal and opposite enhancement of eddy cooling as evidenced by the AXI 2xτ eddies experiment. With only the 2xτ tropical eddy fluxes applied, there is virtually no temperature response anywhere.

The difference between the WP response to doubled optical depth and the AXI responses to doubled optical depth and the doubled-optical-depth eddies is shown in Fig. 4.11. Over most of the tropical atmosphere, the AXI model warms more than the WP model, while the poles warm substantially less, especially aloft in the upper-troposphere and stratosphere (Fig. 4.11, left). Part of the eddy response to a doubled optical depth undoubtedly involves an enhanced poleward energy transport to diffuse the excess energy. While the direct effect of the eddies is to cool the tropics (Fig. 4.11, right), the eddies act to substantially cool the poles and essentially oppose warming at all latitudes.

In terms of zonal momentum, the WP and AXI models do not have substantially different responses in the tropics and midlatitudes (Fig. 4.12). Key zonal wind responses to a doubling of the optical depth include an upward shift of the tropospheric jets, also predicted in coupled models (e.g., McLandress et al. (2011)), and a deceleration of subtropical winds in the mid-troposphere. The upward shift is clearly a signal of the axisymmetric response, as the sign of the changes induced with the 2xτ eddies alone produces the opposite response. Missing from the AXI response is a deceleration of polar

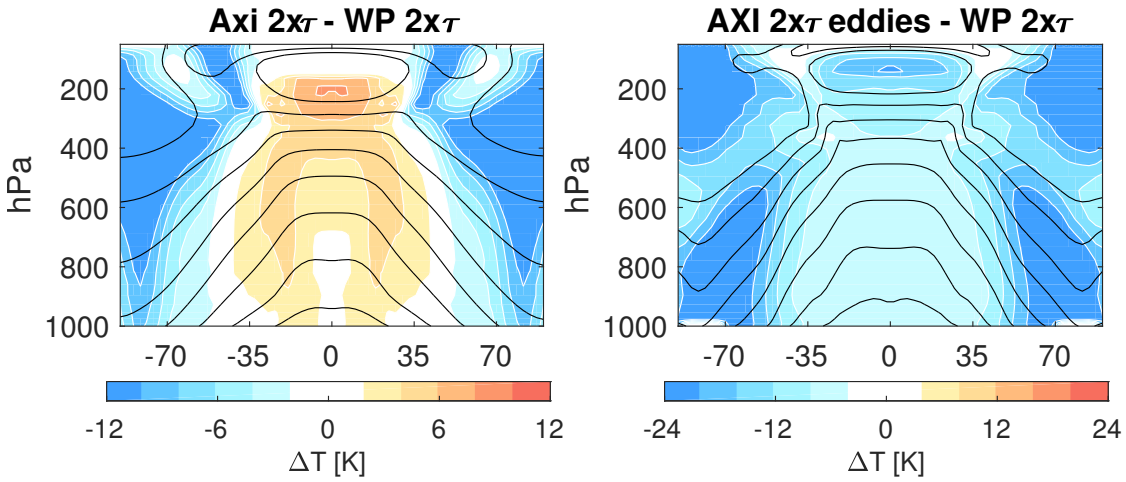

Figure 4.11: The zonal-mean temperature difference between WP response to doubled optical depth and (left) the AXI response to doubled optical depth and (right) the AXI response to doubled-optical-depth eddy fluxes. The control climate temperatures are shown in contours every 10 K.

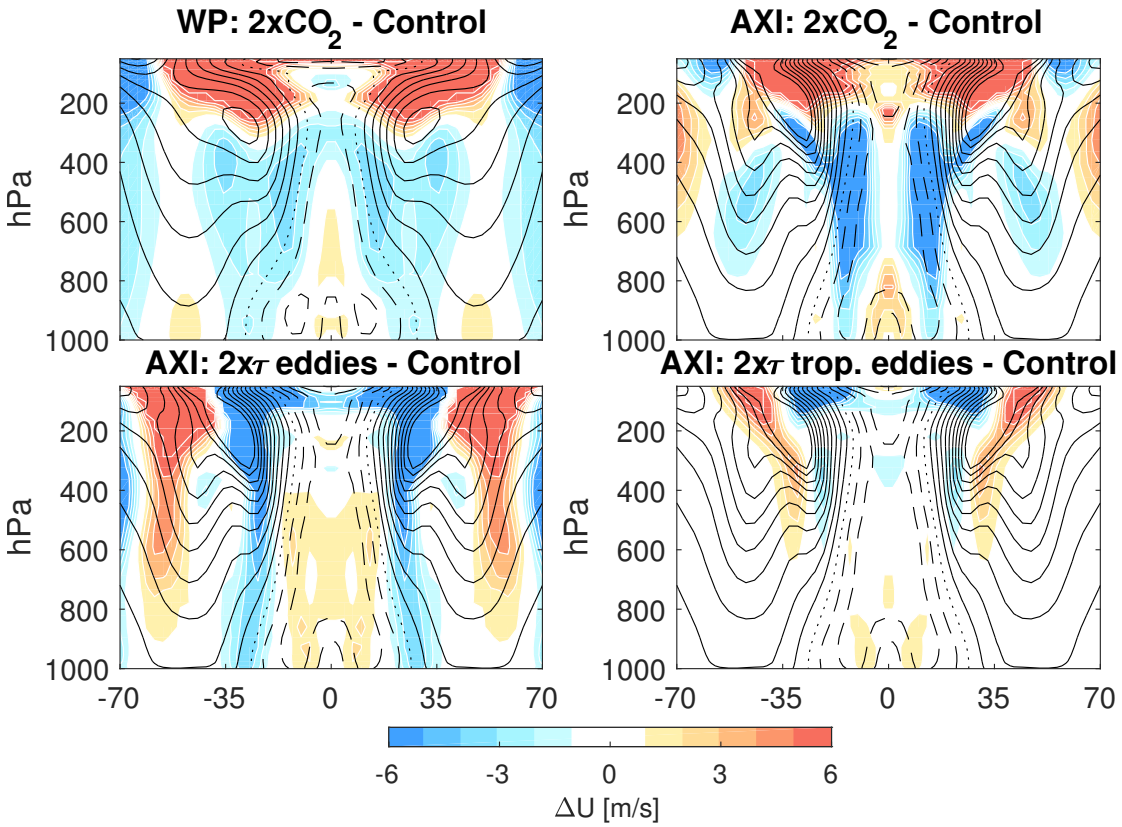

Figure 4.12: The zonal-mean zonal wind response to (upper left) a doubled optical depth in the WP model, (upper right) a doubled optical depth in the AXI model, (bottom left) the doubled-optical-depth eddy fluxes, and (bottom right) the doubled-optical-depth eddy fluxes within the tropics. The control climate zonal wind is shown in contours every 5 m/s.

cap winds associated with polar surface amplification. The eddy driven jet intensifies and shifts slightly poleward in the WP 2xτ experiment, though the response is primarily at the surface. Eddy changes drive the bulk of the shift (Fig. 4.12, bottom left), while the axisymmetric circulation response actively opposes it. The tropical eddy changes by themselves drive substantial zonal wind anomalies in the tropical stratosphere and the midlatitude troposphere and stratosphere, but they are generally out of phase with the total response zonal wind anomalies, again suggesting that the eddies act to oppose at least some of the zonal wind changes in the full response.

While the axisymmetric temperature and zonal wind responses occur throughout the global atmosphere, the meridional circulation changes are confined to the tropics (Fig. 4.13). In the WP and AXI model, the mean meridional circulation weakens over most of the tropics, potentially a reflection of the weakened equator-to-pole temperature gradient (Seo et al., 2014) and increased static stability. Approximately half of this weakening is thermally-driven (Fig. 4.13, upper right), while half is eddy-driven (Fig. 4.13, lower left). All experiments include an upward-shift of the circulation concentrated along the equator. The poleward and downward expansion of the Ferrel cell at the surface appears to be at least partly an axisymmetric circulation response, while its poleward and upward expansion appears to be driven in large part by changes to the eddies.

The Hadley circulation width's response is somewhat surprising, expanding by 1.6 degrees latitude in each hemisphere in the WP model but contracting by -0.8 degrees latitude in each hemisphere in the AXI model. Application of the 2xτ eddy fluxes to the AXI model drives nearly all of the expansion of the circulation. In the midlatitude troposphere the dominant zonal momentum balance is between the eddy momentum flux

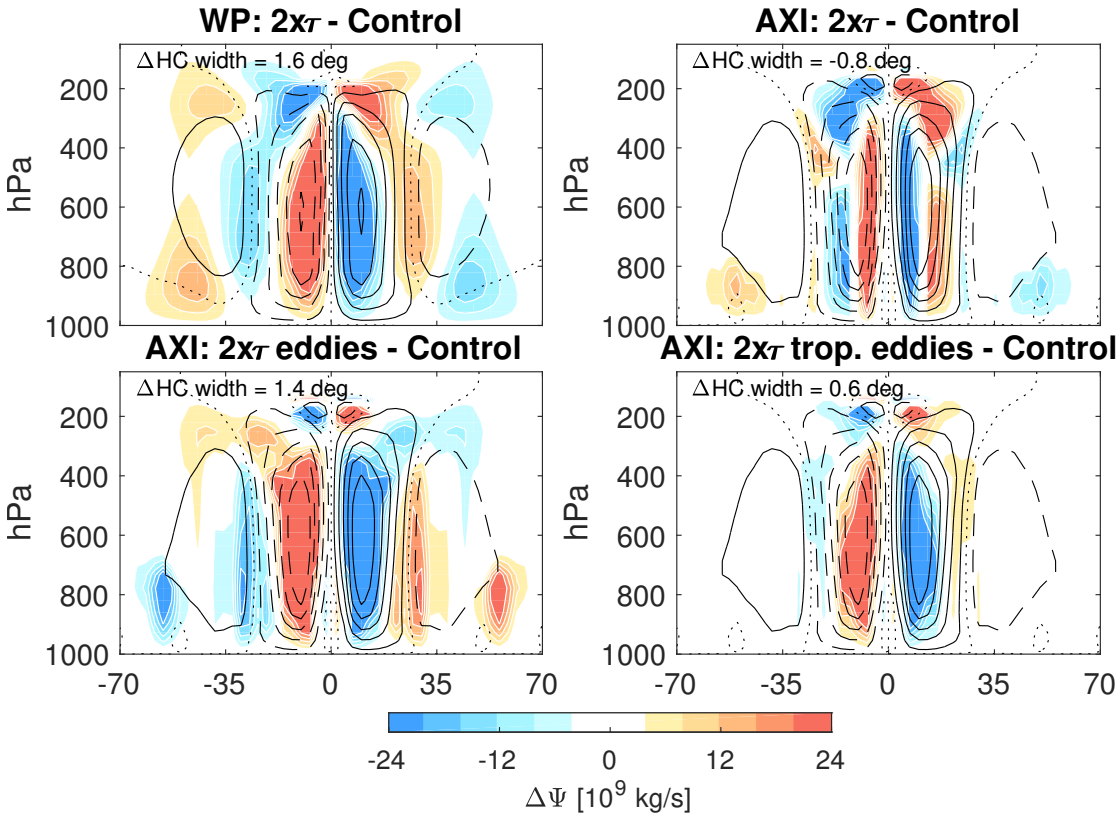

Figure 4.13: The mean meridional streamfunction response to (upper left) a doubled optical depth in the WP model, (upper right) a doubled optical depth in the AXI model, (bottom left) the doubled-optical-depth eddy fluxes, and (bottom right) the doubled-optical-depth eddy fluxes within the tropics. The control climate streamfunction is shown in contours every 40×10^9 kg/s starting at 20×10^9 kg/s.

convergence and the Coriolis torque by the meridional wind. Absent any changes to the former, the circulation has to create substantial anomalies in momentum and heat advection by the mean wind in order to expand. However, one wouldn't expect the Hadley circulation to contract. Increases in the meridional temperature gradient are generally associated with contractions of the Hadley circulation (Adam et al., 2014), so the contraction is somewhat consistent with the difference in the temperature response between the WP and AXI 2xτ experiments (Fig. 4.11). The meridional temperature gradient is indeed slightly larger in the AXI 2xτ experiment than it is in the WP 2xτ

experiment, but the meridional gradient is nevertheless weaker compared to the control climate of both. It is also surprising that the 2xτ eddy changes within the circulation alone are able to drive approximately one-third of the total expansion. These eddy changes exclude any change at and poleward of the Hadley cell edge. Thus, some fraction of expansion is driven from within the tropics, and these changes are enough to oppose the tendency of the axisymmetric circulation to contract. It is also worth noting that though tropospheric static stability increases everywhere, and the circulation deepens, the Hadley circulation does not expand in the AXI 2xτ experiment. This casts doubt on claims that static stability or tropopause height increases are the basic drivers of Hadley circulation expansion.

As a final note, the inclusion of the eddy effects on the surface fluxes of heat, moisture, and momentum is critical to the mean flow response in the AXI experiments (Fig. 4.14). The Hadley cells expand in the AXI 2xτ experiment if the portion of the surface fluxes due to the eddies is not applied. In these simulations, the mean flow must produce all of the surface fluxes, including those at the edges of the Hadley cells where the mean flow in both the zonal and meridional directions is essentially zero. This is obviously unrealistic, but in the model it provides the circulation with an extra degree of freedom that it can use to offset the processes that would otherwise cause the circulation to contract.

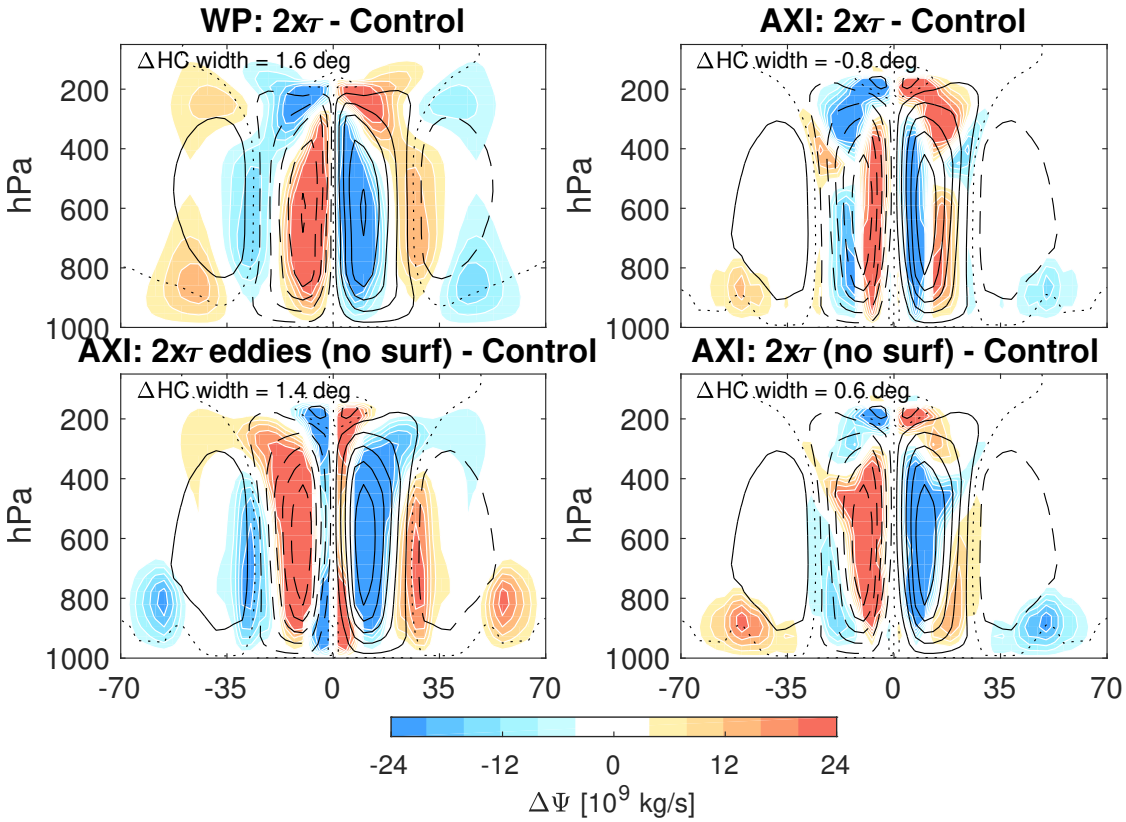

Figure 4.14: The mean meridional streamfunction response to (upper left) a doubled optical depth in the WP model, (upper right) a doubled optical depth in the AXI model, (bottom left) the doubled-optical-depth eddy fluxes excluding the eddy surface fluxes, and (bottom right) the doubled-optical-depth eddy fluxes within the tropics excluding the eddy surface fluxes. The control climate streamfunction is shown in contours every 40×10^9 kg/s starting at 20×10^9 kg/s.

4.4 An energy flux perspective

To gain further insight, we now examine the vertically-integrated heat transport, a measure of the dry and latent energy fluxed by both the mean flow and the eddies. These quantities are more fundamental and more constrained than the momentum budget or the particular structure of the circulation.

The vertically-integrated transport $F(\phi)$ for any field χ is defined as

$$F(\phi) = \frac{2\pi a \cos(\phi)}{g} \int_0^{p_s} [v\chi] dp \tag{11}$$

where a is the radius of the earth, g is the acceleration due to gravity, and p_s is the surface pressure. The integrated quantity can be substituted with $[v'\chi']$ or $[v][\chi]$ to quantify the eddy and mean flow contributions to the flux.

Here, the primary energy of interest is the moist static energy and its dry and latent energy components. Moist static energy is defined as $m = c_pT + \Phi + Lq$, where $c_p = 1004$ J/kg K is the specific heat of dry air, Φ is the geopotential, $L = 2.26 \times 10^6$ J/kg is the latent heat of vaporization, and q is the specific humidity. The components of the moist static energy, hereafter MSE, include the enthalpy, the potential energy, and the latent energy, respectively. $c_pT + \Phi$ is referred to as the dry static energy, hereafter DSE, while Lq is referred to as the latent energy, hereafter LE. MSE is nearly conserved in most atmospheric motions, including during condensation (as LE is simply transformed into DSE), and can be created or destroyed by radiative heating or cooling and surface energy fluxes.

The MSE flux is poleward everywhere in the model (Fig. 4.15). Component-wise, the LE flux is equatorward in the tropics and poleward in the extratropics, while the DSE flux is poleward everywhere. The latter must be true as the average atmospheric temperature generally decreases from the equator to the pole. On the other hand, the LE is not so constrained. Because the LE is concentrated in the lower troposphere, its flux is more sensitive to the near-surface flow which happens to be equatorward in the Hadley circulation. Further, the DSE gradient essentially drives the mean flow and the eddies; the LE gradient is more or less a consequence of the DSE gradient through the Clausius-Clapeyron relation and does not act as a direct thermodynamic driver.

In fact, the Hadley circulation is a somewhat poor mechanism for transporting MSE poleward because of the compensation between the DSE and LE flux. The Hadley

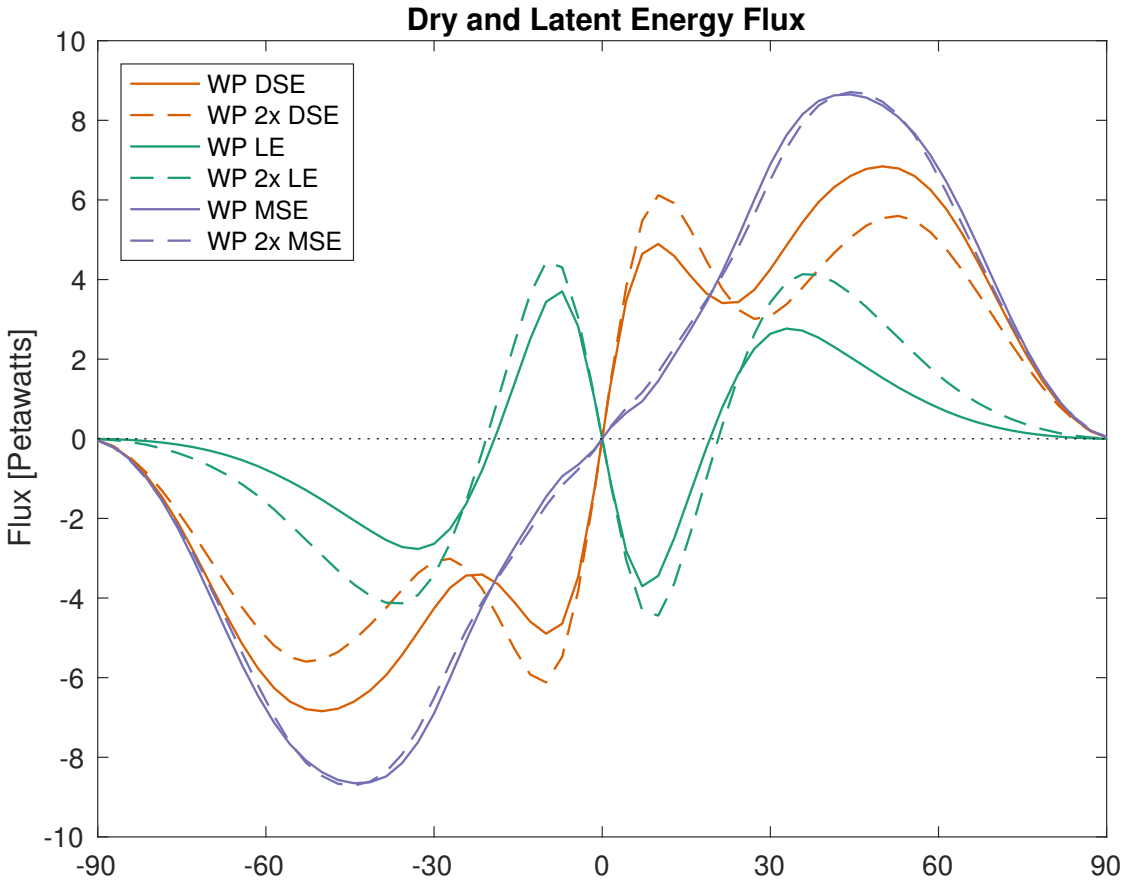

Figure 4.15: WP Control (solid) and WP 2xτ (dashed) total meridional fluxes of dry (orange), latent (green), and total moist static (purple) energy.

circulation converts LE into DSE in the tropics by bringing moist air equatorward and to cooler, higher altitudes within the rising branch of the circulation. It can be deduced from Fig. 4.15 that the storm tracks also convert LE into DSE in the extratropics, but instead do so by moving LE poleward to cooler latitudes.

In response to a doubled optical depth, the MSE flux increases slightly in the tropics and in the midlatitudes, with little change in the subtropics. The changes are relatively small because of nearly-equal and opposite responses in the DSE and LE flux in the tropics and midlatitudes. In the midlatitudes, the LE flux scales with Clausius-Clapeyron, while the DSE flux decreases in part because of the reduction in the meridional temperature

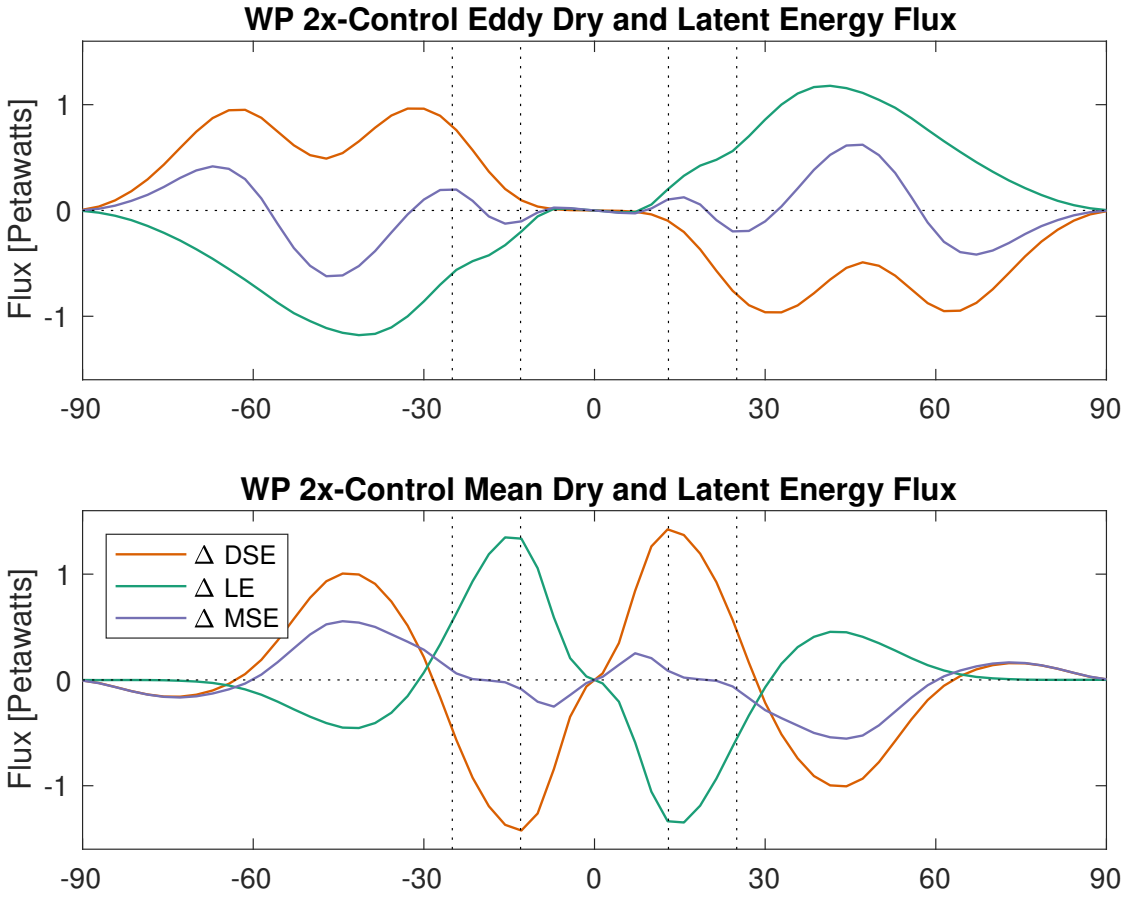

Figure 4.16: Doubled optical depth minus control meridional fluxes of dry (orange), latent (green), and total moist static (purple) energy by the eddies (top) and by the mean flow (bottom). The dotted lines denote the latitude bounds of the subsiding branch of the Hadley circulation in the control climate.

gradient, with the result being a modest increase in the MSE flux (Held and Soden, 2006). Conversely, in the tropics the DSE flux increases substantially while the LE flux decreases, resulting in a modest increase in the poleward MSE flux (Fig. 4.16). Almost all of these changes come from the mean flow, which dominates the energy fluxes at low latitudes (compare Fig. 4.17 and Fig. 4.18). In warmer climates the Hadley circulation becomes more efficient at moving DSE poleward by converting more LE to DSE. This is clearly driven by increases in moisture alone because the same response can be seen in artificially wetter climates (Frierson et al., 2007a).

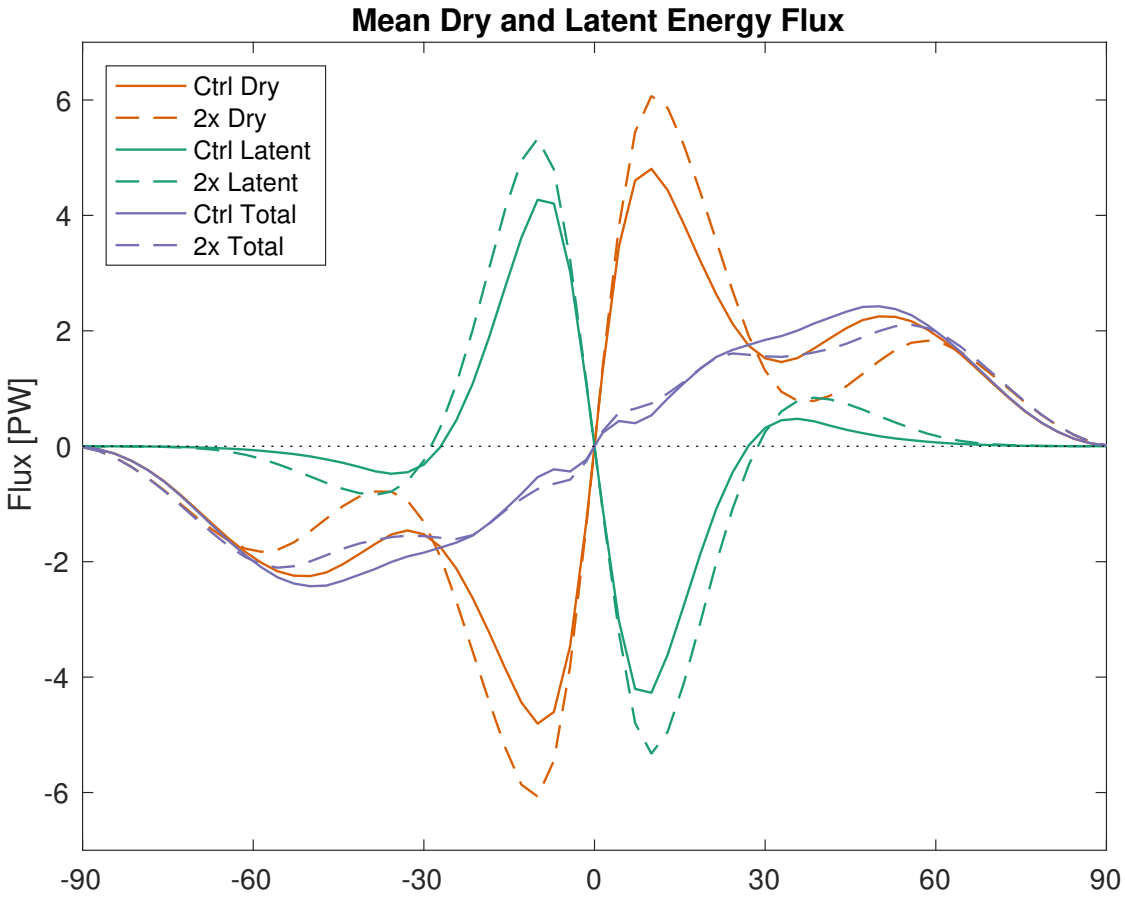

Figure 4.17: Control (solid) and doubled optical depth ("2x", dashed) meridional fluxes of dry (orange), latent (green), and total moist static (purple) energy by the mean flow.

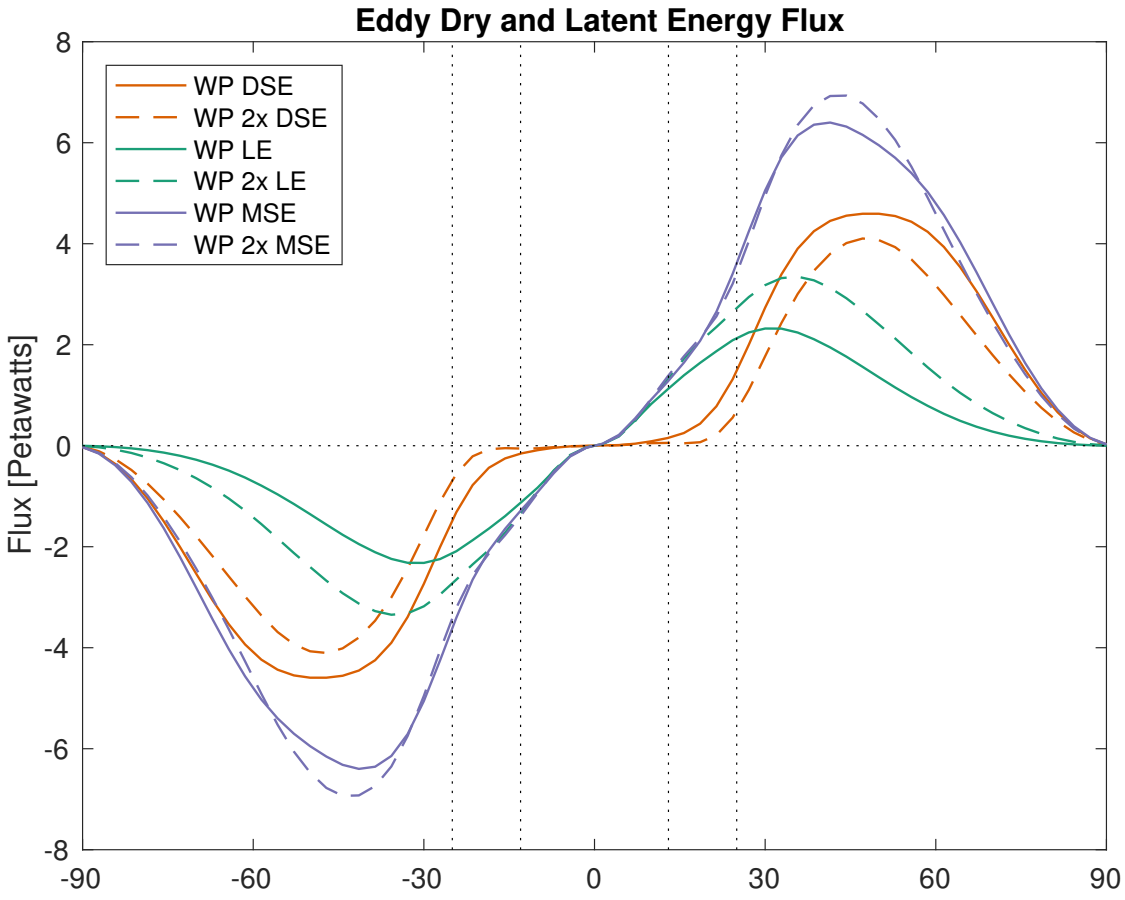

Figure 4.18: Control (solid) and doubled optical depth ("2x", dashed) meridional fluxes of dry (orange), latent (green), and total moist static (purple) energy by eddies. The dotted lines denote the latitude bounds of the subsiding branch of the Hadley circulation in the control climate.

In the multi-model-mean, the response of comprehensive general circulation models to moderate greenhouse gas forcings includes an increase in the MSE flux at all latitudes (Held and Soden, 2006), though there is substantial variability (Hwang and Frierson, 2010), whereas in GRAM there is a slight decrease in the subtropics. This may be due to the climatology of GRAM and the magnitude of the forcing. The peak latitude of the MSE flux in GRAM is comparable to the mean across the comprehensive models, whereas GRAM's Hadley circulation is 3-5 degrees narrower. This creates a gulf between the increases in the DSE flux in the tropics and the increases in the LE flux in the midlatitudes, and may be the source of the subtropical decrease in the MSE flux. Additionally, unlike the slab ocean experiments examined in Held and Soden (2006) and Hwang and Frierson (2010), GRAM does not include prescribed ocean heat fluxes. As a result, the atmosphere in GRAM already transports substantially more heat poleward. Further, the magnitude of the forcing in this experiment - a doubling of the optical depth - is substantially larger than that in standard CMIP scenarios. These may all create some discrepancies in the mean magnitude of the fluxes, their meridional position, and the magnitude of the response. As will hopefully become clear later, though, the absolute values and absolute changes are perhaps not as important as the changes in the gradient.

Unlike the mean fluxes, the changes to the eddy fluxes are modest in the tropics and subtropics (Fig. 4.18). The eddy DSE flux shifts poleward and weakens, becoming more concentrated in latitude, while the eddy LE flux increases and shifts poleward. The net is a strengthening and poleward shift of the eddy MSE flux, which reflects the canonical total MSE flux response (Held and Soden, 2006) purely because the extratropical fluxes are dominated by the eddies. Curiously, the eddy MSE flux decreases at the edge of the

Hadley circulation in the subtropics, in the region where the mean flow enhances its convergence of DSE/MSE (Fig. 4.16). It also increases across the latitude dividing the rising and subsiding branches of the circulation, reflecting a nearly 50% increase in the eddy LE flux. These changes act to reduce the gradient in the eddy MSE flux and hence reduce the MSE flux divergence in the subtropics; the presence of even one of these changes is sufficient to produce this response.

With the mean structure and basic response of the energy fluxes known, we now examine the response of the energy fluxes in the AXI model (Fig. 4.19). Compared to the AXI experiment, the AXI 2xτ response is characterized by a larger DSE flux in the tropics with little change to the DSE flux in the midlatitudes. Comparison of the AXI 2xτ and WP 2xτ responses shows that the reduction in the midlatitude DSE flux is driven primarily by eddy-mean flow changes, whereas the increase in the DSE flux in the tropics is almost entirely due to the mean flow (Fig. 4.20). The tropical increase is because the increased equatorward LE flux by the mean flow in the AXI 2xτ response is converted into DSE and is then transported poleward to the subtropics, with the increase in the LE flux a consequence of Clausius-Clapeyron scaling in lower-tropospheric humidity. In terms of the MSE flux, the AXI experiments do not realize the canonical increase in midlatitude MSE flux because they explicitly exclude any changes to the eddies.

The reduction in the eddy MSE flux divergence in the subtropics is of particular interest for understanding Hadley circulation expansion (Fig. 4.16), as the net poleward flux of energy out of the Hadley circulation by the eddies decreases. The function of the Hadley circulation is to transport heat produced by solar heating and latent heating poleward. Rather than reaching the poles, the circulation terminates in the subtropics - at these

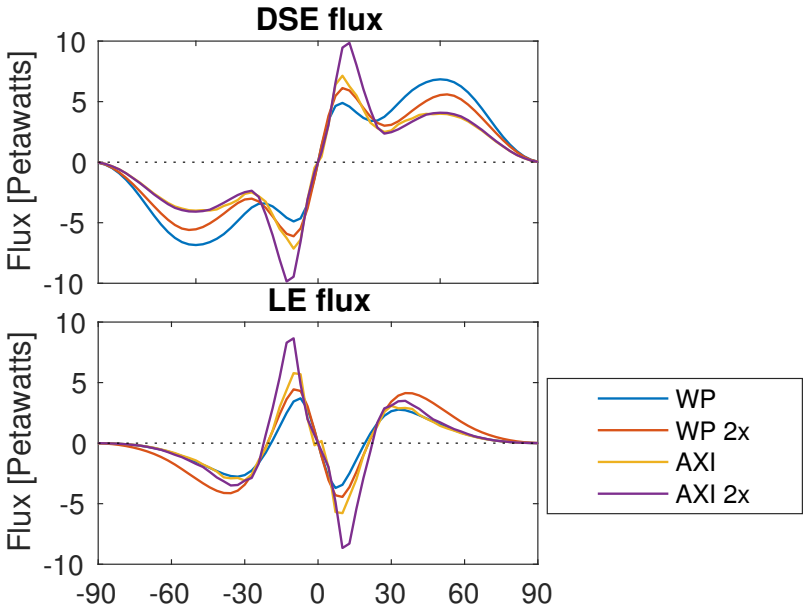

Figure 4.19: The (top) dry static energy flux and (bottom) latent energy flux in the WP, WP 2xτ, AXI, and AXI 2xτ experiments.

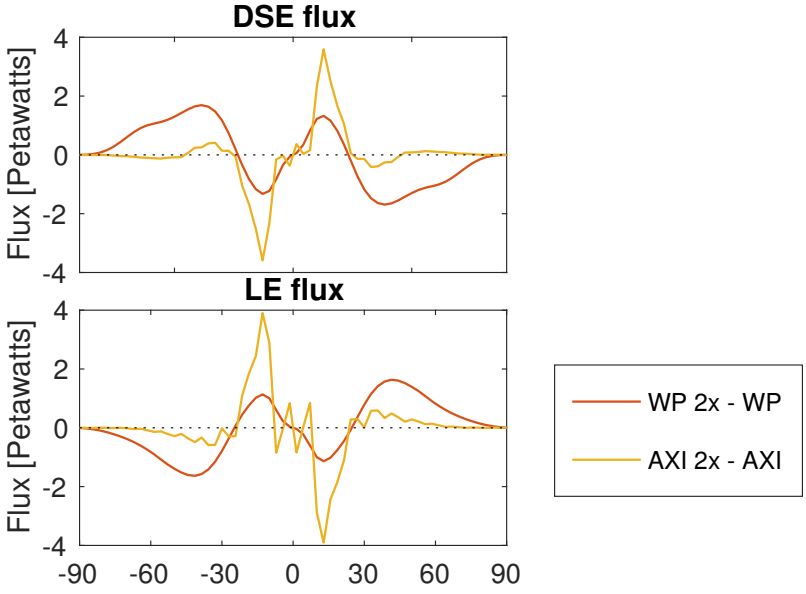

Figure 4.20: The difference in the (top) dry static energy flux and (middle) latent energy flux between the WP and the WP 2xτ and AXI and AXI 2xτ experiments.

latitudes, radiative cooling to space locally dissipates some energy, while eddies flux some remaining fraction of the excess energy poleward (Trenberth et al., 2001). This manifests as a net divergence of energy by the eddies. A moist static energy perspective can incorporate

all of these processes within a simple framework. If one considers the tropics as a location of net moist static energy production, and the subtropics as a location of net moist static energy dissipation (both local and divergence to the midlatitudes), it seems reasonable to posit that the area-integral of each should balance to satisfy conservation of energy.

Here it is hypothesized that the enhanced DSE flux convergence by the mean flow follows directly from the increase in tropical moisture and latent heating due to Clausius-Clapeyron scaling; and further, that the enhanced DSE flux convergence by the mean flow forces a substantial reduction in the eddy MSE flux by reducing the subtropical meridional DSE gradient. In effect, the Hadley circulation response to an increase in surface temperature brought on by a greenhouse-gas-like forcing actively damps the eddy-driving on the circulation by reducing the basic thermodynamic gradient that drives the eddies. Using the equal-area argument, the reduction in eddy MSE flux divergence will reduce the efficiency of moist static energy dissipation and necessarily demand an expansion of the area of subsidence within the circulation - a poleward expansion of the Hadley circulation.

Before fleshing out a theoretical argument, we should assess whether the changes to MSE induced by the Hadley circulation response can act to reduce the eddy MSE flux in the subtropics. Fig. 4.21 displays the vertically-integrated MSE and DSE for the different experiments[3]. MSE and DSE builds up at the equator in the AXI 2xτ experiment in the absence of an eddy flux response, consistent with the temperature response difference between the WP and AXI 2xτ experiments (Fig. 4.10). Further, the gradient of both DSE and MSE decreases in the subtropics within the subsiding branch of the circulation, e.g.,

[3]The AXI Control experiment has a slightly higher tropical and slightly lower polar MSE and DSE than the WP Control experiment, but the differences are small in light of the 2xτ and 2xτ eddy responses.

from 12 to 26.5 degrees latitude, and increases in the extratropics, consistent with the basic temperature response (Fig. 4.10). However, in the control climate the AXI experiment has a slightly stronger meridional gradient in both the MSE and DSE. Thus, we take the difference between the AXI and WP control climate MSE and DSE and apply it as a bias correction to the AXI 2xτ MSE and DSE (purple lines, Fig. 4.21) as a crude correction to this deficiency in the AXI model.

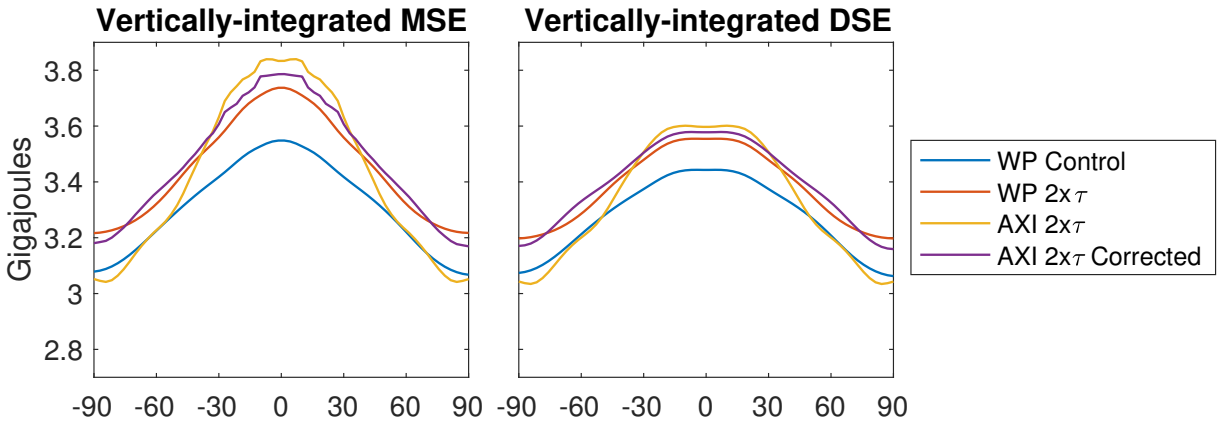

Figure 4.21: Vertically-integrated (left) moist static energy and (right) dry static energy from the 5 experiments.

The WP Control and 2xτ MSE and DSE fluxes are now decomposed into a gradient term and an eddy diffusivity term,

$$\frac{2\pi a\cos(\phi)}{g}\int_0^{p_s}[v'\chi']dp \approx \frac{1}{a}\frac{\partial}{\partial\phi}\left(\frac{2\pi a\cos(\phi)}{g}\int_0^{p_s}[\chi]dp\right)\cdot D_{eddy}(\phi) \tag{12}$$

where $D_{eddy}(\phi)$ is the latitude-dependent eddy diffusivity of MSE or DSE and χ is either MSE or DSE. $D_{eddy}(\phi)$ can be interpreted as the efficiency of the eddies in fluxing MSE and DSE poleward along a given gradient. Here, $D_{eddy}(\phi)$ is calculated from the WP 2xτ run and applied to the meridional gradient of the MSE and DSE in the AXI 2xτ experiment.

The key assumption is that $D_{eddy}(\phi)$ in the WP 2xτ run captures the general features of the eddy response to the optical depth forcing, and that these eddy diffusivity changes are set by non-local changes to the eddies' properties. Such changes can include increases in the eddy phase speeds (Chen and Held, 2007) as well as changes to the depth of the eddies (Korty and Schneider, 2008). In other words, it is assumed that changes to the eddy fluxes of MSE and DSE in the subtropics are primarily governed by local changes to their respective gradients ($\partial_y \chi$) and non-local changes to the eddies that manifest as local changes to the eddy diffusivity (D_{eddy}). If the resulting predictions to the eddy MSE and DSE flux using the AXI 2xτ MSE and DSE gradients match with the actual changes to the fluxes in the WP 2xτ experiment, we can conclude that the change in the eddy energy fluxes follow from changes in the background gradient driven by the mean flow and changes in the eddy (diffusivity) properties set by changes in wave generation in the baroclinic zones. Using the WP Control eddy diffusivity makes the unlikely assumption that mean flow changes lead the eddy changes or cause changes in the properties of the eddies.

Fig. 4.22 displays the eddy DSE flux and the eddy DSE flux in each experiment using the eddy diffusivity derived from the WP 2xτ experiment, while Fig. 4.23 displays the same but for the MSE flux. The change in the meridional DSE gradient predicts a poleward shift of the eddy DSE flux in the subtropics and an increase in the DSE flux in the midlatitudes. Within the confines of the subsiding branch of the Hadley circulation (dotted lines), the reduction in the meridional DSE gradient predicts a relatively strong decrease in the eddy DSE flux, which is in quantitative agreement with what occurs in the WP 2xτ experiment. Thus the changes in the subtropical eddy DSE flux are consistent with changes brought on by the direct radiative and mean flow responses alone.

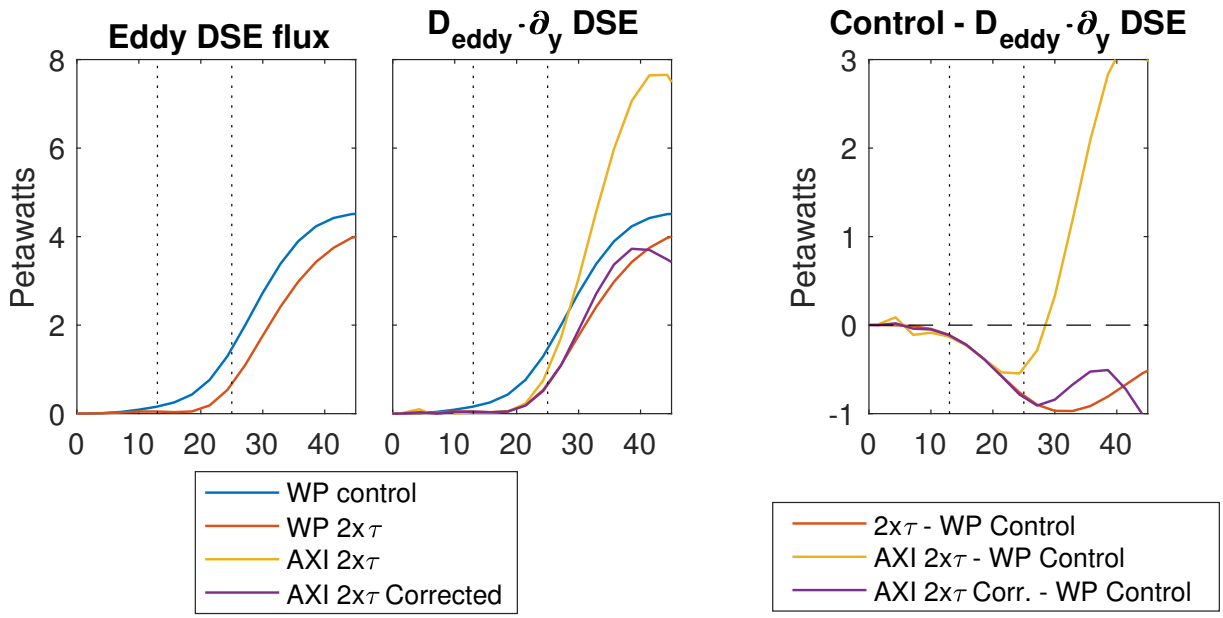

Figure 4.22: (Left) eddy DSE flux from the WP experiments, (middle) eddy DSE flux from the WP experiments and predicted eddy DSE flux from the AXI experiments using the WP 2xτ eddy DSE diffusivity, and (right) change in eddy DSE flux and predicted eddy DSE flux using the WP 2xτ eddy DSE diffusivity.

In similar fashion, the change in the meridional gradient of MSE in the AXI experiments predict a decrease in the eddy moist static energy flux within the subsiding branch of the Hadley circulation. In fact, even the slight increase in the eddy MSE flux at 13 degrees latitude may be due to the mean-flow-driven change in the meridional gradient of MSE. Thus, both the eddy MSE and DSE flux response in the tropics and subtropics are consistent with the eddies responding to changes in the background meridional gradient of MSE and DSE. Such changes in the background gradients are brought on by either and likely both mean flow and radiative-convective processes in the AXI 2xτ experiment. The predicted changes probably do not exactly line up with the realized changes in the WP 2xτ experiment because the mean flow presumably shifts poleward and brings the MSE and DSE gradients with it.

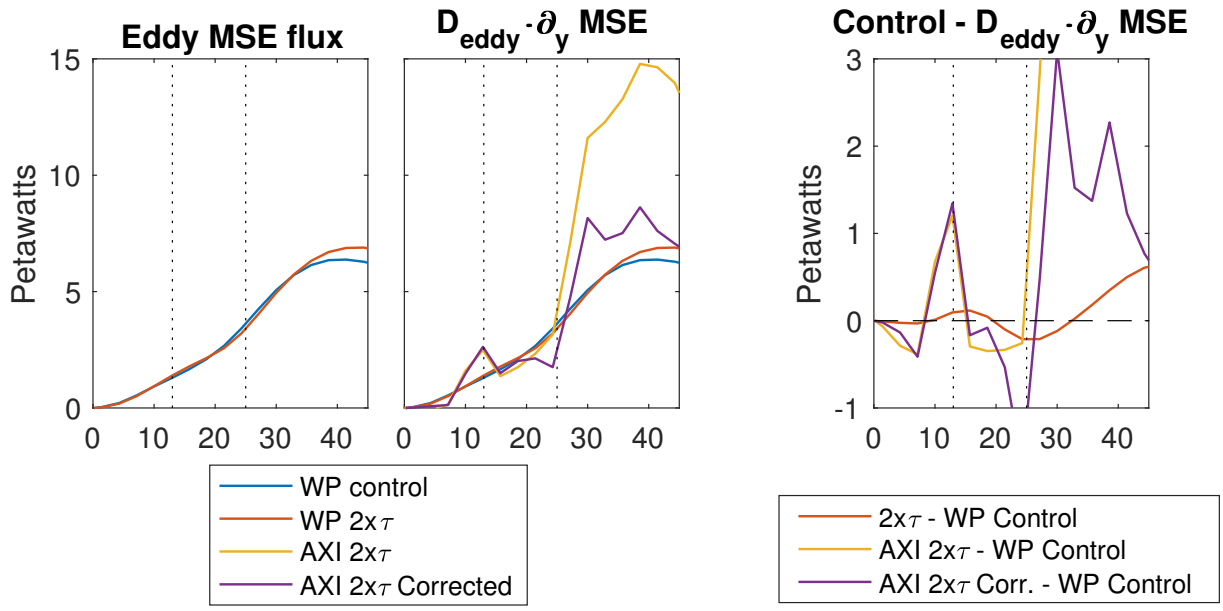

Figure 4.23: As in Fig. 4.22 but for the MSE flux.

The picture that is emerging is that the axisymmetric response is to flatten the meridional DSE and MSE gradients in the subtropics. Without a corresponding eddy response, the circulation contracts. In contrast, when the eddies are allowed to respond to this change in the meridional DSE and MSE gradients, the eddy MSE and DSE flux (and flux divergence) out of the Hadley circulation decreases. This eddy response need only occur within the confines of the circulation - in the AXI 2xτ tropical eddies experiment, where the 2xτ eddy response is only applied equatorward of the Hadley circulation edge, the circulation expands. Hadley circulation expansion, at least in this model, is not simply tied to the balance between the Coriolis torque and the eddy momentum flux convergence at the edge of the circulation. It is driven by a deeper, more integrative energetic balance between the circulation, radiation, and the eddies.

How could a reduction in the eddy-driving produce an expansion of the circulation? A theoretical scaling for the Hadley circulation width will now be derived to place these energetic changes into a predictive context for Hadley circulation expansion.

5 A theory for the width of the Hadley circulation

The vertically-integrated energy perspective shows promise for illuminating the mechanisms by which the eddies drive Hadley circulation expansion in light of the circulation's own tendency to contract in response to greenhouse-gas-like forcings. To that end, it is worth crafting a simple model of the rising and subsiding branches of the circulation based on the vertically-integrated moist static energy flux. In the proceeding section, a perturbation analysis of this model will be used to explore the potential roles of radiation and moisture in driving the observed behavior.

Consider a two-box model of the Hadley circulation (Fig. 5.1), one box for the rising branch and one box for the subsiding branch. Each box represents the full vertical extent of the troposphere. Solar radiation enters the top of the box according to GRAM's parameterization for annual-mean insolation,

$$S(\phi) = \frac{(1-\alpha)S_0}{4}\left[1 + \frac{\Delta_s}{4}(1 - 3\sin(\phi)^2)\right] \tag{1}$$

where α is the albedo, $\Delta_s = 1.4$ shapes the meridional variation of insolation, and $S_0 = 1360$ W/m^2 is the solar constant.

Consider the circulation to be energetically closed in terms of moist static energy $m = c_p T + gz + Lq$, where $c_p = 1004$ J/kg K is the specific heat of dry air, $L = 2.26 \times 10^6$ J/kg is the enthalpy of vaporization, and q is the specific humidity. Moist static energy is conserved during moist convection and in a column-averaged sense is only created or destroyed by surface energy fluxes and net radiative heating or cooling (Riehl and Malkus, 1958; Neelin and Held, 1987).

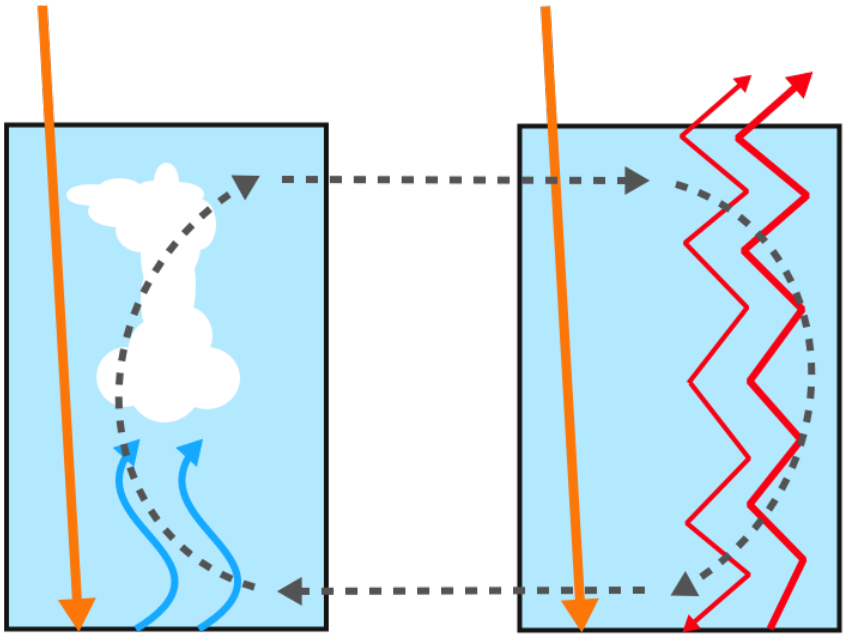

Figure 5.1: A schematic of the model Hadley circulation, with the rising (subsiding) branch on the left (right). The gray arrows indicate the implied circulation. Yellow arrows indicate insolation, red arrows indicate infrared radiation, and blue arrows indicate the latent heat flux.

Assuming that the vertical velocity vanishes at the top and bottom of the troposphere and assuming a steady-state, the vertically-averaged moist static energy budget is given by

$$\langle \nabla \cdot vm \rangle = F_B - F_T \tag{2}$$

where v is the meridional wind and F_B and F_T are the upward-directed energy fluxes at the surface and top of the troposphere, respectively. F_B includes both radiative and surface moisture and heat fluxes, while F_T is purely radiative. Because moist static energy is high in the tropics, we can deduce that the rising branch of the circulation is a region of net moist static energy production while the subsiding branch is a region of net moist static

energy destruction. Thus, for energetic closure we require the total moist static energy production, or moist static energy flux divergence, in the tropics to equal the total moist static energy destruction, or moist static energy flux convergence, in the subtropics,

$$\int_0^{\phi_m} \langle \nabla \cdot vm \rangle \cos(\phi) d\phi = -\int_{\phi_m}^{\phi_H} \langle \nabla \cdot vm \rangle \cos(\phi) d\phi \tag{3}$$

where ϕ_H and ϕ_m are the latitude of the Hadley cell edge and the latitude dividing the rising and subsiding branches of the circulation, respectively. To solve for ϕ_H, we will first find expressions for F_B and F_T in Eq. 2 and use these to develop an expression for $\langle \nabla \cdot vm \rangle$ in Eq. 24.

The atmosphere is taken to be a single layer with a characteristic emissivity for longwave radiation, ϵ, and average temperature T_a, which is not assumed to be equal in both the rising and subsiding branch of the circulation.[4]. For now, assume that all evaporation and sensible heating occurs in the box representing the rising branch of the circulation. Later, it will be noted how this is not so much an approximation as a mathematical trick to avoid an intractable integration in latitude. A schematic for the radiation and moist static energy budget of this model is shown in Fig. 5.2.

For both the tropics and subtropics, the upward longwave flux at the top of the troposphere is given by the sum of the outgoing longwave radiation from the surface not absorbed by the atmosphere and the outgoing longwave radiation from the atmosphere,

$$F_T = -\epsilon \sigma T_a^4 - (1-\epsilon)\sigma T_s^4 \tag{4}$$

[4]This is approach based on the pedagogical idealized greenhouse effect model commonly taught in climate and radiation courses

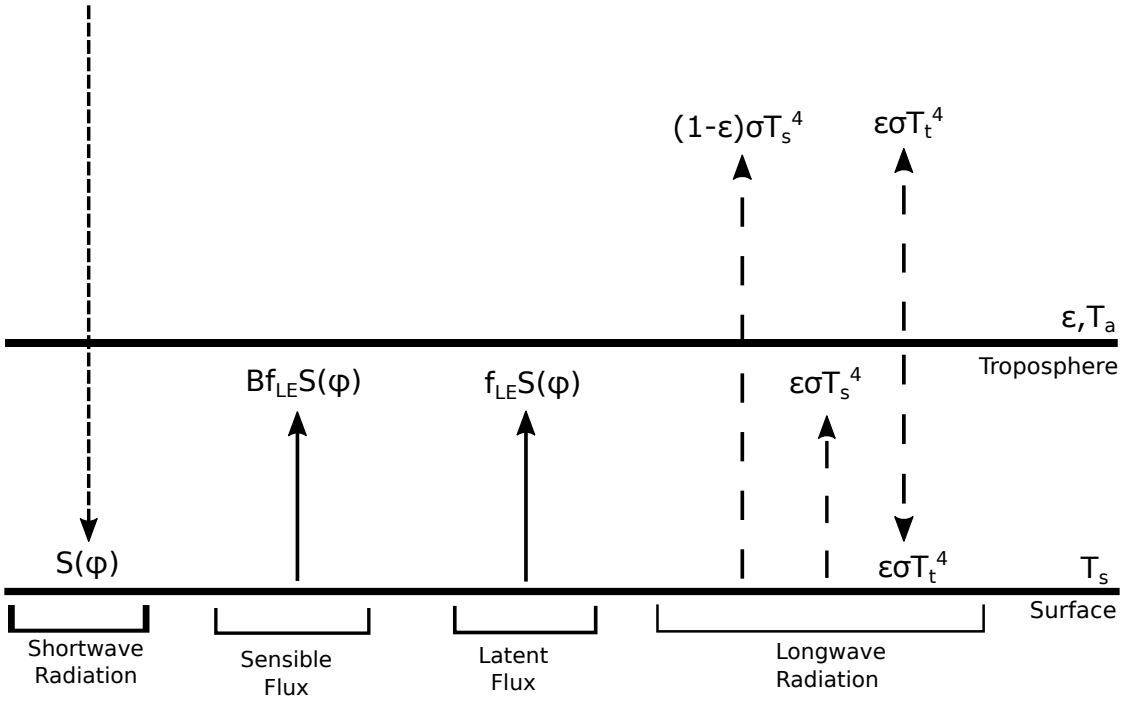

Figure 5.2: Detailed schematic of the energy budget for the model atmosphere, with one surface layer and one atmospheric layer. Long (short) dashes indicate longwave (shortwave) radiation, while the solid arrow denotes the surface latent heat flux. Values displayed are the value of the energy flux at absorption in a given layer. Symbols and variables as in the text.

where T_s is the surface temperature. Assuming no shortwave absorption in the interior of the troposphere, the interior energy budget in the subtropical atmosphere is expressed as a balance between the longwave radiation emitted upward and downward by the atmosphere and the longwave radiation emitted upward from the surface absorbed by the atmosphere,

$$2\epsilon\sigma T_a^4 = \epsilon\sigma T_s^4 \tag{5}$$

which can be substituted into Eq. 4 to yield

$$F_{T,subtropics} = -(1 - 0.5\epsilon)\sigma T_s^4 \tag{6}$$

The upward energy flux at the bottom of the subtropical troposphere is simply given by the upward longwave radiation,

$$F_{B,subtropics} = -\sigma T_s^4 \tag{7}$$

For the tropics, the upward energy flux at the bottom of the subtropical troposphere includes the upward latent heat flux, LE, which is yet to be determined, where L is the latent heat of vaporization for water and E is the evaporation rate,

$$F_{B,tropics} = -\sigma T_s^4 + LE + SH \tag{8}$$

It is assumed that all of this latent energy fluxed into the atmosphere in the tropics is condensed in the tropics - this is a very good approximation, as the air subsiding in the subtropics is incredibly dry. Hence, in the tropics, the interior energy budget in the tropical atmosphere is given by

$$2\epsilon\sigma T_a^4 = \epsilon\sigma T_s^4 + LE + SH \tag{9}$$

which, when substituted into Eq. 4, yields

$$F_{T,subtropics} = -(1 - 0.5\epsilon)\sigma T_s^4 - \frac{LE}{2} - \frac{SH}{2} \tag{10}$$

In the global-mean, the surface latent heat flux is approximately half of the absorbed solar radiation at the surface (Trenberth et al., 2009), and this holds approximately over

the tropical and subtropical latitudes over the oceans (Hartmann, 1994). While there is a dependence on latitude, with the sensible heat flux becoming dominant at the poles, it is minor in the tropics and subtropics (Fig. 5.3). We thus approximate the evaporation rate as equal to half the absorbed insolation at the surface within the rising branch of the circulation,

$$LE(\phi) = S(\phi) f_{LE} \tag{11}$$

where f_{LE}=0.5 is the fraction of absorbed solar radiation converted into latent heat. With f_{LE} known, we can estimate the fraction of absorbed solar radiation converted into sensible heat, f_{SH}, through the Bowen ratio, or the ratio between the sensible and latent heat flux, which is defined as

$$B = \frac{SH}{LE} \tag{12}$$

which, using the bulk formulas for both SH and LE and assuming equivalent bulk drag coefficients, is approximately

$$B \approx \frac{c_p(T_s - T_a)}{L(q_s^* - q_a)} \tag{13}$$

where q_s^* is the saturation specific humidity at the surface, T_a and q_a are the temperature and specific humidity of the atmosphere, and T_s is as before. Assume the air-sea temperature contrast Δ_{sb} is small, e.g. 1 K, so that q_b can be approximated as $RH * q_s^*$. Then we have

$$B \approx \frac{c_p \Delta_{sb}}{L q_s^* (1 - RH)} \tag{14}$$

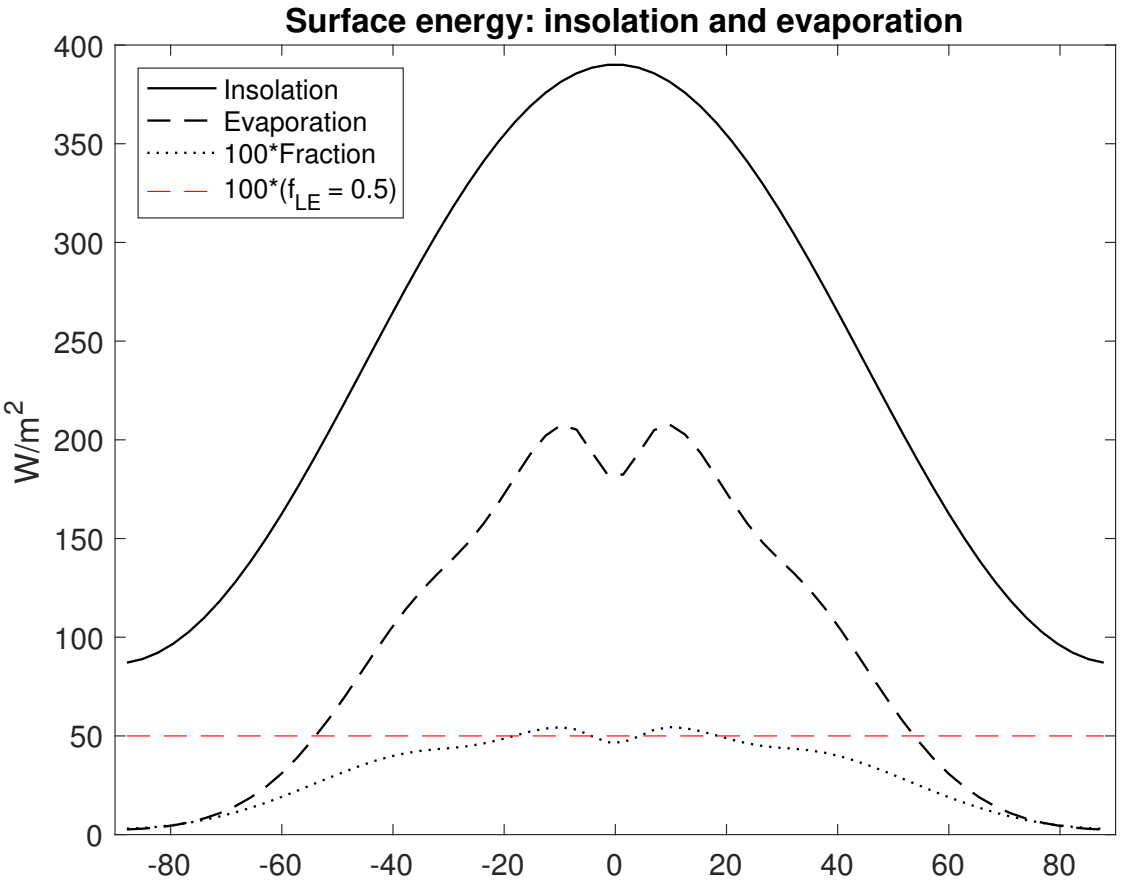

Figure 5.3: Insolation (solid) and evaporation (dashed) in W/m^2 in GRAM The fraction of solar energy converted into latent energy at each latitude is shown multiplied by 100 for scale (dotted), as well as the assumed $f_{LE} = 0.5$ (dashed red).

At a typical tropical surface temperature of 293 K, $q^* \approx .014$ kg/kg. Assuming a relative humidity of 80%, the Bowen ratio is ≈ 0.16, implying that at equilibrium, the fraction of sensible heat flux should scale as

$$SH(\phi) = S(\phi) f_{LE} B \tag{15}$$

where $f_{LE}B \approx 0.08$, which is equivalent to the ratio in GRAM's control climate.

We can now expand Eq. 2 for both the tropics and the subtropics. In the tropics, we have

$$F_B - F_T = -\frac{\epsilon}{2}\sigma T_s^4 + \frac{3}{2}S(\phi)f_{LE}(1+B) \tag{16}$$

whereas in the subtropics we have

$$F_B - F_T = -\frac{\epsilon}{2}\sigma T_s^4 \tag{17}$$

It can be seen from the equation for $F_B - F_T$ that if we allow evaporation and sensible heating to occur in the subtropics, but require that all of the evaporation occur in the tropics, the moist static energy dissipation in the subtropics will decrease by the evaporation rate and the moist static energy loss due to longwave cooling in the tropics will decrease by approximately 50% of the evaporation rate - a 50% compensation between the two budgets. The net result, area-integrating using the model's value for these terms, is a reduction in the predicted width of the circulation of several degrees latitude. However, attempting to include the subtropical surface fluxes and their contribution to the tropical atmosphere's moist static energy budget appears to result in a double integral in latitude that is not solvable analytyically.

Substituting this information into Eq. 24, we have

$$\int_0^{\phi_m}\left(\frac{3}{2}S(\phi)f_{LE}(1+B) - \frac{\epsilon}{2}\sigma T_s^4\right)\cos(\phi)d\phi = -\int_{\phi_m}^{\phi_H} -\frac{\epsilon}{2}\sigma T_s^4\cos(\phi)d\phi \tag{18}$$

ϵ, in some way proportional to the longwave optical depth, has a meridional gradient due to water vapor. For convenience, though, we will assume that both T_s and ϵ are constant within the integration. Integrating, we have

$$\frac{3f_{LE}(1+B)S_0(1-\alpha)\sin(\phi_m)(\Delta_s\cos(2\phi_m)+\Delta_s+8)\sin(\phi_m)}{64} = \frac{\epsilon}{2}\sigma T_s^4\sin(\phi_H) \qquad (19)$$

Solving for ϕ_H requires an expression for ϕ_m. A reasonable parameter is the Rossby radius of deformation, which effectively measures the minimum length scale at which large-scale circulations can be sustained against gravity wave interference. We define ϕ_m as the Rossby radius of deformation in the tropics (Gill, 1980),

$$\phi_m = \frac{1}{a}\sqrt{\frac{c}{2\beta}} \qquad (20)$$

where c is the gravity wave phase speed, a is the radius of the earth, and β is the gradient of the Coriolis parameter at the equator. This closure for ϕ_m can be interpreted as the typical scale of organized disturbances produced by tropical convection which force the ascent in the circulation. The gravity wave phase speed is defined by $c = \sqrt{gH_e}$ where g is gravity and H_e is a characteristic equivalent depth scale. This is equivalent to NH/π, where N is the buoyancy frequency and H is the tropopause height. For a typical gravity wave phase speed of 50 m/s (Gill, 1980), $\phi_m = 0.23$ radians or 13.3 degrees latitude.

With ϕ_m a known quantity, the width of the Hadley circulation is uniquely defined by

$$\phi_H = \sin^{-1}\left(\frac{3f_{LE}(1+B)S_0(1-\alpha)(\Delta_s\cos(2\phi_m)+\Delta_s+8)\sin(\phi_m)}{32\epsilon\sigma T_s^4}\right) \tag{21}$$

The scaling is straightforward to understand: it is the ratio of the total surface latent heat flux in the tropics (and its effects therein) to the total radiative cooling in the circulation. It is actually quite similar to the conceptual radiator-radiator fin model described in Pierrehumbert (1995) used to understand the regulation of tropical sea surface temperatures in the Walker circulation. In the approach we have taken, changes to ϕ_H must originate entirely from changes in the area of the subsiding branch of the circulation if the tropical radius of deformation does not change. ϕ_H is inversely proportional to ϵ and T_s because at higher temperatures or optical depths, the longwave cooling rate increases in the subtropics. It is directly proportional to f_{LE}, which can change through the Clausius-Clapeyron relation as T_s increases.

One obvious way to further generalize the model is to reduce T_s to a function of ϵ and $S(\phi)$ and thus determine an acceptable ϵ so that the model is consistent with the mean state of earth's atmosphere. Consider the surface energy budget of the circulation in the tropics, with incident solar radiation and longwave radiation from the atmosphere, and the surface latent heat flux and outgoing longwave radiation from the surface,

$$S(\phi) + \epsilon\sigma T_a^4 = (1+B)f_{LE}S(\phi) + \sigma T_s^4 \tag{22}$$

Using the interior energy balance of the atmosphere (Eq. 9), we have

$$\epsilon = 2\left(1 - \frac{\left(1 - \frac{f_{LE}(1+B)}{2}\right) S(\phi)}{\sigma T_s^4}\right) \tag{23}$$

The average surface temperature of the subtropics and tropics is $T_s \approx 290$ K, while $f_{LE} \approx 0.5$ and $B \approx 0.18$ as before. For $S(\phi)$, we cannot know ϕ_H ahead of time. However, it seems reasonable to estimate an average value of $S(\phi)$ at latitude ϕ_m - this underestimates the tropical and overestimates the subtropical $S(\phi)$, but is a reasonable approximation to get a bootstrap value for ϵ. At $\phi_m = 13.3$ degrees, $S(\phi) = 381$ W/m^2. Using these values, we find $\epsilon \approx 0.63$. One needs to be careful comparing this number to any real estimate of the optical depth in earth's atmosphere (related to emissivity for a single layer by $\epsilon = 1 - \exp(-\tau)$). This ϵ applies to a single-layer model, while GRAM is a multi-layer model and earth's atmosphere is a continuous realization of radiative transfer.

If we use Eq. 21, the model predicts a Hadley circulation width of 41 deg. By neglecting eddies, we are essentially neglecting an extra sink of moist static energy in the subtropics that would be otherwise diverged poleward (Trenberth and Stepaniak, 2003). If we parameterized a base-state moist static energy flux divergence by the eddies, the predicted width would presumably shrink and converge toward GRAM's modeled 26.3 degrees. Such a parameterization will be added next to examine the response of the circulation to greenhouse gas forcings.

5.1 Eddy effects

Eddies play a fundamental role in the mean-state and response of the general circulation to greenhouse gas forcings. To use this scaling theory to its full effect for predicting the response of the circulation, their impact must be included in some sort of parameterization. The vertically-integrated moist static budget is now separated into mean and eddy components, and it is assumed that (1), the eddies act on the subsiding branch of the circulation only and (2), the eddies export moist static energy to the extratropics,

$$\int_0^{\phi_m} \langle \nabla \cdot [v][m] \rangle \cos(\phi) d\phi = -\int_{\phi_m}^{\phi_H} \langle \nabla \cdot [v][m] \rangle \cos(\phi) d\phi - \int_{\phi_m}^{\phi_H} \langle \nabla \cdot [v'm'] \rangle \cos(\phi) d\phi \quad (24)$$

For now, we define the second term on the right-hand-side as

$$\int_{\phi_m}^{\phi_H} \langle \nabla \cdot [v'm'] \rangle \cos(\phi) d\phi \approx \int_{\phi_m}^{\phi_H} -D_{eddy,0} \cos(\phi) d\phi \quad (25)$$

where $D_{eddy,0}$ is some constant representative of the average eddy moist static energy flux divergence out of the subtropics. The eddy term cannot easily be determined a priori. Instead, it will be parameterized as an empirically-determined average value for the vertically-integrated eddy moist static energy flux divergence over the subtropics. Taking the average over 15-30 degrees latitude reveals $D_{eddy,0} \approx 50$ W/m^2.

This can be substituted into Eq. 18 to yield

$$\int_0^{\phi_m} (S(\phi) f_{LE}(1+B)) \cos(\phi) d\phi = -\int_0^{\phi_H} -\frac{\epsilon}{2}\sigma T_s^4 \cos(\phi) d\phi - \int_{\phi_m}^{\phi_H} -D_{eddy,0} \cos(\phi) d\phi \tag{26}$$

which, when solved for ϕ_H, yields

$$\phi_H = \sin^{-1}\left(\frac{3(1+B) f_{LE} S(1-\alpha)(\Delta_s \cos(2\phi_m) + \Delta_s + 8)\sin(\phi_m)}{64\left(\frac{\epsilon}{2}\sigma T_s^4 + D_{eddy,0}\right)}\right) \tag{27}$$

Using the same values as before, the model predicts a Hadley circulation width of $\phi_H = 25.7$ degrees latitude. This is slightly smaller than the width in GRAM (26.3 degrees), but is far more reasonable than the scaling neglecting the impact of eddies. The impact of eddies on the scaling contrasts with the typical differences in the behavior of the Hadley circulation between axisymmetric and wave-permitting simulations of the general circulation. The former are typically narrower, rather than wider (Kim and Lee, 2001), but the implementation of an axisymmetric simulation is paramount. In particular, the relaxation of the atmosphere to a given temperature structure (Kim and Lee, 2001; Held and Hou, 1980) is substantially different than an explicit modeling of radiative transfer, no matter how primitive. Relaxing to an earth-like climatological temperature may implicitly include the effect of eddies, and could partly explain why GRAM's axisymmetric circulation differs substantially from, e.g., the axisymmetric circulation in Kim and Lee (2001). In short, it's not at all clear whether such results represent a discrepancy with previous work on axisymmetric circulation.

5.2 The moisture-driven response

The hypothesis from the initial examination of the axisymmetric and wave-permitting model runs was that tropical latent heating changes can explain both the thermally-direct and wave-mean flow responses. We now have the theoretical tools to test this hypothesis through perturbation analysis of Eq. 27. Consider the response to a doubled optical depth, with all insolation parameters fixed. The parameters that will change as a result of doubled optical depth are F_{LE}, $D_{eddy,0}$, ϕ_m, and T_s in Eq. 27.

As in Held and Soden (2006), these terms are expanded in terms of the Clasius-Clapeyron scaling response of specific humidity to warming, $\delta q \approx \alpha q \delta T$, where q is the specific humidity and $\alpha = L/RT^2$, where L is the latent heat of vaporization and R is the gas constant for dry air. For the current climate, $\alpha \approx 0.07$ K^{-1} in the mid-troposphere.

For f_{LE}, we assume that the response of the surface latent heat fluxes changes as a function of the difference between the specific humidities of the surface layer and atmosphere,

$$\frac{\delta f_{LE}}{f_{LE}} \approx \frac{\delta(q_s^* - q_a)}{q_s^* - q_a} \approx \frac{\delta q_s^*(1-h)}{q_s^*(1-h)} \tag{28}$$

where $q_s^*(T_s)$ is the saturation specific humidity at the surface temperature T_s just above the ocean surface, h is the relative humidity, and q_a is the humidity in the near-surface boundary layer. Assuming that the relative humidity of the near-surface boundary layer remains constant, the flux will scale as $\delta q/q$. In other words, f_{LE} will scale as

$$\delta f_{LE} \approx f_{LE}(\alpha \delta T_s) \tag{29}$$

Physically, the enhanced downwelling longwave radiation from a warmer atmosphere is partly offset by an increase in the surface latent heat flux (as well as an increase in upwelling longwave from the surface). However, in model simulations the evaporation (and precipitation) does not scale as strongly as Clausius-Clapeyron (Held and Soden, 2006), in part due to increases in near-surface humidity and static stability (Richter and Xie, 2008). A typical average value predicted in models for the scaling is between -1 and 3%/K in the global-mean, with a multi-model-mean of slightly higher than 2%/K. We use a value of 2.5%/K, which is the -30 to 30 degrees latitude average response in GRAM, and define a new $\alpha_{LE} = 0.025$ %/K scaling for f_{LE},

$$\delta f_{LE} \approx f_{LE}(\alpha_{LE}\delta T_s) \tag{30}$$

For the Bowen ratio, note that $B \sim 1/q_s^*$. Assuming the air-sea temperature contrast does not change, the new Bowen ratio B will scale as

$$\frac{B}{B_0} \approx \frac{q_s^*}{q_s^* + \delta q_s^*} = \frac{1}{1 + \alpha\delta T} \tag{31}$$

where B_0 is the Bowen ratio at In other words, the new Bowen ratio is simply

$$B = \frac{B_0}{1 + \alpha\delta T} \tag{32}$$

For a doubling of the optical depth, the new Bowen ratio is 0.13, a 28% reduction in the sensible-to-latent heat flux ratio.

In regard to $D_{eddy,0}$, the latent and dry static energy flux responses constituting the total moist static energy response are of opposite sign (Held and Soden, 2006). As shown in Held and Soden (2006), for perturbations about the current climate the latent energy response scales as

$$\frac{\partial F_L}{F_L} \approx -\left(\frac{\alpha \delta T_s}{1+\mu\xi}\right) \tag{33}$$

where $\mu = .8$ is the approximate ratio between the increase in latent (F_L) and decrease in dry energy transport in the subtropics (see Fig. 4.16) and $\xi = 1.7$ is the approximate ratio between the latent and dry energy transport in the mean (Fig. 4.17). These constants differ from those in Held and Soden (2006), in large part because the midlatitude and subtropical energy responses are of opposite sign and different magnitude. In the midlatitudes, the latent energy flux increase outpaces the reduction in the dry static energy flux decrease, while in the subtropics the reduction in the dry static energy flux dominates. More than half of the meridional mass flux in the subtropics that is swept into the storm tracks occurs above the boundary layer (Fig. **??**). In the subtropics, boundary layer humidity would be expected to scale with Clausius-Clapeyron, but above the boundary layer the dry subsidence of the Hadley circulation dominates. In other words, it is somewhat expected that the poleward latent heat flux out of the subtropics by the eddies increases at a rate below Clausius-Clapeyron because the storm tracks tap both boundary layer and mid-tropospheric air. Further, in response to warming the mean circulation converges more latent energy into the tropics (Fig. 4.16) - there may be a tug-of-war between the mean circulation fluxing the enhanced subtropical water vapor equatorward and the eddies fluxing it poleward.

An expression for F_D, the dry static energy flux, follows from the definition of μ,

$$-\mu\frac{\delta F_D}{F_D} \approx \frac{\delta F_L}{F_L} \tag{34}$$

These two expressions for the dry and moist static energy can be combined into a single expression for the change in total moist static energy transport, F_T, using ξ as a constant of proportionality,

$$\frac{\partial F_T}{F_T} = \frac{\partial F_L + \partial F_D}{F_T} = \frac{\partial F_L}{F_L}\frac{F_L}{F_T} + \frac{\partial F_D}{F_D}\frac{F_D}{F_T} = \frac{\partial F_L}{F_L}\frac{\xi}{1+\xi} + \frac{\partial F_D}{F_D}\frac{1}{1+\xi} \tag{35}$$

which can be solved in terms of known constants using Eq.'s 33 and 34,

$$\frac{\delta F_T}{F_T} \approx \frac{1-\mu\xi}{\mu(1+\xi)}\left(\frac{\alpha\delta T_s}{1+\mu\xi}\right) \tag{36}$$

which is negative for positive δT_s. In other words, there is a reduction in moist static energy flux divergence out of the Hadley circulation by the eddies in response to forcings that globally perturb T_s, which is consistent with the response of the eddy moist static energy transport in GRAM (Fig. 4.16). Extending this to the parameterization of F_T, and assuming that the divergence scales as the flux, we have

$$\delta D_{eddy,0} \approx D_{eddy,0}\frac{1-\mu\xi}{\mu(1+\xi)}\left(\frac{\alpha\delta T_s}{1+\mu\xi}\right) \tag{37}$$

Finally, consider the response of ϕ_m. In the scaling for the mean-state, we considered ϕ_m as equivalent to the equatorial radius of deformation, a lower bound for the scale of

steady circulations in the tropics. In a warmer climate, static stability increases in the tropics through moist adiabatic adjustment and increases the speed at which gravity waves propagate. As a result, the equatorial radius of deformation will necessarily increase by $\delta\phi_m$. We will assess this scaling via changes in static stability alone, e.g.

$$\delta\phi_m \approx \frac{1}{a}\sqrt{\frac{\sqrt{N^2+\delta N^2}H}{2\pi\beta}} \tag{38}$$

where we have assumed that the tropopause height, H, remains approximately constant. As the tropopause height also increases in a warmer climate, $\delta\phi_m$ here can be thought of as a lower bound. If $\delta N^2 \approx \alpha\delta T_s$, i.e., the stability scales with humidity, then the radius of deformation scales as

$$\delta\phi_m \approx \left(\sqrt[4]{1+\alpha\delta T_s}-1\right)\phi_m \tag{39}$$

In other words, the deformation radius scales at approximately 1.5 %/K.

The response of the Hadley circulation width to these perturbations is given by

$$\phi_H + \delta\phi_H = \sin^{-1}\left(\frac{3(\delta f_{LE}+f_{LE})(\frac{B}{1+\alpha\delta T})S(1-\alpha)(\Delta_s\cos(\phi_m+\Delta\phi_m)+\Delta_s+8)\sin(\phi_m+\Delta\phi_m)}{64\left((\epsilon+\delta\epsilon)\sigma(T_s+\delta T_s)^4+D_{eddy,0}+\delta D_{eddy,0}\right)}\right) \tag{40}$$

In GRAM, the surface temperature increase is approximately 8.0 K, which corresponds to $\delta\epsilon \approx 0.14$ in this scaling. We again note that this is not exactly equal to a doubling of the mean-state optical depth because the increase in emissivity in a single-layer atmosphere has a fundamentally different interpretation that it does in a multi-level or continuous

atmosphere. As an example, changes in emissivity modulate outgoing surface longwave in a single-layer model, but modulate outgoing longwave from all levels below in a multi-layer model. The radiative cooling in the "troposphere" increases far more rapidly in the case of the former than it does in the latter.

With this δT_s, $\delta f_{LE} \approx 0.1$, $\delta D_{eddy,0} \approx 3.7$ W/m^2, and $\delta \phi_m \approx 1.6$ degrees latitude (an 12% expansion). The resulting $\delta \phi_H$ is 1.5 degrees, in close agreement with GRAM's 1.8 degrees. If the change in $D_{eddy,0}$ is ignored, the model predicts an expansion of 1.0 degrees. This is the opposite sign of the contraction seen in the axisymmetric model with eddy forcings fixed to their unperturbed state, so in some sense the scaling is unable to explain the behavior of an axisymmetric climate. However, it is similar to the muted expansion seen in the AXI $2x\tau$ experiment when the surface fluxes associated with the eddies are not applied. If the original axisymmetric scaling is used, the model predicts a contraction of 2.0 degrees latitude, which is at least qualitatively similar to GRAM's 0.7 degrees latitude contraction. Without the effect of eddies on the circulation, the axisymmetric scaling argues that the modest increase in tropical evaporation and the area of rising motion in the circulation is outpaced by the enhanced subtropical cooling to space.

It would be useful to compare this number to a set of comprehensive model runs with carbon dioxide forcings, but the correspondence between bulk optical depth changes and changes in a gas active in specific radiation bands is not entirely clear. However, using the surface temperature response as a guide, the mean δT_s in the abrupt4xCO_2 experiment is 4.7 K, hence doubling the optical depth is something like increasing the carbon dioxide concentrations by sixfold to sevenfold. The mean Hadley circulation expansion in the abrupt4xCO_2 experiment in the Southern Hemisphere, which has a climate most like

GRAM, is 1.9 deg latitude, which translates to an expansion of 2.9 degrees latitude if scaled with the surface temperature response. In the Northern Hemisphere, the response is halved, corresponding to a scaled expansion of 1.5 degrees latitude.

5.3 Assessing the mechanism for expansion

In a broad sense the scaling theory predicts a reasonable response of the Hadley circulation to greenhouse gas-like forcings and appears to predicted a reasonable mean Hadley circulation width. However, it is worth exploring the scaling over a range of climates. In particular, it is important to assess the individual components of the scaling to determine which, if any, exhibit unrealistic behavior.

We will examine the scaling theory relative to the control climate optical depth, τ_0. Recall that the control climate optical depth is 6 at the equator and 2 at the poles, which implicitly reflects the effects of water vapor. The full wave-permitting version of GRAM is run in $0.5\times\tau_0$, $0.75\times\tau_0$, $1.5\times\tau_0$, and $2.0\times\tau_0$ configurations, each of which create approximately 4 K changes in global-mean surface temperature.

The model predicts the control climate Hadley cell width to within 1 degree latitude, although some features of the scaling such as the fraction of insolation converted into the surface latent heat flux were tuned directly to the values in GRAM (Fig. 5.4). Within small optical depth perturbations resulting in ± 4 K changes in global-mean surface temperature the predicted widths fall close to modeled value, but at more substantial optical depth changes the predicted width diverges. For a doubling of the optical depth, the scaling slightly underestimates the change in width relative to the control climate, while for a halving of the optical depth it overestimates the change.

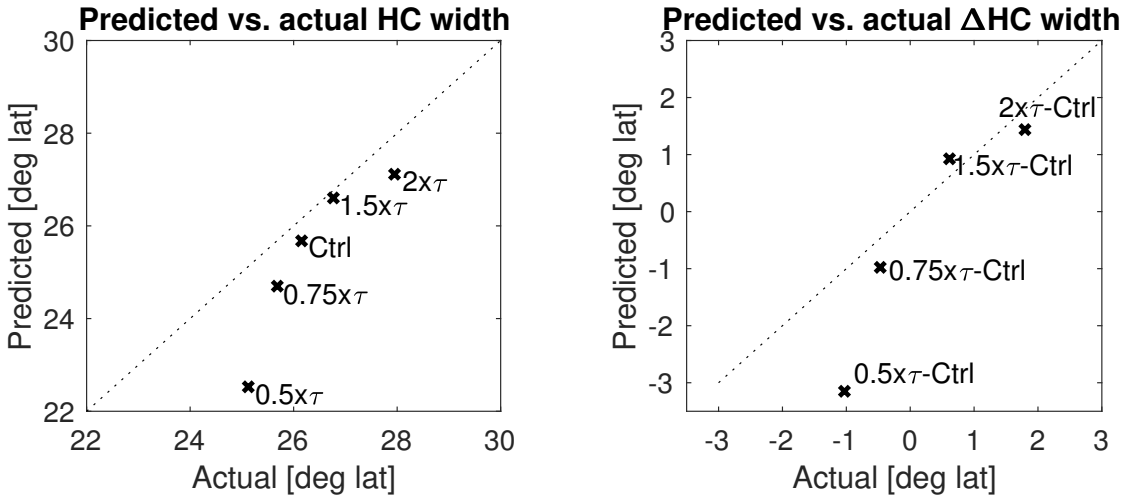

Figure 5.4: The predicted versus actual modeled Hadley cell width and change in Hadley cell width in GRAM Text indicates each experiment's optical depth.

This non-linear behavior at significant optical depth changes seems to be due to the eddy MSE flux divergence scaling (Fig. 5.5), as the other parameters - the surface latent and sensible heat fluxes and the interior longwave cooling - are essentially linear. While these latter processes are essentially local thermodynamic integrals, such as temperature and insolation, the eddy MSE divergence is influence non-locally by the full hemispheric structure of the MSE gradient on which the eddies act.

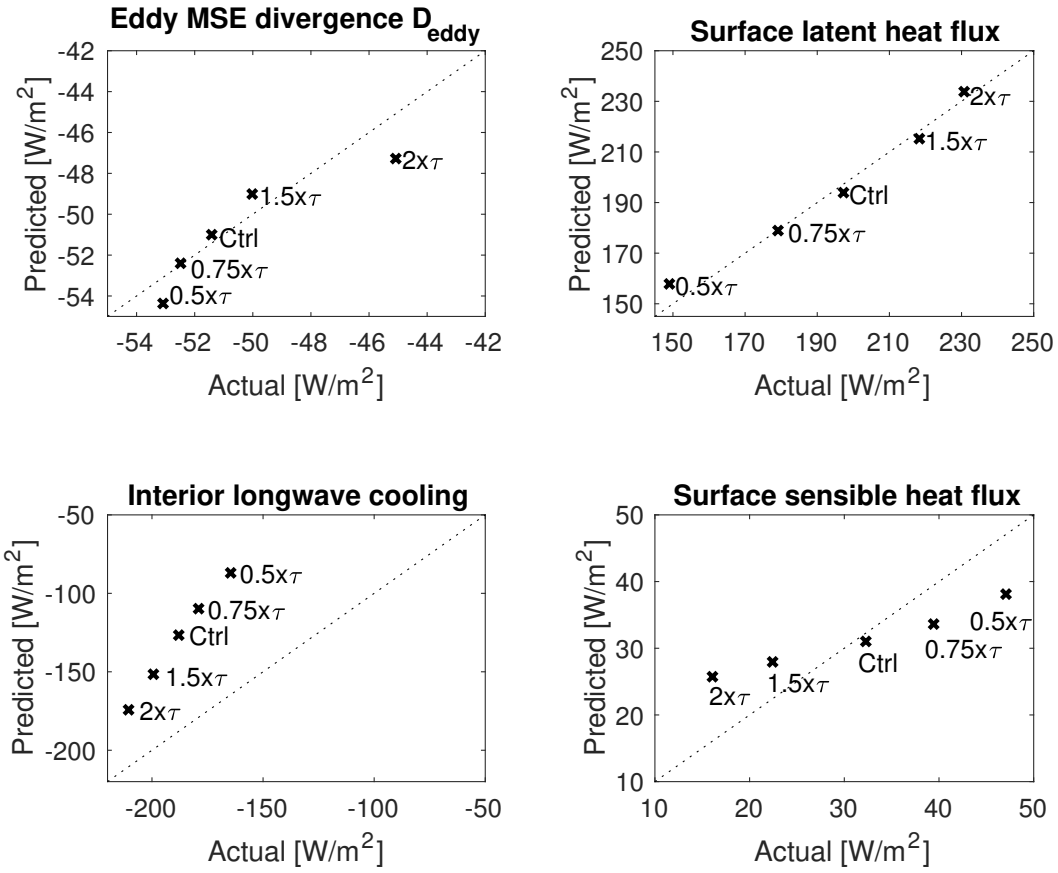

Figure 5.5: The predicted versus actual modeled (upper left) eddy moist static energy divergence, (upper right) surface latent heat flux, (lower left) interior longwave cooling, and (lower right) surface sensible heat flux. See text for details.

While the interior longwave cooling is weaker and more sensitive than the modeled value, the surface sensible heat flux is less sensitive than the modeled value, suggesting some compensation between the errors in the individual parameter scalings. Though it was assumed to be constant, changes to the air-sea temperature contrast would substantially impact the surface sensible heat flux. Additionally, constructing the atmosphere as a single isothermal layer is a severe simplification. Adding another layer to represent the stratosphere may reduce the sensitive of the interior longwave cooling rate, but doing so substantially complicates the scaling theory. Nevertheless, it may be an additional step worth pursuing in later work.

Clausius-Clapeyron scaling is also successful at predicting changes in ϕ_m, the latitude dividing the rising and subsiding branches of the circulation. While there is a consistent offset between the modeled and predicted value, it is entirely due to the arbitrary choice of the gravity wave phase speed. We assumed a value of 50 m/s, but to match the modeled value a phase speed of 42 m/s is needed. Evidently, a substantial fraction of Hadley circulation expansion is due to the change in ϕ_m, which increases the area of rising motion and hence net moist static energy creation in the tropics.

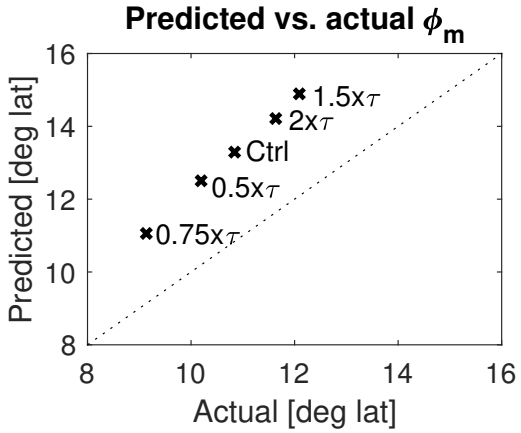

Figure 5.6: The predicted versus actual modeled change in the latitude dividing the rising and subsiding branch of the Hadley cell. See text for details.

5.4 Comparison to the Held-Hou theory

Both the scaling develop here and the Held and Hou (1980) scaling suggest that the Hadley circulation width is proportional, in some way, to the equator-to-pole climate contrast. The Held and Hou (1980) model begins with the definition of a base-state potential temperature field with Δ_h representing the fractional change in the equator-to-pole temperature gradient. Here, the equator-to-pole climate contrast appears in the insolation parameterization as Δ_s, so the precise relationship between the two is not

entirely clear. Within the confines of the scaling, though, we can solve for the equator-to-pole temperature gradient and calculate an analogue to Δ_h in Held and Hou (1980). If we begin from Eq. 22, the surface temperature at latitude ϕ is given by

$$T(\phi) = \left[\frac{\left(1 - \frac{(1+B)f_{LE}}{2}\right)}{\sigma\left(1 - \frac{\epsilon}{2}\right)} \right]^{1/4} \tag{41}$$

where we now assume that the surface energy fluxes to the atmosphere should not be ignored at any latitude (we are no longer interested in only the effects on the Hadley circulation). With the surface temperatures known we can calculate the fractional change in temperature from the equator to the pole as

$$\Delta_h = \frac{2(T_{eq} - T_{pole})}{T_{eq} + T_{pole}} \tag{42}$$

The resulting curves of the Hadley circulation width from the axisymmetric and comprehensive scaling theory, as well as from the Held and Hou (1980) scaling theory, are shown in Fig. 5.7. It is not so surprising that the Δ_h and Δ_s values used in these two scalings are nearly equivalent - they give an equator-to-pole temperature contrast that is close to the observed value and thus a Hadley circulation width that is close to the observed value. The axisymmetric scaling without the addition of a parameterized eddy MSE flux divergence is consistently shifted poleward relative to the scaling with the eddy MSE flux divergence, but is otherwise the same.

In climates with an equator-to-pole temperature gradients close to earth's current climate (dotted lines), the scaling theory and the Held and Hou (1980) scaling are in close

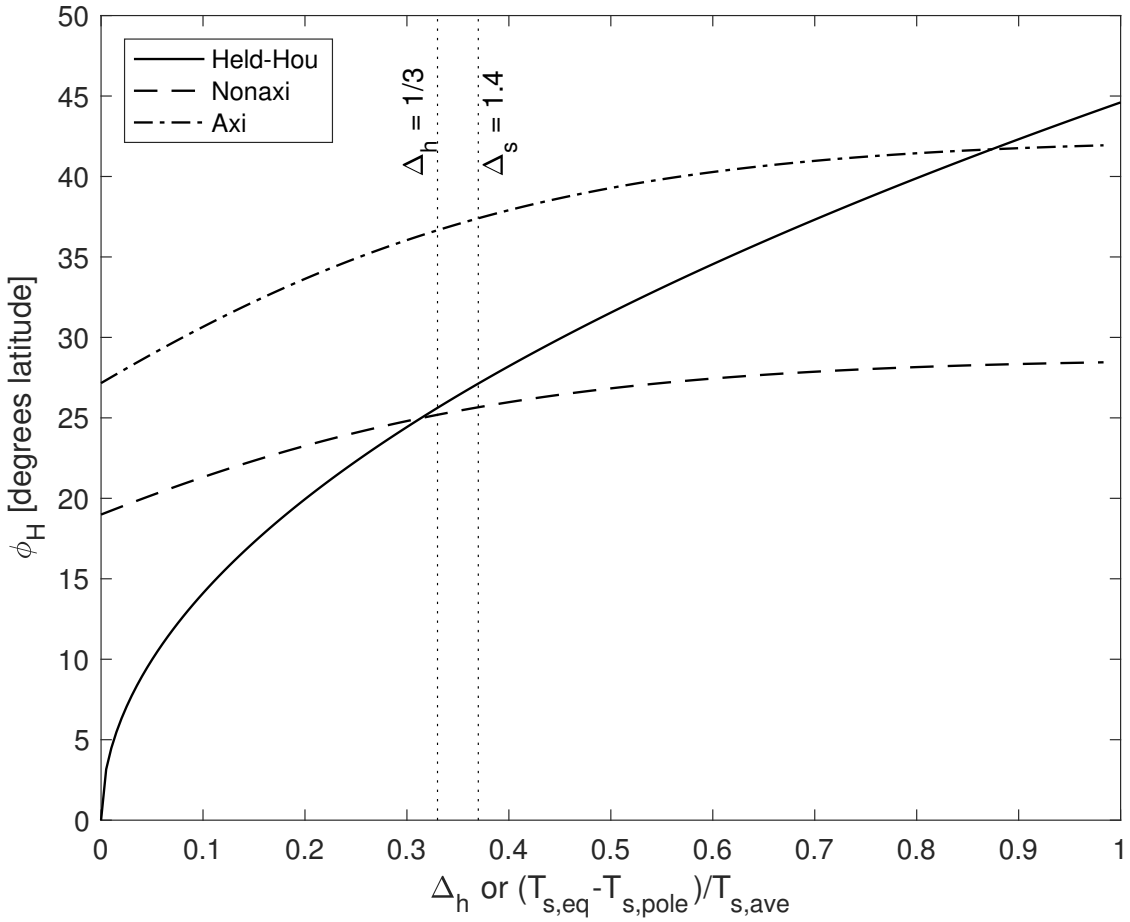

Figure 5.7: The Hadley circulation width as a function of equator-to-pole temperature gradient in the Held-Hou (solid), non-axisymmetric scaling theory (dashed), and axisymmetric scaling theory (dash-dotted). The value of Δ_h used in Held and Hou (1980), and the value of Δ_s converted into an equivalent Δ_h value used in the model simulations here, are shown in the dotted lines.

agreement, but the Held and Hou (1980) scaling is clearly more sensitive. It also converges toward zero as Δ_h approaches zero. On the other hand, there is a minimum Hadley circulation width for the scaling theory examined here, which arises from the definition of ϕ_m. ϕ_m gives a robust lower bound on the circulation, as the rising branch is defined to have a finite width. In a radically different climate with no equator-to-pole temperature gradient, the gravity wave phase speeds that set ϕ_m may be radically different; the scaling examined here essentially makes an approximation to the current climate. It's also

important to note that Fig. 5.7 explores the sensitivity to the equator-to-pole temperature/insolation gradient only. In the scaling theory examined here, f_{LE}, B, and ϕ_m will likely change as Δ_s varies. In the Held-Hou theory, one might expect the functional forms in the equilibrium fields to vary to accommodate some of these changes.

In the same vein, these curves should not be interpreted as predictions of Hadley circulation expansion. Instead, they should be interpreted as predictions for the mean Hadley circulation width in an unperturbed climate when only some specific parameters are varied, and are probably only valid in a small window about the control climate the theories were constructed to replicate. Future work should be cautious to not over-interpret these scalings for the Hadley circulation width. It should also address the shortcomings of all of these theories, specifically their dependence upon so much a priori information. We will have a "real" theory of the Hadley circulation when the only input parameters are the insolation and the concentration of radiatively-active gases in the atmosphere.

6 Conclusions

The goal posed at the outset of this dissertation was to connect the eddy-driven and thermally-direct dynamics of the Hadley circulation within a single framework. However, it was argued that because the thermodynamic gradients set up by differential solar heating are the ultimate driver of the general circulation, any theory for the width of the Hadley cells should be grounded in thermodynamics.

We have shown that Hadley cell expansion is a robust response of the climate system to greenhouse gas forcings. While the expansion scales with increases in static stability, as the Held (2000) theory predicts, it also scales with global-mean surface temperature, stratospheric cooling, and polar amplification. Hadley cell expansion is thus a fundamental response of the atmosphere to increasing greenhouse gas concentrations.

The jet is a manifestation of an angular-momentum-conserving Hadley cell (Held and Hou, 1980). More generally, it is a result of the strong temperature gradient across the Hadley cell edges and a balance of eddy-mean flow dynamics. Given any of the theoretical perspectives of the circulation, it seemed reasonable to predict that the jet latitudes should have some association with the Hadley cell edge latitudes. But the lack of statistical connections between the Hadley cell edge latitudes and the latitudes of the subtropical jets (and tropopause breaks) on any timescale within and across model simulations undermines the validity of Hadley cell scaling theories predicated on angular momentum conservation. How do we square these results with the success of scaling theories, such as Held (2000), that seem to qualitatively and quantitatively predict Hadley cell expansion in response to both greenhouse gas and solar forcings?

Model experiments with eddy forcings on the mean flow fixed to their unperturbed state predict a contraction of the circulation, despite increases in both static stability and global-mean surface temperature. Thus, while expansion scales with static stability and global-mean surface temperature at equilibrium, the model experiments examined here suggest they are not the direct cause or at least not sufficient to cause expansion.

Eddies appear to play a pivotal role in the mean state, variability, and response of the Hadley circulation to radiative forcings. In the mean, the total eddy driving on the Hadley cells is closely related to their mean width and intensity. On monthly timescales the eddy-driven jet latitudes are strongly coupled to the Hadley cell edge latitudes; both scale in response to forcings, and both exhibit a robust forced response in models. The eddies and the Hadley cells are closely linked in all moments, and an energetic perspective provides a clear argument for why this must be the case. To create a seamless poleward transport of energy that balances the asymmetry of incoming solar radiation, the poleward energy flux by the eddies and the mean flow must respond to changes in one another (Trenberth and Stepaniak, 2003).

This energetic perspective is more fundamental and constrained than the dry eddy-mean flow dynamics. There is a well-defined poleward energy transport that must be sustained to create a consistent, month-to-month and year-to-year climatology. On the other hand, the total momentum transport is not so constrained; the annular modes and other patterns of variability make this clear. The momentum transport is a manifestation of Rossby wave propagation and mean flow advection, while the energy transport is the convolution of both with thermodynamic gradients. Compared to the relatively invariant poleward energy flux, the momentum transport and thermodynamic gradients have more degrees of freedom so long as they maintain a balance.

Dry static energy captures the meridional gradients of dry energy that directly drive the general circulation (Lorenz, 1955)[5], while the moist static energy includes the compounding effects of water vapor phase changes. Through this lens, the Hadley cells can be understood as massive latent-to-dry static energy conversion engines, while the eddies operate diffusively on the equator-to-pole gradients of both. It is this contrast in the circulations' latent energy fluxes - the Hadley circulation as "anti-diffusive" and the eddies as diffusive - that may in part give rise to Hadley cell expansion.

To untangle the eddy-mean flow interactions that comprise the circulation response to radiative forcings, a new modeling framework was developed in an idealized gray radiation aquaplanet model that is able to isolate the mean flow response from the total eddy-mean flow response. The direct response of the mean circulation to a greenhouse-gas-like forcing is a contraction of the Hadley cells, while the response of the eddies to the same forcing

[5]Available potential energy is related to the internal and potential energies, while dry static energy is the sum of the enthalpy and potential energy, so these two are not exactly the same.

drives expansion. An eddy diffusivity framework provides some evidence that the changes to the subtropical eddy moist and dry static energy fluxes may be a response to enhanced subtropical dry static energy convergence by the overturning circulation. This convergence reduces the meridional dry static energy gradient that drives the eddies and is argued to essentially push the subtropical eddy regime poleward. Such a change is an inevitable result of the Hadley cells' equatorial convergence of latent energy scaling by Clausius-Clapeyron in a warmer climate.

How this change might impact the Hadley circulation is less clear, so a simple theoretical scaling based on moist static energy was developed. The scaling naturally selects the most salient processes: radiative cooling, surface heat fluxes, and the eddy moist static energy flux divergence. In this simple interpretation of the circulation, the latent and sensible heating in the tropics is balanced by radiative cooling in the tropics and subtropics and the eddy moist static energy flux divergence in the subtropics. In concert with the model results, a plausible hypothesis is that the decrease in the eddy moist static energy flux divergence, which may be driven by the mean flow response itself, acts to reduce the efficiency of the subtropics at dissipating moist static energy and thus tips the energetic scale toward expansion. The scaling is somewhat inconsistent in this regard, and more work is needed to understand why.

The model used to separate the eddy-mean flow response from the direct mean flow response includes no cloud radiative effects, an unrealistic treatment of radiative transfer, and a bias in its mean climate and energy fluxes. These factors may influence the applicability of this models' results to earth's atmosphere, as such processes are indeed contributors to the Hadley circulation response to forcings (Feldl and Bordoni, 2016). This

final analysis also focused on a single model. If the earlier analyses in this work are any indication, it is impossible to make any informed judgment about the validity of a hypothesis using one model alone. However, there are fingerprints of the mechanisms presented here that could be assessed in more comprehensive model simulations, including the particular eddy moist static energy flux divergence and mean energy flux changes that are associated with expansion in GRAM.

The scaling theory derived in this dissertation is simple, but it contains some ad hoc components and is not derived from a complete set of dynamic and thermodynamic equations. On the bright side, that means there are endless opportunities to improve the model. Radiation could be treated more realistically with the addition of a second radiating layer, and a more robust closure theory for the surface fluxes could be developed to eliminate another ad hoc construction in the model. Perhaps the clunkiest feature of the model is the scaling for the eddy moist static energy flux divergence. There may be a way to define a gradient of moist static energy between the rising and subsiding branches of the circulation from the axisymmetric scaling. This could be combined with an assumed (or measured) value of eddy diffusivity to more accurately predict the mean state of and changes in the eddy moist static energy flux divergence. Additionally, if the moist static energy or its gradient between the rising and subsiding branches of the circulation could be estimated, then so could the mean flow intensity as the only remaining unknown in the vertically-integrated moist static energy budget would be $[v]$. For now, this scaling theory is probably more suited as a pedagogical model of the circulation, but it is the author's intent to continue to revisit it from time to time to see if it can be improved.

Though this work was motivated by the influence of the Hadley circulation on the surface climate of the tropics and subtropics, the zonally-resolved aspects of the circulation that project onto regional climates were not examined. However, the zonal-mean analysis has revealed that the surface zonal circulation is strongly coupled to the variability and response of the zonal-mean meridional overturning circulation. Future work can use the subtropical ridge (Choi et al., 2014) and the closed subtropical highs (Sun et al., 2017) as a framework for understanding the zonal manifestation of the Hadley circulation, its regional circulation impacts, and its impacts on surface climate and clouds. Additionally, the energy flux framework explored here can be translated to zonally-resolved circulations to quantify the regional thermodynamic processes driving and being driven by the Hadley circulation. An important consideration for future work is how these regional circulations project back onto the zonal-mean Hadley cells - on which theoretical scalings are based.

It is my hope that the work presented here tells a convincing story of the Hadley circulation, its variability, its response to forcings, and its connection to other circulations within the climate system. I also hope that the modeling technique developed here, and my own attempt at unraveling the eddy-mean flow conundrum, can be useful and instructive to others. But more than that, I hope it inspires others to improve upon this method, solve the problems I couldn't solve, and avoid the limitations that prevent this work from being more conclusive.

References

Adam, O., T. Schneider, and N. Harnik, 2014: Role of Changes in Mean Temperatures versus Temperature Gradients in the Recent Widening of the Hadley Circulation. *J. Climate*, **27**, 7450–7461, doi:10.1175/JCLI-D-14-00140.1.

Allen, R. J., and M. Kovilakam, 2017: The Role of Natural Climate Variability in Recent Tropical Expansion. *J. Climate*, doi:10.1175/JCLI-D-16-0735.1, in press.

Allen, R. J., J. R. Norris, and M. Kovilakam, 2014: Influence of anthropogenic aerosols and the Pacific Decadal Oscillation on tropical belt width. *Nature Geosci.*, **7**, 270–274, doi:10.1038/ngeo2091.

Allen, R. J., and S. C. Sherwood, 2011: The impact of natural versus anthropogenic aerosols on atmospheric circulation in the Community Atmosphere Model. *Climate Dyn.*, **36**, 1959–1978, doi:10.1007/s00382-010-0898-8.

Allen, R. J., S. C. Sherwood, J. R. Norris, and C. S. Zender, 2012: Recent Northern Hemisphere tropical expansion primarily driven by black carbon and tropospheric ozone. *Nature*, **485**, 350–354, doi:10.1038/nature11097.

Andrews, D. G., and M. E. McIntyre, 1976: Planetary Waves in Horizontal and Vertical Shear: The Generalized Eliassen-Palm Relation and the Mean Zonal Acceleration. *J. Atmos. Sci.*, **33**, 2031–2048.

Anthes, R. A., and Coauthors, 2008: The COSMIC/Formosat-3 mission: Early results. *B. Am. Meterol. Soc.*, **89**, 313–333.

Ao, C. O., and A. J. Hajj, 2013: Monitoring the width of the tropical belt with GPS radio occultation measurements. *Geophys. Res. Lett.*, **40**, 6236–6241, doi:10.1002/2013GL058203.

Archer, C. L., and K. Caldeira, 2008: Historical trends in the jet streams. *Geophys. Res. Lett.*, L08803, doi:10.1029/2008GL033614.

Barnes, E. A., and L. Polvani, 2013: Response of the Midlatitude Jets, and of Their Variability, to Increased Greenhouse Gases in the CMIP5 Models. *J. Climate*, **26**, 7117–7135, doi:10.1175/JCLI-D-12-00536.1.

Becker, E., G. Schmitz, and R. Geprägs, 1997: The feedback of midlatitude waves onto the Hadley cell in a simple general circulation model. *Tellus A*, **49**, 182–199, doi:10.1034/j.1600-0870.1997.t01-1-00003.x.

Béguin, A., O. Martius, M. Sprenger, P. Spichtinger, D. Folini, and H. Wernli, 2013: Tropopause level Rossby wave breaking in the Northern Hemisphere: a feature-based validation of the ECHAM5-HAM climate model. *Int. J. Climatol.*, **33**, 3073–3082, doi:10.1002/joc.3631.

Bengtsson, L., K. I. Hodges, and S. Hagemann, 2004: Sensitivity of the ERA40 reanalysis to the observing system: determination of the global atmospheric circulation from reduced observations. *Tellus A*, **56**, 456–471, doi:10.1111/j.1600-0870.2004.00079.x.

Birner, T., 2010: Recent widening of the tropical belt from global tropopause statistics: Sensitivities. *J. Geophys. Res.*, **115**, doi:10.1029/2010JD014664.

Birner, T., S. M. Davis, and D. J. Seidel, 2014: The changing width of Earth's tropical belt. *Phys. Today*, **67**, 38–44, doi:10.1063/PT.3.2620.

Bosilovich, M. G., and Coauthors, 2015: MERRA-2: Initial Evaluation of the Climate. *NASA/TM-2015-104606*, **43**.

Boville, B. A., 1991: Sensitivity of Simulated Climate to Model Resolution. *J. Climate*, **4**, 469–485.

Bretherton, C. S., M. Widmann, V. P. Dymnikov, J. M. Wallace, and I. Blade, 1999: The Effective Number of Spatial Degrees of Freedom of a Time-Varying Field. *J. Climate*, **12**, 1990–2009, doi:10.1175/1520-0442(1999)012⟨1990:TENOSD⟩2.0.CO;2.

Burt, M. A., D. A. Randall, and M. D. Branson, 2016: Dark Warming. *J. Climate*, **29**, 705–718, doi:10.1175/JCLI-D-15-0147.1.

Butler, A. H., D. W. J. Thompson, and R. Heikes, 2010: The Steady-State Atmospheric Circulation Response to Climate Change-like Thermal Forcings in a Simple General Circulation Model. *J. Climate*, **23**, 3474–3496, doi:10.1175/2010JCLI3228.1.

Caballero, R., 2008: Hadley cell bias in climate models linked to extratropical eddy stress. *Geophys. Res. Lett.*, **35**, L18709, doi:10.1029/2008GL035084.

Ceppi, P., and D. L. Hartmann, 2013: On the Speed of the Eddy-Driven Jet and the Width of the Hadley Cell in the Southern Hemisphere. *J. Climate*, **26**, 3450–3465, doi:10.1175/JCLI-D-12-00414.1.

Ceppi, P., Y.-T. Hwang, D. M. W. Frierson, and D. L. Hartmann, 2012: Southern Hemisphere jet latitude biases in CMIP5 models linked to shortwave cloud forcing. *Geophys. Res. Lett.*, **39**, L19708, doi:10.1029/2012GL053115.

Ceppi, P., M. D. Zelinka, and D. L. Hartmann, 2014: The response of the Southern Hemispheric eddy-driven jet to future changes in shortwave radiation in CMIP5. *Geophys. Res. Lett.*, **41**, 3244–3250, doi:10.1002/2014GL060043.

Charney, J. G., and P. G. Drazin, 1961: Propagation of planetary-scale disturbances from the lower into the upper atmosphere. *J. Geophys. Res.*, **66**, 83–109, doi:10.1029/JZ066i001p00083.

Chen, G., and I. M. Held, 2007: Phase speed spectra and the recent poleward shift of Southern Hemisphere surface westerlies. *Geophys. Res. Lett.*, **34**, L21805, doi:10.1029/2007GL031200.

Chen, S., K. Wei, W. Chen, and L. Song, 2014: Regional changes in the annual mean Hadley circulation in recent decades. *J. Geophys. Res.*, **119**, 7815–7832, doi:10.1002/2014JD021540.

Choi, J., S.-W. Son, J. Lu, and S.-K. Min, 2014: Further observational evidence of Hadley cell widening in the Southern Hemisphere. *J. Climate*, **27**, 5538–5559, doi:10.1002/2014GL059426.

Davis, N. A., and T. Birner, 2013: Seasonal to multi-decadal variability of the width of the tropical belt. *J. Geophys. Res.*, **118**, 7773–7787, doi:10.1002/jgrd.50610.

Davis, N. A., and T. Birner, 2016: Climate model biases in the width of the tropical belt. *J. Climate*, **29**, 1935–1954, doi:10.1175/JCLI-D-15-0336.1.

Davis, S. M., T. Birner, and D. Seidel, 2016: How do climate variations affect the width of the tropics? *Eos*, **97**, doi:10.1029/2016EO049309.

Davis, S. M., and K. H. Rosenlof, 2012: A Multidiagnostic Intercomparison of Tropical-Width Time Series Using Reanalyses and Satellite Observations. *J. Climate*, **25**, 1061–1078, doi:10.1175/JCLI-D-11-00127.1.

Dee, D. P., and Coauthors, 2011: The ERA-Interim reanalysis: configuration and performance of the data assimilation system. *Q. J. R. Meteorol. Soc.*, **137**, 553–597, doi:10.1002/qj.828.

Domeison, D. I. V., L. Sun, and G. Chen, 2013: The role of synoptic eddies in the tropospheric response to stratospheric variability. *Geophys. Res. Lett.*, **40**, 4933–4937, doi:10.1002/grl.50943.

Dorigo, W., R. de Jeu, D. Chung, R. Parinussa, Y. Liu, W. Wagner, and D. Fernàndez-Prieto, 2012: Evaluating global trends (1988-2010) in harmonized multi-satellite surface soil moisture. *Geophys. Res. Lett.*, **39**, L18405, doi:10.1029/2012GL052988.

Edmon, H. J., B. J. Hoskins, and M. E. McIntyre, 1980: Eliassen-Palm Cross Sections for the Troposphere. *J. Atmos. Sci.*, **37**, 2600–2616.

Eyring, V., and Coauthors, 2008: Overview of the New CCMVal Reference and Sensitivity Simulations in Support of Upcoming Ozone and Climate Assessments and the Planned SPARC CCMVal. *SPARC Newsletter*, **30**, 20–26.

Feldl, N., and S. Bordoni, 2016: Characterizing the Hadley Circulation Response through Regional Climate Feedbacks. *J. Climate*, **29**, 613–622, doi:10.1175/JCLI-D-15-0424.1.

Feng, S., and Q. Fu, 2013: Expansion of global drylands under a warmer climate. *Atmos. Chem. Phys.*, **13**, 10 081–10 094, doi:10.5194/acp-13-10081-2013.

Ferrel, W., 1856: An essay on the winds and currents of the ocean. *Nashville J. Med. and Surg.*, **11**, 287–301.

Frierson, D. M. W., 2007: The Dynamics of Idealized Convection Schemes and Their Effect on the Zonally Averaged Tropical Circulation. *J. Atmos. Sci.*, **64**, 1959–1976, doi:10.1175/JAS3935.1.

Frierson, D. M. W., I. M. Held, and P. Zurita-Gotor, 2006: A Gray-Radiation Aquaplanet Moist GCM. Part I: Static Stability and Eddy Scales. *J. Atmos. Sci.*, **63**, 2548–2566, doi:10.1175/JAS3753.1.

Frierson, D. M. W., I. M. Held, and P. Zurita-Gotor, 2007a: A Gray-Radiation Aquaplanet Moist GCM. Part II: Energy Transports in Altered Climates. *J. Atmos. Sci.*, **64**, 1680–1693, doi:10.1175/JAS3913.1.

Frierson, D. M. W., J. Lu, and G. Chen, 2007b: Width of the Hadley cell in simple and comprehensive general circulation models. *Geophys. Res. Lett.*, **34**, L18804, doi:10.1029/2007GL031115.

Fu, Q., and P. Lin, 2011: Poleward Shift of Subtropical Jets Inferred from Satellite-Observed Lower Stratospheric Temperatures. *J. Climate*, **24**, 5597–5603, doi:10.1175/JCLI-D-11-00027.1.

Garfinkel, C. I., D. W. Waugh, and L. M. Polvani, 2015: Recent Hadley cell expansion: The role of internal atmospheric variability in reconciling modeled and observed trends. *Geophys. Res. Lett.*, **42**, 10 824–10 831, doi:10.1002/2015GL066942.

Gastineau, G., H. L. Treut, and L. Li, 2008: Hadley circulation changes under global warming conditions indicated by coupled climate models. *Tellus*, **60A**, 863–884, doi:10.1111/j.1600-0870.2008.00344.x.

Gill, A. E., 1980: Some simple solutions for heat-induced tropical circulation. *Q. J. R. Meteorol. Soc.*, **106**, 447–462, doi:10.1002/qj.49710644905.

Grassi, B., G. Redaelli, P. O. Canziani, and G. Visconti, 2012: Effect of the PDO Phase on the Tropical Belt Width. *J. Climate*, **25**, 3282–3290, doi:10.1175/JCLI-D-11-00244.1.

Grise, K. M., and L. M. Polvani, 2014: Is climate sensitivity related to dynamical sensitivity? A Southern Hemisphere perspective. *Geophys. Res. Lett.*, **41**, 534–540, doi:10.1002/2013GL058466.

Grise, K. M., and L. M. Polvani, 2016: Is climate sensitivity related to dynamical sensitivity? *J. Geophys. Res.*, **121**, doi:10.1002/2015JD024687.

Grise, K. M., and L. M. Polvani, 2017: Understanding the timescales of the tropospheric circulation response to abrupt CO2 forcing in the Southern Hemisphere: Seasonality and the role of the stratosphere. *J. Climate*, in review.

Hadley, G., 1735: Concerning the cause of the general trade winds. *Phil. Trans. Roy. Soc.*, **29**, 58–62.

Hartmann, D. L., 1994: *Global Physical Climatology*. 1st ed., Academic Press, 103-113 pp.

Hawkins, E., and R. Sutton, 2009: The potential to Narrow Uncertainty in Regional Climate Predictions. *Bull. Amer. Meteor. Soc.*, **90**, 1095–1107, doi:10.1175/2009BAMS2607.1.

Held, I. M., 2000: The general circulation of the atmosphere. *2000 Program in Geophysical Fluid Dynamics*, Woods Hole, Mass., Woods Hole Oceanographic Institude, 30–36.

Held, I. M., R. S. Hemler, and V. Ramaswamy, 1993: Radiative-Convective Equilibrium with Explicit Two-Dimensional Moist Convection. *J. Atmos. Sci.*, **50**, 3909–3927, doi:10.1175/1520-0469(1993)050⟨3909:RCEWET⟩2.0.CO;2.

Held, I. M., and A. Y. Hou, 1980: Nonlinear Axially Symmetric Circulations in a Nearly Inviscid Atmosphere. *J. Atmos. Sci.*, **37**, 515–533, doi:10.1175/1520-0469(1980)037⟨0515:NASCIA⟩2.0.CO;2.

Held, I. M., and P. J. Phillipps, 1993: Sensitivity of the Eddy Momentum Flux to Meridional Resolution in Atmospheric GCMs. *J. Climate*, **6**, 499–507, doi:http://dx.doi.org/10.1175/1520-0442(1993)006⟨0499:SOTEMF⟩2.0.CO;2.

Held, I. M., and B. J. Soden, 2006: Robust Responses of the Hydrological Cycle to Global Warming. *J. Climate*, **19**, 5685–5699, doi:10.1175/JCLI3990.1.

Helm, K. P., N. L. Bindoff, and J. A. Church, 2010: Changes in the global hydrological-cycle inferred from ocean salinity. *Geophys. Res. Lett.*, **37**, L18701, doi:10.1029/2010GL044222.

Hu, Y., and Q. Fu, 2007: Observed poleward expansion of the Hadley circulation since 1979. *Atmos. Chem. Phys.*, **7**, 5229–5236, doi:10.5194/acp-7-5229-2007.

Hu, Y., L. Tao, and J. Liu, 2013: Poleward Expansion of the Hadley Circulation in CMIP5 Simulations. *Adv. in Atmos. Sci.*, **30**, 790–795, doi:10.1007/s00376-012-2187-4.

Hu, Y., C. Zhou, and J. Liu, 2011: Observational evidence for the poleward expansion of the Hadley circulation. *Adv. Atmos. Sci.*, **28**, 33–44, doi:10.1007/s00376-010-0032-1.

Hudson, R. D., 2012: Measurements of the movement of the jet streams at midlatitudes, in the Northern and Southern Hemispheres, 1979 to 2010. *Atmos. Chem. Phys.*, **12**, 7797–7808, doi:10.5194/acp-12-7797-2012.

Hudson, R. D., A. D. Frolov, M. F. Andrade, and M. B. Follette, 2003: The total ozone field separated into meteorological regimes. *J. Atmos. Sci.*, **60**, 1669–1677, doi:10.1175/1520-0469(2003)060⟨1669:TTOFSI⟩2.0.CO;2.

Huneeus, N., and Coauthors, 2014: Forcings and feedbacks in the GeoMIP ensemble for a reduction in solar irradiance and increase in CO_2. *J. Geophys. Res.*, **119**, 5226–5239, doi:10.1002/2013JD021110.

Hwang, Y.-T., and D. M. W. Frierson, 2010: Increasing atmospheric poleward energy transport with global warming. *Geophys. Res. Lett.*, **37**, L24807, doi:10.1029/2010GL045440.

Johanson, C. M., and Q. Fu, 2009: Hadley Cell Widening: Model Simulations versus Observations. *J. Climate*, **22**, 2713–2725, doi:10.1175/2008JCLI2620.1.

Juckes, M. N., 2000: The static stability of the midlatitude troposphere: the relevance of moisture. *J. Atmos. Sci.*, **57**, 3050–3057, doi:10.1175/1520-0469(2000)057⟨3050:TSSOTM⟩2.0.CO;2.

Kalnay, E., and Coauthors, 1996: The NCEP/NCAR 40-Year Reanalysis Project. *Bull. Amer. Meteor. Soc.*, **77**, 437–471, doi:10.1175/1520-0477(1996)077⟨0437:TNYRP⟩2.0.CO;2.

Kang, S. M., C. Deser, and L. M. Polvani, 2013: Uncertainty in Climate Change Projections of the Hadley Circulation: The Role of Internal Variability. *J. Climate*, **26**, 7541–7554, doi:10.1175/JCLI-D-12-00788.1.

Kang, S. M., and J. Lu, 2012: Expansion of the Hadley Cell under Global Warming: Winter versus Summer. *J. Climate*, **25**, 8387–8393, doi:10.1175/JCLI-D-12-00323.1.

Kang, S. M., and L. M. Polvani, 2011: The interannual relationship between the eddy-driven jet and the edge of the Hadley cell. *J. Climate*, **24**, 563–568, doi:10.1175/2010JCLI4077.1.

Karnauskas, K. B., and C. C. Ummenhofer, 2014: On the dynamics of the Hadley circulation and subtropical drying. *Clim. Dyn.*, 2259–2269, doi:10.1007/s00382-014-2129-1.

Kidston, J., and E. P. Gerber, 2010: Intermodel variability of the poleward shift of the austral jet stream in the CMIP3 integrations linked to biases in 20th century climatology. *Geophys. Res. Lett.*, **37**, L09708, doi:10.1029/2010GL042873.

Kidston, J., G. K. Vallis, S. M. Dean, and J. Renwick, 2011: Can an increase in the eddy length scale under global warming cause the poleward shift of the jet streams? *J. Climate*, **24**, 3764–3780.

Kim, H.-K., and S. Lee, 2001: Hadley Cell Dynamics in a Primitive Equation Model. Part II: Nonaxisymmetric Flow. *J. Atmos. Sci.*, **10**, 2859–2871.

Kobayashi, S., and Coauthors, 2015: The JRA-55 Reanalysis: General Specifications and Basic Characteristics. *J. Meteor. Soc. Japan*, **93**, 5–48, doi:10.2151/jmsj.2015-001.

Korty, R. L., and T. Schneider, 2008: Extent of Hadley circulations in dry atmospheres. *Geophys. Res. Lett.*, **35**, L23803, doi:10.1029/2008GL035847.

Kravitz, B., A. Robock, O. Boucher, H. Schmidt, K. E. Taylor, G. Stenchikov, and M. Schulz, 2011: The Geoengineering Model Intercomparison Project (GeoMIP). *Atmos. Sci. Lett.*, **12**, 162–167, doi:10.1002/asl.316.

Kushner, P. J., I. M. Held, and T. L. Delworth, 2001: Southern-hemisphere atmospheric circulation response to global warming. *J. Climate*, **14**, 2238–2249.

Kushner, P. J., and L. M. Polvani, 2004: Stratosphere-troposphere coupling in a relatively simple AGCM: The role of eddies. *J. Climate*, **17**, 629–639, doi:10.1175/JCLI4007.1.

Landu, K., L. R. Leung, S. Hagos, V. Vinoj, S. A. Rauscher, T. Ringler, and M. Taylor, 2014: The Dependence of ITCZ Structure on Model Resolution and Dynamical Core in Aquaplanet Simulations. *J. Climate*, **27**, 2375–2385, doi:10.1175/JCLI-D-13-00269.1.

Lanzante, J. R., 2005: A cautionary note on the use of error bars. *J. Climate*, **18**, 3699–3703.

Levine, X. J., and T. Schneider, 2015: Baroclinic Eddies and the Extent of the Hadley Circulation: An Idealized GCM Study. *J. Atmos. Sci.*, **72**, 2744–2761, doi:10.1175/JAS-D-14-0152.1.

Lindzen, R. S., and A. Y. Hou, 1988: Hadley Circulations for Zonally Averaged Heating Centered off the Equator. *J. Atmos. Sci.*, **45**, 2416–2427.

Lorant, V., and J.-F. Royer, 2001: Sensitivity of Equatorial Convection to Horizontal Resolution in Aquaplanet Simulations with a Variable-Resolution GCM. *Mon. Wea. Rev.*, **129**, 2730–2745, doi:10.1175/1520-0493(2001)129⟨2730:SOECTH⟩2.0.CO;2.

Lorenz, D. J., and E. T. DeWeaver, 2007: Tropopause height and zonal wind response to global warming in the IPCC scenario intergrations. *J. Geophys. Res.*, **112**, D10119, doi:10.1029/2006JD008087.

Lorenz, E. N., 1955: Available Potential Energy and the Maintenance of the General Circulation. *Tellus*, **7**, 157–167, doi:10.1111/j.2153-3490.1955.tb01148.x.

Lorenz, E. N., 1967: The nature and theory of the general circulation of the atmosphere. *Geneva: World Meteorological Organization*, pp. 161.

Lu, J., G. Chen, and D. M. W. Frierson, 2008: Response of the Zonal Mean Atmospheric Circulation to El Niño versus Global Warming. *J. Climate*, **21**, 5835–5851, doi:10.1175/2008JCLI2200.1.

Lu, J., C. Deser, and T. Reichler, 2009: Cause of the widening of the tropical belt since 1958. *Geophys. Res. Lett.*, L03802, doi:10.1029/2008GL036076.

Lu, J., G. A. Vecchi, and T. Reichler, 2007: Expansion of the Hadley cell under global warming. *Geophys. Res. Lett.*, **118**, L06805, doi:10.1029/2006GL028443.

Lucas, C., and H. Nguyen, 2015: Regional characteristics of tropical expansion and the role of climate variability. *J. Geophys. Res.*, **120**, 6809–6824, doi:10.1002/2015JD023130.

Lucas, C., H. Nguyen, and B. Timbal, 2012: An observational analysis of Southern Hemisphere tropical expansion. *J. Geophys. Res.*, **117**, D17112, doi:10.1029/2011JD017033.

Lucas, C., B. Timbal, and H. Nguyen, 2014: The expanding tropics: a critical assessment of the observational and modeling studies. *WIREs Clim. Change*, **5**, 89–112, doi:10.1002/wcc.251.

Manabe, S., and R. T. Wetherald, 1967: Thermal Equilibrium of the Atmosphere with a Given Distribution of Relative Humidity. *J. Atmos. Sci.*, **24**, 241–259, doi:10.1175/1520-0469(1967)024⟨0241:TEOTAW⟩2.0.CO;2.

Maycock, A. C., M. M. Joshi, K. P. Shine, and A. A. Scaife, 2013: The Circulation Response to Idealized Changes in Stratospheric Water Vapor. *J. Climate*, **26**, 545–561, doi:10.1175/JCLI-D-12-00155.1.

McLandress, C., T. G. Shepherd, J. F. Scinocca, D. A. Plummer, M. Sigmond, A. I. Jonsson, and M. C. Reader, 2011: Separating the Dynamical Effects of Climate Change and Ozone Depletion. Part II: Southern Hemisphere Troposphere. *J. Climate*, **24**, 1850–1868, doi:10.1175/2010JCLI3586.1.

Miller, R. L., G. A. Schmidt, and D. T. Shindell, 2006: Forced annular variations in the 20th century Intergovernmental Panel on Climate Change Fourth Assessment Report models. *J. Geophys. Res.*, **111**, D18101, doi:10.1029/2005JD006323.

Min, S.-K., and S.-W. Son, 2013: Multimodel attribution of the Southern Hemisphere Hadley cell widening: Major role of ozone depletion. *J. Geophys. Res.*, **118**, 3007–3015, doi:10.1002/jgrd.50232.

Mitas, C. M., and A. Clement, 2006: Recent behavior of the Hadley cell and tropical thermodynamics in climate models and reanalyses. *Geophys. Res. Lett.*, **33**, L01810, doi:10.1029/2005GL024406.

National Research Council, 2015: *Climate Intervention: Reflecting Sunlight to Cool Earth.* Washington, D. C., doi:10.17226/18988.

Neelin, J. D., and I. M. Held, 1987: Modeling Tropical Convergence Based on the Moist Static Energy Budget. *Mon. Wea. Rev.*, **115**, 3–12, doi:10.1175/1520-0493(1987)115⟨0003:MTCBOT⟩2.0.CO;2.

New, M., M. Todd, M. Hulme, and P. Jones, 2001: Precipitation measurements and trends in the twentieth century. *Int. J. Climatol.*, **21**, 1899–1922, doi:10.1002/joc.680.

Nguyen, H., A. Evans, C. Lucas, I. Smith, and B. Timbal, 2013: The Hadley circulation in reanalyses: climatology, variability and expansion. *J. Climate*, **26**, 3357–3376, doi:10.1175/JCLI-D-12-00224.1.

Nguyen, H., C. Lucas, A. Evans, B. Timbal, and L. Hanson, 2015: Expansion of the Southern Hemisphere Hadley Cell in REsponse to Greenhouse Gas Forcing. *J. Climate*, **28**, 8067–8077, doi:0.1175/JCLI-D-15-0139.1.

Numaguti, A., 1993: Dynamics and Energy Balance of the Hadley Circulation and the Tropical Precipitation Zones: Significance of the Distribution of Evaporation. *J. Atmos. Sci.*, **50**, 1874–1887, doi:10.1175/1520-0469(1993)050⟨1874:DAEBOT⟩2.0.CO;2.

Phillips, N. A., 1951: A simple three-dimensional model for the study of larger-scale extratropical flow patterns. *J. Meteor.*, **8**, 381–394, doi:10.1175/1520-0469(1951)008⟨0381:ASTDMF⟩2.0.CO;2.

Pierrehumbert, R. T., 1995: Thermostats, Radiator Fins, and the Local Runaway Greenhouse. *J. Atmos. Sci.*, **52**, 1784–1806, doi:10.1175/1520-0469(1995)052⟨1784:TRFATL⟩2.0.CO;2.

Pithan, F., and T. Mauritsen, 2014: Arctic amplification dominated by temperature feedbacks in contemporary climate models. *Nat. Geosci.*, **7**, 181–184, doi:10.1038/ngeo2071.

Polvani, L. M., and P. J. Kushner, 2002: Tropospheric response to stratospheric perturbations in a relatively simple general circulation model. *Geophys. Res. Lett.*, **29**, L014284, doi:10.1029/2001GL014284.

Polvani, L. M., M. Previdi, and C. Deser, 2011a: Large cancellation, due to ozone recory, of future Southern Hemisphere atmospheric circulations trends. *Geophys. Res. Lett.*, **38**, L04707, doi:10.1029/2011GL046712.

Polvani, L. M., D. W. Waugh, G. J. P. Correa, and S.-W. Son, 2011b: Stratospheric ozone depletion: the main driver of 20th Century atmospheric circulation changes in the Southern Hemisphere. *J. Climate*, **24**, 795–812, doi:10.1175/2010JCLI3772.1.

Quan, X.-W., M. P. Hoerling, J. Perlwitz, H. F. Diaz, and T. Xu, 2014: How fast are the tropics expanding? *J. Climate*, **27**, 1999–2013, doi:10.1175/JCLI-D-13-00287.1.

Rauscher, S., T. Ringler, W. Skamarock, and A. Mirin, 2012: Exploring a Global Multi-Resolution Modeling Approach Using Aquaplanet Simulations. *J. Climate*, **26**, 2432–2452, doi:10.1175/JCLI-D-12-00154.1.

Richter, I., and S.-P. Xie, 2008: Muted precipitation increase in global warming simulations: A surface evaporation perspective. *J. Geophys. Res.*, **113**, doi:10.1029/2008JD010561, d24118.

Riehl, H., and J. S. Malkus, 1958: On the heat balance in the equatorial trough zone. *Geophysica*, **6**, 503–538.

Rienecker, M. M., and Coauthors, 2011: MERRA - NASA's Modern-Era Retrospective Analysis for Research and Applications. *J. Climate*, **24**, 3624–3648, doi:10.1175/JCLI-D-11-00015.1.

Romps, D. M., 2011: Response of Tropical Precipitation to Global Warming. *J. Atmos. Sci.*, **68**, 123–138, doi:10.1175/2010JAS3542.1.

Saha, S., and Coauthors, 2010: The NCEP Climate Forecast System Reanalysis. *Bull. Amer. Meteor. Soc.*, **91**, 1015–1057, doi:10.1175/2010BAMS3001.1.

Santer, B. D., and Coauthors, 2008: Consistency of modelled and observed temperature trends in the tropical troposphere. *Int. Jour. Climat.*, **28**, 1703–1722, doi:10.1002/joc.1756.

Scheff, J., and D. M. W. Frierson, 2012: Robust future precipitation declines in CMIP5 largely reflect the poleward expansion of model subtropical dry zones. *Geophys. Res. Lett.*, **39**, L18704, doi:10.1029/2012GL052910.

Schneider, T., 2006: The general circulation of the atmosphere. *Ann. Rev. of Earth and Plan. Sci.*, **34**, 655–688, doi:10.1146/annurev.earth.34.031405.125144.

Schneider, T., and S. Bordoni, 2008: Eddy-Mediated Regime Transitions in the Seasonal Cycle of a Hadley Circulation and Implications for Monsoon Dynamics. *J. Atmos. Sci.*, **65**, 915–933, doi:10.1175/2007JAS2415.1.

Seidel, D. J., Q. Fu, W. J. Randel, and T. J. Reichler, 2008: Widening of the tropical belt in a changing climate. *Nat. Geoscience*, **1**, 21–24, doi:10.1038/ngeo.2007.38.

Seidel, D. J., and W. J. Randel, 2007: Recent widening of the tropical belt: Evidence from tropopause observations. *J. Geophys. Res.*, **112**, D20113, doi:10.1029/2007JD008861.

Seo, K.-H., D. M. W. Frierson, and J.-H. Son, 2014: A mechanism for future changes in Hadley circulation strength in CMIP5 climate change simulations. *Geophys. Res. Lett.*, **40**, 5251–5258, doi:10.1002/2014GL060868.

Shaw, T. A., and A. Voigt, 2015: Tug of war on summertime circulation between radiative forcing and sea surface warming. *Nat. Geosci.*, **8**, 560–566, doi:10.1038/ngeo2449.

Shepherd, T. G., and C. McLandress, 2010: A Robust Mechanism for Strengthening of the Brewer-Dobson Circulation in Response to Climate Change. *J. Atmos. Sci.*, **68**, 784–797, doi:10.1175/2010JAS3608.1.

Simmons, A. J., and D. M. Burridge, 1981: An Energy and Angular-Momentum Conserving Vertical Finite-Difference Scheme and Hybrid Vertical Coordinates. *Mon. Wea. Rev.*, **40**, 758–766, doi:10.1175/1520-0493(1981)109⟨0758:AEAAMC⟩2.0.CO;2.

Sobel, A. H., and T. Schneider, 2009: Single-layer axisymmetric model for a Hadley circulation with parameterized eddy momentum forcing. *J. Adv. Model. Earth Syst.*, **1**, doi:10.3894/JAMES.2009.1.10, 10.

Solomon, A., L. M. Polvani, D. W. Waugh, and S. M. Davis, 2016: Contrasting upper and lower atmospheric metrics of tropical expansion in the Southern Hemisphere. *Geophys. Res. Lett.*, **43**, 10,496–10,503, doi:10.1002/2016GL070917.

Son, S.-W., N. F. Tandon, L. M. Polvani, and D. W. Waugh, 2009: Ozone hole and Southern Hemisphere climate change. *Geophys. Res. Lett.*, **36**, L15605, doi:10.1029/2009GL038671.

Stachnik, J. P., and C. Schumacher, 2011: A comparison of the Hadley circulation in modern reanalyses. *J. Geophys. Res.*, **116**, D22102, doi:10.1029/2011JD016677.

Staten, P. W., K. M. Grise, and S. M. Davis, 2016: The Width of the Tropics: Climate Variations and Their Impacts. *SPARC Newsletter*, **46**, 26–31.

Staten, P. W., and T. Reichler, 2014: On the ratio between shifts in the eddy-driven jet and the Hadley cell edge. *Climate Dyn.*, **42**, 1229–1242, doi:10.1007/s00382-013-1905-7.

Sun, X. J., P. X. Wang, and J. X. L. Wang, 2017: An assessment of the atmospheric centers of action in the northern hemisphere winter. *Clim. Dyn.*, **48**, 1031?1047, doi:10.1007/s00382-016-3126-3.

Swart, N. C., and J. C. Fyfe, 2012: Observed and simulated changes in the Southern Hemisphere surface westerly wind-stress. *Geophys. Res. Lett.*, **39**, L16711, doi:10.1029/2012GL052810.

Tandon, N. F., E. P. Gerber, A. H. Sobel, and L. M. Polvani, 2013: Understanding Hadley Cell expansion versus contraction: insights from simplified models and implications for recent observations. *J. Climate*, **26**, 4304–4321, doi:10.1175/JCLI-D-12-00598.1.

Tandon, N. F., L. M. Polvani, and S. M. Davis, 2011: The response of the tropospheric circulation to water vapor-like forcings in the stratosphere. *J. Climate*, **24**, 5713–5720, doi:10.1175/JCLI-D-11-00069.1.

Tao, L., Y. Hu, and J. Liu, 2015: Anthropogenic forcing on the Hadley circulation in CMIP5 simulations. *Clim. Dynamics*, doi:10.1007/s00382-015-2772-1.

Taylor, K. E., R. J. Stouffer, and G. A. Meehl, 2012: An overview of CMIP5 and the experiment design. *B. Am. Meteorol. Soc.*, **93**, 485–498, doi:10.1175/BAMS-D-11-00094.1.

Thuburn, J., and G. C. Craig, 1997: GCM Tests of Theories for the Height of the Tropopause. *J. Atmos. Sci.*, **54**, 869–882, doi:10.1175/1520-0469(1997)054⟨0869:GTOTFT⟩2.0.CO;2.

Trenberth, K., J. Fasullo, and J. Kiehl, 2009: Earth's global energy budget. *Bull. Amer. Meteor. Soc.*, **90**, 311–323, doi:10.1175/2008BAMS2634.1.

Trenberth, K. E., and A. Solomon, 1994: The global heat balance: heat transports in the atmosphere and ocean. *Climate Dynamics*, **10**, 107–134, doi:10.1007/BF00210625.

Trenberth, K. E., and D. P. Stepaniak, 2003: Seamless poleward atmospheric energy transports and implications for the Hadley circulation. *J. Climate*, **16**, 3706–3722, doi:10.1175/1520-0442(2003)016⟨3706:SPAETA⟩2.0.CO;2.

Trenberth, K. E., D. P. Stepaniak, J. W. Hurrell, and M. Fiorino, 2001: Quality of Reanalyses in the Tropics. *J. Climate*, **14**, 1499–1510, doi:10.1175/1520-0442(2001)014⟨1499:QORITT⟩2.0.CO;2.

Vallis, G. K., 2006: *Atmospheric and Oceanic Fluid Dynamics*. 5th ed., Cambridge University Press, 51-62 pp.

Vallis, G. K., P. Zurita-Gotor, C. Cairns, and J. Kidston, 2015: Response of the large-scale structure of the atmosphere to global warming. *Q.J.R. Meteorol. Soc.*, **141**, 1479–1501, doi:10.1002/qj.2456.

Vecchi, G. A., and B. J. Soden, 2007: Global warmng and the weakening of the tropical circulation. *J. Climate*, **20**, 4316–4340, doi:10.1175/JCLI4258.1.

Voigt, A., and T. A. Shaw, 2015: Circulation response to warming shaped by radiative changes of clouds and water vapour. *Nat. Geosci.*, **8**, 102–106, doi:10.1038/ngeo2345.

Waliser, D. E., Z. Shi, J. R. Lanzante, and A. H. Oort, 1999: The Hadley circulation: assessing NCEP/NCAR reanalysis and sparse in-situ estimates. *Clim. Dynamics*, **15**, 719–735.

Waugh, D. W., C. I. Garfinkel, and L. M. Polvani, 2015: Drivers of the Recent Tropical Expansion in the Southern Hemisphere: Changing SSTs or Ozone Depletion? *J. Climate*, **28**, 6581–6586, doi:10.1175/JCLI-D-15-0138.1.

White, A. A., and N. Wood, 2012: Consistent approximate models of the global atmosphere in non-spherical geopotential coordinates. *Q. J. R. Meteorol. Soc.*, **138**, 980–988, doi:10.1002/qj.972.

Wilcox, L. J., B. J. Hoskins, and K. P. Shine, 2011: A global blended tropopause based on ERA data. Part II: Trends and tropical broadening. *Quart. J. Roy. Meteor. Soc.*, **138**, 576–584, doi:10.1002/qj.910.

Wu, Y., and T. A. Shaw, 2016: The impact of the Asian summer monsoon circulation on the tropopause. *J. Climate*, doi:10.1175/JCLI-D-16-0204.1.

Yin, J. H., 2005: A consistent poleward shift of the storm tracks in simulations of 21st century climate. *Geophys. Res. Lett.*, **32**, L18701, doi:10.1029/2005GL023684.

Yu, J., and J. D. Neelin, 1997: Analytic Approximations for Moist Convectively Adjusted Regions. *J. Atmos. Sci.*, **54**, 1054–1063, doi:10.1175/1520-0469(1997)054⟨1054:AAFMCA⟩2.0.CO;2.

Zhang, X., F. W. Zwiers, G. C. Hegerl, F. H. Lambert, N. P. Gillett, S. Solomon, P. A. Stott, and T. Nozawa, 2007: Detection of human influence on twentieth-century precipitation trends. *Nature*, **448**, 461–465, doi:10.1038/nature06025.

Zhou, Y. P., K.-M. Xu, Y. C. Sud, and A. K. Betts, 2011: Recent trends of the tropical hydrological cycle inferred from Global Precipitation Climatology Project and Internaional Satellite Cloud Climatology Project data. *J. Geophys. Res.*, **116**, D09101, doi:10.1029/2010JD015197.

Appendix: Governing Physics and Description of the Idealized Gray Radiation Aquaplanet Model (GRAM)

The following sections detail the governing physics behind GRAM (and general circulation models in general), its parameterizations, and modifications that have been made to the model, including the ozone parameterization.

1 Newton's First Law and the Material Derivative on a Rotating Earth

The physics governing all atmospheric circulations can be condensed into Newton's First Law, which states that the acceleration of a given mass is proportional to the forces acting upon it,

$$\frac{Du}{Dt} = \sum_{j=1}^{J} (F_j) \tag{1}$$

where u is the velocity, $\frac{D}{Dt}$ is the acceleration following the flow, and the right-hand side is the sum of J body forces F_j acting on the fluid. In this formulation the density factor is implicit as the forces F_j are per unit mass. As atmospheric circulations are studied relative to fixed positions on the rotating earth, rather than in a fixed inertial frame relative to the stars, a transformation must be made to account for the apparent forces acting on the flow.

Consider a vector $\vec{A}$ with fixed length rotating around an axis in space with angular velocity Ω. In the rotating frame the vector is stationary, but in the intertial frame, the

vector's position changes as[6]

$$\left(\frac{D\vec{A}}{Dt}\right)_i = \Omega \times \vec{A} \tag{2}$$

where i indicates the acceleration in the inertial frame of reference. $\Omega \times \vec{A}$ can be understood as the acceleration vector for rotation about an axis at a fixed radius, at all times pointing in "the direction of rotation" so as to advance the rotating frame of reference at angular velocity Ω in the inertial frame. The rate of change of a vector $\vec{B}$ allowed to change in both the inertial and rotating frame of reference is thus given by

$$\left(\frac{D\vec{B}}{Dt}\right)_i = \left(\frac{D\vec{B}}{Dt}\right)_r + \Omega \times \vec{B} \tag{3}$$

where r indicates the acceleration in the rotating frame of reference. Eq. 3 relates positions, velocities, and forces in the two frames of reference and can be used to apply the equations of motions to fluids on the rotating earth. Applying to the position vector r of a mass rotating in space, we find

$$\left(\frac{D\vec{r}}{Dt}\right)_i = \left(\frac{D\vec{r}}{Dt}\right)_r + \Omega \times \vec{r} \tag{4}$$

Noting that the derivative of position is velocity, this can be written as

$$\vec{v_i} = \vec{v_r} + \Omega \times \vec{r} \tag{5}$$

where v_i is the velocity relative to fixed position in space and v_r is the velocity relative to

[6]This discussion follows from Vallis (2006)

the rotating frame of reference. Similarly applying Eq. 3 to v_r and using Eq. 5, it can be shown that

$$\left(\frac{D\vec{v_i}}{Dt}\right)_i = \left(\frac{D\vec{v_r}}{Dt}\right)_r + 2\Omega \times v_r - \Omega^2\vec{r} \tag{6}$$

The second term on the right-hand side is the Coriolis acceleration and the third term is the centrifugal acceleration. Both are so-called "apparent" forces in the rotating frame of reference, because they can only accelerate a moving object and not a stationary object.

2 Governing Equations

Returning to Eq. 1, consider flow in the earth's atmosphere with the pressure gradient force, gravity, and friction as the relevant forces,

$$\frac{D\vec{v_i}}{Dt} = -\frac{1}{\rho}\nabla p - \nabla\phi_g + \vec{F} \tag{7}$$

where ρ is the density, p is the pressure, ϕ_g is the gravitational potential, $\vec{F}$ includes friction and other non-conservative forces, and $\vec{v} = (u, v, w)$ is the vector wind in the rotating frame of reference . Applying Eq. 6, the rate of change of velocity in the rotational frame of reference is given by

$$\frac{D\vec{v}}{Dt} = -\frac{1}{\rho}\nabla p - \nabla\phi_{g^*} + \vec{F} - 2\Omega \times \vec{v} \tag{8}$$

where ϕ_{g^*} is the apparent gravitational potential that includes the centrifugal acceleration, and the r subscript on the velocities has been dropped. In expanded form these three equations govern the zonal, meridional, and vertical flows in the atmosphere and are a

statement of conservation of momentum in three dimensions. In spherical coordinates, the expanded form of the equations is[7]

$$\frac{Du}{Dt} = 2\Omega \sin(\phi)v - 2\Omega \cos(\phi)w + \frac{uv \tan(\phi)}{r} - \frac{uw}{r} - \frac{1}{\rho r \cos(\phi)} \frac{\partial p}{\partial \lambda} + F_\lambda \tag{9}$$

$$\frac{Dv}{Dt} = -2\Omega \sin(\phi)u - \frac{u^2 \tan(\phi)}{r} - \frac{vw}{r} - \frac{1}{\rho r} \frac{\partial p}{\partial \phi} + F_\phi \tag{10}$$

$$\frac{Dw}{Dt} = 2\Omega \cos(\phi)u + \frac{u^2 + v^2}{r} - \frac{1}{\rho} \frac{\partial p}{\partial r} - g + F_r \tag{11}$$

where ϕ and λ are latitude and longitude, r is the distance from the center of the earth, and the material derivative is given by

$$\frac{D}{Dt} = \frac{u}{r \cos(\phi)} \frac{\partial}{\partial \lambda} + \frac{v}{r} \frac{\partial}{\partial \phi} + w \frac{\partial}{\partial r} \tag{12}$$

Eq.'s 9-11 are the primitive equations. For flows in which the characteristic horizontal scale is much larger than the characteristic vertical scale, it is appropriate to make the hydrostatic approximation and rewrite Eq. 11 as

$$\frac{\partial p}{\partial z} = -\rho g_0 \tag{13}$$

which states that the vertical pressure gradient force balances the weight of the atmosphere. The gravitational acceleration is approximated as $g_0 = 9.81$ m/s^2, as the variations in the acceleration due to gravity in the vertical are small relative to its mean value at the earth's surface.

[7]This discussion follows from "The Spectral Dynamical Core" hosted at `https://www.gfdl.noaa.gov/wp-content/uploads/files/user_files/pjp/spectral_core.pdf`

However, to conserve energy, both the horizontal Coriolis accelerations and the metric terms involving vertical motion in the zonal and meridional momentum equations must be neglected or else they will act as spurious sources or sinks that would have otherwise been balanced by the neglected terms in Eq. 11. To conserve angular momentum, r must also be replaced with $a = 6.371 \times 10^6$ m, the mean radius of the earth. The resulting equations for u and v form the basis of the dynamical core of the model and are referred to as the shallow atmosphere hydrostatic primitive equations (White and Wood, 2012),

$$\frac{Du}{Dt} = 2\Omega \sin(\phi)v + \frac{uv\tan(\phi)}{a} - \frac{1}{\rho a \cos(\phi)}\frac{\partial p}{\partial \lambda} \tag{14}$$

$$\frac{Dv}{Dt} = -2\Omega \sin(\phi)u + \frac{u^2\tan(\phi)}{a} - \frac{1}{\rho a}\frac{\partial p}{\partial \phi} \tag{15}$$

Two more equations for ρ and p are necessary to form a complete solution and model the evolution of the atmosphere. An obvious constraint is that the circulation conserve mass, which is satisfied via the continuity equation,

$$\frac{D\rho}{Dt} = -\rho \nabla \cdot \vec{v} \tag{16}$$

which balances changes in the density following the flow with convergence or divergence.

Some constraint on the thermodynamics is also needed. The First Law of thermodynamics in general form is

$$\frac{D\mathbf{U}}{Dt} = \mathbf{Q} + \mathbf{W} \tag{17}$$

where **U** is the internal energy of an air parcel, **Q** is the diabatic heating of an air parcel, **W** is the work done on the air parcel, and bold font indicates extensive variables. Air parcels are allowed to expand or contract in response to diabatic heating or internal energy changes. These volume changes lead to density changes which drive vertical motion. Assuming pressure is instantaneously adjusted in a rising or sinking parcel, we approximate the First Law with the isobaric form,

$$\mathbf{Q} = \frac{D\mathbf{U}}{Dt} + p\frac{D\mathbf{V}}{Dt} \tag{18}$$

where **V** is the volume of the air parcel. The enthalpy of an air parcel is the sum of its internal energy and the energy (work) necessary to displace the environment, or $\mathbf{H} = \mathbf{U} + p\mathbf{V} = \frac{c_p}{\mathbf{m}}T$, where **m** is the mass of the air parcel, c_p is the specific heat of dry air, and T is the temperature. By applying this to Eq. 18, it can be shown that

$$c_p\frac{DT}{Dt} = Q + \frac{1}{\rho}\frac{Dp}{Dt} \tag{19}$$

where Q is the heating per unit mass. This is referred to as the thermodynamic energy equation.

Eq.'s 14, 15, 16, 19 form a set of four prognostic equations for u, v, ρ, and T, with p determined diagnostically through the Ideal Gas Law. To simplify the numerics of the model, we transform these equations into pressure coordinates. In the momentum equations the pressure gradient takes the form of the gradient of the geopotential $\Phi = g_0 z$, while the vertical motion is now defined as the pressure velocity ω in the material derivative,

$$\frac{Du}{Dt} = 2\Omega \sin(\phi)v + \frac{uv\tan(\phi)}{a} - \frac{1}{a\cos(\phi)}\frac{\partial \Phi}{\partial \lambda} + F_\lambda \tag{20}$$

$$\frac{Dv}{Dt} = -2\Omega \sin(\phi)u + \frac{u^2\tan(\phi)}{a} - \frac{1}{a}\frac{\partial \Phi}{\partial \phi} + F_\phi \tag{21}$$

$$\frac{D}{Dt} = \frac{u}{r\cos(\phi)}\frac{\partial}{\partial \lambda} + \frac{v}{r}\frac{\partial}{\partial \phi} + \omega\frac{\partial}{\partial p} \tag{22}$$

The continuity equation takes on a simpler form,

$$\frac{\partial \omega}{\partial p} + \nabla \cdot \vec{v_h} = 0 \tag{23}$$

where $\vec{v_h} = (u, v)$. Integrating Eq. 23 from the surface to the top of the atmosphere yields a prognostic equation for the surface pressure (p_s) tendency,

$$\frac{\partial p_s}{\partial t} = -\nabla \cdot \int_0^{p_s} \vec{v}_h dp \tag{24}$$

Hydrostatic balance can be written in terms of the geopotential,

$$\frac{\partial \Phi}{\partial ln(p)} = -R_d T \tag{25}$$

Finally, a more useful form of Eq. 19 is found by applying the Ideal Gas Law and noting that $\omega = \frac{Dp}{Dt}$,

$$\frac{DT}{Dt} = \frac{R_d T\omega}{c_p p} + \frac{Q}{c_p} \tag{26}$$

where $R_d = 287$ J/kg·K is the specific gas constant for dry air. Eq.'s 20, 21, 23, 24, 25, and 26 constitute the set of equations solved by the dynamical core of the model. In the

following sections[8], we will discuss the surface, the boundary layer, and the radiation schemes, and other physical parameterizations.

3 Surface Properties

The surface of the model is an ocean mixed-layer with no internal dynamics, a so-called "slab" ocean. It has no physical depth, but instead has a specified heat capacity and a single temperature that is allowed to interact with the atmosphere through radiative, sensible, and latent heat fluxes. The governing equation for this mixed-layer ocean is

$$C_o \frac{\partial T_o}{\partial t} = R_{SW} - R_{LW,up} + R_{LW,dn} - L_v E - S \tag{27}$$

where $C_o = 1 \times 10^7$ J/K·m^2 is the mixed-layer heat capacity, R_{SW} is the net shortwave flux, $R_{LW,up}$ the upward longwave flux, $R_{LW,dn}$ the downward longwave flux, $L_v = 2.5 \times 10^6$ J/kg the latent heat of vaporization, E the evaporative flux, and S the sensible heat flux. The mixed-layer heat capacity corresponds to a depth of 2.5 m. While this is small in relation to the depth of earth's real oceanic mixed layer it allows the modeled climate to adjust within a reasonable time frame.

4 Surface Fluxes

The evaporative and sensible heat fluxes and the surface stress are parameterized using standard bulk formulas,

$$E = \rho C |\vec{v_h}| (q_a - q_s^*) \tag{28}$$

[8]This discussion follows the models details in (Frierson et al., 2006).

$$S = \rho c_p C |\vec{v_h}| (\theta_a - \theta_s) \tag{29}$$

$$(\tau_\lambda, \tau_\phi) = \rho C |\vec{v_h}| \vec{v_h} \tag{30}$$

where C is the drag coefficient, q_a the specific humidity of the lowest model level, q_s^* the saturation specific humidity at the ocean surface temperature, θ_a the potential temperature of the lowest model level, θ_s the potential temperature of the ocean surface. The density and horizontal wind vector are evaluated at the lowest model level. Potential temperature is defined as $\theta = T(p_0/p)^{R_d/c_p}$ with $p_0 = 1000$ hPa.

For the axisymmetric simulations to remain stable, a constant gustiness parameter is added to the wind speed in the bulk flux formulas for all experiments to ensure that the fluxes do not go to zero when the surface wind speed approaches zero outside of the axisymmetric Hadley cells. The wind speed magnitude is defined by $|\vec{v_h}| = \sqrt{u^2 + v^2 + v_{gust}^2}$, where v_{gust} is a constant, arbitrary wind speed. This gustiness parameter is set to 3 m/s in the axisymmetric simulations as the surface fluxes would otherwise vanish (with no eddy fluxes there is no mechanism to maintain surface winds). Gustiness is set to 3 m/s in the non-axisymmetric simulations for continuity with the axisymmetric simulations.

The drag coefficient is parameterized using a simplified Monin-Obukhov similarity theory, a closure scheme for the turbulence and flow in the surface layer, and is defined as

$$C = \begin{cases} \kappa^2 \left(ln(\frac{z_a}{z_0}) \right)^{-2} & \text{for } Ri_a < 0 \\ \kappa^2 \left(ln(\frac{z_a}{z_0}) \right)^{-2} \left(1 - \frac{Ri_a}{Ri_c} \right)^2 & \text{for } 0 > Ri_a > Ri_c \\ 0 & \text{for } Ri_a > Ri_c \end{cases} \tag{31}$$

where κ is the von Karman constant, z_a is the height of the lowest model level, z_0 is the surface roughness length, and Ri_a and Ri_c are the bulk Richardson and critical Richardson numbers for the surface layer. The von Karman constant sets the logarithmic scaling of velocity with height in the surface layer, while the roughness length is the height at which the wind speed is zero in the surface layer, here taken to be 3.21 $\times 10^{-5}$ m as in Frierson et al. (2006).

The bulk Richardson number is the ratio of buoyant dissipation of turbulence to the generation of turbulence by vertical shear,

$$Ri_a = \frac{g_0 z (c_p (T_a - T_s) + g z_a)}{c_p T_s |v(z_a)|^2} \tag{32}$$

where T_a and T_s are the temperature of the surface layer and the mixed layer and z_a is the height of the lowest model level. Physically, the bulk Richardson number parameterizes the magnitude of turbulence in the surface layer. As the bulk Richardson number approaches the critical Richardson number, the turbulent mixing of momentum, heat, and moisture decreases to zero as static stability overwhelms shear production.

5 Diffusivity

The planetary boundary layer height h is parameterized as the level where the Richardson number exceeds the critical Richardson number, $Ri(z) \geq Ri_c$. Within the boundary layer, the surface layer is set to occupy a fraction f_b of the boundary layer depth, here taken to be 0.1. Vertical diffusive fluxes of heat, momentum, moisture and other tracers are assumed to be constant within the surface layer and decrease to zero at the boundary layer top, with the diffusivity coefficients satisfying

$$K(z) = \begin{cases} K_b(z) & \text{for } z < f_b h \\ K_b(f_b h)\frac{z}{f_b h}\left[1 - \frac{z - f_b h}{(1-f_b)h}\right]^2 & \text{for } f_b h < z < h \end{cases} \tag{33}$$

and in the surface layer satisfying

$$K_b(z) = \begin{cases} \kappa u_a \sqrt{C} z & \text{for } Ri_a < 0 \\ \kappa u_a \sqrt{C} z \left[1 + \frac{Ri}{Ri_c}\frac{ln(z/z_0)}{1 - Ri/Ri_c}\right]^{-1} & \text{for } Ri_a > 0 \end{cases} \tag{34}$$

where the coefficient and parameters are as before and the subscript a denotes values in the lowest model level. Dry static energy rather than temperature is diffused vertically so that the scheme conserves energy. The heating due to this vertical diffusion is given by

$$Q_{diff} = \frac{c_p}{\rho}\frac{\partial}{\partial z}\left[K(z)\rho\frac{T}{\theta}\frac{\partial \theta}{\partial z}\right] \tag{35}$$

The momentum tendency due to diffusion is

$$\left(\frac{\partial u}{\partial t}_{diff}, \frac{\partial v}{\partial t}_{diff}\right) = \frac{1}{\rho}\frac{\partial}{\partial z}\left[K(z)\rho\frac{\partial(u,v)}{\partial z}\right] \tag{36}$$

Specific humidity and any other tracers are diffused similarly. There is no diffusion in the free atmosphere of the model. For the axisymmetric simulations, this is analogous to the "nearly-inviscid" axisymmetric simulations in Held and Hou (1980).

6 Moisture

A unique feature of this model is the ability to simulate water vapor transport and large scale condensation. Water vapor enters the atmosphere through the evaporative flux at the surface. The saturation vapor pressure is defined as

$$e^*(T) = f_{e_0} \cdot e_0^* \exp\left[-\frac{L_v}{R_v}\left(\frac{1}{T} - \frac{1}{T_0}\right)\right] \tag{37}$$

where $e_0^* = 610.78$ Pa is the saturation vapor pressure at 273.16 K, $R_v = 461.5$ J/kg·K is the gas constant for water vapor, and f_{e_0} is a constant that can be varied to artificially modulate the saturation vapor pressure. Water vapor is a passive tracer in the model until a grid box reaches or exceeds saturation. At this point, the specific humidity is adjusted so that only the water vapor that exceeds saturation is condensed,

$$\delta q_{lsc} = \frac{q^* - q}{1 + \frac{L_v}{c_p}\frac{dq^*}{dT}} \tag{38}$$

where q and q^* are the specific humidity and saturation specific humidity and δq_{lsc} is the specific humidity "removed" by large-scale condensation. The latter can be used to directly calculate the condensational heating in the grid box. The condensed vapor is assumed to immediately convert to precipitation and fall out of the grid box. However, the precipitation is re-evaporated by any unsaturated grid boxes below so that only saturated columns can produce surface precipitation.

7 Convective Adjustment

Solar heating of earth's surface produces convection which redistributes heat and temporarily stabilizes the atmosphere against further overturning. If one considers the atmosphere as composed of discrete parcels of air, vertical instabilities to dry and moist convection can only be realized when individual parcels are perturbed in the vertical. This process generally occurs at scales much smaller than the grid scale and must be parameterized.

In dry experiments, when the potential temperature of a layer at pressure p_t is less than the potential temperature of the layer below at pressure p_b, the potential temperature of both layers is adjusted to

$$\theta_{final} = \frac{\int_{p_b}^{p_t} T dp}{\int_{p_b}^{p_t} \left(\frac{p}{p_0}\right)^{R_d/c_p} dp} \tag{39}$$

so that the final lapse rate is neutral to dry convection and the scheme conserves energy.

In earth's atmosphere, latent heating by convection is a substantial fraction of the energy transferred from the surface to the atmosphere (Trenberth et al., 2009). Moist

convection plays an especially crucial role in vertically distributing heat and water vapor in the axisymmetric experiments as there is neither a meridional circulation nor baroclinic wave activity necessary to produce large-scale ascent. While the model can be run with large-scale condensation alone, this produces significant grid size sensitivities in the tropics (Frierson et al., 2006). To eliminate these sensitivities a simplified Betts-Miller moist convective adjustment scheme described in Frierson (2007) is used in all experiments to adjust conditionally unstable profiles of temperature and specific humidity.

The scheme adjusts the vertical profile of temperature to the virtual psuedoadiabat and the vertical profile of humidity to a fixed relative humidity of 70%. Higher and lower relative humidities both produce an intensified Hadley circulation (Frierson, 2007). These profiles are calculated using the moist static energy of a parcel in the boundary layer (Yu and Neelin, 1997) and are not drawn from an offline database of profiles. After the reference profiles of T_{ref} and q_{ref} are calculated, the specific humidity and temperature profiles are relaxed as a first guess according to

$$\delta q = -\frac{q - q_{ref}}{\tau_{SBM}} \tag{40}$$

$$\delta T = -\frac{T - T_{ref}}{\tau_{SBM}} \tag{41}$$

where τ_{SBM} is the convection relaxation time, here taken to be 10 hours. The modeled climate is relatively insensitive to τ_{SBM} so long as it is equal to or faster than the timescale of large-scale condensation (approximately 12 hours) (Frierson, 2007).

As a diagnostic for whether the convection scheme initiates shallow or deep convection, the hypothetical precipitation due to drying and warming are

$$P_{\delta q} = -\int_{p_0}^{p_{LZB}} \delta q \frac{dp}{g_0} \tag{42}$$

$$P_{\delta T} = \int_{p_0}^{p_{LZB}} \frac{c_p}{L_v} \delta T \frac{dp}{g_0} \tag{43}$$

where p_{LZB} is the level of zero buoyancy for a parcel from the surface layer. For the convective scheme to activate at all $P_{\delta T}$ must be positive, which indicates a net warming in the column from condensation. If $P_{\delta q}$ is positive, the column is more moist than the reference profile and thus net precipitation must occur, whereas if it is negative then the convection can produce no net precipitation.

The deep convection scheme is initiated if $P_{\delta T} > 0$ and $P_{\delta q} > 0$. As these quantities are not guaranteed to be equal, the scheme requires that the reference temperature profile be adjusted so that $P_{\delta T} = P_{\delta q}$. The adjustment to T_{ref} necessary to conserve enthalpy is given by

$$T_{ref2} = T_{ref} - \frac{\Delta k}{c_p} \tag{44}$$

where T_{ref2} is the adjusted reference profile and Δk is the adjustment to enthalpy defined by

$$\Delta k = \frac{1}{\Delta p} \int_{p_0}^{p_{LZB}} -(c_p T + L_v q - c_p T_{ref} - L_v q_{ref}) dp \tag{45}$$

The adjusted reference temperature and original reference humidity profiles are then used in Eq. 41 and Eq. 40.

In the case of negative $P_{\delta q}$, the shallow convection scheme is initiated. The scheme first calculates the highest level p_{shall} for which the total precipitation is exactly zero,

$$0 = \int_{p_0}^{p_{shall}} \delta q \; dp \tag{46}$$

The scheme proceeds as before, with the reference temperature profile adjusted to conserve enthalpy and the reference humidity profile preserved. However, the scheme limits the depth of the temperature and humidity adjustments to between p_0 and p_{shall} rather than p_0 and p_{LZB}. The shallow convection scheme can be modified to adjust the reference temperature and humidity profiles without altering the depth of convection, however the impact on the resulting precipitation and vertical motion characteristics is negligible (Frierson, 2007).

The condensational heating or cooling in a given layer resulting from large-scale condensation or moist convective adjustment is simply

$$Q_c = -\frac{L_v}{c_p}\delta q \tag{47}$$

8 Radiation

Idealized general circulation models often relax the temperature field to some equilibrium climate through Newtonian cooling. However, this limits the ability of the circulation to shape the simulated climate. Further, a prescribed temperature field consistent with earth's atmosphere implicitly includes the effect of eddies on the circulation. Prescribing such a temperature field to both axisymmetric and non-axisymmetric circulations may understate the differences between the two.

This model employs a simplified radiative transfer scheme. Rather than prescribed temperatures, the atmosphere has prescribed shortwave optical depths associated with ozone and water vapor, and a longwave optical depth associated with water vapor and greenhouse gases. Longwave absorption and emission and shortwave absorption is "grey" with the emissivity equal at all wavelengths. No line-by-line or correlated-line methods are employed. The model instead uses bulk radiative fluxes.

The insolation R_S at the top of the atmosphere has no diurnal cycle or seasonality and is defined by

$$R_S = R_{S0}\left[1 + \frac{\Delta_s}{4}\left(1 - 3\sin^2(\phi)\right)\right] \tag{48}$$

where $R_{S0} = 968.7$ W/m^2 is the net solar constant taking into account an albedo of 0.29 and $\Delta_s = 1.4$ is the meridional variation of insolation.

8.1 Optical Depth

The optical depth of a medium measures the fraction of incident radiation that is transmitted through the medium. In this model it is a basic measure of the opacity of the

atmosphere to longwave and shortwave radiation and factors directly into the equations of radiative transfer.

Shortwave absorption by the atmosphere is split into two idealized functional forms, the optical depth associated with stratospheric ozone absorption (τ_s) and the optical depth associated with water vapor absorption (τ_{wv}). Stratospheric absorption is a new addition to the model to fix its poor representation of the stratosphere (Frierson et al., 2006) and introduce a quasi-realistic zonal-mean climate.

The climatological zonal-mean temperatures and zonal winds from model simulations with and without stratospheric ozone absorption are shown in Fig. 6.1 and Fig. 6.2. The stratosphere in the simulation without this shortwave optical depth is unrealistic, with a climate that essentially decays upward from what is set in the troposphere. An excessively cold polar lower stratosphere results in the extension of the tropospheric eddy-driven jets 100 hPa above the subtropical jets, while in earth's atmosphere the two are at similar altitudes. As the zonal-mean zonal wind is in approximate thermal wind balance, the most direct approach to fixing the stratosphere and the eddy-driven jets is to modify the temperature field through shortwave absorption. This conserves energy within the model and is more analogous to earth's atmosphere, unlike the application of a specific diabatic heating distribution.

In earth's climate, the concentration of ozone peaks at approximately 80 hPa at the poles with a 70 hPa half-width and at approximately 30 hPa at the equator with a 20 hPa half-width (Fig. 6.3), with the total column ozone peaking at the poles. To model the

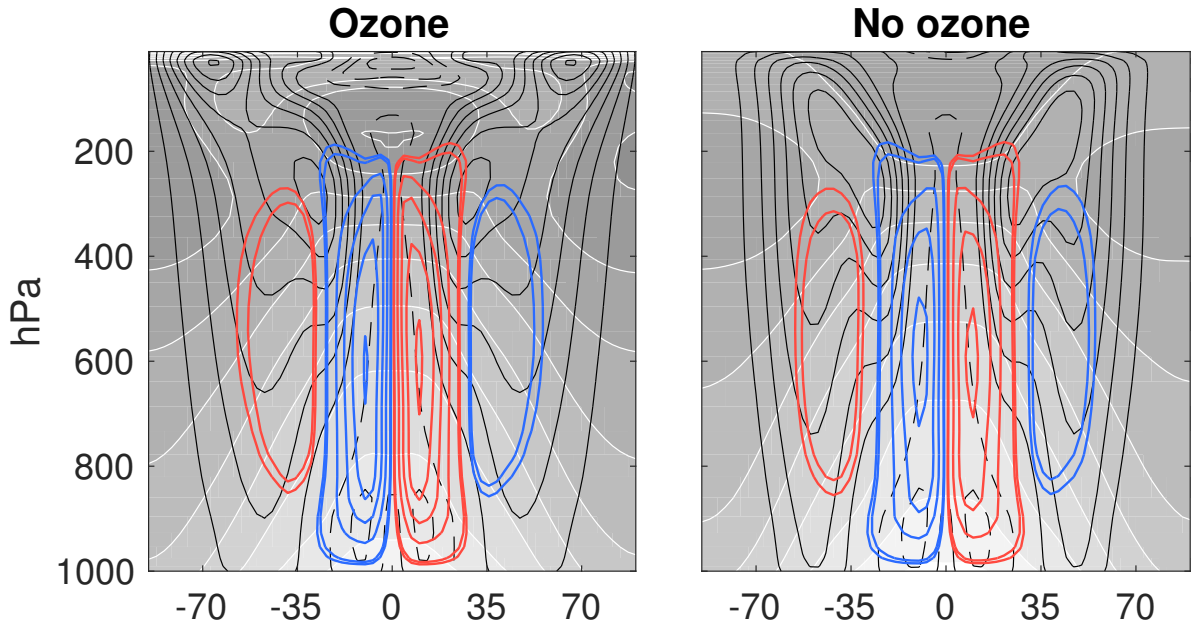

Figure 6.1: Zonal-mean temperature (shading), zonal wind (contours, every 5 m/s, negative values dashed), and the mean meridional streamfunction (every 40×10^9 kg/s from 20×10^9, red indicates clockwise flow) from the model simulations (left) with and (right) without ozone.

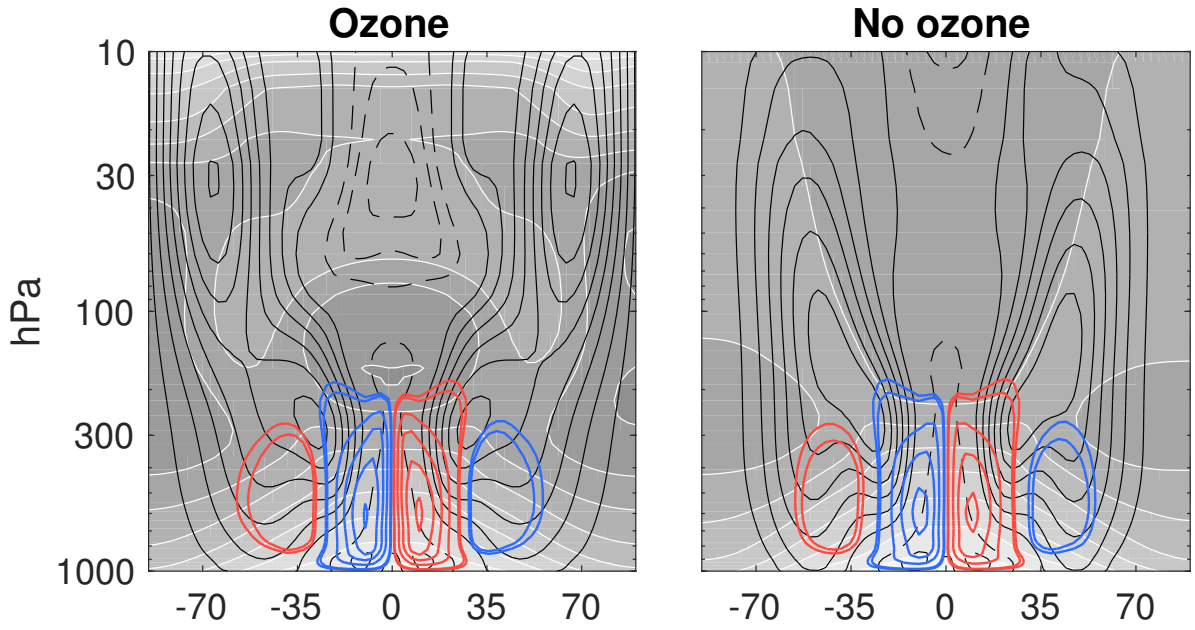

Figure 6.2: As in Fig. 6.1 but with a stratospheric perspective.

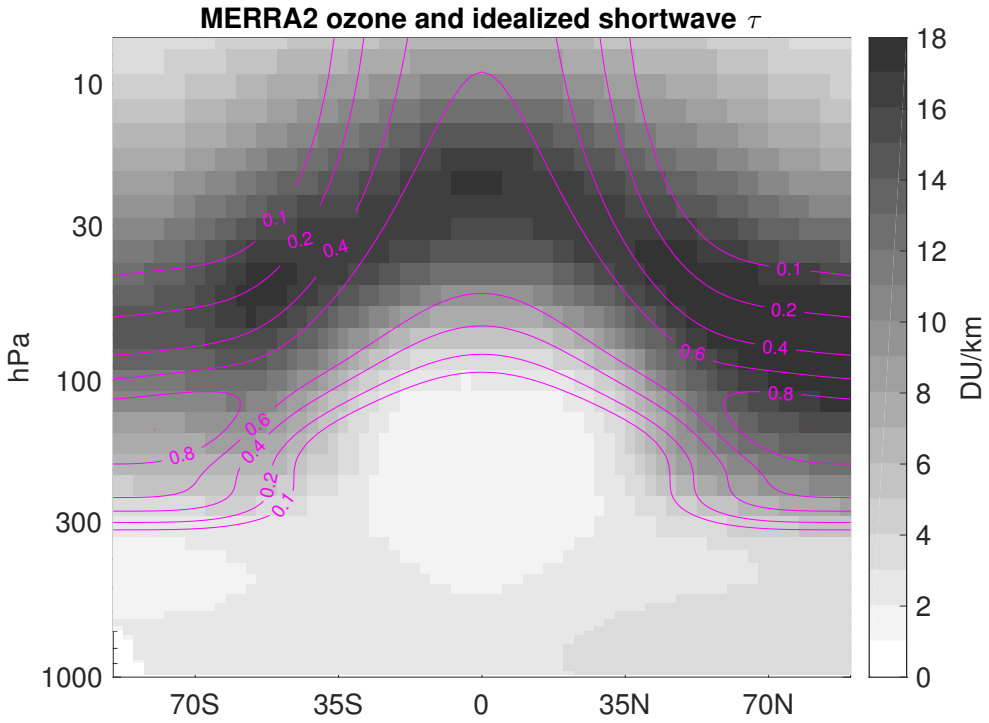

Figure 6.3: Ozone concentrations (Dobson units per km) in shading from the MERRA2 reanalysis, and the prescribed shortwave cross-section (arbitrary units) in magenta contours.

effects of ozone absorption, the shortwave optical depth is prescribed as

$$\tau_s(p) = 0.1(\tau_{0,s}\sqrt{\pi})\Bigg\{ \cos^2(0.3\phi) \cdot \left[\cos^2(0.3\phi) \cdot \operatorname{erf}\left(\frac{p - p_{center}}{p_{width}}\right) + 1\right] + \exp\left(-8\cos^4(\phi)\right)\left[\operatorname{erf}\left(\frac{p-240}{60}\right) + \operatorname{erf}\left(\frac{p-150}{60}\right) + 2\right]\Bigg\} \tag{49}$$

where $\tau_{0,s} = 0.045$ is the maximum fraction of solar radiation absorbed in the column, p_{center} and p_{width} are the central pressure and half-width of the psuedo-ozone distribution, defined as

$$p_{center} = 130 - 100\cos^2(0.8 \cdot \phi) \tag{50}$$

$$p_{width} = 45 + 20\sin^6(\phi) \tag{51}$$

Fig. 6.4 displays the resulting shortwave absorption cross-section in arbitrary units for this optical depth distribution, produced by taking the derivative of Eq. 49 with respect to pressure. While the polar ozone distribution is shifted downward in pressure relative to observations, it still generally reflects the structure of observed ozone (Fig. 6.3).

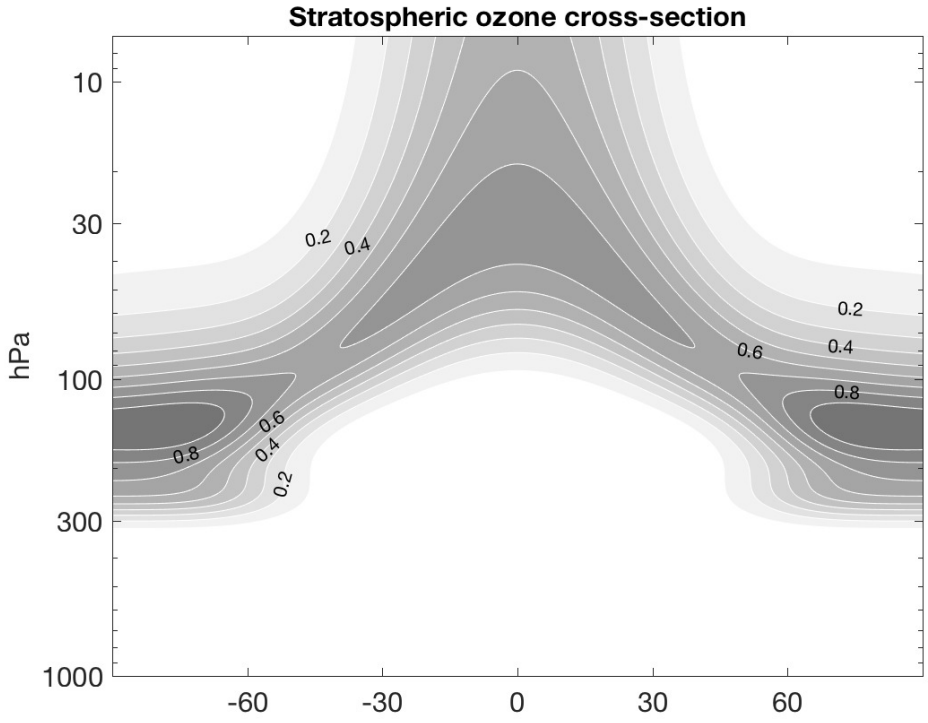

Figure 6.4: Ozone cross-section (arbitrary units), where dark colors indicate a higher cross-section.

Stratospheric jets are produced by adding a psuedo-ozone cross-section that peaks higher in the tropical than extratropical stratosphere (Fig. 6.3 and the first term of Eq. 49). Further, the eddy-driven jet can be lowered toward the altitude of the subtropical jet by extending the shortwave cross-section in the extratropics down to the pressure level of the tropopause (approximately 300 hPa; Fig. 6.3 and the second term of Eq. 49). Ozone absorption effects are quasi-linear within the model up to approximately 10 hPa, which is

the fourth highest nominal model level. It is unclear whether the departure from linearity is physical or merely due to proximity to the model lid.

The longwave optical depth is modeled as latitude-dependent to model the effects of water vapor, with the surface optical depth τ_0 defined as

$$\tau_0(\phi) = \tau_{0,eq} + (\tau_{0,p} - \tau_{0,eq}) \sin^2(\phi) \tag{52}$$

where $\tau_{0,eq} = 6$ and $\tau_{0,p} = 2.0$ are the longwave optical depths at the surface at the equator and the pole. The longwave optical depth decreases with height as

$$\tau(p, \phi) = \tau_0(\phi) \left[f_l \left(\frac{p}{p_0} \right) + (1 - f_l) \left(\frac{p}{p_0} \right)^4 \right] \tag{53}$$

where f_l weights the linear and quartic terms, respectively, here taken as $f_l = 0.1$. The linear term is added so that the stratosphere does not have an unrealistically-long radiative timescale. Fig. 6.5 shows the longwave optical depth for the full atmosphere.

8.2 Radiative Heating and Cooling

Shortwave and longwave radiation is approximated with the plane-parallel, two-stream model. The upward and downward longwave fluxes are

$$\frac{dF_\uparrow}{d\tau} = F_\uparrow - \sigma T^4 \tag{54}$$

$$\frac{dF_\downarrow}{d\tau} = \sigma T^4 - F_\downarrow \tag{55}$$

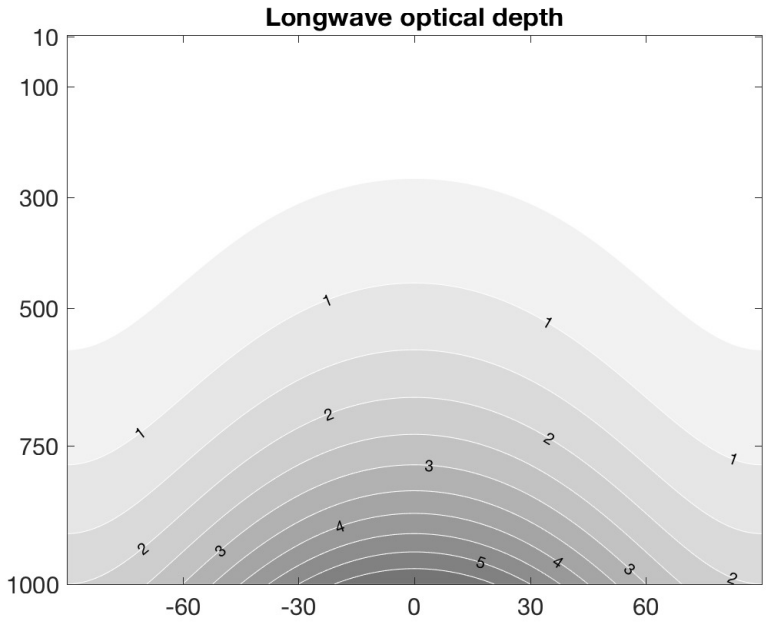

Figure 6.5: Longwave optical depth.

where $F_\uparrow$ and $F_\downarrow$ are the upward and downward longwave fluxes and σ is the Stefan-Boltzmann constant. Because shortwave radiation is only absorbed and not emitted, its radiative flux equation is simply

$$\frac{dR_\downarrow}{d\tau} = R_\downarrow \tag{56}$$

Radiative heating and cooling in pressure coordinates is given by

$$Q_{rad} = \frac{g}{c_p}\frac{d(F_\uparrow - F_\downarrow - R_\downarrow)}{dp} \tag{57}$$

9 Dynamical Core

Taking into account the parameterized processes described before, the full set of primitive equations the model solves is

$$\frac{\partial u}{\partial t} + \vec{v_h} \cdot \nabla u + \omega \frac{\partial u}{\partial p} = fv + \frac{uv \tan(\phi)}{a} - \frac{1}{a \cos(\phi)} \frac{\partial \Phi}{\partial \lambda} + g \frac{\partial \tau_\lambda}{\partial p} + \frac{\partial u}{\partial t}_{diff} \tag{58}$$

$$\frac{\partial v}{\partial t} + \vec{v_h} \cdot \nabla v + \omega \frac{\partial v}{\partial p} = -fu + \frac{u^2 \tan(\phi)}{a} - \frac{1}{a} \frac{\partial \Phi}{\partial \phi} + g \frac{\partial \tau_\phi}{\partial p} + \frac{\partial v}{\partial t}_{diff} \tag{59}$$

$$\frac{\partial T}{\partial t} + \vec{v_h} \cdot \nabla T + \omega \frac{\partial T}{\partial p} = \frac{R_d T \omega}{c_p p} + Q_{rad} + Q_{diff} + Q_c + \frac{g}{c_p} \frac{\partial S}{\partial p} \tag{60}$$

$$\frac{\partial \Phi}{\partial ln(p)} = -R_d T \tag{61}$$

$$\nabla \cdot \vec{v_h} + \frac{\partial \omega}{\partial p} = 0 \tag{62}$$

where F_λ, F_ϕ, and Q have been written explicitly in terms of the boundary layer fluxes and diffusion and $f = 2\Omega \sin \phi$ is the planetary vorticity.

Water vapor is modeled using the standard tracer equation with a surface evaporative flux and condensation as source/sink terms,

$$\frac{\partial q}{\partial t} + \vec{v_h} \cdot \nabla q + \omega \frac{\partial q}{\partial p} = g \frac{\partial E}{\partial p} - \frac{c_p}{L_v} Q_c \tag{63}$$

Eq. 24 provides a surface pressure tendency based on divergence of mass into or out of the column. This simple prognostic lends itself to the choice of sigma coordinates for the vertical discretization of the model.

9.1 Vertical Differencing

A sigma coordinate system casts the equations of motion in terms of $\sigma = p/p_s$, where p_s is the surface pressure. Allowing the surface pressure to vary while fixing the values of σ for each vertical level requires that the pressure of each vertical level vary in time.

The vertical coordinate and differencing scheme used in this model is described in Simmons and Burridge (1981). The atmosphere is divided into N layers, with the pressures $p_{k-1/2}; k = 1 : N + 1$ bounding each layer. Each layer has a thickness of

$$\Delta p_k = p_{k+1/2} - p_{k-1/2} \tag{64}$$

The surface pressure p_s is $p_{N+1/2}$ while the top of the atmosphere is $p_{1/2}$, which is here taken to be zero. The pressure at the center of each layer is then defined as

$$p_{k-1/2} = A_{k-1/2} p_{ref} + B_{k-1/2} p_s, \;\; k = 1 : N + 1 \tag{65}$$

where p_{ref} is the global-mean surface pressure. The A coefficients define isobaric levels while the B coefficients define sigma levels. Here we set all A coefficients to zero so that the model reduces to sigma coordinates,

$$p_{k-1/2} = \sigma_{k-1/2} p_s, \;\; k = 1 : N + 1 \tag{66}$$

The sigma coordinates here are defined as in Frierson et al. (2006) as

$$\sigma = e^{(-5(0.05\tilde{z}+0.95\tilde{z}^3))} \tag{67}$$

where $\tilde{z}$ is evenly spaced over the unit interval with 41 levels. These sigma values are displayed in Fig. 6.6. Assuming a global-mean surface pressure of 1000 hPa, there are 11 model levels below 850 hPa to ensure an accurate representation of boundary layer processes and 10 levels above 100 hPa to reasonably represent stratospheric processes. The

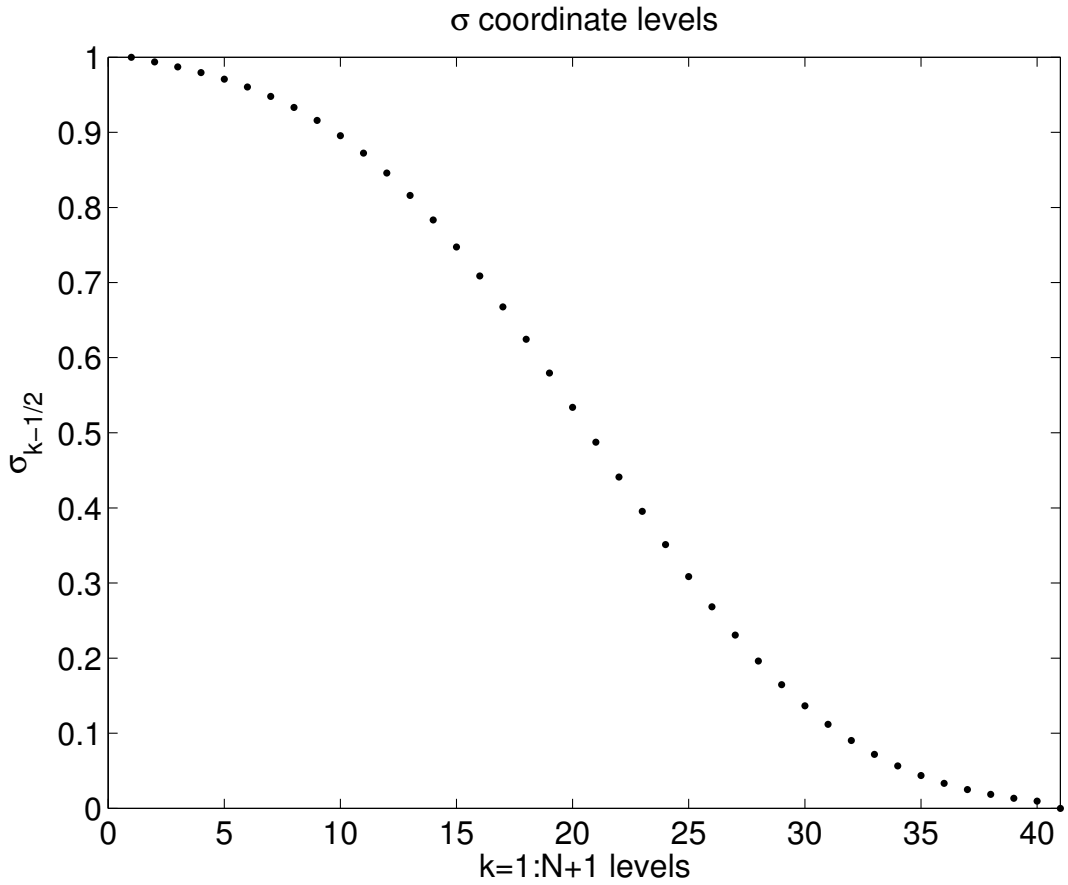

Figure 6.6: The sigma values for all 41 levels in the model.

central pressure of each layer, or "full level" pressures, can be defined as

$$\ln p_k = \frac{1}{\Delta p_k}\left(p_{k+1/2}\ln p_{k+1/2} - p_{k-1/2}\ln p_{k-1/2}\right) - 1 \tag{68}$$

9.2 Discretization

Rather than solving prognostic equations for the wind field, which are vector quantities, the model instead solves prognostic equations for relative vorticity and divergence. The advantages to this formulation are twofold: vorticity and divergence are scalars that are coordinate-system invariant and the resulting elliptic equations are trivial to solve in spectral space.

The surface pressure tendency is given by the divergence of mass within the discretized layers,

$$\frac{\partial p_s}{\partial t} = -\sum_{k=1}^{N} D_k \tag{69}$$

where the divergence operator D is defined by

$$D_k = \nabla \cdot (\vec{v}_{h,k}\Delta p_k) \tag{70}$$

The vertical advection operator $W_k(\epsilon)$, for any quantity or tracer ϵ, is defined as

$$W_k(\epsilon) = \frac{-1}{2\Delta p_k}\left(M_{k+1/2}(\epsilon_{k+1} - \epsilon_k) + M_{k-1/2}(\epsilon_k - \epsilon_{k-1})\right) \tag{71}$$

where M is the downward mass flux per unit area across the $k+1/2$ level, given by

$$M_{k+1/2} = -\sum_{r=1}^{k} D_r - \frac{\partial p_{k+1/2}}{\partial t} = -\sum_{r=1}^{k} D_r - \sigma_{k+1/2}\frac{\partial p_s}{\partial t} \tag{72}$$

A second-order centered difference scheme is used for vertical advection.

The zonal (Eq. 58) and meridional (Eq. 59) momentum equations can be tranformed into

$$\frac{\partial u_k}{\partial t} = (f+\zeta_k)v_k - \frac{1}{acos(\phi)}\left(\frac{\partial E_k}{\partial \lambda} + R_d T_k \frac{\partial \ln p_k}{\partial \lambda}\right) + W_k(u) \tag{73}$$

$$\frac{\partial v_k}{\partial t} = -(f+\zeta_k)u_k - \frac{1}{a}\left(\frac{\partial E_k}{\partial \phi} + R_d T_k \frac{\partial \ln p_k}{\partial \phi}\right) + W_k(v) \tag{74}$$

where ζ_k is the vertical component of relative vorticity,

$$\zeta_k = \frac{1}{a\cos\phi}\left(\frac{\partial v_k}{\partial \lambda} - \frac{\partial (u_k \cos\phi)}{\partial \phi}\right) \tag{75}$$

and E_k is the mechanical energy, or the sum of the kinetic and potential energies,

$$E_k = \Phi_k + \frac{1}{2}\left(u_k^2 + v_k^2\right) \tag{76}$$

The quantities U_k and V_k are defined as

$$U_k = (f+\zeta)v_k - \frac{R_d T_k}{a\cos\phi}\frac{\partial \ln p_s}{\partial \lambda} + W_k(u) \tag{77}$$

$$V_k = -(f+\zeta)u_k - \frac{R_d T_k}{a}\frac{\partial \ln p_s}{\partial \phi} + W_k(v) \tag{78}$$

Additionally, the expanded divergence operator is

$$D_k = \frac{1}{a\cos\phi}\left(\frac{\partial u_k}{\partial \lambda} + \frac{\partial (v_k \cos\phi)}{\partial \phi}\right) \tag{79}$$

The time tendencies of Eq. 75 and Eq. 79 can now be written in terms of U_k and V_k,

$$\frac{\partial \zeta_k}{\partial t} = \nabla \cdot T_{\perp k} \tag{80}$$

$$\frac{\partial D_k}{\partial t} = \nabla \cdot T_k - \nabla^2 E_k \tag{81}$$

where $T_k = (U_k, V_k)$ and $T_{\perp k} = (V_k, -U_k)$.

The thermodynamic energy equation is discretized similarly,

$$\frac{\partial T_k}{\partial t} + \vec{v}_h \cdot \nabla T_k = \frac{R_d T_k}{c_p}\left(\frac{\omega}{p}_k\right) + \frac{Q_{rad} + Q_c + Q_{diff} + (g/c_p)(\partial S/\partial p)}{c_p} \tag{82}$$

where the pressure velocity term is

$$\left(\frac{\omega}{p}\right)_k = -\frac{1}{\Delta p_k}\left[(\ln p_{k+1/2} - \ln p_{k-1/2}) + (\ln p_k - \ln p_{k-1/2})\right]\sum_{r=1}^{k} \nabla \cdot (v_r \Delta p_r) + v_k \cdot \left(\frac{\nabla p}{p}\right)_k \tag{83}$$

Finally, $\ln p_s$ rather than p_s is a prognostic variable,

$$\frac{\partial \ln p_s}{\partial t} = -\frac{1}{p_s}\sum_{k=1}^{N} \nabla \cdot (v_k \Delta_k p) \tag{84}$$

This is a more useful formulation as the natural logarithm of pressure is used in the geopotential equation and in all of the pressure gradient terms. However, the model cannot

conserve mass using $\ln p_s$. An additive constant is applied to surface pressure at each time step to ensure that the global-mean surface pressure does not change. Humidity and energy are also not conserved exactly - while an additive constant is applied to ensure conservation of thermal and kinetic energy, a hole-filling algorithm is used to ensure humidity advection does not produce negative values.

9.3 Spectral Formulation

The spectral dynamical core of the model solves the prognostic equations for relative vorticity, divergence, temperature, and surface pressure. All variables are expressed in terms of a truncated series of spherical harmonic functions. For any variable $\psi(\lambda, \phi)$, its spectral representation is given by

$$\psi(\lambda, \phi) = \sum_{m=-\infty}^{\infty} \sum_{l=|m|}^{\infty} \hat{\psi}_{l,m} Y_{l,m}(\lambda, \phi) \tag{85}$$

where m is the zonal wavenumber and $l - m$ is the meridional wave number. $Y_{l.m}$ are the spherical harmonic functions, which are the product of the associated Legendre polynomial function $P_{l,m}$ and a Fourier mode,

$$Y_{l,m}(\lambda, \phi) = N_{l,m} P_{l,m}(\phi) e^{im\lambda} \tag{86}$$

where $N_{l,m}$ is a normalizing coefficient based on l and m,

$$N = \sqrt{(2l+1)\frac{(l-m)!}{(l+m)!}} \tag{87}$$

The associated Legendre functions have the form

$$P_{l,m}(\mu) = \frac{(1-\mu^2)^{\frac{m}{2}}}{2^l l!} \frac{d^{l+m}(\mu^2-1)^l}{d\mu^{l+m}} \tag{88}$$

where $\mu = \sin\phi$.

The complex coefficients $\hat{\psi}_{l,m}$ can be determined through the integral

$$\hat{\psi}_{m,l} = \frac{1}{4\pi} \int \int \psi(\lambda,\phi) Y_{l,m}(\lambda,\phi) d\lambda d\phi \tag{89}$$

For practical reasons, an infinite number of zonal wavenumbers cannot be retained. Typically, M zonal wavenumbers are retained, with the maximum meridional wavenumber given by $T = M$. This "triangular truncation" will be used for all experiments. All dynamical processes are solved in the spectral domain, while physical processes (e.g., convection, surface fluxes) are solved in the grid domain. Two transform steps between spectral and physical space are necessary at each time step.

For a given spectral resolution with M total wavenumbers, the model requires at least $(3M+1)/2$ latitude and at least $3M+1$ longitude grid points in physical space. This physical space grid is a so-called "Gaussian grid". Gaussian latitudes are defined as the zeros of the $3M+1$'th Legendre polynomial, while all longitudes are equally-spaced. Nevertheless, the resulting grid is nearly evenly-spaced in latitude.

9.4 Integration Scheme

This model uses a semi-implicit leapfrog time stepping scheme to integrate the model over timesteps of length Δt, here taken to be 600 seconds. Explicit schemes solve the future state of a system of equations based on its current state, while implicit schemes solve for the future and present states of a system simultaneously. Implicit schemes are thus computationally more expensive but allow a longer time step by reducing the integration error. As the name implies, the scheme used here includes both explicit and implicit integration.

As an illustration of the model's integration scheme, consider the state of the model as V and the operator N as an operator describing the future evolution of the system. The operator N is assumed to be linear and split into an explicit and implicit component, $N = N_e + N_i$. The centered semi-implicit leapfrog scheme is then

$$\frac{\partial V}{\partial t} \approx \frac{V(t+1) - V(t-1)}{2\Delta t} = N_e(V(t)) + N_i(\alpha V(i+1) + (1-\alpha)V(i-1)) \qquad (90)$$

where α defines a centered difference scheme when $\alpha = 0.5$. The particular form of the implicit and explicit operators are further described in the GFDL Spectral Core manual, but the essence is that terms relevant for gravity wave propagation are treated implicitly so that they do not severely restrict the time step of the model.

At initialization, ζ, D, T, p_s, u, and v are specified in the physical domain, from which ζ, D, T, and $\ln p$ can be known in the spectral domain. The model is initialized at a state of rest with no circulation and a temperature and specific humidity of 250 K and 3.0×10^{-6} kg/kg everywhere, respectively. Surface pressure is uniform at 1000 hPa.

Initializing the model with no zonal asymmetries is sufficient to produce an axisymmetric climate. For the non-axisymmetric simulations, a small perturbation relative vorticity of 1.0×10^{-7} s^{-1} is applied to the second grid point in latitude and longitude with the origin in the arbitrary southwest corner of the model (e.g., close to one pole).

The control experiments are run for a period of 4000 days, with the final 1000 days used for analysis. Incremental experiments are run for 2000 days, with the final 1000 days used for analysis. The climate of the model generally adjusts to external forcings within 100 to 200 days.

The model's workflow is as follows for each time step:

1. Compute physical grid tendencies of u, v, T, and tracers due to radiation, diffusion, surface fluxes, large-scale condensation, and convective adjustment.

2. Calculate global additive constants to ensure mass, energy, and tracer conservation.

3. Compute the full and half-level pressures based on surface pressure and the geopotential.

4. Compute surface pressure gradients and use these along with the physical grid divergence to calculate vertical mass fluxes, the surface pressure tendency, and the pressure gradient term in the vorticity, divergence, u, and v equations.

5. Calculate the vertical advection of u, v, and T and add them to their respective tendency equations.

6. Find $(\zeta + f)v$ and $-(\zeta + f)u$ and add these to the u, v, and T tendencies.

7. Take the divergence and curl of the u and v tendencies in physical space to find the ζ and D tendencies in the spectral domain.

8. Add horizontal temperature advection to the T tendency and convert the T tendency to the spectral domain.

9. Calculate the mechanical energy on the grid at time t, transform to the spectral domain, and add $-\nabla^2 E$ to the spectral divergence tendency.

10. Use the semi-implicit scheme to correct the T, D, and p_s tendencies.

11. Compute the tendencies of ζ, D, and T in the spectral domain due to damping. With limited spectral resolution, the enstrophy cascade to higher wavenumbers is parameterized as fourth-order hyperdiffusion, $-\nu\nabla^4$.

12. Use the leapfrog scheme to integrate ζ, D, T, and $\ln p_s$ to $t + \Delta 4$. A Robert-Asselin filter is applied to damp spurious oscillations between timesteps inherent to the leapfrog method. The filter nudges the current model state to the mean of the future and previous model states,

$$V(t) = (1 - 2r)V(t) + r(V(t + 1) + V(t - 1)) \tag{91}$$

where r is the Robert-Asselin coefficient, here taken to be 0.03. While it suppresses the spurious computational mode in the leapfrog scheme it does slightly impact the mean value of the model state. Such an impact is inevitable and cannot be avoided in this time-stepping formulation.

13. Compute u and v from ζ and D in the spectral domain at time $t + \Delta t$. Convert ζ, D, u, v, T, $\ln p_s$, and p_s to physical space values at $t + \Delta t$.

14. Advect physical space tracers such as moisture. Begin with an updated tracer field at $t + \Delta t$ based on physical tendencies. Advect tracers at $t + \Delta t$ horizontally using finite-volume advection to create an updated $t + \Delta t$ field, then advect the updated field vertically to create a yet-again-updated $t + \Delta t$ field. Perform hole-filling as necessary to prevent negative tracer values. Apply the Robert-Asselin filter. Advection is done with velocities at time t.